UNIVERSITY OF SOUTHAMPTON

FACULTY OF ENGINEERING AND THE ENVIRONMENT

Civil, Maritime and Environmental Engineering & Science

Some factors affecting the cyclic stiffness of railway formation material

by

Letisha Rorke

Thesis towards a degree of Doctor of Philosophy

April 2016

UNIVERSITY OF SOUTHAMPTON

ABSTRACT

FACULTY OF ENGINEERING AND THE ENVIRONMENT
Civil, Maritime and Environmental Engineering & Science

Doctor of Philosophy

SOME FACTORS AFFECTING THE CYCLIC STIFFNESS OF RAILWAY FORMATION MATERIAL

by Letisha Rorke

Engineered pavements are a key part of the transport asset that includes flexible road pavements, railway formations and airport runways. Their design, construction and maintenance need to be economically and environmentally optimised, while meeting serviceability criteria over the design life of the pavement. The main serviceability criteria used for railway track design are the permanent deformation and track stiffness. Subgrade stiffness influences the design depth of ballast and compacted formation layers are used to improve stiffness and reduce stresses induced in the natural subgrade. The track stiffness also influences vehicle/track interaction and wear, energy required for movement, and ride quality. Knowledge of the stiffness is required for safe and economic design of the railway track structure. Several factors influence the stiffness or resilient modulus of compacted formation material including stress state, material type, and soil physical state (density and water content). A laboratory investigation was conducted on a representative subballast material, at a range of water contents, using a Cyclic Triaxial Apparatus and Cyclic Hollow Cylinder Apparatus to investigate these aspects. The resilient modulus of the clayey sand material reduced as the applied deviator stress increased, and increased under higher confining stresses and matric suction. It was found that the resilient modulus increased by a factor of six due to a reduction in water content, and thus the increase in matric suction. Principal stress rotation, representative of train induced stresses, reduced the measured resilient modulus by approximately 13% for optimum water content specimens with reducing influence for dry of optimum specimens. The results from this work emphasise the benefit of matric suction, and thus the need for well drained formation layers. They also highlight the risk of reduced stiffness and increased deformation of railway formation subject to long periods of rainfall or wetting and the potential impact of predicted climate change. Simplified stress path testing using a Cyclic Triaxial Apparatus overestimates resilient modulus, especially for saturated material subject to large number of cycles. However, the use of more advanced testing of the resilient modulus using the Cyclic Hollow Cylinder Apparatus is only suggested where high cyclic shear stresses are expected.

Contents

List of Figures

List of Tables

Declaration of Authorship

I, Letisha Rorke , declare that the thesis entitled *Some factors affecting the cyclic stiffness of railway formation material* and the work presented in the thesis are both my own, and have been generated by me as the result of my own original research. I confirm that:

- this work was done wholly or mainly while in candidature for a research degree at this University;
- where any part of this thesis has previously been submitted for a degree or any other qualification at this University or any other institution, this has been clearly stated;
- where I have consulted the published work of others, this is always clearly attributed;
- where I have quoted from the work of others, the source is always given. With the exception of such quotations, this thesis is entirely my own work;
- I have acknowledged all main sources of help;
- where the thesis is based on work done by myself jointly with others, I have made clear exactly what was done by others and what I have contributed myself;

Signed:.....

Date:.....

Acknowledgements

I am both thankful and grateful.

- Engineering and Physical Science Research Council, EPSRC. Track for the 21st century (Track21) project grant EP/H044949/1.
- Network Rail - University of Southampton Strategic Research Partnership.
- Aurecon SA.
- Supervisory team: Professor Chris Clayton and Professor William Powrie.
- Laboratory technician: Mr Harvey Skinner.
- Dr Snehasis Tripathy at Cardiff University.
- Family and friends (old and new).

I would like to specially thank Prof Chris for his patience, encouragement and diligence.

Aan God al die lof en eer.

Nomenclature

Abbreviations

AASHTO	American Association of State Highway and Transportation Officials
ASTM	American Society for Testing and Materials
BS	British standard
CBR	California bearing ratio
CSL	Critical state line
CSS	Cyclic simple shear apparatus
CTX	Cyclic triaxial apparatus
EF	Engineered fill
HCA	Cyclic hollow cylinder apparatus
LVDT	Linear variable differential transformer
MR_{PSR}	Modulus ratio of principal stress rotation influence
MR_s	Modulus ratio of suction influence
NCHRP	National Cooperative Highway Research Program
NR	Network Rail
NSW	New South Wales
OCR	Overconsolidation ratio
ORE	Office for research and experiments
PI	Plasticity index
PSD	Particle size distribution
PSR	Principal stress rotation
QS	Soil quality class
RailCorp	Rail Corporation
SA	South Africa
SB	Subballast layer
SP	Stress path
SSB	Special subballast layer
SSCC	Suction stress characteristic curve
SWRC	Soil water retention curve
TC	Triaxial compression

TE	Triaxial extension
TT	True triaxial
UEF	Un-engineered fill
UIC	International Union of Railways
UK	United Kingdom
USA	United States of America

List of Latin symbols

a_w	Water activity
b	Relative relationship of intermediate principal stress
$c^{'}$	Effective cohesion intercept
e	Void ratio
g	Gravitational acceleration
h	height
k_n	Regression coefficient
m_w	Mass of water
m_s	Mass of solids
n	Porosity
p	Mean principal stress
p_a	Atmospheric pressure
p_i	Internal cell pressure
p_o	External (outer) cell pressure
p_r	Net mean stress reference pressure
q	Deviator stress
q_{cyc}	Cyclic deviator stress or maximum deviator stress difference
q_{max}	Maximum deviator stress
q_{min}	Minimum deviator stress
r_i	Inner radius
r_o	Outer radius
u	neutral stress
u_a	Pore-air pressure
u_w	Pore-water pressure
u_{w-sat}	Positive pore-water pressure
u_i	Radial movement of specimen wall (internal)
u_o	Radial movement of specimen wall (outer)
w	Gravimetric water content
w_i	Compaction gravimetric water content
w_f	Gravimetric water content after testing
w_r	Residual gravimetric water content

A	Activity
A_t	Cross-sectional area (total) through a soil mass
A_a	Cross-sectional area of air
E	Young's modulus
$E_{compaction}$	Compaction energy per unit volume
E_p	Potential energy
G	Shear modulus
G_0	Small strain shear modulus
H	Modulus of the soil structure with respect to matric suction
K_0	Earth pressure coefficient at rest
M	Molecular mass
M_R	Resilient modulus
M_T	Torque
N	Number of load cycles
P	Period
R	Universal gas constant
S	Sleeper length
S_e	Effective degree of saturation
S_r	Degree of saturation
T	Temperature
V	Total volume
V_v	Volume of voids
V_w	Volume of water
W	Axial (vertical) load

List of Greek symbols

α	Angle of major principal stress relative to vertical
χ	Bishop's effective stress parameter
ϵ	Normal strain
ϵ_R	Recoverable (elastic) strain
ϵ_V	Volumetric strain
$\overline{\epsilon}_r$	Average radial strain
$\overline{\epsilon}_\theta$	Average circumferential strain
$\overline{\epsilon}_z$	Average axial strain
γ	Shear strain
ν	Specific volume
$\overline{\gamma}_{\theta,z}$	Average shear strain
$\phi^{'}$	Effective mobilised angle of shearing resistance
π	Osmotic suction
ψ	Total suction

ψ_a	Air entry pressure
ψ_d	Displacement pressure
ψ_m	Matric suction
σ	Total stress
$\sigma^{'}$	Effective stress
σ_{cap}	Capillary stress
σ_n	Net normal stress
σ_{pc}	Physiochemical stress
σ_s	Suction stress
σ_{sb}	Stress directly beneath the sleeper
σ_r	Radial stress
$\overline{\sigma}_r$	Average radial stress
$\overline{\sigma}_\theta$	Average circumferential stress
$\overline{\sigma}_z$	Average vertical stress
ρ_d	Dry density
σ_C	Intergranular stress
σ_{C0}	Intergranular bonding stress
σ_H	Horizontal stress
σ_V	Vertical stress
σ_1	Major principal stress
σ_2	Intermediate principal stress
σ_3	Minor principal stress
τ	Shear stress
τ_{oct}	Octahedral shear stress
$\overline{\tau}_{\theta,z}$	Average shear stress
θ	Angular circumferential displacement
θ_w	Volumetric water content
θ_r	Residual volumetric water content
θ_s	Saturated volumetric water content
υ	Poisson's ratio
Δ	Indicates the magnitude of change
Θ	Bulk stress (total stress)
Θ_i	Intergranular bulk stress
Θ_{net}	Net bulk stress

Chapter 1

Introduction

The background to the research as well as the research objectives, scope and methodology are outline in this introductory chapter. The organisation of the thesis is then presented.

1.1 Background

The movement of people and goods are an essential part of economic, socio-economic and political activities. Road, rail and air transport require suitable pavement structures to safely distribute the applied vehicle loads to the natural ground. Rail transport is regarded as a more environmentally responsible mode of transport and forms part of plans to reach environmental goals of reduced carbon emissions (Greening, 2012).

Network Rail (2012) predicts the demand for passenger and freight services in Britain to double over the next 30 years. The rail industry has moved towards faster, heavier, and more frequent trains to increase capacity of existing railway infrastructure (Priest et al., 2010). In addition to the design of new lines, engineers are faced with ageing infrastructure that requires suitable maintenance and improvement strategies. Increased pressure on the network is expected to impact the performance of this infrastructure asset.

Operational efficiency and good ride quality is important for mass transport systems such as railways to be competitive with other modes of transport. The stiffness of the railway track structure is used to critically evaluate track performance. The formation layers play an important role in the behaviour as it is the foundation of the railway structure. The rail foundation is regarded as a type of pavement structure (Brown, 1996) and is not dissimilar from flexible road pavements. Railway formation design approaches vary between countries and is based on the historical development and practical experience.

An emphasis on total life cycle cost and performance efficiency has led to increased research efforts over the past few decades to improve our understanding of the behaviour

of railway track infrastructure. It is expected that this will require improvements in mainly empirical approaches to track design and construction currently in use, towards more rational design methods. Research towards this goal has been undertaken over the past few decades.

The aim of this research is to determine the importance of different factors affecting the measured resilient modulus of railway formation material. The focus falls on increasing the knowledge of unsaturated subgrade soil and its behaviour when subject to cyclic train loading. The difficulties and limitations related to different laboratory test methods have been recognised, and cyclic stiffness results from two laboratory tests compared.

1.2 Research objectives

The objectives of the research are:

- The review of current and past methods of designing track foundations.
- To critically appraise the methods of determining resilient modulus used as part of modern mechanistic-empirical track design.
- To review and where possible assess the effects of stress level, strain level, principal stress rotation and cyclic stress excursion on measured stiffness.
- To measure the soil suction of rail foundation material using the Chilled-Mirror Dew-point Potentiometer and compare the soil water retention curve with that obtained previously using pressure plate, high-capacity tensiometer and filter paper methods, on similar material reported by Otter (2011).
- To determine the resilient modulus measured with and without principal stress rotation, PSR, on unsaturated specimens in the Hollow Cylinder Apparatus, HCA, and Cyclic Triaxial Apparatus, CTX, and compare these values with those obtained on saturated specimens by Gräbe (2002) and at very small strain levels, on unsaturated material, by Otter (2011).
- To carry out cyclic triaxial testing on unsaturated specimens of formation material to evaluate the effect of load staging and cyclic deviator stress excursions.
- Compare the use of suction stress and matric suction for analysing the measured resilient modulus of unsaturated formation material.
- To assess the relative importance of different factors affecting measured resilient modulus.
- To make a preliminary assessment of the use of flexible pavement M_R models for tested formation material.

1.3 Scope of the research

The focus of this research is on the foundation layers of railway track, which include the subballast and the compacted subgrade layers. The ballast layer has not been considered in this study which was focussed on the formation layers less accessible for maintenance and remedial work. The behaviour of ballast is considered by other researchers.

A clayey sand material representative of a subballast material, used in the Coal Line in South Africa, was selected for the laboratory investigations. The specimens for laboratory element testing were dynamically compacted, at a range of water contents, to the same target dry density. Tests on the unsaturated specimens were open to atmosphere (drained) to allow dissipation of pore pressure. No control or measurement of suction was made during laboratory element testing due to the required equilibrium time required for suction measurements. Matric suction was estimated using the soil water retention curve determined for the material. The testing stresses were based on values used in previous railway foundation studies, and on those recommended for flexible highway pavement testing strategies.

1.4 Methodology

The methodology followed in order to achieve the objectives is outlined below.

- Literature review focussed on railway foundation and highway pavement design and testing methods.
- Literature review of unsaturated soil mechanics frameworks and some constitutive models used in pavement design strategies.
- Laboratory measurements of suction using a Chilled Mirror Dewpoint Hygrometer.
- Laboratory testing on a representative unsaturated railway formation material. Tests were conducted using a Cyclic Triaxial Apparatus and a Hollow Cylinder Apparatus to assess the stress-strain response during cyclic, drained (open to atmosphere) loading.
- Analysis of the results to evaluate the effect of principal stress rotation, matric suction, confining stress, deviator stress and laboratory test method on the resilient modulus.
- Preliminary evaluation of the ability of mechanistic-empirical pavement design models to predict the measured resilient modulus from the cyclic triaxial tests.

1.5 Organisation of the thesis

Chapter 2 includes a review of current design methodologies and requirements used for railway track formation material. The expected loading conditions for a soil element in the formation are also discussed. Factors that influence the resilient behaviour of the formation are discussed in Chapter 3. The factors investigated include stress, material type and the soil physical state. Unsaturated soil mechanics frameworks using two independent stress state variables are discussed. The influence of the different factors varies and an improved, more scientific understanding of the various impacts is required in order to improve design and maintenance strategies.

Laboratory methods for determining the stiffness of formation material under expected loading condition are introduced in Chapter 2. The laboratory test procedures used are described in Chapter 4. This chapter includes the description of the representative formation material, material mixing and specimen preparation. The test methodology for determining the total suction using the Chilled Mirror Dewpoint Hygrometer is presented. This is followed with the description of the laboratory element test methods using the Cyclic Triaxial Apparatus and the Hollow Cylinder Apparatus.

The results are presented and discussed in Chapter 5. This chapter presents the resilient modulus measurements made in the different tests performed. Specimens, at a range of water contents and thus suctions, were tested under cyclic stress conditions, with and without principal stress rotation. The conclusions and recommendations of the research are summarised in Chapter 6. Future work is suggested for furthering the understanding of the resilient modulus and deformation of compacted railway formation material.

Chapter 2

Ballasted track structure

Any track structure needs to be suitable for safe and economical operation of trains at the relevant designed loads and speeds (Brown and Selig, 1991; NSW Transport RailCorp, 2012). Ballasted track structure components and function are briefly introduced in this chapter. Loading conditions are considered as well as potential failure mechanisms. The chapter continues by investigating current engineering practices for track subgrade formation design with specific focus on the stiffness and factors influencing it, as later discussed in Chapter 3.

2.1 Track components and function

A ballasted track structure can be divided into the superstructure and substructure (Selig and Li, 1994) as indicated in Figure 2.1. The superstructure includes the rails, fastening system and sleepers to guide the wheels and to distribute the wheel loads (Brown and Selig, 1991). The substructure includes the layers below the sleeper. Granular layers form part of the substructure and consist of ballast and subballast layers. The foundation level is at the top of the subballast layer (Brown and Selig, 1991) and forms the basis for the ballast layer. A sand blanket or capping layer, referred to in several design methodologies (International Union of Railways, 2008; NSW Transport RailCorp, 2010; Network Rail, 2005), is considered a subballast layer. The subgrade formation is below the subballast and can include engineered fill or placed soil layers above the natural ground.

The function of the different interacting track substructure elements such as the ballast, subballast and subgrade formation layers, are discussed by Selig and Li (1994) and include:

- stress distribution,
- retaining track geometry,
- facilitating drainage, and
- ease of re-alignment (maintenance).

The applied train loads are carried through the superstructure (rail and sleeper system) to the ballast layer which is the main load distributing layer. An adequate granular layer depth is needed to reduce stresses induced on the formation to an acceptable level to prevent subgrade failure (Selig and Li, 1994; Li and Selig, 1998a). The ballast layer is considered the most important granular layer and can be tamped to adjust the vertical level of the rails during maintenance (Esveld, 2001; Indraratna and Salim, 2005). Ballast is very coarse unbound granular material with specific properties, including particle size, shape and strength. Ballast properties and mechanical behaviour are extensively discussed by Indraratna and Salim (2005) and Esveld (2001). This research does not consider the ballast layer, but is aimed to assess the formation layer less accessible for maintenance or remedial work.

Brown and Selig (1991) include the railway substructure as a specific type of pavement element that forms the foundation for the superstructure above. Apart from improving track strength and stiffness (International Union of Railways, 2008) the subballast has the important function of separating the ballast from the subgrade formation material, to reduce interpenetration at the interface (Selig and Li, 1994). Waterlogged formation conditions can result in subgrade pumping due to pore water pressure build-up leading to reduced subgrade strength (Li and Selig, 1998b). Therefore, adequate drainage is one of the most important requirements for a stable track (Spoornet, 2006). The blanket layer (subballast layer) plays an important role as a drainage layer and is designed accordingly (Selig and Li, 1994). A well drained formation provides a good platform for the main structural element (ballast layer), which is particularly important during construction (Brown and Selig, 1991).

2.2 Train loading and formation failure

The stress conditions induced in the railway foundation due to a moving train are considered in Section 2.2.1. The potential formation failure mechanisms relating to serviceability criteria, including permanent deformation and cyclic stiffness, are presented in Section 2.2.2.

2.2.1 Cyclic train loading

A reasonable calculation of the stresses induced in the subgrade is a key element for track design (Heath et al., 1972; Li and Selig, 1998a; Gräbe and Clayton, 2009). Complex cyclic stress conditions are applied to the soil under a railway (Brown, 1996; Priest et al., 2010). The externally induced substructure stress condition can be considered cyclic, as rail traffic produces a non-static repetitive load condition (Kramer, 1996). Figure 2.2a illustrates the stress variation with time under a single moving wheel load, as presented by Brown (1996) for a pavement element. The vertical stress, horizontal stress and shear stress as induced by a moving wheel load have been modelled as sinusoidal waves. The directional change in the applied shear stress under a moving wheel is shown in Figure 2.2b and results in the rotation of the principal stress planes (Chan and Brown, 1994; Brown, 1996).

When the train is directly above the soil element, the major principal stress is generally taken as vertical and the independent shear stress as zero; the horizontal stress is assumed to be the minor principal stress (Heath et al., 1972; Brown, 1996; Li and Selig, 1998a; Gräbe, 2002). For compacted fill an apparent overconsolidation ratio, OCR, in the range of 2-5 is likely (Brown and Selig, 1991). The OCR can be used to determine the earth pressure coefficient at rest (K_0) from Equation 2.1 proposed by Mayne and Kilhawy (1982).

$$\boldsymbol{K}_0 = (1 - \sin\phi^{'})R^{\sin\phi^{'}} \tag{2.1}$$

Where:
K_0 = earth pressure coefficient at rest, ($\frac{\sigma_H}{\sigma_V}$);
$\phi^{'}$ = angle of shearing resistance with respect to effective stress;
R = overconsolidation ratio.

Using this equation, K_0 will range between 0.5 to 1.1 for the most likely OCR values, assuming an angle of shearing resistance in the range of 30 to 45 degrees for granular material (Jin et al., 1994). This indicates that the assumption of the direction of principal stresses is reasonable for compacted layers as the major principal stress is likely to be vertical.

Principal stress rotation, PSR, relates to the change in the angle, α, of the major principal stress (σ_1) direction relative to the vertical (Symes et al., 1988; Kramer, 1996; Brown, 1996; Hight and Leroueil, 2003). As the train moves, the principal stress angle (of a fixed soil element in the foundation) changes depending on the magnitude of the induced vertical and shear stress (Brown, 1996) as well as the in-situ principal stress direction and magnitude (Hight et al., 1983; Yang et al., 2009). The principal stress axis rotates in a continuous manner as the wheel passes over the element in the subgrade (Brown, 1996; Gräbe, 2002).

Using two and three dimensional numerical models Powrie et al. (2007) analysed the principal stress direction in the substructure resulting from a passing freight train (25.4 tonne axle load). The principal stress direction was shown to be sensitive to K_0 and confining stress which increase with depth. The potential degree of PSR in the longitudinal direction (x-direction, along direction of travel) is shown in Figure 2.3a for $K_0 = 1$ conditions (Powrie et al., 2007). It can be seen that the amount of rotation decreases with depth below the sleeper soffit.

The magnitude, frequency and number of load cycles resulting from train traffic should be considered when evaluating the long term stress-strain behaviour of the subgrade (Li and Selig, 1998b). A 2D dynamic system (finite element) analysis based on a freight line in South Africa was conducted by Yang et al. (2009). Stiffness parameters for the track layers were based on in-situ measurements presented by Gräbe et al. (2005). The changes in vertical stress, horizontal stress and shear stress resulting from the passing of three wagons are shown in Figure 2.4 at different depths below the sleeper soffit (0.45m, 0.75m and 1.2m) (Yang et al., 2009). The different depths represent different substructure layers (SSB, A and natural ground level) which are part of the Spoornet (2006) design discussed in Section 2.3. The stresses have been normalized with the stress directly beneath the sleeper (σ_{sb}).

The magnitude of change in vertical stress, horizontal stress and shear stress is dependent on the axle load applied and the physical track geometry such as sleeper spacing and gauge width. The load spreading is dependent on several factors, including the layer stiffness assumed for the various layers, especially that of the ballast layer. Following from the dynamic FE-analysis results by Yang et al. (2009), a magnitude of change in vertical stress for a formation layer 0.75 m below the sleeper soffit (A-layer Spoornet (2006)) ranges between 15% and 20% the stress at the sleeper/ballast interface (Figure 2.4b). Therefore, for a standard gauge railway track carrying 250 kN axle load wagons the vertical stress change will range between approximately 64 kPa and 85 kPa. This is comparable to field-measurements by Gräbe et al. (2005). Shaw (2005) reported substructure pressures from field measurements at the Bloubank site, South Africa, of between 50 kPa and 70 kPa for depths below the sleeper soffit of 0.6 m and 0.8 m.

Results from stress modeling (static analysis) by Powrie et al. (2007) predicted a change in vertical stress, for the A-layer, of less than 10% (Figure 2.3b) the stress at the sleeper/ballast interface (thus less than 45 kPa). The differences in the predicted stresses, compared to Yang et al. (2009) and site measurements (Shaw, 2005), is largely due to the dynamic versus static analysis. The static analysis does not include for dynamic effects, but only the quasi-static response of the soil as for train speeds below 140 km/h (Powrie et al., 2007). A dynamic amplification factor, DAF, can be applied to stresses determined from static analysis, normally ranging between 1.1 and 2.8 (Esveld, 2001) depending on the track condition and train speed.

Prior to the use of multi-layer, finite element packages (such as ILLI-TRACK and GEO-TRACK) or models (Yang et al., 2009) the theory of elasticity was used to estimate the stresses in the pavement (Brown, 1996). The theory of elasticity assumes a semi-infinite, homogeneous, isotropic mass which does not reflect the layered, non-linear elastic soil substructure system (Brown, 1996; Li and Selig, 1998b). The change in (static) vertical stress below a sleeper (centre), at 0.75 m (A-layer) depth, due to a 250 kN axle load applied over two sleepers as a distributed load, is approximately 45 kPa when calculated using the Fadum Chart (reproduced by Craig (2004)). This does not take into account the influence of rail bending or load spreading over several sleepers as would be expected. The estimated dynamic vertical stress change can thus be estimated as between 50 kPa and 98 kPa for the range of DAF values.

The importance of carrying out representative laboratory tests on formation material for design of transport infrastructure has been stressed by Shahu et al. (1999). The behaviour of soil is influenced by factors such as stress reversals and strain rate effects (O'Reilly and Brown, 1991). Cyclic hollow cylinder tests conducted on dry crushed dolomitic limestone by Chan and Brown (1994) indicated a significant change in plastic strain development, particularly horizontal strain patterns, due to PSR. However, in flexible pavement design and research the cyclic triaxial test, which does not impose PSR, is widely employed to simulate the cyclic stresses due to moving wheel loads.

The resilient modulus, M_R, is used as a long term and short term pavement performance prediction parameter (Khoury and Zaman, 2004). The mechanistic-empirical design procedure for pavement design uses the resilient modulus, M_R, as the basis for material characterisation, assuming that pavement materials can be represented by a quasi-elastic modulus (AASHTO, 1993). The resilient modulus is used as a combined representation of stress, water content and dry density or void ratio as these factor will influence the modulus value (Lekarp et al., 2000).

The resilient modulus, M_R, is a form of secant Young's modulus (Ng et al., 2013) and is sometimes referred to as resilient Young's modulus (Li and Selig, 1994). M_R is defined as the maximum (cyclic) deviator stress difference, q_{cyc}, over the recoverable strain, ϵ_R, calculated per load cycle as given in Equation 2.2. Figure 2.5 illustrates the definition of M_R.

$$M_R = \frac{q_{cyc}}{\epsilon_R} \tag{2.2}$$

Where:
M_R = resilient modulus;
q_{cyc} = maximum deviator stress difference or cyclic deviator stress; and
ϵ_R = recoverable (or elastic) strain.

The resilient modulus, M_R, depends on the deviator stress pulse magnitude and the effective stress or soil suction (Brown and Selig, 1991). The formation response to loading is dependent on several factors including stress history, soil physical state and

material type (Brown and Selig, 1991; Li and Selig, 1994; Nazarian et al., 1996; Li and Selig, 1996; Gräbe and Clayton, 2009). Some of these factors are further discussed in Chapter 3. The specification of a single resilient modulus in flexible highway pavement design (AASHTO, 1993) has led to increased research on the effects of water content (or suction) on M_R.

Principal stress rotation, PSR, occurs due to externally applied stresses induced by passing trains. For unsaturated soil the change in total suction or suction stress is an additional stress state variable that influences the behaviour of the soil (Lu and Likos, 2006; Fredlund et al., 2012). The soil suction needs to be considered for unsaturated compacted fill and formations with deep water tables (Brown and Selig, 1991). The effects of PSR due to train loading and different suction stresses on resilient modulus has not, to date, been researched.

2.2.2 Formation failure

The subgrade formation is required to provide a stable platform without failure or excessive deformation resulting from traffic-induced stresses, and to resist various environmental factors (Gräbe, 2002). The environmental factors include rainfall and temperature which influence the soil water content and suction. This may cause differential settlement of the subgrade in addition to settlements due to cyclic loading from trains (Moco Ferreira et al., 2011). Progressive shear failure and excessive plastic deformation are considered the two most common subgrade failure mechanisms due to repeated traffic loads that cause excessive vertical deformation of the track structure (Heath et al., 1972; Selig and Li, 1994; Li and Selig, 1998b; Network Rail, 2005).

Progressive shear failure or plastic flow (Figure 2.6a) is a result of the repeated overstressing of the material (Heath et al., 1972; Li and Selig, 1996). As the material is sheared it pushes up and out from underneath the granular layers (Selig and Li, 1994; Li and Selig, 1998b). A cess heave to the side of the embankment is usually noticeable.

Excessive plastic deformation is an accumulation of compressive strains most prominent in the subgrade layer below the edge of the sleeper (Li and Selig, 1998b). This results in formation of ruts, known as ballast pockets, within the structure (Figure 2.6b). Both of these phenomena cause rail alignment and track drainage problems resulting in train operation restrictions and increased maintenance.

Other subgrade related problems, which are related to permanent deformation and shear strength, as discussed by Selig and Li (1994) and Li and Selig (1998a) are:

- Differential settlement at transition zones (between earthwork embankments and structures of higher relative stiffness such as culverts, level crossings or bridges).

- Subgrade attrition (by ballast) with mud pumping and ballast fouling.
- Major subgrade shear failure (such as slope stability failure).
- Excessive consolidation settlement due to self-weight.

Mishra et al. (2012) identified different factors contributing to the development of differential movement at railway bridge approaches (one example of track transition zones) by installing multidepth deflectometers and strain gauges. The sudden change in track deformation, significantly smaller on the bridge deck, resulting from differences in substructure and loading conditions on the bridge deck and the approach track embankment results in extreme dynamic loading conditions and ultimately rapid deterioration (Mishra et al., 2012). The impact on ride quality and dynamic impact loads are more critical at the exit end of a bridge (Read and Li, 2006) when moving from high-stiffness to a low-stiffness track. Higher deterioration rates of superstructure components (rail and sleepers) occur for a low to high-stiffness track change (Li and Davis, 2005) such as a bridge approach. Li and Davis (2005) concluded that track geometry degradation was primarily caused by inadequate ballast and subballast layer performance.

One of the design criteria for railway foundations, the California Bearing Ratio, CBR, value, could be considered an indication of strength and stiffness (Brown and Selig, 1991). In pavement engineering the resilient modulus, M_R, is one of the main design parameters used in the mechanistic-empirical design guide (AASHTO, 1993). The thickness and resilient modulus of the granular layers (ballast and subballast) are the most important factors influencing the load conditions, and thus resulting deformations, in the underlying layers (Brown and Selig, 1991; Li and Selig, 1998a) as they distribute stress. Considering linear elastic material behaviour, the load spreading capability of a layer is related to the stiffness, with higher stiffness having better load spreading capabilities as demonstrated in Figure 2.7 (Brown and Selig, 1991). The basic principle of pavement design is a compromise between stiffness, layer thickness and tensile strength of the structural pavement layer(s) for good load spreading (protecting the subgrade), without significant cracking and deformation of the layer itself (Brown and Selig, 1991).

Apart from its significance in spreading the load, the stiffness of the total track system is important because the dynamic effects and ride quality are influenced by deflections at the wheel-rail interface (Indraratna and Salim, 2005). Track structure stiffness is used as a serviceability criterion by Network Rail (2005) in the United Kingdom (UK) as deflections under a moving train needs to be managed. Wheel and rail wear as well as the power required for movement are influenced by the deflections (Brown and Selig, 1991). Uniformity in the stiffness of the layers is important to prevent differential settlement from altering the vertical alignment of the rails (Moco Ferreira et al., 2011). The subgrade stiffness was identified by Selig and Li (1994) as the most influential parameter affecting the ballasted track moduli.

The subgrade response to cyclic train loading will influence both the ride quality (Steenbergen, 2013; Hendry et al., 2010) and the rate of deterioration of the track (Shahu et al., 2000). The focus of this research is on the factors that influence the stiffness of the track foundation. The design criteria (factors) used in current practise are discussed in Section 2.3.

2.3 Track foundation engineering considerations

Ballasted track structure design varies across the world and is mainly based on empirical methods (Brown and Selig, 1991; Burrow et al., 2007). Design specifications include similar components but detailed requirements and assumptions vary (Brown and Selig, 1991; Burrow et al., 2007). Some railway formation design strategies are summarised in Section 2.3.1 with associated advanced formation material testing introduced in Section 2.3.2. The design strategies are further discussed in Section 2.3.3.

2.3.1 Some railway design strategies

A tabulated summary of the design requirements for a railway foundation (the subballast and the subgrade formation layers) is included in Appendix A. The following railway design methodologies are discussed below:

- British Railways, United Kingdom (UK),
- the International Union of Railways (UIC) design, Europe,
- the New South Wales (NSW) RailCorp standard, Australia,
- the Spoornet design specification, South Africa (SA),
- Network Rail (NR) standards, (UK), and
- the method by Li and Selig (1998a,b), United States of America (USA) with additional work by Shahu et al. (2000) in India following similar principles.

British Railways

Research efforts by British Railways were focused on developing a rational method of track design in order to allow large step changes in railway operations. Heath et al. (1972) presented a design chart for ballast depth with the subgrade threshold stress and heaviest commonly occurring axle load as input parameters (Figure 2.8). Using simple elastic theory the ballast depth is calculated to reduce the induced vertical stress on the subgrade to below the threshold stress. The threshold stress is defined as the maximum

deviator stress ($\sigma_1 - \sigma_3$) resulting in less than 10% cumulative plastic strain after 10^6 cycles. Drained cyclic triaxial compression tests (vertical stress cycles with constant radial stress) were used to determine the threshold stress (Section 2.3.2).

It was found, mainly for London Clay, that deviator stresses resulting in elastic strains of less than 0.65% did not cause cumulative (plastic) strains of more than 10%. The Office for Research and Experiments (ORE) of the UIC subsequently adopted the research programme initiated by British Railways (Heath et al., 1972).

International Union of Railways, UIC

The UIC (2008) code 719R for the design of earthworks and track bed for railway lines makes use of a classification system approach. The required subgrade bearing capacity class (P1=poor; P2=average; P3=good subgrade) is chosen for a railway line depending on the track configuration, traffic category and loading (as per leaflet 714R International Union of Railways (1988)). The bearing capacity class is a function of the drainage conditions, minimum California Bearing Ratio, CBR, value and soil quality class. The soil quality class (QS0 to QS3) is mainly dependent on particle size, plasticity and susceptibility to weathering.

A prepared subgrade layer of minimum depth, to improve the in-situ bearing capacity class, must comply with specifications for dry density and deformation modulus from plate load tests. A blanket layer is also part of the design, aimed at improving drainage and bearing capacity by means of increased stiffness and height above the subgrade (International Union of Railways, 2008).

RailCorp and Spoornet

The NSW Transport RailCorp (2010, 2012) and Spoornet (2006) railway earthworks designs specify material properties, density and CBR strength requirements for subballast and subgrade formation layers. The foundations are designed to require only a minimum ballast depth of 300 mm. The RailCorp layer design thickness for the subballast is dependent on the CBR value of the subgrade. The Spoornet layer design considers a range of design axle loads up to 30 tonne. The material properties considered include particle size grading, Atterberg limits (plasticity index, plastic limit and liquid limit) and durability for rock material.

Li and Selig (1998a)

The railway track substructure design method (to determine granular layer thickness) developed by Li and Selig (1998a) is aimed at limiting plastic flow at the subgrade

surface and cumulative plastic deformation caused by repeated traffic. It is similar to the British Rail method in that it uses a serviceability type criterion and considers the deviator stress in the soil, induced by the axle loads, to be the most significant factor influencing the subgrade performance. Analysis of the stresses and deformation is done using GEOTRACK (Chang et al., 1980) - an elastic, multilayer and three-dimensional model. In order to calculate the allowable deviator stress, additional information required includes:

- the cumulative tonnage expected over the design life,
- the subgrade soil type,
- the compressive strength, and
- the resilient modulus.

The soil type parameters (dependent on plasticity and clay content) are determined from advanced repeated load tests (Li and Selig, 1996) or alternatively using the suggested values for the particular soil class. The influence of the soil physical state (water content and dry density) is indirectly represented by the soil compressive strength (Li and Selig, 1996) discussed in Section 2.3.2. The method for obtaining the resilient modulus or allowable deviator stress is not explicitly stated in the design.

Network Rail

Network Rail specifications for formation treatment and earthworks (Network Rail, 2005, 2010) are maintenance focused, as the railway operator's main objective is asset management. The required trackbed stiffness is specified, depending on the speed of traffic on a new track (above or below 100 mph) and the inclusion of geogrid reinforcement in existing main lines (maximum axle load of 25 tonnes). The trackbed stiffness is measured, as a dynamic sleeper support stiffness [kN/mm/sleeper end] from vertical displacement of a sleeper end, resulting from a passing train (of known mass). The thickness of the granular layers is graphically determined using the undrained subgrade modulus and the relevant trackbed stiffness curve (Figure 2.9). This curve is thought to be based on the results from advanced material testing on clay subgrade by Heath et al. (1972).

2.3.2 Advanced formation material testing

Railway subgrade material (London Clay) was tested by Heath et al. (1972) using a CTX compression test with drainage allowed. In these tests the confining pressure (minor principal stress, σ_3) was kept constant and the vertical stress (major principal stress, σ_1) cycled. A square load pulse, with a maximum load frequency of 0.5 Hz, was used

as a simplification of induced stresses resulting from closely spaced axles (Heath et al., 1972). The highest deviator stress ($q_{cyc} = \sigma_1 - \sigma_3$) for which the rate of deformation was reducing with cycles, and a stable condition attained, is defined as the threshold stress. A limit of 10% plastic strain and 0.65% resilient strain were arbitrarily chosen and evaluated after 1000 cycles (Heath et al., 1972; Shahu et al., 2000). The threshold stress/confining pressure relationship was found to be approximately linear and it was subsequently assumed that the threshold stress increases with construction depth (Heath et al., 1972). The threshold stress derived from cyclic triaxial tests is lower than the static strength (Heath et al., 1972; Li and Selig, 1996, 1998a; Shahu et al., 2000) and emphasises the need for representative stress path testing (Lambe, 1967).

Li and Selig (1998a) do not propose a method for evaluating the threshold stress (Shahu et al., 2000). However, flexible pavement CTX test regimes used in the USA for evaluating M_R, including AASHTO T292-91, T294-92, T P46-94 and NCHRP 1-28, are selected based on material type. Harrigan (2004) described the CTX test methodology and loading sequences used for granular and fine-grained subgrade materials as part of the NCHRP Project 1-28A outcomes. For a granular subgrade material the confining stress used ranges between 13.8 kPa and 82.8 kPa with a ratio of deviator stress to confining stress ranging from 0.5 to 3.0. A preconditioning phase is included. The tests are performed on specimens at the expected in-situ water content and density conditions, while open to atmosphere.

Nazarian et al. (1996) reviewed the T294-92 testing sequence for the Texas department of transport and subsequently reduced the stress magnitudes and number of cycles used, to avoid high deviator stresses at low confining pressures. The preconditioning phase was also removed, following improved specimen to platen connection by means of grouting, to avoid changes in M_R due to changes in the stress history prior to testing. The stresses used in the AASHTO T294-92 testing sequences for base materials are lower than the stresses used in the European standard. The European standard (BS EN 13286-7:2004) for CTX testing is thus applicable only to stiff unbound base materials due to very high load sequences specified.

Typical confining pressures of 20 kPa, 40 kPa and 100 kPa are proposed for railway subgrade testing by Shahu et al. (2000), but is expected to be less than 35 kPa. The Network Rail (2005) formation treatment document specifies undrained repeated load triaxial testing to evaluate the undrained modulus of poorly performing subgrade. Prescribed test parameters include a 30 kPa confining stress and deviator stress of 30 kPa. This does not allow for assessing different in-situ depths or load cases. Brown et al. (1975) found that the resilient strain was mainly affected by the applied stresses, while stress history is an important parameter for permanent strain.

A limitation of the CTX, used for advanced laboratory testing of railway foundation materials, is that it cannot apply continuous principal stress rotation (Kramer, 1996; Brown,

1996; Gräbe, 2002; ASTM D5311-11:, 2011). The principal stress direction can only be instantaneously cycled between the vertical (triaxial compression, TC) and horizontal (triaxial extension, TE). More representative stress path testing for railway foundation material has been proposed (Gräbe, 2002; Powrie et al., 2007; Gräbe and Clayton, 2009) and some work has been done using the cyclic hollow cylinder apparatus, HCA. The Cyclic Simple Shear, CSS, is also able to induce principal stress rotation, however the stress state is only known on one plane. Gräbe and Clayton (2009) suggest the use of a railway subgrade testing method that can induce PSR. This recommendation followed HCA testing on saturated subgrade materials, some of which indicated a significant influence of PSR on the permanent deformation and stiffness of rail track foundations (Gräbe, 2002).

2.3.3 Discussion on design strategies

A specific railway foundation design approach (below ballast level) follow from work by British Rail Research in the 70's by Heath et al. (1972). However, historically in the UK embankments were built by end-tipping spoil material from nearby cuttings (Powrie, 2014a) resulting in an embankment structure consisting of clods of intact clay between softened material (O'Brien, 2007). In South-Africa the historic railway foundation design is also unspecified, however Rhind (1997) reported that construction of the Richardsbay Coal Line, around 1973 to 1975, included the removal of soft materials in a marshy section, at Richardsbay, subsequently filled with 'filler material' prior to track construction. Rhind (1997) further reported current problems on the 30 km section closest to the coast, associated with insufficient shear strength of saturated clays, requiring remedial action. A design approach is expected to identify problem sections and aid the proposal of an appropriate design to prevent failure.

Several railway foundation design strategies have briefly been summarized above in Section 2.3.1. The strategies are explicitly or implicitly concerned with strength, permanent deformation and/or stiffness to prevent formation failure (Section 2.2.2). A number of the methods are of empirical nature (such as the UIC, NSW and Spoornet designs) and make use of California Bearing Ratio (CBR) tests and material properties including particle size distribution and Atterberg limits as main design parameters. The CBR test is an empirical reference test and the value is influenced by both the shear strength and the stiffness of the soil (Brown and Selig, 1991). Changes in traffic loading and environmental conditions (such as rainfall and temperature) that fall outside the limiting conditions under which the empirical design guidelines were developed (Road Research Laboratory, 1952) suggest caution when using current design methods (Burrow et al., 2007). Insufficient granular layer thickness will lead to failure (Heath et al., 1972; Li and Selig, 1998a; Shahu et al., 2000) and empirical or semi-empirical designs for lighter,

slower and less frequent trains will result in difficult and costly maintenance for changing traffic conditions (Shahu et al., 2000).

The British Rail design strategy as summarised by Heath et al. (1972) determines the required granular layer thickness (ballast and sand blanket) to prevent failure of the in-situ material, of which only London Clay was reported. The threshold stress used as criteria was determined using drained cyclic triaxial tests (applied cyclic stress incrementally increased until shake down is evident). Following from British Rail is the Network Rail formation treatment strategy (Network Rail, 2005) that determines the required ballast thickness for badly performing track substructure based on the undrained subgrade modulus (tested for one stress condition only, $\sigma_c = q_{cyc} = 30$ kPa). The more comprehensive substructure design approach by Li and Selig (1998b) requires the resilient modulus and compressive strength of materials as the main input parameters. These parameters, presumably, assessed using CTX testing are required for the railway stress and strain analysis using the GEOTRACK (Chang1980) software and subsequent ballast depth determination through iteration. The required software input parameters can however be selected based on the material type (from a data bank of tests).

In contrast, the other three methods considered (Spoornet (2006); NSW Transport RailCorp (2010) and UIC (2008)) limits the ballast depth (generally 300 mm) while specifying required subballast layers (or engineered fill) mainly based on material properties, including particle size distribution, Atterberg limits and free swell index, as well as CBR value (see Appendix A). The UIC method also includes a minimum deformation modulus from plate load tests. Comparing the particle size distribution specified, for similar design layers - QS3 material (UIC, 2008) and SB material (Spoornet, 2006) as plotted in Figure 4.1 based on a 100 mm maximum particle size, it is evident that the UIC grading envelope is broader. While the QS3 material should have 0-10% fines (<0.075 mm) the SB material require between 5% and 20% fines. The inclusion of fines has a potentially significant role in the response of the layer when considering the influence on matric suction development (Section 3.1.4).

An investigation into railway design methodologies reported by Burrow et al. (2007) found significant variation in the calculated granular layer thickness when using different design methods. The need for a more rational method of material testing representative of railway substructure conditions is recognised (Brown, 1996; Li and Selig, 1998a; Lekarp et al., 2000). The British Rail method has formed the basis for further work into developing a railway design method using representative soil testing techniques. The cyclic triaxial test is used to investigate the permanent deformation (Heath et al., 1972) or resilient modulus (Li and Selig, 1998a; Network Rail, 2005) related to an applied vertical deviator stress to simulate train induced stresses.

Some designers (e.g. Heath et al. (1972) and Li and Selig (1998a)) have moved towards a design strategy based on permanent deformation criteria and resilient modulus. The

total track structure stiffness is used as the main track substructure suitability criterion by Network Rail (2005). A higher overall track stiffness is generally considered better than a lower stiffness with benefits including reduced energy required for pulling trains and a reduced rate of ballast wear (Brown and Selig, 1991). A very low track stiffness is regarded as an indication of an inferior track substructure (Brown and Selig, 1991) requiring further investigation and maintenance action (Network Rail, 2005). However, very high track stiffness may also be undesirable when resulting in an increased deterioration rate of track and vehicle components (Brown and Selig, 1991).

The resilient modulus is incorporated in the mechanistic-empirical design strategy for road pavement design. The AASHTO (1993) guide for design of pavement structures describes the mechanistic-empirical method as a procedure to translate the analytical calculations of pavement response to physical distress (namely performance). It has been recognised that mechanistic methods are unable to model all the factors that influence pavement performance. Therefore, calibration is necessary using empirical correlations from performance observations (AASHTO, 1993).

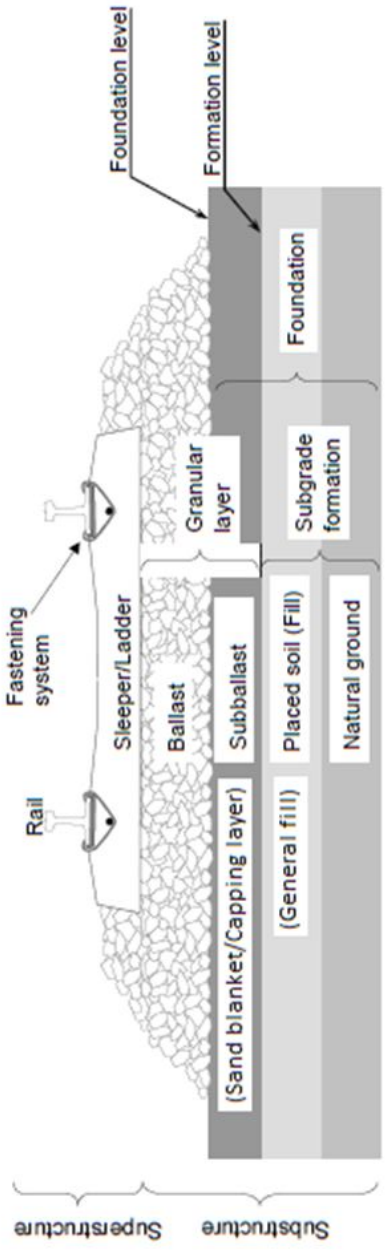

Figure 2.1: Ballasted track structure components (as adapted by Gräbe (2002) from Selig and Li (1994))

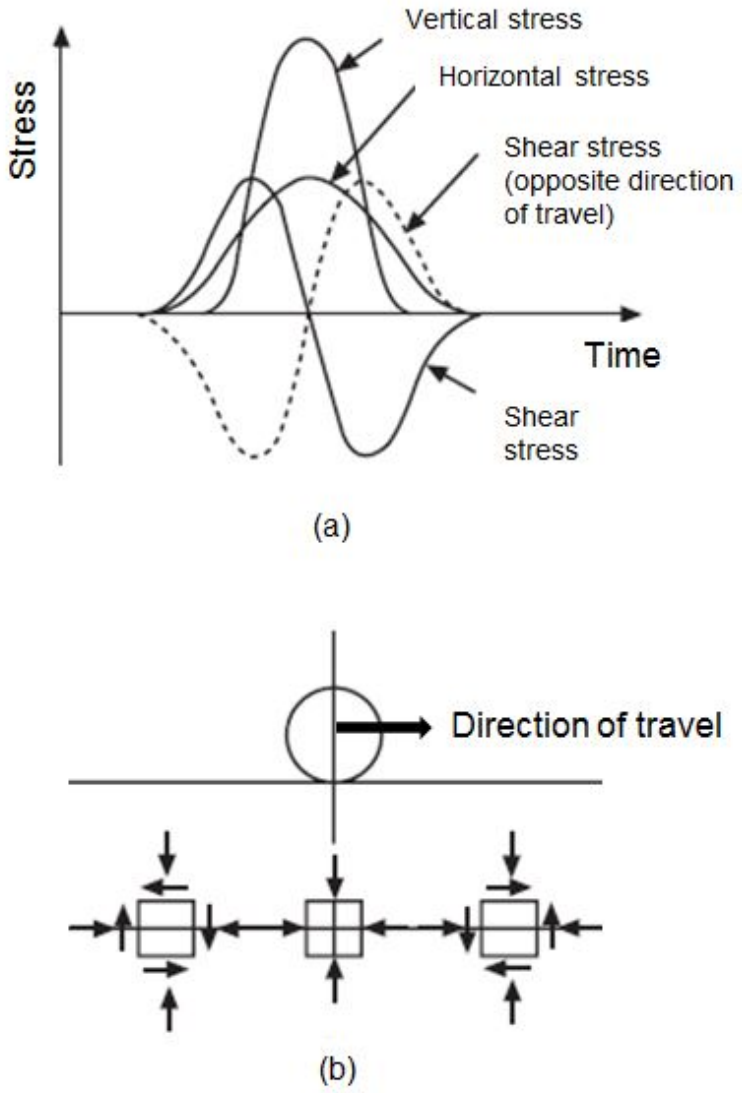

Figure 2.2: Stress induced by a moving wheel load (from Brown (1996)) (a) Variation of stresses with time; and (b) shear stress reversal applied to a soil element

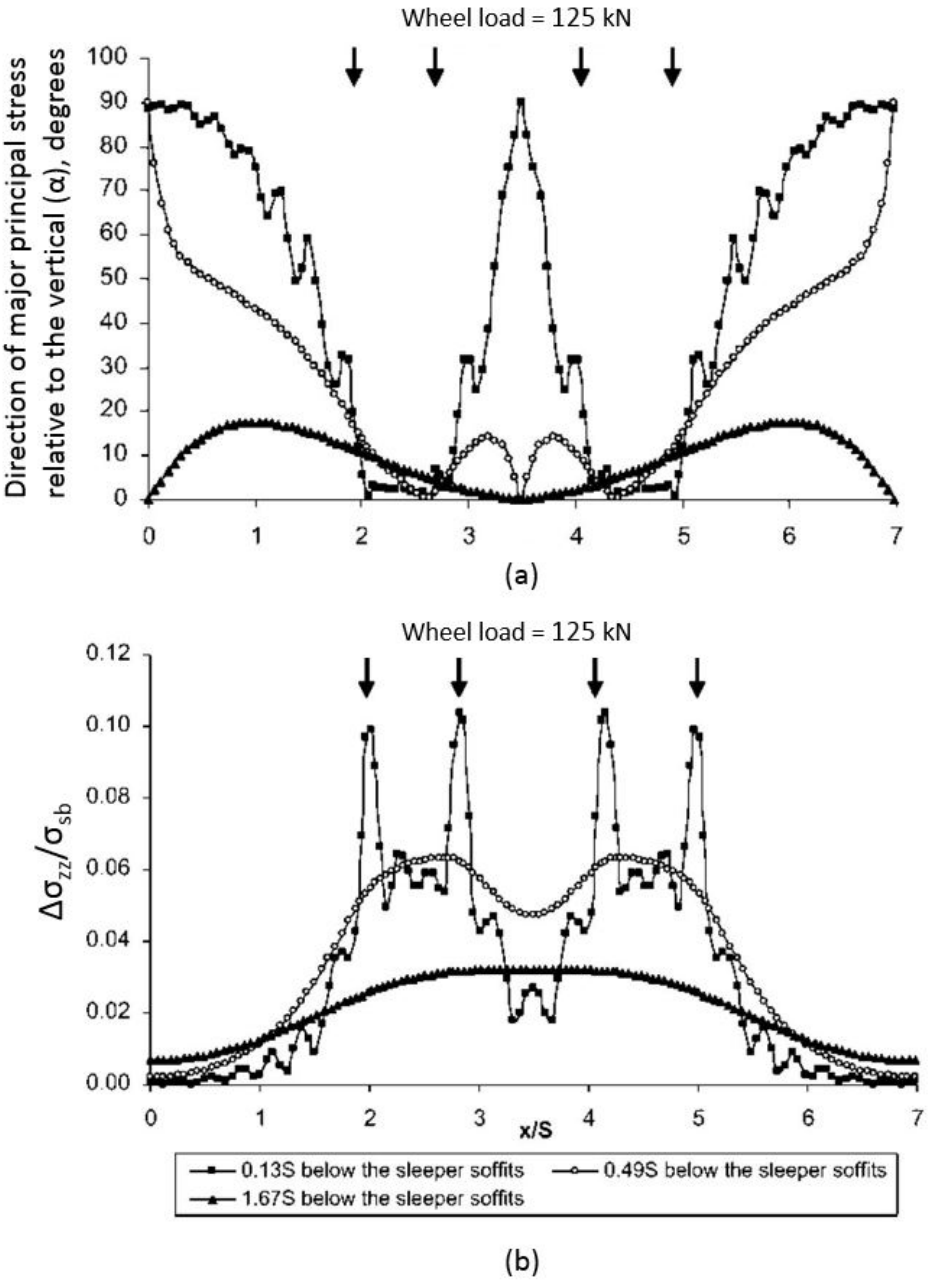

Figure 2.3: Results from dynamic finite element analysis conducted by Powrie et al. (2007) indicating (a) Variation in degree of PSR with depth (normalised by sleeper length, S) in the longitudinal direction below the centre-line ($K_0 = 1$), and (b) Variation in vertical stress, σ_{zz}, on the centre plane with longitudinal distance, for different depths (3D FEA with E=30+10.89.(z/S), without initial stresses)

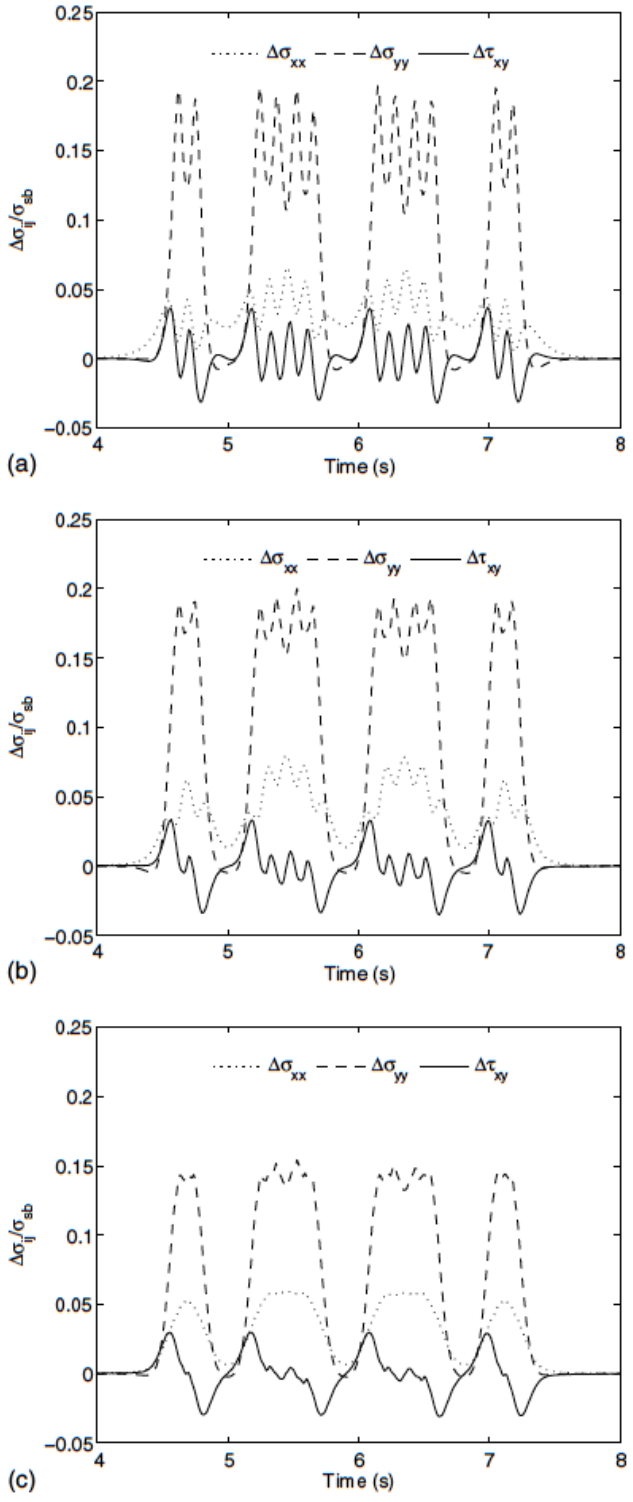

Figure 2.4: Normalised change in vertical stress $\Delta\sigma_{yy}$, horizontal stress $\Delta\sigma_{xx}$ and shear stress $\Delta\tau_{xy}$ at different depths below the sleeper soffit due to the passing of three wagons on a heavy haul rail line in South Africa (Yang et al., 2009); (a) 0.45 m, special sub-ballast layer; (b) 0.75 m, A-layer; and (c) 1.2 m, natural ground level

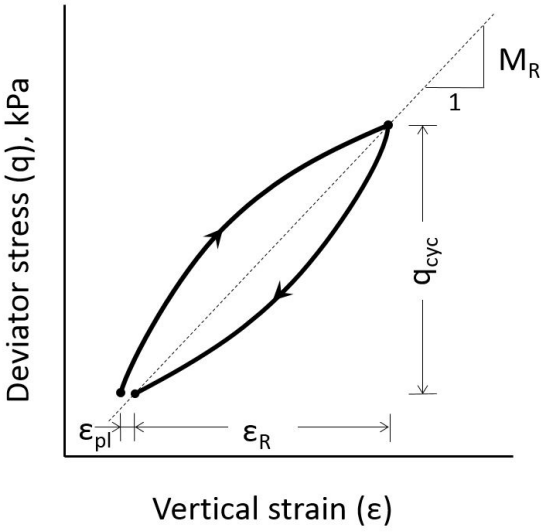

Figure 2.5: Illustration of resilient modulus, M_R, or equivalent Youngs' modulus, E_{eq}, per cycle defined by Equation 2.2

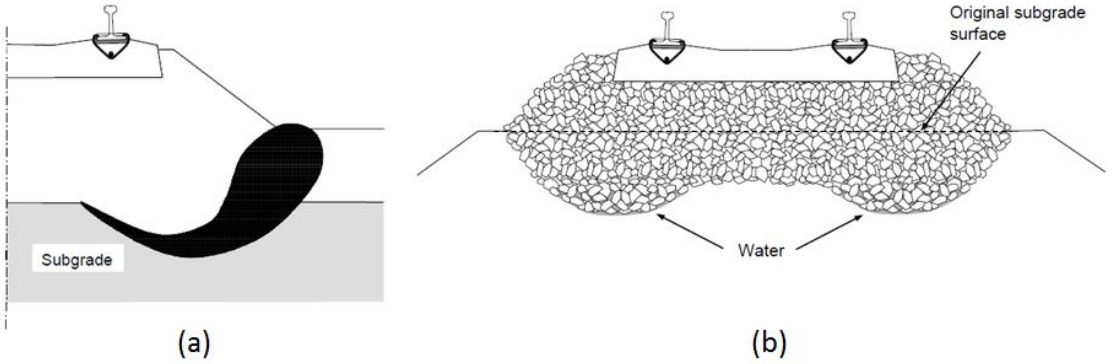

Figure 2.6: Subgrade failure mechanisms due to repeated traffic loading (redrawn by Gräbe (2002) from Li and Selig (1998a)). (a) Progressive shear failure in the subgrade. (b) Excessive plastic deformation or ballast pockets

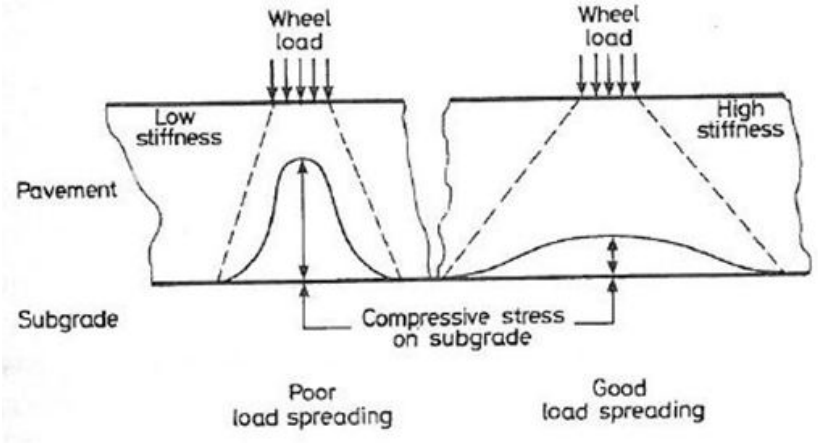

Figure 2.7: Load spreading based on linear elastic theory for pavement material (Brown and Selig, 1991)

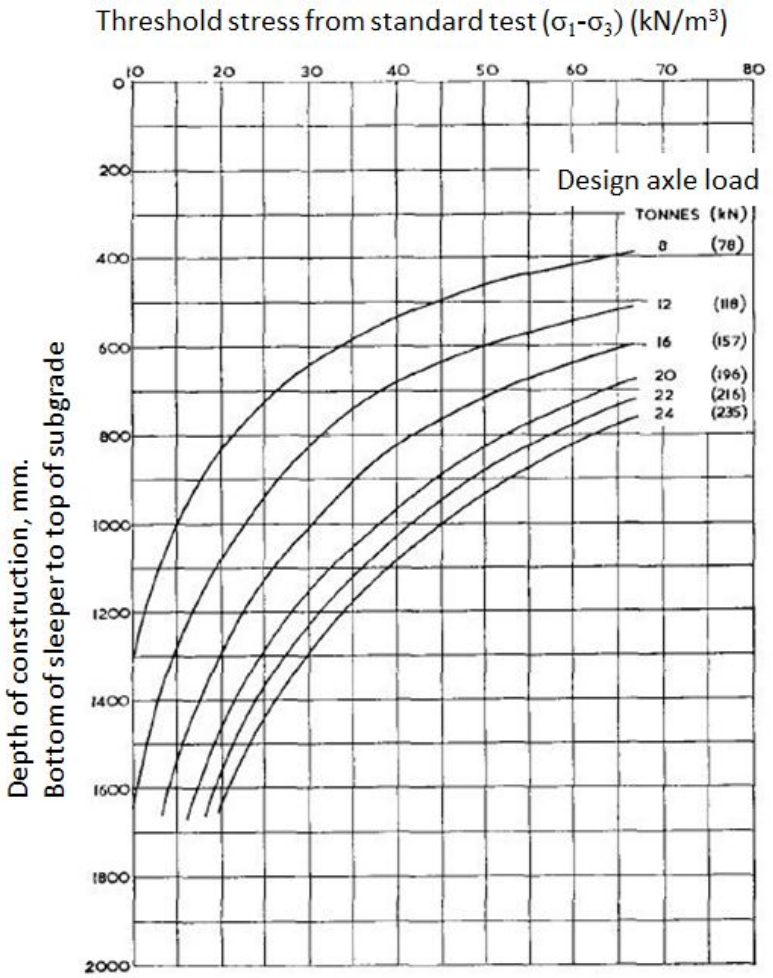

Figure 2.8: Design chart for granular layer depth based on simple elastic theory and subgrade threshold stress by Heath et al. (1972)

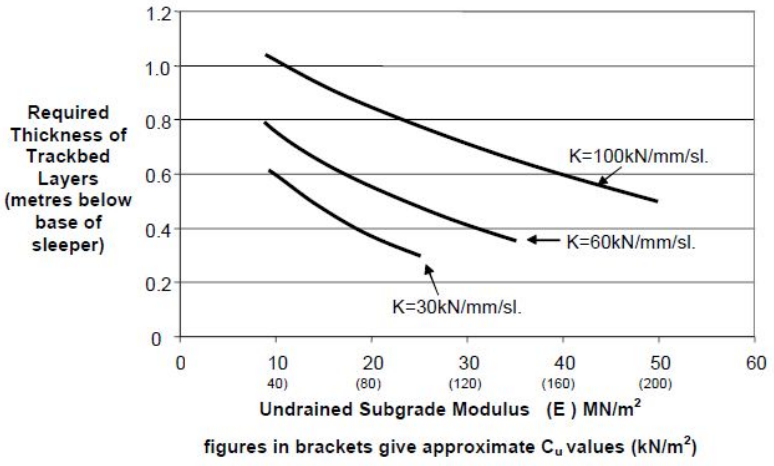

Figure 2.9: Design chart for granular layer depth (trackbed layer thickness) in order to achieve the required trackbed stiffness (K) by Network Rail (2005)

Chapter 3

Factors influencing measured railway formation stiffness

The stiffness of the track system is an important track performance measure (Network Rail, 2005) as discussed in Chapter 2. Specification of material properties, including particle size distribution and Atterberg limits, together with a required California bearing ratio are used in empirical designs for railway foundation layers, but resilient Young's modulus is used in more advanced design methods following the trend of the mechanistic-empirical highway design strategy. The resilient modulus, M_R, is used as a long term and short term pavement performance prediction parameter (Khoury and Zaman, 2004) and has been included in railway formation design by Li and Selig (1998a,b).

Several factors influence the shear strength, volume change and stress-strain behaviour of soil. Some factors that influence the railway formation stiffness including stress, material type and soil physical state (density and water content) are considered next. The importance of these parameters has been acknowledged by the inclusion thereof in empirical design strategies and is herein further investigated within an unsaturated soil mechanics framework.

Section 3.1 introduces the stress state variables used to describe the stress state of unsaturated soils. The two different approaches selected and used are presented. The chapter continues with discussion on the effect of the two independent stress state variables (net normal stress and suction), material type and soil physical state (density and water content) on the stress-strain response of compacted formation material.

3.1 Stress

The two stress state variables used to describe the stress state of unsaturated soil, namely net normal stress and suction, are considered. The influences of the net normal

stress, including confinement and deviatoric stress, on the resilient modulus of pavement materials are discussed. The potential influence of principal stress rotation, stress history and strain level are included. Finally, the influence of suction on soil stiffness is presented.

3.1.1 Mean effective stress

Terzaghi (1936) introduced the principle of effective stress for saturated soils. The well establishes principle attributes all volume and shear strength changes to the change in effective stress (Jennings and Burland, 1962). The effective stress, $\sigma^{'}$, is defined as the difference between the total stress, σ, and the neutral stress, u, or the pore water pressure.

$$\sigma^{'} = \sigma - u \tag{3.1}$$

The assumptions or conditions for which Equation 3.1 are valid include:

- The principal stresses (σ_1, σ_2 and σ_3) acting in a point can be used to determine the stresses in that point (Terzaghi, 1936).
- The neutral stress, u, acts with equal intensity in all directions in the water and in the solid (Terzaghi, 1936).
- The effective stress is independent of the magnitude of the pore pressure. Thus, the effective stress is seated exclusively in the solid phase with only change in effective principal stresses resulting in measurable change such as compression, distortion and a change of shearing resistance (Mitchell and Soga, 2005).
- The pore pressure in the interparticle zone can be related to a remote measuring point (Mitchell and Soga, 2005).
- The solid particles and water are incompressible (Terzaghi, 1936; Bishop and Blight, 1963; Mitchell and Soga, 2005).

However, pavements including railway foundations are near surface structures and therefore prone to change in degree of saturation due to rainfall, relative humidity and temperature conditions (Jin et al., 1994; Brown, 1996; Selig and Li, 1994; Moco Ferreira et al., 2011). This is especially true in more arid countries where the water table is deeper (Jennings and Burland, 1962; Fredlund and Rahardjo, 1993). Compacted layers in fill are constructed as unsaturated materials and are likely to stay unsaturated as they are above the water table (Croney and Coleman, 1961). There is a definite focus on adequate drainage in railway track design methods including Spoornet (2006); NSW Transport RailCorp (2010) and International Union of Railways (2008). Adequate drainage prevents the build-up of positive pore water pressure that results in reduced strength (Li and Selig, 1998a). Additionally, formation performance is likely to benefit

from additional strength and reduced compressibility in the unsaturated state (Mitchell and Soga, 2005).

3.1.2 Shear stress

Understanding and predicting soil behaviour is important for engineering design, evaluation and maintenance. The stress-strain behaviour, volumetric change and shear strength of a soil cannot be explained by the total stress alone (Mitchell and Soga, 2005). The development of an unsaturated soil mechanics framework has been a research focus for several decades and include work by Jennings (1957); Croney et al. (1958); Bishop (1959); Aitchison (1960); Jennings and Burland (1962); Fredlund et al. (1987); Fredlund (1979); Toll (1990); Alonso et al. (1990); Wheeler (1991); Houlsby (1997) and Lu and Likos (2006).

The Terzaghi effective stress (Equation 3.1) is a single stress state variable used to describe the mechanical behaviour of saturated soil. Unsaturated soil has been shown to require two independent stress state variables (Fredlund, 1979; Fredlund and Rahardjo, 1993; Houlsby, 1997) to specify the stress state (Croney and Coleman, 1961) when the soil particles and water are assumed incompressible (Fredlund and Rahardjo, 1993).

3.1.2.1 Net normal stress and matric suction

The most commonly used pair of stress state variables for unsaturated soil, introduced by Bishop and Blight (1963), is the net normal stress, σ_n, and matric suction, ψ_m, selected by Fredlund (1979); Fredlund et al. (1987) as most satisfactory for engineering purposes. The net normal stress is the difference between the total stress, σ, and the pore air pressure, u_a (Equation 3.2).

$$\sigma_n = \sigma - u_a \tag{3.2}$$

Total soil suction, ψ, includes matric suction, ψ_m, and osmotic suction, π, components (Equation 3.3).

$$\psi = \pi + \psi_m \tag{3.3}$$

Osmotic suction, π, is related to salt concentrations in the pore-water. Matric suction, ψ_m, is defined as the difference between the pore-air pressure, u_a, and the pore-water pressure, u_w (Equation 3.4).

$$\psi_m = u_a - u_w \tag{3.4}$$

Environmental changes, such as rainfall or a rise in the water table, are often the cause of engineering problems associated with unsaturated soils (Fredlund and Rahardjo, 1993).

However, osmotic suction is not significantly affected by such changes and therefore, changes in matric suction are normally assumed representative of changes in total suction (Fredlund and Rahardjo, 1993). Osmotic suction has an effect on the mechanical behaviour of saturated and unsaturated soil and should be considered where the engineering application is related to chemical changes in the soil.

The net normal stress and matric suction are part of several interparticle stresses that exist within a particulate system, such as a soil mass, that contribute to the intergranular stress condition (Mitchell and Soga, 2005). The interparticle forces have been categorised into three microscale categories by Santamarina (2003) and further discussed by Mitchell and Soga (2005). The forces, shown in Figure 3.1, include:

1. Skeletal forces due to external loading (Figure 3.1a).
2. Particle level forces including particle weight forces, buoyancy forces when submerged, and seepage forces due to fluid flow (Figure 3.1b).
3. Contact level forces including electrical forces, capillary forces if unsaturated, and cementation-reactive forces (Figure 3.1c).

The net normal stress (Equation 3.2) is considered a global stress that propagates through the soil skeleton (Fredlund and Morgenstern, 1977; Lu and Likos, 2006). It is expected that an externally applied boundary load will distribute through the soil skeleton by means of force chains (Jennings and Burland, 1962; Mitchell and Soga, 2005). The mechanical response to the skeletal force would, to some degree, be influenced by the compressibility of particle contacts (Bishop and Blight, 1963). However, particles are considered incompressible by Terzaghi's law for saturated soil and this has been proven to be a good assumption for most engineering applications (Mitchell and Soga, 2005).

The remaining stress components in the particulate system are distributed local stresses (particle and contact level stresses) which must be self-balanced between adjacent particles for a soil to be in an equilibrium state (Mitchell and Soga, 2005; Lu and Likos, 2006). Particle and contact level forces influence particle rearrangement (Jennings and Burland, 1962; Mitchell and Soga, 2005). Capillary forces are contact level forces which has a bonding effect (Tarantino and Tombolato, 2005), increasing the shear resistance at the interparticle contact level (Mancuso et al., 2002). Matric suction ($u_a - u_w$) represents the pressure difference in the pore spaces due to surface tension (Bishop and Blight, 1963) analogous to the capillary tension of water in a small tube (Aitchison, 1960). The boundary between the water and the air has been classified as a separate phase by Fredlund (1979) termed the meniscus or contractile skin.

The surface tension (meniscus) acts only on part of the soil particles' surface area. Therefore, difficulties arise when including the matric suction, ψ_m, as part of a single

macroscopic effective stress, because it is not a neutral stress (Bishop and Blight, 1963). The effects of σ_n and ψ_m are considered separately as two stress state variables and are not equivalent (Toll, 1990). This is because they have different soil properties (i.e. porosity) which should not be included in the stress state description (Fredlund and Rahardjo, 1993).

Representation of soil behaviour is extended from a two dimensional space in saturated conditions to include a third dimension, matric suction, in unsaturated conditions. Figure 3.2 and 3.3 show examples of an extended Mohr-Coulomb diagram and a plot of the void ratio/stress relationship respectively.

Fredlund and Rahardjo (1993) discuss constitutive relationships for unsaturated soils. The elastic stress-strain relationship (based on Hooke's law) for saturated soils has been extended for unsaturated soils using the stress state variables σ_n and ψ_m (Fredlund, 1979). For an isotropic non-linear elastic stress-strain relationship a small increment is assumed linear and the normal strain increment represented by Equation 3.5 for the x-,y-, or z-direction.

$$d\epsilon_x = \frac{d(\sigma_x - u_a)}{E} - \frac{\upsilon}{E}(\sigma_y + \sigma_z - 2u_a) + \frac{d(u_a - u_w)}{H} \tag{3.5}$$

Where:
d = indicates an increment;
ϵ_x = normal strain in the x-direction;
$\sigma_{x,y,z}$ = total normal stress in the denoted direction (x, y or z);
E = modulus of elasticity or Young's modulus for the soil structure;
υ = Poisson's ratio; and
H = modulus of elasticity for the soil structure with respect to a change in matric suction.

Change in the volumetric strain (Equation 3.6) can be calculated by summing the change in normal strains for the x-, y- and z-directions (Fredlund and Rahardjo, 1993).

$$d\epsilon_V = 3(\frac{1-2\upsilon}{E})d(\sigma_{mean} - u_a) + \frac{3}{H}d(u_a - u_w) \tag{3.6}$$

Where:
$d\epsilon_V$ = increment of volumetric strain; and
σ_{mean} = average total normal stress (i.e. $\frac{\sigma_x+\sigma_y+\sigma_z}{3}$).

The shear strain can be represented by Equation 3.7.

$$\gamma_{xy} = \frac{\tau_{xy}}{G} \tag{3.7}$$

Where:
γ_{xy} = directional shear strain;
τ_{xy} = directional shear stress; and
G = shear modulus.

Calculating strain using Equation 3.5 and 3.6 require knowledge of the modulus of elasticity for the soil structure with respect to a change in matric suction. After construction, an increase in water content of a pavement layer, to an equilibrium condition, is expected (Sauer and Monismith, 1968) with resulting decrease in matric suction. The resulting deformation due to changes in matric suction is not well documented. The shrinkage curve is used to present the influence of matric suction on the volumetric deformation and is further discussed in Section 3.2. Incorporating matric suction in practice is difficult and the second framework for unsaturated soil, the intergranular stress, has been developed for practical implementation.

3.1.2.2 The intergranular stress

Lu and Likos (2006) propose the use of the a suction stress to relate the microscale forces to the macroscopic definition of a true intergranular stress (or equivalent effective stress) for practical application within current effective stress based design concepts. Instead of considering only matric suction, several interparticle physiochemical stresses (contact level forces) including cementation, van der Waals attraction, double-layer repulsion, capillary stress arising from surface tension, and negative pore-water pressure are grouped as a single parameter namely suction stress, σ_s (Equation 3.8).

$$\sigma_s = \Delta\sigma_{pc} + \sigma_{cap} + \chi(u_a - u_w) \tag{3.8}$$

Where:
σ_s = suction stress;
$\Delta\sigma_{pc}$ = change in physiochemical stress (relative to saturated conditions);
σ_{cap} = capillary stress;
χ = Bishop's effective stress parameter that could be linked as representing $(1 - \frac{A_a}{A_t})$ (Mitchell and Soga, 2005; Lu and Likos, 2006); and
A_a = area of air within a cross-sectional area, A_t, through a soil mass.

The suction stress parameter groups stresses that influence the interparticle stress condition, but do not propagate to the boundary where measurements of total stress and pore-pressures are made (Lu and Likos, 2006). Lu and Likos (2006) used microscopic interparticle force and stress analyses to develop the intergranular stress, σ_C, equation (Equation 3.9) which describes the stress state of a soil.

$$\sigma_C = (\sigma - u_a) + \sigma_s + \sigma_{C0} \tag{3.9}$$

Where:
σ_C = intergranular stress;
σ = total stress;
σ_{C0} = intergranular bonding stress;
σ_s = suction stress as given in Equation 3.8.

The intergranular bonding stress, σ_{C0}, is said to represent the component of intergranular stress that results in the apparent cohesion intercept and is estimated from shear tests on saturated materials using Equation 3.10.

$$\sigma_{C0} = c^{'} / \tan \phi^{'} \tag{3.10}$$

Where:
$c^{'}$ = effective cohesion intercept from saturated tests;
$\phi^{'}$ = effective mobilised angle of shearing resistance.

The interparticle stresses cannot be measured directly (Fredlund and Rahardjo, 1993). A suction stress characteristic curve, SSCC, is used to represent the suction stress relative to water content, degree of saturation, or matric suction. This concept is similar to the soil water retention curve, SWRC, used to relate (matric) suction to water content or degree of saturation.

For strength applications the suction stress has been quantified using water-content-controlled macroscopic shear strength tests on unsaturated specimens (Lu and Likos, 2006; Heath et al., 2004). The method is presented in Figure 3.4 where the Mohr failure envelope for each test (on the τ versus σ_n axis) is extended to the suction stress axis (negative x-axis). The method assumes a linear failure envelope for the full range of net normal stresses and therefore is only valid for critical state analysis. The suction stress determined is plotted relative to the appropriate matric suction (negative y-axis) as estimated from the soil water retention curve, SWRC. The SWRC and SSCC are further discussed in Section 3.2.

The intergranular stress model was validated by Lu and Likos (2006) using shear strength test data from the literature. It is claimed that the intergranular stress represents the true effective stress. Considering the definition of effective stress, it is claimed to describe shear strength, volumetric change and stress-strain behaviour of the soil (Terzaghi, 1936). However, the model has not been proven to represent volumetric change or the non-linear stress-strain behaviour of soil.

The resilient modulus, M_R, is a measure of the elastic modulus of a soil at a given stress state (Yau and Von Quintus, 2004) and is highly stress dependent (Ng et al., 2013). The influence of the stress state variables, net normal stress and suction (matric suction or suction stress), on the stiffness of pavement subgrade soil is discussed in Section 3.1.3 and 3.1.4.

3.1.3 Net normal stress influence on formation stiffness

The net normal stress (σ_n) is defined by Equation 3.2 as the mathematical difference between the total stress and pore-air pressure. σ_n is considered to represent the skeletal forces due to externally applied loads (Fredlund and Rahardjo, 1993; Lu and Likos, 2006) and to play an equivalent role to that of effective stress in saturated soil (Mancuso et al., 2002). As discussed previously in Section 3.1.2, σ_n is one of two stress state variables controlling the behaviour of unsaturated soils. Applied total principal stresses, made up of the confining stress of the overburden and cyclic train stresses, minus the pore air pressure are therefore considered as net normal stress components applied to a soil element in a railway formation. Considering drained conditions expected for formation layers above the water table, pore-air pressure is assumed to be zero.

3.1.3.1 Confining stress

The importance of testing formation materials using the appropriate stress conditions (or confinement) has been emphasised (Seed et al., 1967; Hicks and Monismith, 1971; Brown and Hyde, 1975; Khedr, 1985). An increase in confining stress, σ_c, is known to result in higher resilient modulus values (M_R) (Seed et al., 1967), confirmed by Ooi et al. (2004); Liang et al. (2008); Thom et al. (2008); Cary and Zapata (2011) and Salour et al. (2014) for different unsaturated subgrade materials.

Two cohesive silts, high clay content Hawaiian subgrade soils, were tested at six different physical states (density and water content) by Ooi et al. (2004). The influence of confining stress was evaluated for specimens compacted and tested at optimum water content. Their results (Figure 3.5) not only showed higher M_R values for higher confining stresses, but also indicated that the low-plasticity silt tested (Waipio) was more sensitive to the stress state compared to the high-plasticity silt (Wahiawa). Resilient modulus values ranged from approximately 80 MPa to 240 MPa.

Results reported by Salour et al. (2014) for two silty sand subgrade materials suggest that materials with lower fines content are more sensitive to changes in confining stress. Tests conducted by Seed et al. (1967) on aggregate base materials, including gravels and crushed rock, found the confining stress to be the main parameter to influence M_R which led to a predictive model based on σ_c alone. The effect of σ_c is thus particularly important for coarse (low fines content) formation materials. Test done by Cary and Zapata (2011) further confirms that the net normal confining stress has a larger influence on a granular base material compared to a clayey sand subgrade. The Bulk Stress Model (k-Θ model) in Equation 3.11 developed by Hicks and Monismith (1971) is considered suitable for unbound granular materials and is often use due to its simplicity (Lekarp et al., 2000). However, the influence of other net normal stresses (such as the

deviator stress due to applied vehicle loads) should not be disregarded, especially for finer subgrade materials.

$$M_R = k_1 p_a \left(\frac{\Theta}{p_a}\right)^{k_2} \tag{3.11}$$

Where:

- M_R = Resilient modulus;
- Θ = Bulk stress = sum of principal stresses (maximum per cycle), $(\sigma_1 + \sigma_2 + \sigma_3)$;
- p_a = Atmospheric pressure (100 kPa); and
- k_n = regression coefficients.

Craciun (2009) investigated the influence of the cyclic loading conditions and matric suction on the deformation and resilient modulus of unbound granular base material. A cyclic triaxial device was modified to allow suction control and measurement. Test pairs including cyclic and non-cyclic confining pressures indicated lower permanent axial deformation and higher M_R for tests conducted under cyclic confining stresses. The cyclic confining stress caused specimens to dilate when considering volumetric strain. This observation opposes Brown et al. (1975) who concluded that both resilient modulus and permanent strain were of similar values for tests conducted at a constant (average) and cyclic confining stress. The influence of the traffic induced cyclic confining stresses has mainly been considered for coarse unbound granular base materials and is expected to reduce in significance for finer subgrade materials, due to the reduced influence of confinement as fines content increases (Karasahin and Dawson, 1994).

3.1.3.2 Deviator stress

A moving vehicle induces a combination of cyclic stresses as discussed in Section 2.2.1. The largest in magnitude and most commonly considered in flexible pavement material testing is the cyclic vertical stress. For triaxial tests in compression (TC) the vertical stress is equal to the major principal stress (σ_1) and the deviator stress (q, given by Equation 4.12) reduces to the difference between σ_1 and σ_3 (Equation 4.14). M_R is defined as the cyclic deviator stress ($q_{cyc} = q_{max} - q_{min}$) divided by the recoverable strain, ϵ_R (Equation 2.2). Assuming pore-air pressure remains constant for each load cycle, the deviator stress calculated using total stresses is equal to the deviator stress in the net normal stress plane.

Ng et al. (2013) investigated the influence of q_{cyc} on M_R of unsaturated completely decomposed tuff (CDT) using a modified cyclic triaxial apparatus for suction controlled

unsaturated soil testing. They found that M_R reduced with an increase in q_{cyc} (Figure 3.6). Ceratti et al. (2004) and Ooi et al. (2004) reported the same trend for compacted residual lateritic soil and cohesive silts respectively. Thom et al. (2008) and Sivakumar et al. (2013) tested compacted kaolin and also reported a reduction in M_R with increase in applied q_{cyc}.

For a clay subgrade soil Seed et al. (1967) reported that the rate at which M_R decreased due to increased q_{cyc} depended on the water content. Ng et al. (2013) showed that the magnitude of M_R reduced more significantly due to the same increase in q_{cyc} for higher suction conditions (Figure 3.6), which is in agreement with the observations made by Seed and his co-workers relative to water content. An increase in q_{cyc} results in increased permanent strain levels (Thom et al., 2008; Sivakumar et al., 2013). Therefore a reduction in stiffness due to an increase in q_{cyc} is expected, considering the non-linear stress-strain behaviour of soil (Atkinson, 2000) with decreasing stiffness at higher strain levels. The softening effect is ascribed to increased mobilisation at the particle level. The constitutive model, for M_R, known as the Universal Model (Equation 3.12) is often used for mechanistic-empirical pavement design (Salour and Erlingsson, 2015). The Universal Model is an adaptation of the model developed by Uzan (1985), which includes the deviator stress. Other constitutive models, based on total stress parameters, are summarised by Lekarp et al. (2000).

$$M_R = k_1 p_a \left(\frac{\Theta}{p_a}\right)^{k_2} \left(\frac{\tau_{oct}}{p_a} + 1\right)^{k_3} \tag{3.12}$$

Where:

- Θ = bulk stress = sum of principal stresses (maximum per cycle), $(\sigma_1 + \sigma_2 + \sigma_3)$;
- τ_{oct} = octahedral shear stress ($\frac{\sqrt{2}}{3}(\sigma_1 - \sigma_3)$ for triaxial compression);
- p_a = atmospheric pressure (100 kPa); and
- k_n = regression coefficients.

The testing of unsaturated specimens under constant water content conditions and subject to compressive strain due to q_{cyc} will result in an increase in the degree of saturation. An increase in degree of saturation is expected to result in the further decrease of M_R due to the reduced matric suction, discussed in Section 3.1.4.

The influence of q_{cyc} on coarse unbound granular base materials is different. It has been shown that M_R of base materials (unbound granular materials) increases with the increase of deviator stress (increases Θ), while that of subgrade materials decreases (Seed et al., 1967; Hicks and Monismith, 1971). Brown et al. (1975) reported an increase in M_R relative to q_{cyc} for well-graded crushed stone road base material ($\leq$5 mm), irrespective

of stress history. No conclusive relationship was found by Khedr (1985) for untreated granular crushed limestone base course material tested at a range of water contents. Specimens were compacted at various water contents, to the same dry density, and tested under a range of confining stresses. No regard for the suction condition was considered during the interpretation of results, possibly affecting the ability to identify the effect of q_{cyc}.

The Spoornet and UIC railway formation design strategies, discussed in Section 2.3, regards a well graded coarse grained material that includes some fines (approximately 10% passing the 0.075mm sieve) as a suitable subgrade formation material (See Figure 4.1). A granular base material (7% passing the 0.075 mm sieve) tested by Cary and Zapata (2011) have material properties satisfying requirements for a subballast (SB) material in the Spoornet formation design and a QS3 material in the UIC design. Results reported by Cary and Zapata (2011) indicate a reduction in M_R for an increase in τ_{oct}, however the influence was significantly smaller than that for a clayey sand subgrade with high fines content (47% passing 0.075 mm sieve) reported in the same study further discussed in Section 3.1.4. A reduction in M_R due to q_{cyc} is thus expected for a typical railway formation material as seen for other flexible pavement subgrade materials.

3.1.3.3 Principal stress rotation

The traffic induced stresses, discussed in Chapter 2, not only include cyclic vertical stress, but also horizontal and shear stress cycles. Shear stress reversal induces a certain degree of principal stress rotation, PSR. The effect of PSR on the response of dry crushed dolomitic limestone pavement base material was tested using a hollow cylinder apparatus, HCA, by Chan and Brown (1994). No particular trend of plastic strain in the vertical direction was observed due to PSR and it was reasoned that this was due to the relatively small shear stress, compared to the applied q_{cyc}. The horizontal strain development was significantly influenced. With application of PSR the initial horizontal strain was dilatant, but after 100 to 300 cycles the strain measured tended to change to compression. However, the study did not assess the impact on M_R.

Tests on saturated specimens representative of railway subballast and subgrade materials were conducted by Gräbe (2002) using a hollow cylinder apparatus. Test pairs consisted of one specimen subject to cyclic triaxial loading (no PSR), and the other subject to simultaneous vertical and shear stress cycling (with PSR). Figure 3.7 compares the permanent axial strain development as presented by Gräbe and Clayton (2009). It can be seen that the permanent axial strain was compressive and increased considerably when specimens were subjected to PSR. This is expected to affect the M_R based on non-linear soil behaviour.

Gräbe and Clayton (2014) reported the influence of PSR on M_R for four representative subgrade materials with different percentages of fines (clay content). The measured M_R for specimens subject to PSR was approximately 20% less than M_R measured under cyclic triaxial compression conditions only. The inclusion of PSR resulted in the highest reduction of M_R for the tested material with the lowest clay content, however the differences in the effect of PSR on the formation materials for the different fines content materials tested were marginal. The effect of PSR on unsaturated formation material has not yet been assessed.

3.1.3.4 Number of load cycles

The number of load cycles, N, are considered important when evaluating the impact of traffic (applied stresses) on the foundation behaviour over the service life of the foundation (Li and Selig, 1998b). A change in M_R with progressive cycles has been shown to correspond to the development of strain (Thom et al., 2008; Ng et al., 2013; Sivakumar et al., 2013). Ng et al. (2013) reported the dilation of unsaturated specimens (under controlled matric suction condition, thus drained) under cyclic loading in contrast to compression of the equivalent saturated specimens. The values of M_R were normalised in Figure 3.8 by Ng and his co-workers using the modulus measured in the first cycle for the particular loading sequence. The increase in M_R of saturated material (Figure 3.8a), due to the number of cycles, has been ascribed to the progressive densification of the soil (Dehlen, 1969). The influence of N was less significant for unsaturated conditions. Figure 3.8b indicates a slight reduction in M_R measured by Ng and his colleagues due to dilation.

Loading history is generally not considered in standard testing (AASHTO, 1993) as it is considered to have little impact on the resilient strain (Brown et al., 1975; Hicks and Monismith, 1971). Nazarian et al. (1996) discussed the influence of loading history for laboratory testing, especially the effect of pre-conditioning of test specimens, which could lead to unrepresentative M_R results (Cerni et al., 2015).

3.1.3.5 Summary of net normal stress influence

Summarising the effect of net normal stresses as discussed above.

- Confining stress, deviator stress sequence and stress history are important when evaluating the permanent deformation of pavement materials (Brown et al., 1975; Nazarian et al., 1996; Andrei et al., 2004).
- The influence of deviator stress on M_R needs to be considered for finer subgrade materials, such as those used in railway formation layers.

- The number of load cycles has been shown to be less significant for unsaturated soil stiffness development (Ng et al., 2013).
- Evaluation of strain accumulation, due to PSR (Chan and Brown, 1994; Gräbe and Clayton, 2009) and cyclic confining stress (Craciun, 2009), should be considered as this could change the development of M_R.

The influence of PSR on the resilient modulus of unsaturated railway foundation material has not yet been considered. Soils are not ideal elastic materials and the stress-strain response depends on the stress path and testing rates used (Bishop and Blight, 1963). For unsaturated soils, there are two stress path functions to consider namely the net normal stress (σ_n) and matric suction (ψ_m). The influence of matric suction is discussed in Section 3.1.4.

3.1.4 Matric suction influence on formation stiffness

The second stress state variable used to describe the stress state of an unsaturated soil is suction. As discussed in Section 3.1.2, matric suction (Equation 3.4) is used as equivalent to total suction for most engineering applications. The changes in matric suction in a railway foundation are mainly due to environmental changes, including rainfall (infiltration) and relative humidity (Moco Ferreira et al., 2011).

The net normal stress and matric suction approach (Fredlund and Morgenstern, 1977), previously discussed, has been used in some studies investigating the role of suction (or water content) on the resilient modulus of flexible pavement materials. Matric suction is considered important for understanding the behaviour of unsaturated pavement materials subject to cyclic loading (Parreira and Goncalves, 2000; Yang et al., 2008; Craciun and Lo, 2010; Cary and Zapata, 2011; Ng et al., 2013). The intergranular stress approach, which includes the suction stress to obtain a comparable effective stress has been used in some stiffness evaluations of unsaturated subgrades (Heath et al., 2004; Yang et al., 2005; Liang et al., 2008).

3.1.4.1 Soil suction influence on resilient modulus

Sauer and Monismith (1968) investigated the effect of in-situ soil suctions on the resilient modulus and rate of permanent deformation of southern Saskatchewan highway pavements. Cyclic triaxial compression tests were performed on glacial till material, similar to the material used in the pavement layers. Specimens were statically compacted, to 100% AASHTO (American Association of State Highway and Transportation Officials) dry density (1756 kg/m^3), at different water contents representative of field conditions. In Figure 3.9 the resilient modulus is plotted against suction. The original curve proposed by Sauer and Monismith (1968) (Figure 3.9 insert), representing resilient modulus

versus suction, was shown to increase towards an asymptote value of M_R. However, a second order polynomial can also be fitted to the data (Figure 3.9) suggesting a reduction in M_R at higher suctions. This indicates a reduced influence at higher suctions as seen by Otter (2011) for shear stiffness of clayey sand specimens (Figure 3.10) compacted at a range of water contents (to the same target density). However, the trend can not be conclusively changed due to insufficient data points in the 300 kPa to 500 kPa suction range.

An increase in M_R corresponding to an increase in matric suction has been reported by Sivakumar et al. (2013) for Kaolin clay, compacted and tested at a range of water contents. Figure 3.11 represents specimens tested under a range of cyclic vertical and confining stresses (discussed in Section 3.1.3). Figure 3.11a are results for tests on specimens statically compacted using a 400 kPa vertical stress (classified by the authors as un-engineered fill, UEF), while Figure 3.11b shows results for specimens compacted under 800 kPa vertical stress (engineered fill, EF). More noticeable in the UEF (less dense specimens) is the slight drop in M_R at higher suctions. The influence of suction is more pronounced for specimens tested at lower confining stress. However, specimens were prepared using equal compaction energy, at various water contents, therefore produced specimens of varied density.

The method of investigating the influence of matric suction, by changing the preparation water content as done by Sauer and Monismith (1968); Otter (2011); Sivakumar et al. (2013), is debated due to the expected difference in microstructure as discussed by Alonso et al. (2013). Specimens prepared at different water contents, to the same density/apparent void ratio, will have inconsistent pore structures (Jennings and Burland, 1962). However, this is more prominent for high clay content materials. The approach used, for specimen preparation at a range of water contents, is a practical approach (Heath et al., 2004) and M_R results for highly compacted formation materials are regarded as indicative of the influence of matric suction.

Ng et al. (2013) prepared specimens, of completely decomposed tuff (silt), at optimum water content to the same density. Specimens were tested under a range of induced matric suction values, using an adapted Cyclic Triaxial Apparatus for unsaturated testing using the axis translation technique. Specimens under higher suctions tended to dilate under expected cyclic traffic loading, while specimens under low suctions contracted. The phenomena was ascribed to suction induced dilatancy (Ng et al., 2013). The resilient modulus measured by Ng and his co-workers increased with an increase in matric suction up to 350 kPa. An increase in M_R was also reported by Ceratti et al. (2004), for residual lateritic soil (Brazilian shale), and Yang et al. (2008), who tested pulverised residual mudstone. However, Ng et al. (2013) reported different M_R values for specimens tested at the same matric suction, but subject to different suction history. They reported higher M_R values for specimens on the wetting path versus those on the drying

path. This contradicts the observations made by Ceratti et al. (2004), of a significant reduction in M_R for specimens tested after a drying-then-wetting cycle.

3.1.4.2 Resilient modulus model including matric suction

Advances on constitutive M_R models based on total stress analysis, summarised by Lekarp et al. (2000), have been made over recent years. Several models, which include for matric suction, have been proposed (Parreira and Goncalves, 2000; Sawangsuriya et al., 2009; Cary and Zapata, 2011; Ng et al., 2013) as reviewed by Salour and Erlingsson (2015). The constitutive model proposed by Cary and Zapata (2011) is an extension of the Universal model (Equation 3.12) as given by Equation 3.13.

$$M_R = k_1 p_a \left(\frac{\Theta_{net} - 3\Delta u_{w-sat}}{p_a}\right)^{k_2} \left(\frac{\tau_{oct}}{p_a} + 1\right)^{k_3} \left(\frac{\psi_m - \Delta\psi_m}{p_a} + 1\right)^{k_4} \tag{3.13}$$

Where:

- Θ_{net} = net bulk stress = sum of principal net normal stresses, $(\sigma_1 + \sigma_2 + \sigma_3 - 3u_a)$;
- τ_{oct} = octahedral shear stress ($\frac{\sqrt{2}}{3}(\sigma_1 - \sigma_3)$ for triaxial compression);
- ψ_m = matric suction (u_a - u_w);
- $\Delta\psi_m$ = relative change in matric suction with respect to the initial ψ_m;
- p_a = atmospheric pressure (100 kPa);
- u_{w-sat} = positive pore water pressure for saturated conditions ($\psi_m = 0$); and
- k_n = regression coefficients.

Suction controlled CTX testing conducted by Cary and Zapata (2011) on a granular base material and a clayey sand indicated the significant effect matric suction has on M_R. M_R measured by Cary and Zapata (2011) ranged between 100 MPa and 900 MPa for the granular base material and between 80 MPa and 570 MPa for the clayey sand. From their analysis of the results using the expanded M_R model given by Equation 3.13 it was shown that the clayey sand was significantly more sensitive to changes in matric suction ($k_4^{'}$=1.650), compared to the granular base material ($k_4^{'}$=0.180) as indicated on Figure 3.12. The granular base material was most sensitive to the net bulk stress ($k_2^{'}$=0.628), while the clayey sand was most sensitive to the octahedral shear stress ($k_3^{'}$=-2.982).

Ng et al. (2013) proposed and verified a semi-empirical equation, representing the stress-dependency of M_R, that includes matric suction. Salour and Erlingsson (2015) presented the equation by Ng et al. (2013) in the three-dimentional stress form as Equation 3.14.

$$M_R = k_1 p_a \left(\frac{\Theta_{net}}{p_a}\right)^{k_2} \left(\frac{\tau_{oct}}{p_a} + 1\right)^{k_3} \left(\frac{\psi_m}{\Theta_{net}} + 1\right)^{k_4} \tag{3.14}$$

To capture the trend of reduced M_R with an increase in q_{cyc} for subgrade materials, discussed in Section 3.1.3, the regression coefficient k_3 should be negative. k_2 is expected to be a positive value, as it was shown that M_R increases with confinement stress. k_4 in the matric suction models should be positive, as M_R increases with matric suction over the expected formation conditions. The regression exponents are material dependent. Andrei et al. (2004) stressed the importance of a rational stress sequence for M_R testing to insure a more accurate prediction for the stress dependent M_R.

3.1.4.3 Resilient modulus using the intergranular stress method

The use of an equivalent effective stress, or intergranular stress method (Section 3.1.2), to adapt total stress M_R models to include the effect of matric suction, has been proposed by Heath et al. (2004); Yang et al. (2005) and Liang et al. (2008). The benefit of using a suction stress ($\sigma_s = \chi\ \psi_m$) approach is the use of existing models. The M_R model proposed by Liang et al. (2008), to include the effect of matric suction or suction stress, is given by Equation 3.15.

$$M_R = k_1 p_a \left(\frac{\Theta + \chi\psi_m}{p_a}\right)^{k_2} \left(\frac{\tau_{oct}}{p_a} + 1\right)^{k_3} \tag{3.15}$$

Where:

- Θ = bulk stress;
- χ = Bishop's effective stress parameter; and
- $\chi\psi$ = suction stress, σ_s.

However, determining suction stress is difficult. Determining the relationship of suction stress with respect to water content or matric suction, SSCC, was described by Heath et al. (2004) and Lu and Likos (2006) using shear strength data. Figure 3.13 shows the suction stress versus matric suction determined by Oh et al. (2013) for two different soils, using K_0 consolidation and shear strength test results. Also shown is an estimate of the SSCC using the soil water retention curve, SWRC, discussed in Section 3.3.1. Their work suggests that a unique SSCC exist for a soil. However, this is based on limited tests results.

Determining the suction stress characteristic curve, SSCC, based on the stress-strain (modulus) response is suggested by Heath et al. (2004). However, strain influence should be considered.

3.2 Material type influence on formation stiffness

Material type is one of the factors considered to influence the resilient modulus, M_R, and permanent deformation of pavement formations (Li and Selig, 1994). The classification of soils is routinely done using particle size distribution and Atterberg limits (Powrie, 2014b). Railway foundation design guidelines include specification of particle size distribution and Atterberg limits, as discussed in Chapter 2. Spoornet (2006) and International Union of Railways (2008) designs specify the use of well-graded material, with the inclusion of some fines for use in formation layers (Figure 4.1b).

Yau and Von Quintus (2004) and Soliman and Shalaby (2013) set out to establish a relationship between the physical properties of pavement subgrade materials, including subgrade soils, and M_R using the long-term pavement performance program database in the USA. They concluded that no accurate prediction of M_R can be made based on the classification data (including Atterberg limits, density and water content) as captured in the database, also concluded by Ooi et al. (2004) following statistical evaluations. Properties found to relate, to some degree, to M_R did include percentage fines (clay and silt), plasticity index (PI), liquid limit, water content and density (Yau and Von Quintus, 2004).

The particle size distribution curve, PSD, indicates the cumulative percentage by mass of particles passing a certain (sieve) size. The particle size distribution, PSD, relates to the distribution of pore spaces or void spaces in a soil body (Fredlund et al., 2012; Powrie, 2014b). The void spaces are of particular interest in unsaturated soil mechanics as the development of matric suction relates to the pore sizes and the ability to retain water in capillary tension (Fredlund and Rahardjo, 1993). Soil suction is regarded as a stress state variable (Fredlund and Morgenstern, 1977; Alonso et al., 1990; Lu and Likos, 2006; Fredlund et al., 2012) and the influence on M_R is discussed in Section 3.1.4. Ng et al. (2013) and Salour et al. (2014) noted the influence of suction on M_R as more prominent for material with higher fines content, and the influence on plastic deformation was more significant for materials with lower plasticity index, PI. Yau and Von Quintus (2004) also found percentage clay content to influence M_R for all soil groups. The inclusion of some fines in the Spoornet (2006) empirical design strategy is thus significant, considering the influence on matric suction development and its influence on M_R.

Grain size distribution is an indication of the particle size distribution of dry material. For an in-situ material the apparent particle size distribution could be different from the laboratory determined value. This is due to the potential of fine materials (clay) to tightly clump together to form clay aggregates (Jennings and Burland, 1962). This could lead to a more open macro-structure soil matrix influencing the mechanical behaviour, especially in collapsible soils.

Apart from the influence of PSD on the matric suction development, the response of material to net normal stress is also influenced by the material type. As discussed in Section 3.1.3, and observed by Yau and Von Quintus (2004), M_R of coarse unbound base material increases with increase in deviator stress while fine subgrade material M_R reduces. The ability to resist shear is also influenced by particle shape. Particle shape refers to three properties namely particle form, particle roundness, and surface texture (Bui, 2009). These properties will influence the contact interaction between particles in the soil matrix. Interlocking capabilities are improved when material is well-graded and angular (Powrie, 2014b).

Other material properties which need to be considered when assessing the long term behaviour of formation material is the susceptibility to weathering, as it will be exposed to changes in moisture and temperature (International Union of Railways, 2008).

3.3 Soil physical state

The soil physical state (water content and dry density) is the third factor considered to influence the behaviour of the railway foundation (Li and Selig, 1994), with stress and material type discussed in previous sections. The empirical methods for railway formation design, discussed in Chapter 2, stipulate the construction of engineering layers to be done at optimum water content to achieve the maximum dry density. The quality of compaction plays a significant role in the bearing-deformation properties, volumetric change, hydraulic properties and stability of soil (Brandl, 2001).

The matric suction relationship with water content is dependent on the material type and density or void ratio (Fredlund and Rahardjo, 1993; Yang et al., 2004), and is generally represented by a soil-water retention curve. The soil-water retention curve, SWRC, is introduced below with discussion of the key characteristics (Section 3.3.1). Estimating the suction stress characteristic curve, SSCC, from the SWRC using the effective degree of saturation is briefly introduced. The influence of void ratio or density and water content on the formation stiffness is discussed in Sections 3.3.2 and 3.3.3 respectively.

3.3.1 The Soil-Water Retention Curve

The relationship between suction and water content (gravimetric, $w = \frac{m_w}{m_s}$, or volumetric, $\theta_w = \frac{V_w}{V}$) or degree of saturation (S_r) is commonly referred to as the soil-water retention curve, SWRC (Figure 3.14a). The ability of a soil to retain water is reflected in the soil-water retention curve, SWRC, which is also referred to as the soil-water characteristic curve, SWCC (Mitchell and Soga, 2005). The SWRC is a semi-log plot with matric suction presented on the log scale axis. The matric suction is plotted on the y-axis in Figure 3.14, but is also plotted on the x-axis in various other publications

(Fredlund and Rahardjo, 1993). The choice of axis is dependent on the method used to determine the relationship.

3.3.1.1 Key characteristics of the SWRC

It is known that wetting and drying paths lead to scanning curves (Croney and Coleman, 1961; Fredlund and Rahardjo, 1993). It is reasoned to be due to the ink bottle effect (Figure 3.14b), or irreversible change in fabric and shrinkage during drying (Mitchell and Soga, 2005). Important characteristics of the SWRC, discussed by Mitchell and Soga (2005), as indicated in Figure 3.15, include the following.

- Saturated water content (θ_s). Water content at which suction changes do not change the saturated state.
- Air entry pressure or air entry value (ψ_a). Suction point at which the pore-air phase becomes interconnected (Fredlund and Rahardjo, 1993).
- Displacement pressure (ψ_d; $< \psi_a$). Point at which first de-saturation occurs during a drainage cycle (Corey, 1994).
- Residual water content (θ_r). An increase in suction does not result in any further reduction of water content. The water phase is discontinuous beyond this value (Yang et al., 2004). The residual water content can be associated with two different suction values depending on whether the soil is drying (ψ_r) or wetting (ψ_w) (Yang et al., 2004).

Four different behavioural regimes have been identified, as discussed by Lu and Likos (2006) (Figure 3.15). The regimes, as differentiated by the state of saturation and the dominant water adsorption mechanism, are summarised below. Regime I and II is of most interest for flexible pavement and railway formation applications.

- Regime I: Saturated regime. The system remains saturated under negative pore pressure until the air entry value (ψ_a) is reached.
- Regime II: Capillary regime. Water is retained under capillary tension and is primarily a function of the pore size distribution.
- Regime III: Hydration regime. Short range hydration mechanisms at the particle surfaces becomes comparable to capillary mechanisms.
- Regime IV: Residual regime. Changes in suction do not influence the water content as pore water is primarily retained on the particle surfaces.

The shape of the SWRC is a function of the grading of the soil, its compressibility, its density and the mineral nature of the soil particles (Croney and Coleman, 1961). Yang et al. (2004) compared the factors affecting the SWRC for sandy soils and compared SWRCs estimated from the particle size distribution with that of measured results. It was found that the SWRC has a consistent relationship with the particle size distribution of the soil, with some variation due to dry density. The shape and key characteristics of the SWRC are associated with material type (Section 3.2) as illustrated in Figure 3.16.

3.3.1.2 The suction stress characteristic curve

The suction stress has been defined as the work done by matric suction (Lu et al., 2010). The relationship between matric suction and suction stress as presented by Lu et al. (2010) is given by Equation 3.16. The effective degree of saturation (S_e) is used similarly to the Bishop's χ-factor to obtain the equivalent effective stress or intergranular stress as discussed in Section 3.1.2

$$\sigma_s = -\frac{\theta - \theta_r}{\theta_s - \theta_r}(u_a - u_w) = -S_e(u_a - u_w) \tag{3.16}$$

Where:
σ_s = suction stress;
θ = volumetric water content;
θ_r = residual volumetric water content;
θ_s = saturated volumetric water content;
S_e = effective or normalised degree of saturation.

A similar relationship in terms of degree of saturation (Lu et al., 2010), as used by Baille et al. (2013), was also developed. Figure 3.17 presents an idealised relationship between the SWRC and the SSCC (Lu et al., 2010). The effective degree of saturation, S_e, is linked to SWRC-curve fit parameters from van Genuchten (1980). Alonso et al. (2013) incorporates a similar approach to capture the degree of saturation in the macropore structure by introducing a microstructure state parameter (ksi = e_m/e). The microstructure state parameter is used to reduce the full saturation range (S_R) of the soil to the effective saturation (S_e) in the macropores as illustrated by Alonso et al. (2013) (Figure 3.18). The suction stress is material dependent and Figure 3.19 depicts trends for sand and clay respectively (Lu and Likos, 2006).

3.3.1.3 Methods for determining the SWRC

Several methods are available for determining the soil-water retention curve. These include, the axis translation technique (pressure plate and suction-controlled oedometer),

the filter paper technique (direct and indirect measurements), tensiometer, osmotic technique, the hanging column, the chilled mirror psychrometer method, and the centrifuge technique. The use and limitations of the different techniques are discussed by Mitchell and Soga (2005) and Fredlund et al. (2012) and is not considered here. The Chilled-Mirror Dew-point Potentiometer is introduced in Chapter 4, as this technique was used during this study. It allowed for quick assessment of the suction for comparison with previously obtained results from pressure plate, filter paper and tensiometer techniques reported by Otter (2011) for a representative railway formation material.

3.3.2 Void ratio influence on formation stiffness

Compaction requirements are normally specified to achieve the maximum dry density, or a minimum percentage thereof, based on the expected energy input from the construction methods (Ceratti et al., 2004). Compacted soil is evaluated for its dry density which reflects the void ratio, e, or void spaces, which influences the development of matric suction. The dry density versus water content relationship is established using standardised laboratory methods. The dynamic compaction method used in this study is further discussed in Section 4.1.4.

The compaction water content influences the pore structure of the compacted material (Jennings and Burland, 1962). The optimum water content is used as the target water content (within 1%) for railway foundation (Spoornet, 2006) and pavement (AASHTO, 1993) construction. Compaction at lower than optimum water contents could lead to an open microstructure susceptible to collapse upon first wetting (Alonso et al., 2013), although this is more prominent in cohesive (high fines content) materials (Jennings and Burland, 1962). Microstructure has been defined as the ratio of microvoid volume to total void volume (Alonso et al., 2013).

The method of compaction influences the resilient modulus, M_R, measured (Yau and Von Quintus, 2004). Therefore, laboratory compaction methods need to be representative of field construction methods. Ceratti et al. (2004) showed that static compaction yields specimens with the highest M_R while specimens compacted by kneading achieved the lowest M_R. This outcome is as expected and reported in the literature summarised by (Nazarian et al., 1996). Dynamic compaction results fell between static and kneading compaction (Ceratti et al., 2004).

The method of compaction is likely to influence the arrangement of particles and the internal pore structure. Kneading and dynamic compaction results in localised shearing of clay material when compacted wet, for degree of saturations higher than approximately 85% (Seed et al., 1962). The shear strain induced, significantly influenced by the compaction method, causes clay particles to arrange parallel to each other forming a dispersed structure (Seed et al., 1962). When clay particles are randomly orientated

(as opposed to parallel) the clay structure is defined as flocculated (Craig, 2004). Clay compacted dry of optimum was identified by (Seed et al., 1962) as having a similar, flocculated structure irrespective of the compaction method used. Static compaction results in a flocculated structure irrespective of the compaction water content, wet or dry, as localised shearing is minimal (Seed et al., 1962).

The influence of compaction on the resilient modulus of highway subgrade materials (including silty clay and clay) was investigated by Seed et al. (1962). They found a distinct difference in behaviour (resilient modulus) of material compacted wet and dry of the ′line of optimums′ (S_R ±85% corresponding roughly to the 3% air voids line, A=3%). Figure 3.20a indicates the sensitivity of M_R to small changes in water content and density for wet material, while material on the dry side of optimum is less sensitive. At constant water content, an increase in density resulted in the increase of M_R (decrease in ϵ_R) for dry of optimum conditions, while M_R reduced as density increased for wet of optimum conditions. These differences in behaviour was ascribed to the differences in material structure. For both dry and wet conditions M_R reduced (increase in resilient axial strain, ϵ_R) as water content increased (thus soil suction decreased) shown in Figure 3.20b when considering particular density.

The void ratio or pore space is of particular interest in unsaturated soil mechanics. Alonso et al. (2010) divides the total void space into two categories namely micropores and macropores. Water in the micropores are regarded as immobile, while the water in the marcopores are ′free′ water influencing the mechanical behaviour of the soil (Alonso et al., 2010). Micropores are normally associated with high plasticity clays, while granular materials have less of a bi-modal structure (no clay). Alonso et al. (2013) has introduced a microstructure indicator to use in constitutive modelling of unsaturated soils. Their model excludes suction (water) in the micropores (e_m) from the calculation of intergranular stress by using an effective degree of saturation of the macropores (Figure 3.18). For material at a high density the distinction between micro- and macrostructure reduces (Alonso et al., 2010). The variation in microstructure for specimens compacted at different water contents reduces as seen in Figure 3.21 for Boom clay reported by Alonso et al. (2013).

Hicks and Monismith (1971); Jin et al. (1994) and Sivakumar et al. (2013) reported an increase in M_R for compacted specimens of higher density. This is related to the amount and size of particle contacts and the size of voids. The density achieved is important, however to a lesser extent when compared to the influence of the stress state (Hicks and Monismith, 1971).

3.3.3 Water content influence on formation stiffness

Jin et al. (1994) investigated the seasonal change in resilient modulus, M_R, of pavement

materials. They monitored the moisture conditions and temperature for two sites to develop a representative laboratory tests program using a cyclic triaxial cell. The increase in resilient modulus was attributed to a decrease in water content (thus increased soil suction). Over recent years the influence of matric suction on the resilient modulus of flexible pavement subgrade materials has been of particular interest to assess the impact of changes in environmental conditions (Ooi et al., 2004; Heath et al., 2004; Khoury and Zaman, 2004; Yang et al., 2005; Thom et al., 2008; Yang et al., 2008; Cary and Zapata, 2011; Ng et al., 2013; Azam et al., 2013; Sivakumar et al., 2013; Salour et al., 2014). Several M_R prediction models have been developed to include matric suction, as discussed in Section 3.1.4.

In-situ measurement of the water content or soil suction of formation layers are rare. Difficulties with instrumentation of layerworks and data capturing limits the availability of field data (Puppala et al., 2012; McCartney and Khosravi, 2013). Prediction of temperature and water movement in a pavement system is currently done with the Enhanced Integrated Climatic Model (EICM) (Zapata and Houston, 2008).

Variations of in-situ gravimetric water content at flexible pavement sites in Ohio was measured by Liang et al. (2006) to compare different drainable base and subbase materials. Significant variations in water content was measured for base, subbase and most subgrade layers due to heavy rainfall during construction, prior to surfacing. The water content of the base and subbase layers was measured to cycle between 5% and 10%, seemingly as a result of rainfall events. The saturation water content for both the base and subbase materials was estimated as between 15% and 20% depending on the site and formation layer. Therefore, the base and subbase did not saturate as free water drained sufficiently between rainfall events.

Railway foundation layers below the ballast layer are open to atmosphere (not sealed). It is thus expected that the water content of the layers would be sensitive to rainfall events, similarly to that shown by Liang et al. (2006) for the pavement layers during construction prior to surfacing. For well drained granular sand blanket (or subballast) layers the material is not expected to saturate, as shown for the base and subbase pavement materials monitored by Liang et al. (2006). An instrumented test railway track, at the University of Pretoria, South Africa (Vorster and Gräbe, 2013), was built in accordance to the Spoornet (2006) formation specifications (Section 2.3.1). Preliminary, unpublished results of water content (Vorster, 2016) for the various layers (SSB, SB, A-layer and B-layer) is in agreement with the results by Liang et al. (2006). The coarse, granular layers (SSB and SB) drained freely as it did not saturate even for artificially induced wetting. From an initial assessment of the water content measurements the SSB and SB layers tended to de-saturate within a day, after wetting or rainfall stopped, to an approximately degree of saturation of 60% due to the high permeability. The A-layer and B-layer, with increased amount of fines, desaturated over two to three days

to approximately 80% saturation. However, further analysis of the data is necessary to confirm the initial assessment.

Liang et al. (2006) also reported changes in water content of the subgrade layers, for the surfaced pavement, to be less distinctive compared to the base and subbase, however seasonal variations were measured. One of the A-6a subgrade layers at 0.5 m depth, for example, ranged from around 10% to approximately 13% (saturated) depending on the season. Other, similar subgrade layers from the different sites assessed varied seasonally from approximately 20% to 28% (saturated). No density information or material properties were provided for the subbase and subgrade layers. Changes in water content of the subgrade materials over shorter periods (of a few days) was within approximately 1% and probably related to rainfall events, however the accuracy of measurements were not reported.

Puppala et al. (2012) and McCartney and Khosravi (2013) measured the seasonal changes in the soil suction of clay subgrades at instrumented sites in Texas and Arkansas respectively. The periodic soil suction and water content measurements by Puppala et al. (2012), for an expansive clay site (PI=33%) using a thermal conductivity-based suction sensor, was conducted over a year and a half. They reported the average monthly gravimetric water content of the grassy fill slope to be between 17% and 24% over the period between April 2007 and June 2008 with the largest variation for measurements nearer the ground surface. The field suction measurements ranged between approximately 450 kPa and 900 kPa, and compared well with estimated total suction from the SWRC (Puppala et al., 2012). A larger range of suction, between 50 kPa and 3000 kPa, was measured by McCartney and Khosravi (2013) for a clay subgrade in the paved shoulder of a roadway using a new dielectric sensor system. However, they reported that the subgrade was near saturation (ψ_m=50 kPa) for most of the measurement period between September 2009 and March 2011, except for the summer of 2010 for which a large increase in suction (decrease in water content) was measured.

The effect of seasonal variation of water content on M_R was investigated by Khoury and Zaman (2004) for a sandy clay and a clayey subgrade soil. They tested specimens at the same bulk water content, but with different suction histories (wetting and drying paths). Figure 3.22 indicates the three dimensional relationship between water content, suction and the resulting resilient modulus. It can be seen that the relationship for M_R versus water content is not enough to explain M_R, due to the hysteresis of suction, therefore it was concluded that changes in M_R would be better understood if related to suction. The influence of changes in water content were impacted by the initial moisture state and the extent of wetting (Khoury and Zaman, 2004). The water content gradient was reported to have little influence on M_R, and the bulk water content (average) was used. The influence of water content on the resilient modulus has been discussed in Section 3.1.4 in terms of matric suction as stress variable.

3.4 Implication for railway track formations

Railway foundation layers are part of the track structure, required to provide a stable platform for train traffic. Trains induce complex cyclic stress conditions which result in the cyclic rotation of principal stresses working in a soil element in the track. The need for representative laboratory tests for assessing the resilient modulus of formation material, under train induced stresses, has been emphasised.

Together with permanent deformation, the stiffness of a track system is used as the main track substructure stability criteria, as it influences ride quality and wheel-rail interaction and wear. The resilient modulus is used as a long term and short term pavement performance prediction parameter in mechanistic-empirical design procedures. The cyclic triaxial is used as the main laboratory testing method (Section 4.3.6). Railway substructure design approaches are of empirical nature and requirements include material properties, such as particle size distribution, and CBR values (Chapter 2). Construction criteria specify compaction density and water content to achieve a suitable formation layer.

The factors considered to influence the measured railway formation stiffness has been grouped as three main factors. The three independent factors are stress, material type and soil physical state as defined by Li and Selig (1998a). Compacted railway formation materials are expected to be unsaturated and should be assessed within an appropriate unsaturated soil mechanics framework. Two frameworks selected for use in this study are the framework in terms of net normal stress and matric suction (Fredlund et al., 2012), and the intergranular stress approach incorporating a suction stress parameter (σ_s=$\chi\psi_m$) in the existing effective stress framework (Lu and Likos, 2006).

The material type and soil physical state are considered factors which influence the stress-strain response of soil. These factors are key soil characteristics that influence the matric suction in unsaturated soils, such as compacted pavement layers. The unsaturated soil mechanics stress state variables and their influence on M_R and permanent deformation have been discussed. The key net normal stress parameters include the confining stress, cyclic deviator stress magnitude and number of load cycles as well as shear stress reversal (PSR). Studies investigating the influence of matric suction has increased as the change in soil physical state (water content and density) are understood to be important.

Understanding unsaturated soil behaviour is key in finding better, more scientific design and maintenance strategies for pavement infrastructure including railways.

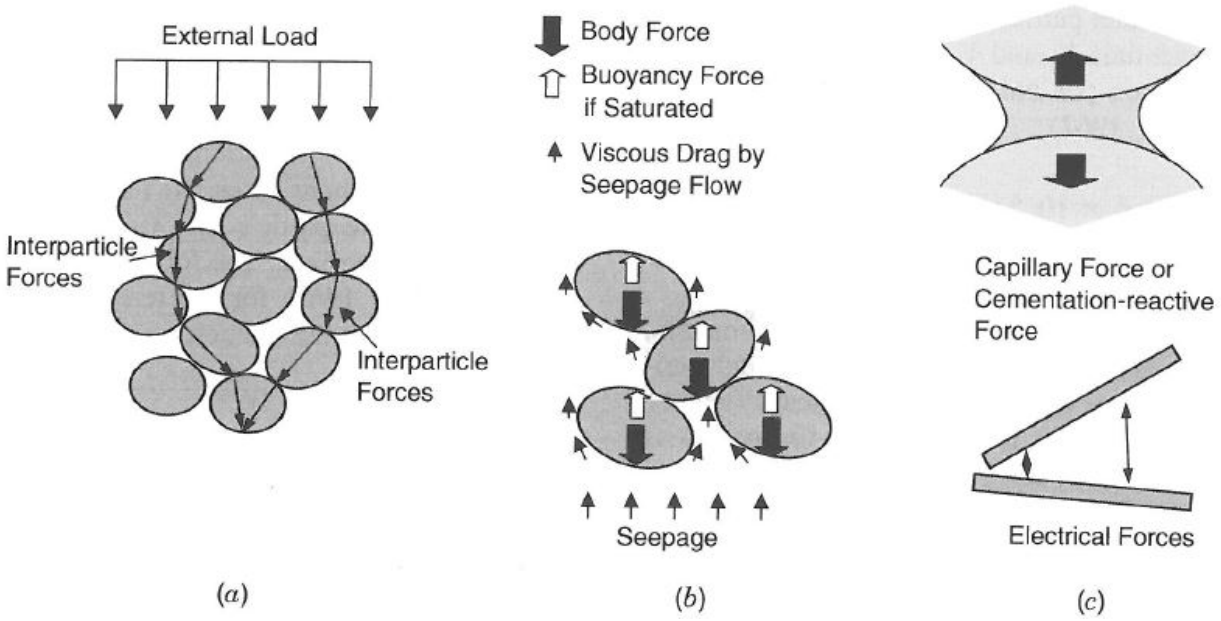

Figure 3.1: Interparticle forces at the particle level: (a) skeletal forces by external loading; (b) particle level forces; and (c) contact level forces (from Mitchell and Soga (2005) after Santamarina (2003))

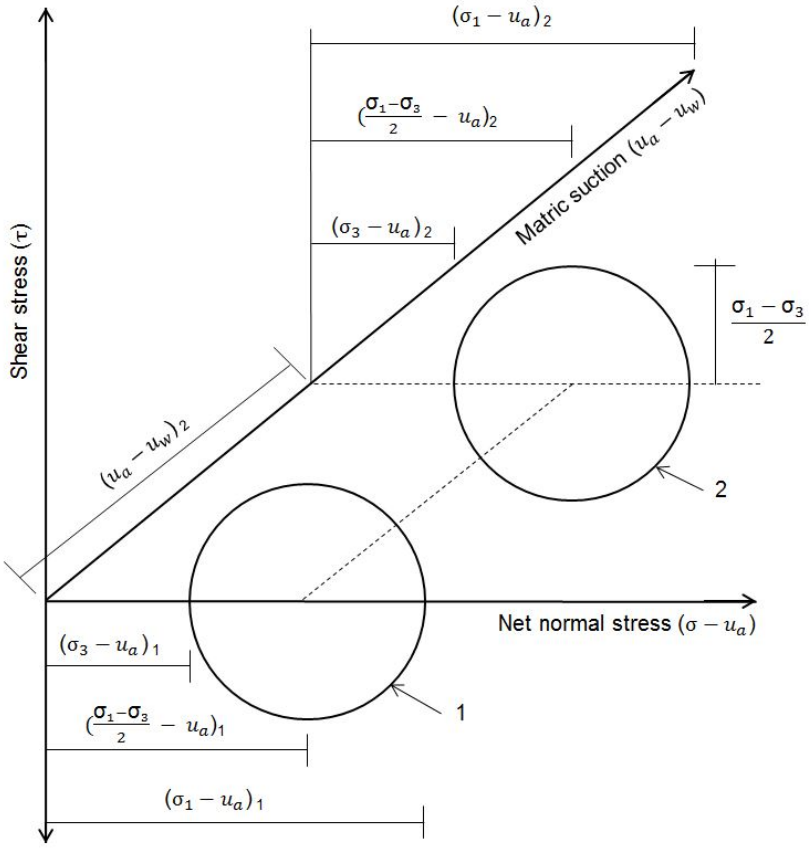

Figure 3.2: Extended Mohr-Coulomb diagram for unsaturated soils in terms of net normal stress and matric suction (redrawn from Fredlund and Rahardjo (1993))

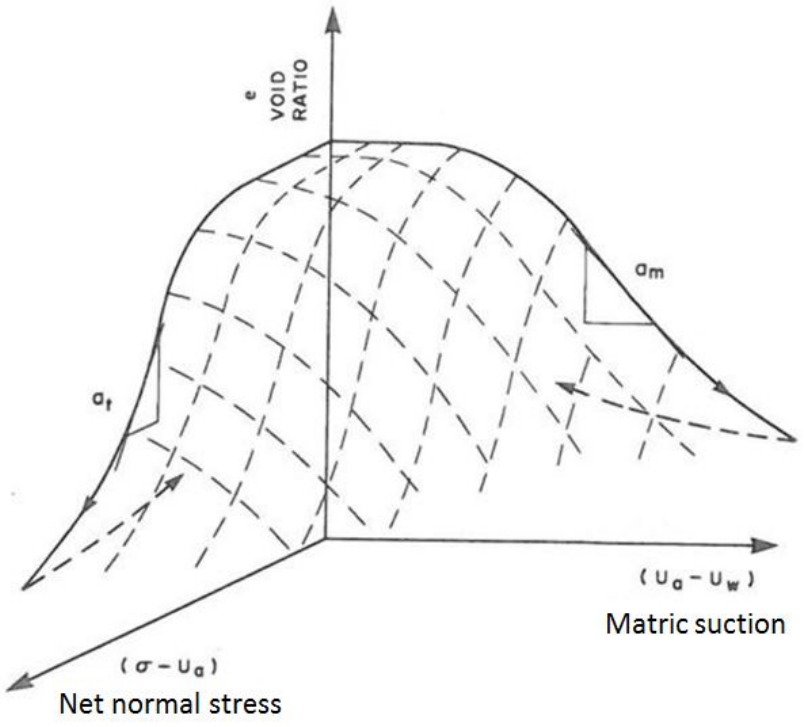

Figure 3.3: Extended void ratio versus stress diagram for unsaturated soils in terms of net normal stress and matric suction (from Fredlund (1979))

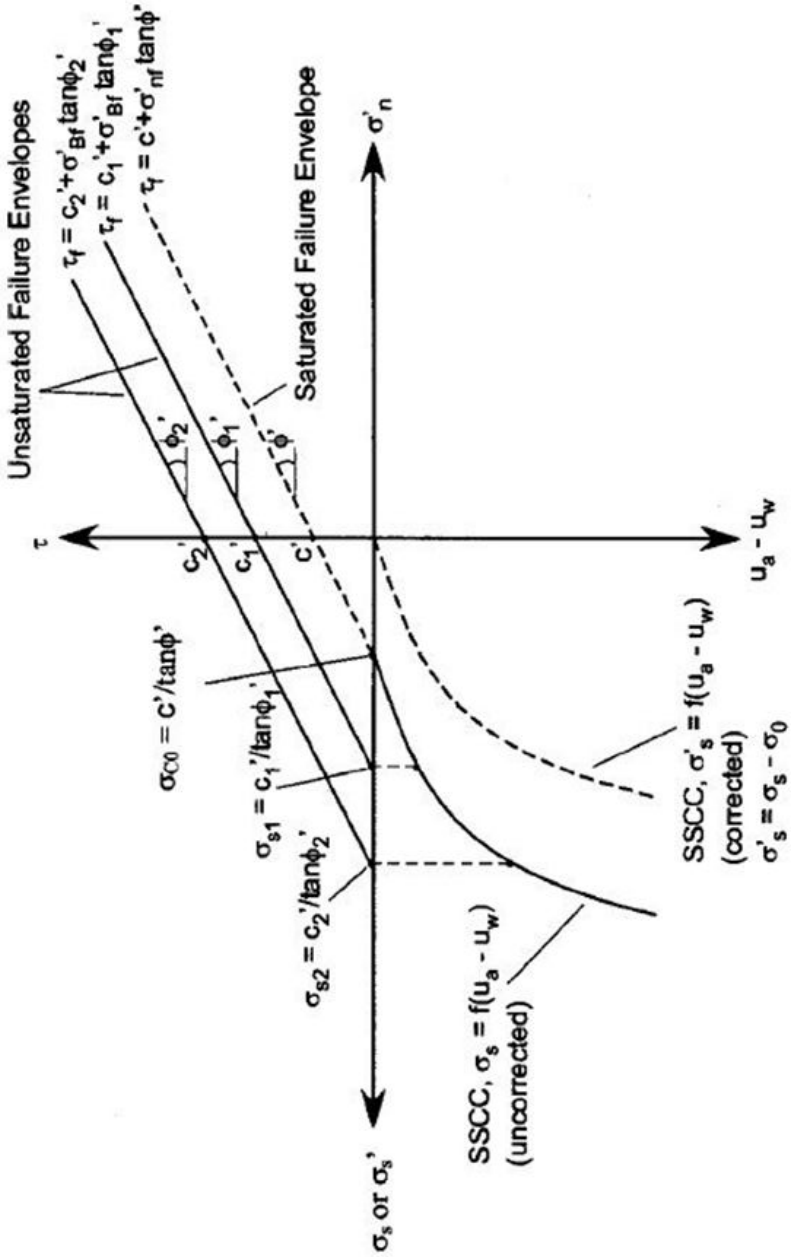

Figure 3.4: Suction stress determination using direct shear test data from Escario (1980) on Madrid grey clay presented by Lu and Likos (2006)

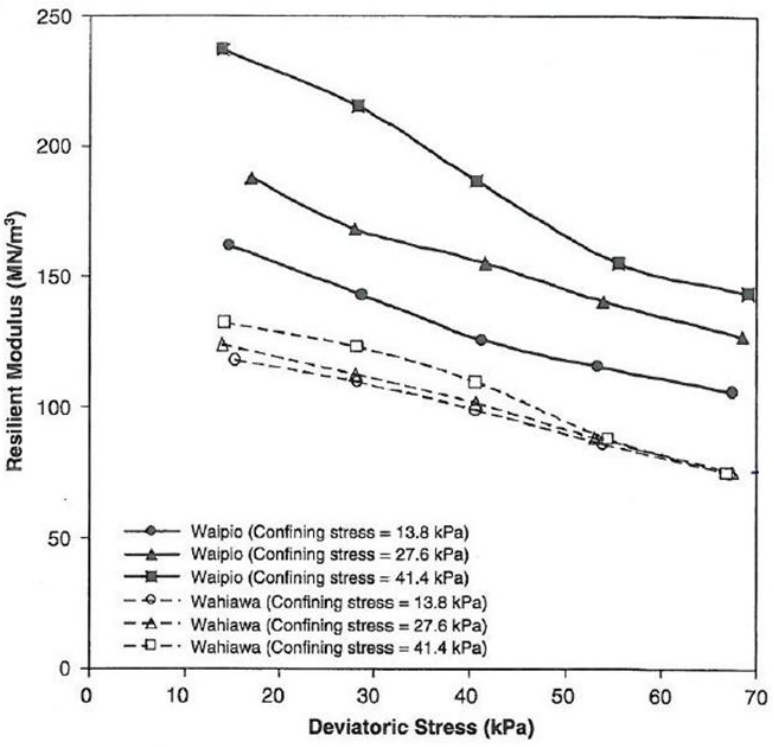

Figure 3.5: Comparison of resilient modulus for low-plasticity (Waipio) and high-plasticity (Wahiawa) silt at optimum water content as reported by Ooi et al. (2004)

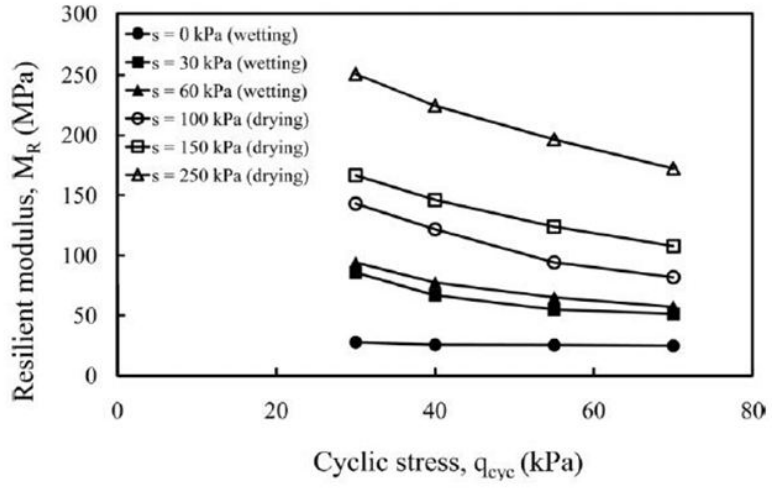

Figure 3.6: Influence of cyclic stress on resilient modulus for different controlled matric suction values, s, reported by Ng et al. (2013) for completely decomposed tuff ($p_o = 30\ kPa$)

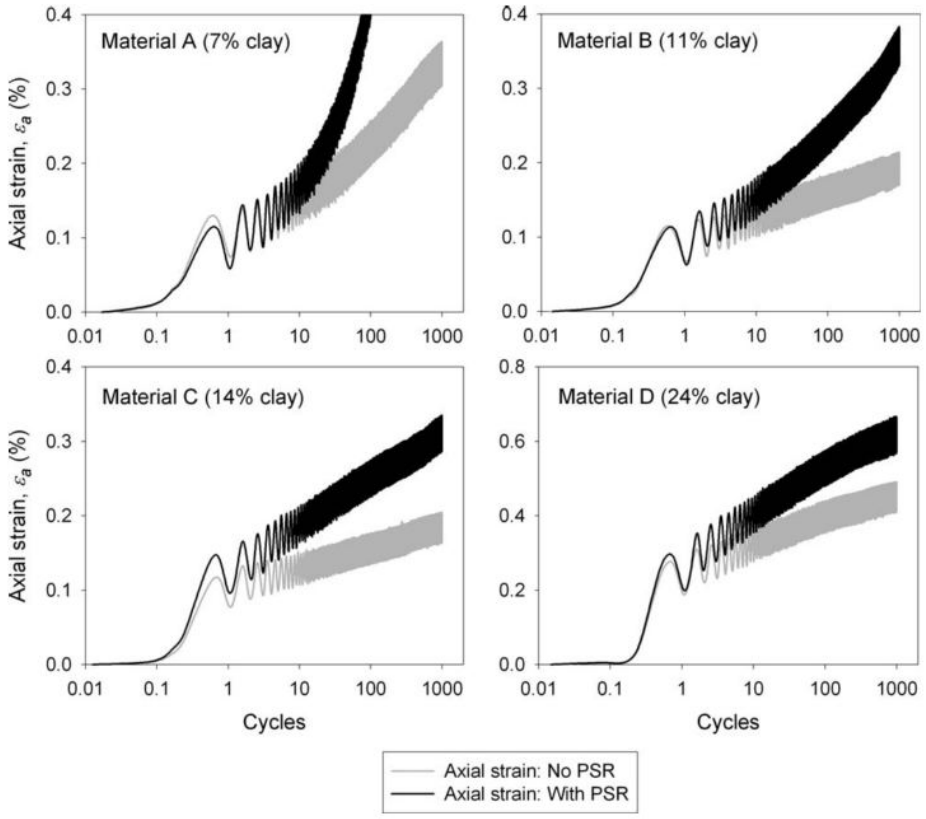

Figure 3.7: Permanent deformation of representative formation material (Material A,B,C and D) as a result of cyclic loading with and without principal stress rotation (PSR) (Gräbe and Clayton, 2009)

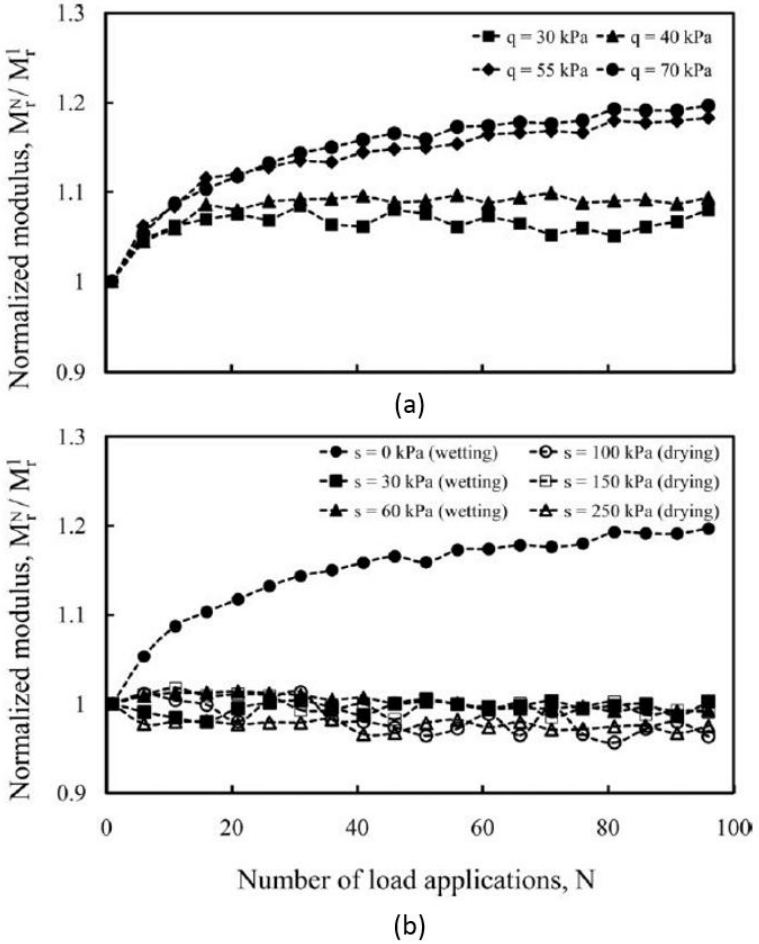

Figure 3.8: (a) Relationship between normalised resilient modulus and number of load cycles for different q_{cyc} at zero suction, (b) relationship between normalised resilient modulus and number of load applications at a cyclic stress of 70kPa for samples at different induced suctions (Ng et al., 2013)

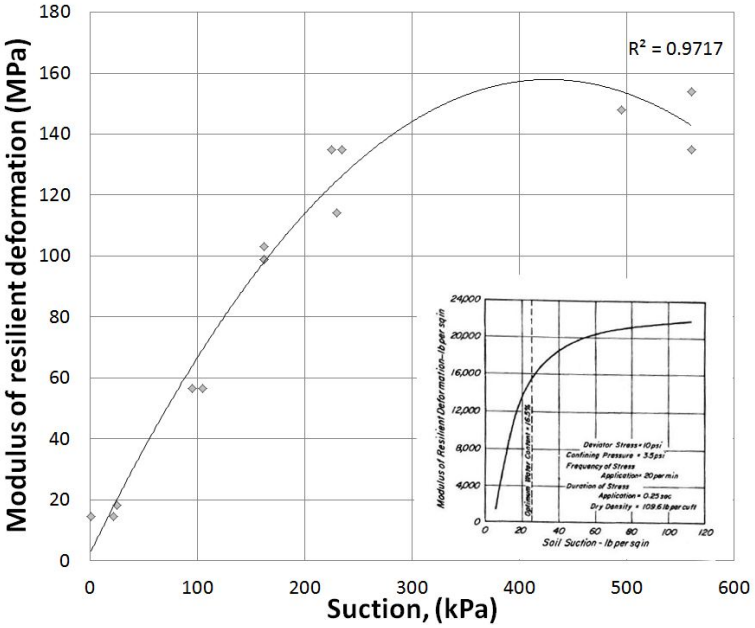

Figure 3.9: Measured resilient modulus plotted relative to measured suctions on duplicate samples of glacial till replotted from Sauer and Monismith (1968); Insert: M_R versus suction prediction (Sauer and Monismith, 1968)

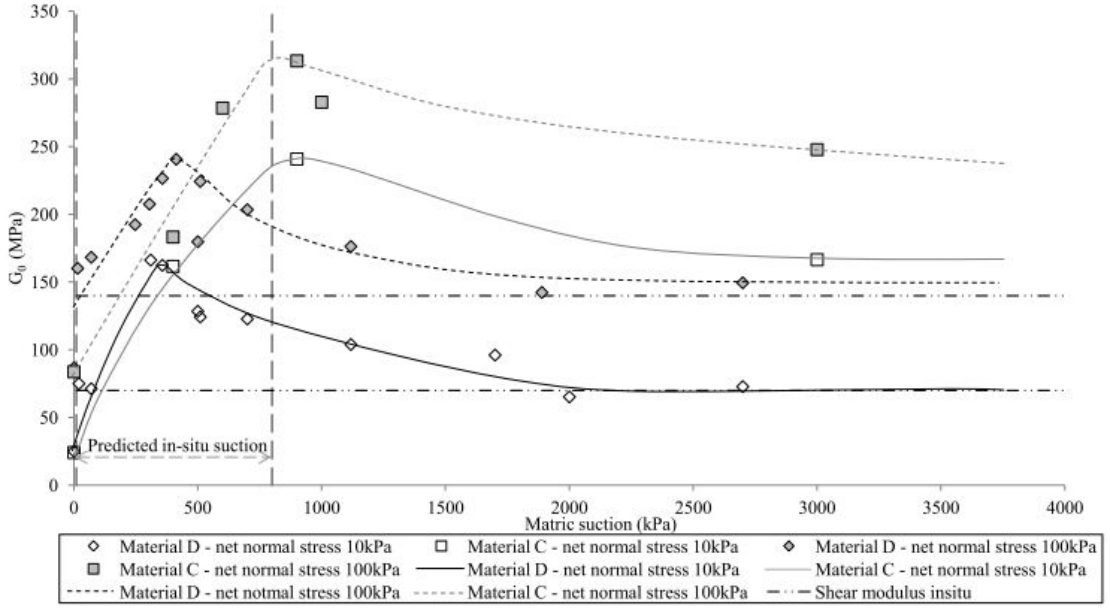

Figure 3.10: Resonant column results for two compacted railway foundation material at different confining stresses, G_0 versus matric suction (Otter, 2011)

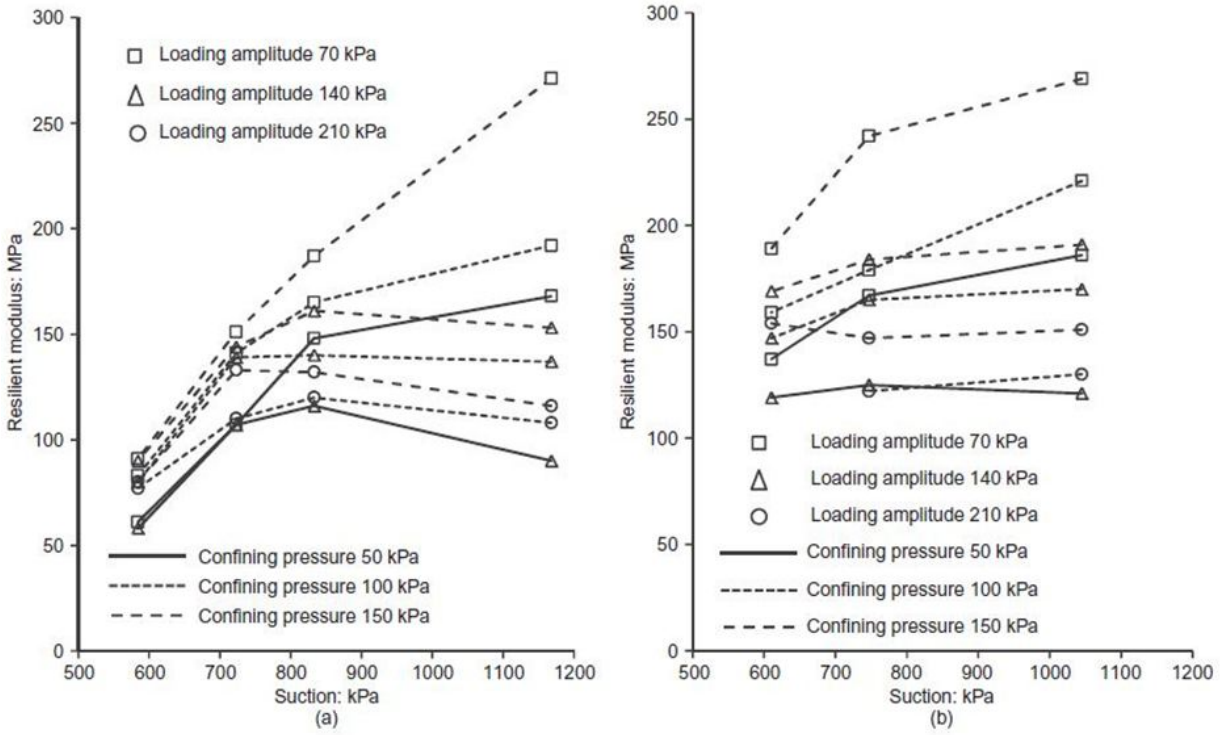

Figure 3.11: Measured resilient modulus of Kaolin plotted relative to initial induced suction, indicating effect of loading amplitude and confining pressure for (a) un-engineered fill, and (b) engineered fill (Sivakumar et al., 2013)

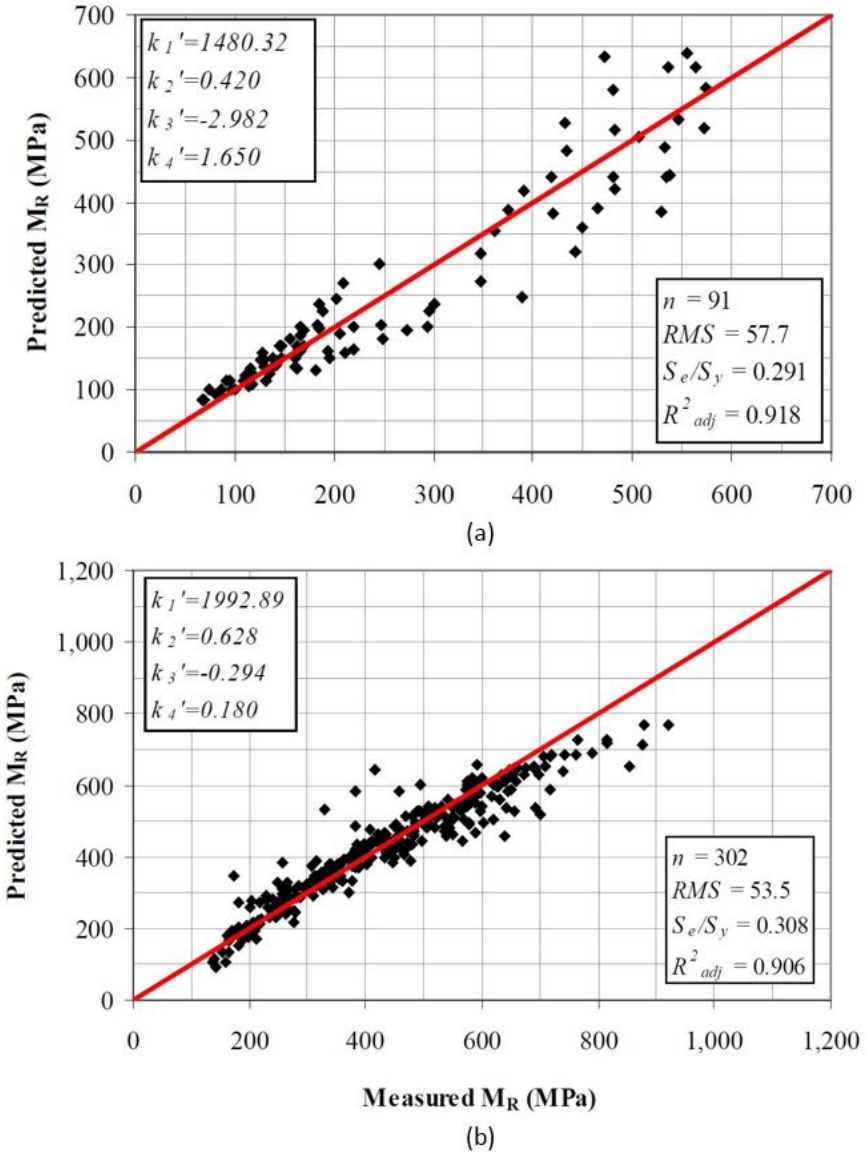

Figure 3.12: Predicted versus measured resilient modulus reported by Cary and Zapata (2011) for (a) granular base material and (b) clayey sand, indicating model coefficients for Equation 3.13

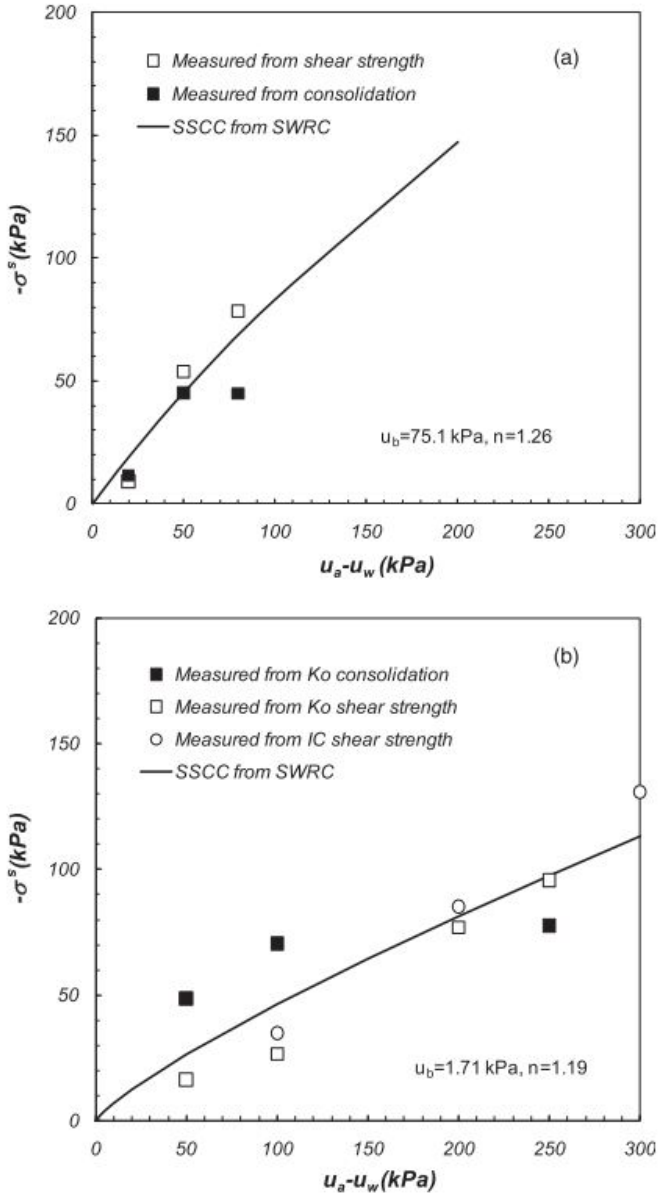

Figure 3.13: Comparison of SSCC deduced from SWCC test, shear strength failure test, and K_0 consolidation test (a) for Iksan soil and (b) for Gimcheon soil (Oh et al., 2013)

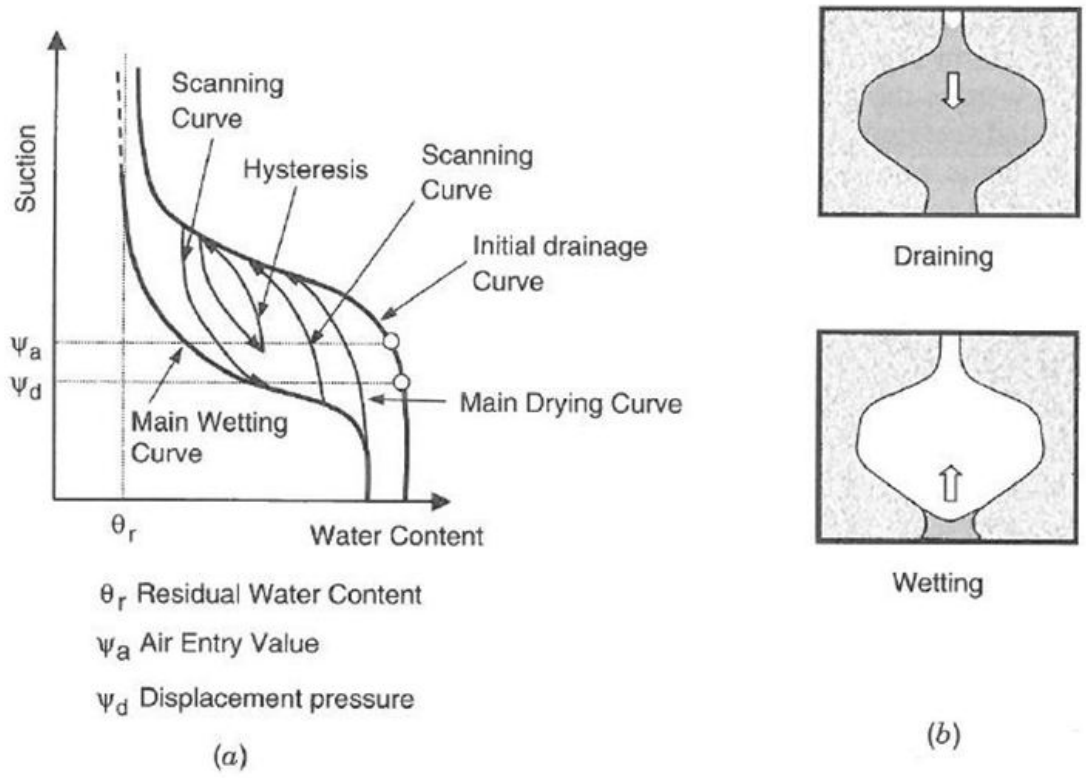

Figure 3.14: (a) Example of a soil-water retention curve (SWRC) indicating expected scanning curves; (b) the ink bottle effect (presented by Mitchell and Soga (2005))

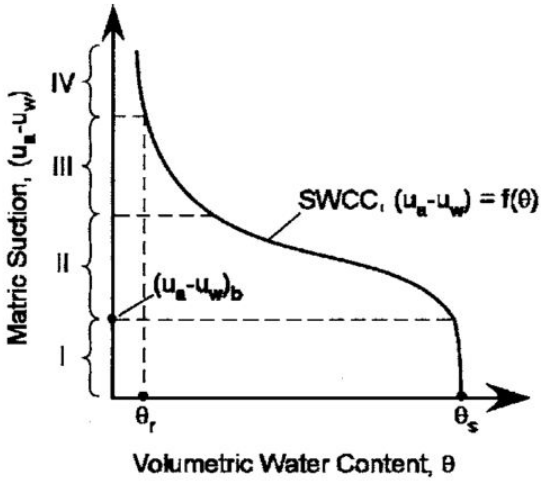

Figure 3.15: Conceptual illustration of behavioural regimes of the soil-water retention curve, SWRC (Lu and Likos, 2006)

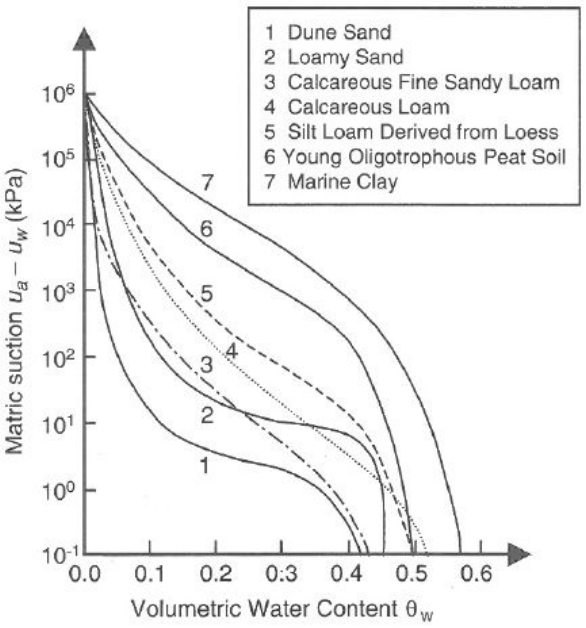

Figure 3.16: Soil-water characteristic (retention) curves for some Dutch soils, copied from Mitchell and Soga (2005)

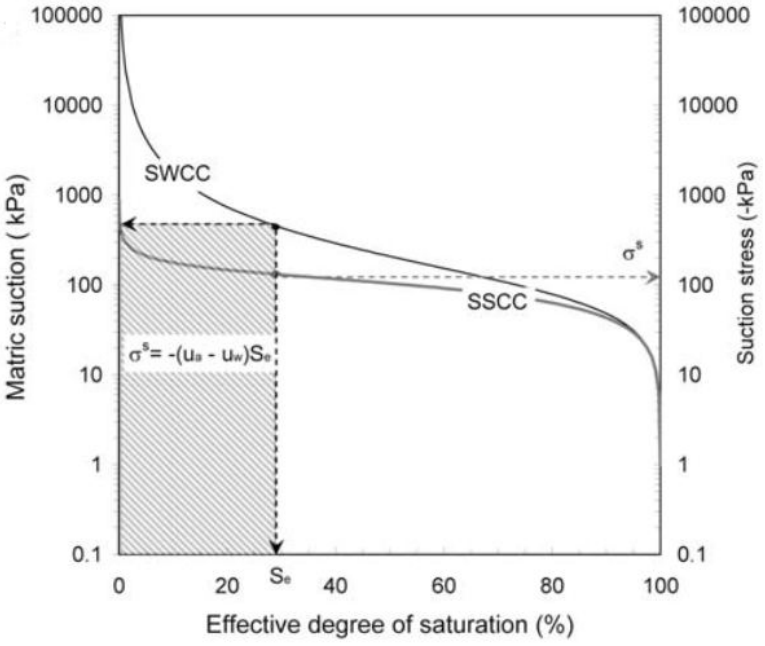

Figure 3.17: Soil suction characteristic curve and the soil-water characteristic (retention) curve relative to the effective degree of saturation, presented by Lu et al. (2010)

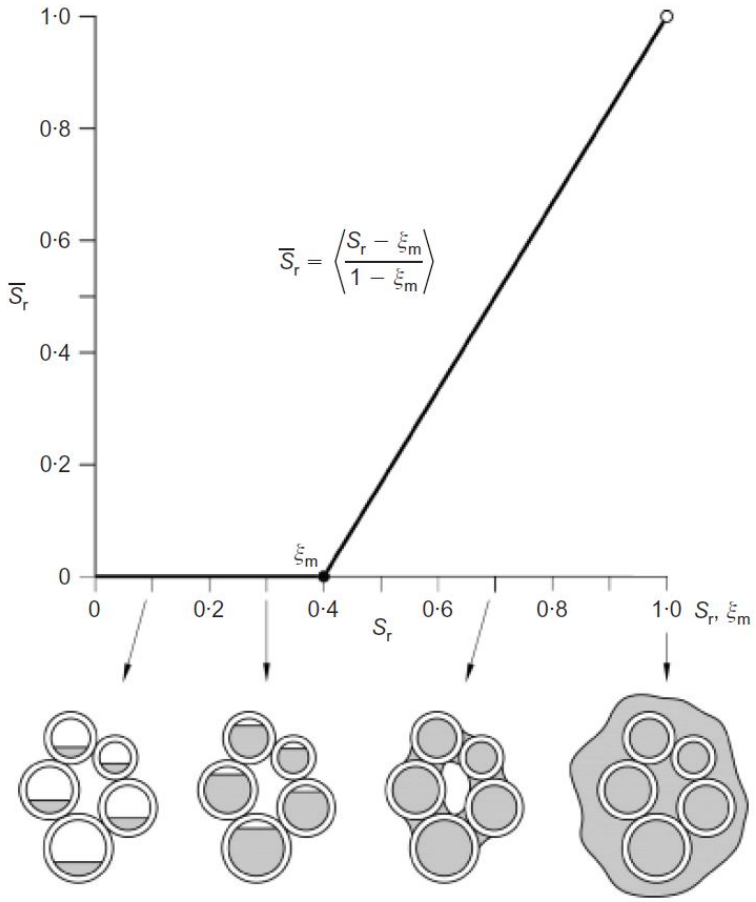

Figure 3.18: The effective degree of saturation, $\overline{S_r}$ or S_e, (within the macropores) illustrated by Alonso et al. (2013) showing the meaning of the microstructure indicator

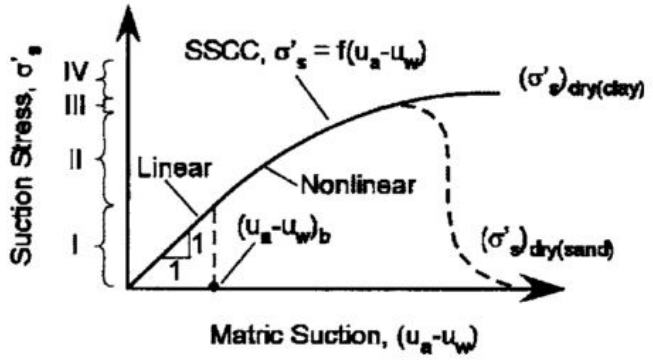

Figure 3.19: Soil suction characteristic (retention) curve indicating effect of material type, presented by Lu and Likos (2006)

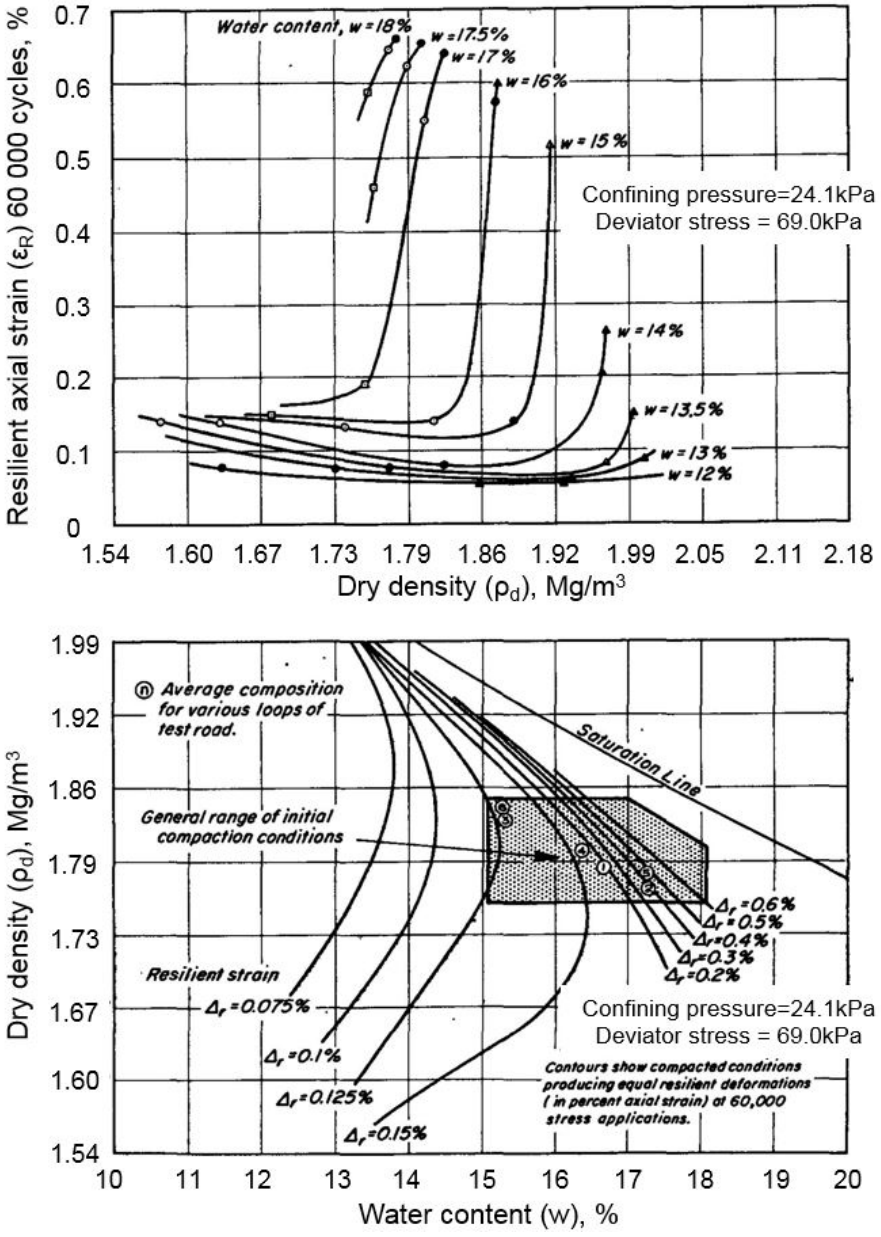

Figure 3.20: Relationship between dry density, water content (w) and resilient strain (ϵ_R or Δ_r) for AASHO road test subgrade soil prepared by kneading compaction as taken from Seed et al. (1962)

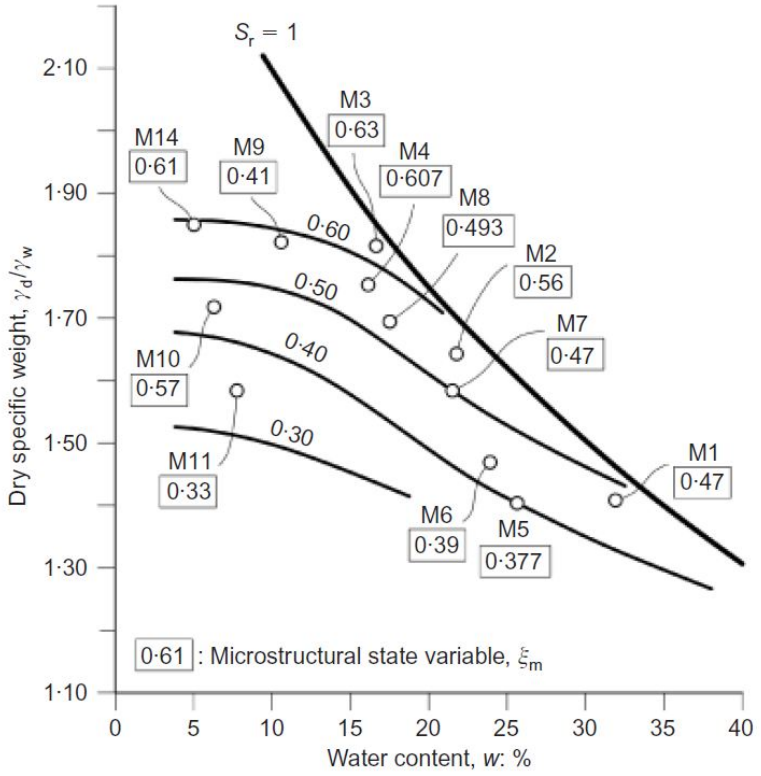

Figure 3.21: Contours of equal microstructure parameter (microvoid indicator, e_m/e) for compacted Boom clay as replotted and presented by Alonso et al. (2013)

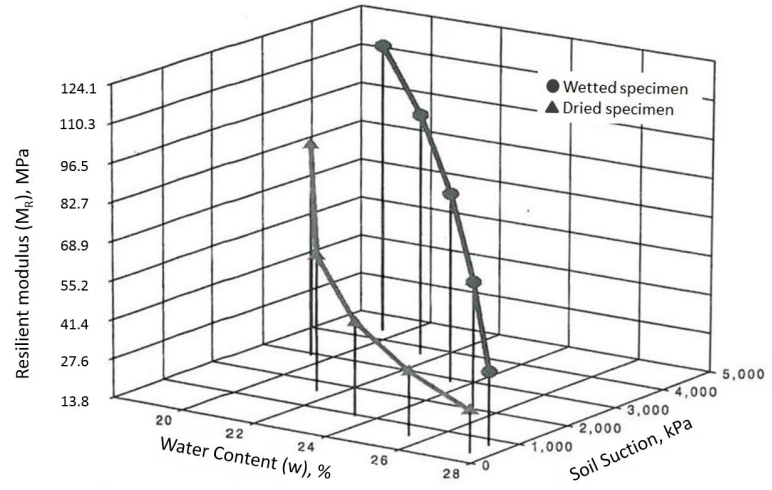

Figure 3.22: Three dimensional illustration of M_R with water content and soil suction presented by Khoury and Zaman (2004)

Chapter 4

Laboratory testing on railway formation material

The laboratory material and methods selected for testing unsaturated railway formation material stiffness are outlined and discussed in this chapter. Material preparation, specimen and apparatus preparation and set-up are presented for the soil element testing conducted in the cyclic triaxial (Section 4.3) and cyclic hollow cylinder apparatus (Section 4.4). Sections 4.3 and 4.4 also includes tests stresses and typical results for the respective test methods. Determination of soil suction of the material using the Chilled-Mirror Dew-Point Potentiometer is described as used to evaluate suctions against previous measurements made by Otter (2011) (Section 4.2).

4.1 Formation material

This section discusses the selection of a material representative of railway formation for laboratory testing. The material description, including Atterberg limits (liquid and plastic) and particle grading, is presented. Compaction characteristics and details of specimen preparation are presented.

4.1.1 Material selection

Information on the geomaterials from the Coal Line (COALlink) railway in South Africa was analysed by Gräbe (2002), who selected representative laboratory mixes based on the in-situ material properties. He selected four materials (named Material A, B, C and D) for laboratory testing, made from a combination of commercially available clay (Hymod Prima clay), silt (HPF4 later replaced with equivalent HPF5) and sand (Leighton

Buzzard Sand). The material mixes were developed to achieve a desired grading, plasticity and clay activity close to the material used in the CoalLine formation.

For this study a clayey sand, namely Material B, was selected enabling comparison with previous work done by Gräbe (2002); Otter (2011) and Mamou (2013). This material was previously tested in the unsaturated state by Otter (2011) and its soil-water retention curve, SWRC, is available. Material B, containing 11% clay, is considered to be representative of an engineered subballast layer as in the Spoornet (2006) S410 railway formation design. Based on its particle size, Material B would be considered a granular subgrade material in the Harmonized Test Methods for Laboratory Determination of Resilient Modulus for Flexible Pavement Design (NCHRP Project 1-28A) (Harrigan, 2004). The quantities of the constituent materials of Material B are given in Table 4.1.

4.1.2 Material description and grading

The particle size distribution of the representative subballast material, Material B, developed by Gräbe (2002) is shown in Figure 4.1a. The grading envelope of the Coal Line material it represents is also shown. It can be seen that the material in the Coal Line has more fines than included in the S410 (Spoornet, 2006) subballast (SB) and UIC (International Union of Railways, 2008) soil quality class 3 (QS3) material specifications shown in Figure 4.1b. The particle grading envelopes representing the design specifications were calculated in terms of a 75 mm maximum particle size.

Constraints such as specimen size and preparation method need to be considered in laboratory testing. To measure representative behaviour in an element test the minimum specimen dimension should not be smaller than the shear band thickness. The shear band thickness for granular materials is approximated from laboratory observations by Roscoe (1970) as 10 times the maximum particle size, substantiated by Muhlhaus and Vardoulakis (1987), and as 7-8 times the mean particle size by Oda and Kazama (1998) from x-ray image analysis. The material type influences the specimen size and the specimen preparation method used in pavement material testing protocols (Andrei et al., 2004). The maximum particle size of Material B was limited by Gräbe (2002) to 1.18 mm (Leighton Buzzard Fraction B) for reasons relating to particle crushing during mixing, sample preparation by trimming, and to reduce membrane penetration (Gräbe, 2002). The hollow cylinder test specimens have a wall thickness (minimum specimen dimension) of 20 mm, thus more than 10 times the 1.18 mm maximum particle size, allowing representative testing.

The Atterberg limits of Material B determined according to BS1377:1990 (Part 2, Method 5) (British Standards Institution, 2012) are given in Table 4.2. The values are comparable with those determined by Gräbe (2002) and Otter (2011) for the same

material. Activity, A, is calculated as the plasticity index, PI, divided by the percentage clay content.

4.1.3 Material preparation

The aggregate quantities, as given in Table 4.1, were mixed together by hand in batches of 3 kg. The correct amount of each aggregate was weighed out and carefully mixed, in a bowl, for 5-10 minutes to ensure uniformity. The aggregates used were air dry. The mixed material was stored in sealed plastic bags until use.

An approach similar to that of Sauer and Monismith (1968) and Otter (2011) was followed to create specimens at a range of matric suction conditions. A specific amount of water was added to a known amount of dry material to create a mix of known gravimetric water content. A range of gravimetric water content was used to create a set of specimens.

The required amount of dry material was transferred into seal-able plastic bags containing no more than 800 g per bag. Water was added incrementally, and thoroughly mixed in while the bag was sealed to prevent moisture and material loss. The wetted material was mixed by hand through the sealed bag for a minimum of 15 minutes, breaking up lumps in the material. During wetting, the fine (clay and silt) particles tend to lump together. Care was taken to reduce any lumps of fines as much as possible as this could lead to variable fabric upon compaction. The mix was considered homogeneous when no dry lumps of fines (clay and silt) could be found in the mix (visually assessed).

The method used by Tarantino and Tombolato (2005) and Thom et al. (2008) to reduce Kaolin clay lumps, or clay aggregates, was to pass the wetted material through a sieve after initial mixing. Any remaining lumps after sieving are broken down and re-sieved. This method was not employed as changes in the material composition might occur if wetted fines remain on the sieve. Moisture loss to the atmosphere from the clayey sand material tested occurs quickly, and moisture loss during sieving would be difficult to control.

After mixing, the wet material was left for a minimum of 24 hours in a temperature controlled room at 20 ^oC. Care was taken to prevent moisture loss during this period by sealing the first bag inside a second. The amount of wet material needed to make a specimen was weighed out and put aside once specimen preparation, by means of compaction, could commence.

4.1.4 Compaction characteristics

Construction requirements for soil compaction, including optimum water content and dry density, are specified based on standard laboratory compaction tests. The objective

of these tests is to determine the relationship between compacted dry density (ρ_d) and soil water content (w) for a specific compactive effort (British Standards Institution, 2012). The method of compaction influences the mechanical behaviour measured in the laboratory (Ceratti et al., 2004), as discussed in Section 3.3.2.

Different compaction test methods are used in practice depending on particle size and compaction effort used during construction. The compaction energy applied has been calculated for several dynamic compaction test methods including BS1377-4:1990 (British Standards Institution, 2012), ASTM D1557-07 (ASTM D1557-07:, 2007), AASHTO Method A (WAQTC, 2011) and TMH1 Method A7 (Lockyer, 1986) as summarised in Table 4.3. The amount of overfill (up to 5% of the mould volume) was not considered and therefore the energy calculated is only an approximation for comparison purposes.

The energy calculated is based on the principle of energy conservation. The potential energy of the falling rammer weight applied in each method was calculated per volume of material (Equation 4.1).

$$E_{compaction} = \frac{(n_{blows})(n_{layers})(m_{rammer})gh_r}{V_{mould}} \tag{4.1}$$

Where:
$E_{compaction}$ = Compaction energy applied per unit volume, J/m^3;
m_{rammer} = mass of rammer, kg;
g = gravitational acceleration, $9.81 m/s^2$;
h_r = height through which the weight is dropped, m;
n_{blows} = number of blows applied per layer;
n_{layers} = number of layers;
V_{mould} = volume of compaction mould, m^3.

The compaction test method used in South Africa, TMH1 Method A7, is based on the AASHTO T180 heavy compaction method (Lockyer, 1986). It is noted that the number of blows per layer specified in the THM1 Method A7 (55 blows per layer) is less than the AASHTO T180 (56 blows per layer), resulting in approximately 10% less energy applied. In comparison the compaction energy applied using the BS1377-4:1990, ASTM D1557-07 and AASHTO Method A (T90 and T180) are deemed equivalent. The BS1377-4:1990 was used in this study.

Both the BS1377-4:1990, 2.5 kg rammer and 4.5 kg rammer compaction tests were used to determine the density-water content relationships for Material B as shown in Figure 4.2. The maximum dry density achieved using the 2.5 kg rammer compaction method (2.17 Mg/m^3 at w=7%) is 96% of the maximum dry density achieved using the 4.5 kg rammer compaction method (2.26 Mg/m^3 at w=4.8%). The S410 railway specifications (Spoornet, 2006) specify a minimum achieved compaction density of 95% of the modified AASHTO (T180 4.5 kg rammer compaction) density for the subballast

layer. The 2.5 kg rammer compaction method was considered suitable for compaction of the laboratory specimens and allows comparison with previous work by Otter (2011).

A target dry density of 2.10 Mg/m^3 for test specimens was selected by Otter (2011), equivalent to the dry density of specimens (made from a slurry) tested in the Hollow Cylinder apparatus by Gräbe (2002) (also approximately 2.10 Mg/m^3). The same target dry density for the laboratory test specimens was therefore used in this research. The target dry density, lower than the maximum dry density (2.10 Mg/m^3), allows for a larger water content range in investigating the influence of water content or matric suction.

To achieve the 2.10 Mg/m^3 target dry density the number of blows required for specimen compaction at different water contents were determined by trial and error. The required compaction energy was evaluated using the BS1377-4:1990 1 litre mould and 2.5 kg rammer with 3 layer compaction. Material at a particular water content was compacted by varying the number of blows. The density was assessed and the rammer blows adjusted as required. The required numbers of blows per layer as used for different water contents are given in Table 4.4.

The 100 mm diameter by 204 mm high specimens tested in the cyclic triaxial and the cyclic hollow cylinder apparatus were compacted in layers of similar thickness used in the BS 1 litre compaction mould. Thus the same energy per unit volume was applied to compact the specimens as calculated in Table 4.4. This approach was used by Jin et al. (1994) and led to compaction of the 204 mm high specimens in 5 layers as suggested by Bishop and Henkel (1957). Some density variation within the compacted specimen is expected as observed by Otter et al. (2015) from X-ray images of compacted specimens. However, the thickness of the compaction layers was kept constant to represent construction practice.

4.2 Determining soil suction

The soil water retention curve, SWRC, is an important relationship used in unsaturated soil mechanics and has been discussed in Section 3.2. The relationship between water content (gravimetric or volumetric) or degree of saturation and suction (total suction or matric suction) can be determined using different techniques as discussed by Mitchell and Soga (2005) and Fredlund et al. (2012). Otter (2011) determined the SWRC for the representative subballast material (Material B) based on results from pressure plate (axis translation technique), filter paper and high-capacity (Ridley) tensiometer tests. During this study, additional testing was carried out on Material B using a chilled-mirror dew-point potentiometer (CMD) to compare and substantiate previous results by Otter (2011).

Different soil suction measurement techniques is frequently used in combination, to complement each. A study was conducted by Tarantino et al. (2011) to establish the repeatability of suction measurements using different techniques, including axis translation (pressure plate and suction-controlled oedometer), high-capacity tensiometer and the osmotic technique. The investigation was carried out by eight teams of the Mechanics of Unsaturated Soils for Engineering (MUSE) network in Europe. A mix of uniform sand, sodium bentonite (active clay) and kaolinite clay (non-active clay) were tested along the drying path.

Figure 4.3 shows soil suction results from various techniques used by the different MUSE teams. Particular attention is drawn to the medium suction range at 70-80% saturation as an expected range for granular railway formation material (Section 3.3.3). Suction was measured between 200 kPa (tensiometer) and 400 kPa (pressure plate) for the same water content (w=30%) when using different measurement techniques. This was attributed to the influence of applied air pressure in the axis translation technique (pressure plate) changing the pressure of occluded air within the soil (Marinho et al., 2008), resulting in higher suction measurements when using the pressure plate compared to the tensiometer. However, Tripathy et al. (2012) stated that the use of slurried kaolin paste as an interface between the soil sample and the ceramic disc (for tensiometer testing) causes a reduction in suction of soil samples. A chilled-mirror dew-point potentiometer (CMD) was used, by Tarantino et al. (2011) to complete the measurements in the high suction range (2-100 MPa), however suctions in the lower range were not reported for the CMD and therefore comparison with other methods cannot be made.

Tripathy et al. (2014) tested the soil suction of statically compacted silty sand, Jeffara soil (JF), of low plasticity (PI=7%) with 11% clay and 24.4% silt content. They compared measurements from the CMD technique and the filter paper method with the SWRC determined using a pressure plate. From Figure 4.4 Tripathy and his co-workers concluded that for suctions less than approximately 400 kPa the CMD and filter paper techniques measured higher suctions compared to the pressure plate. Suction measurements larger than 400 kPa was similar for most of the methods used (Tripathy et al., 2014). However, suction measurements from null-type axis translation tests measured significantly lower which was ascribed to lack of continuity in the water phase (Tripathy et al., 2012). Tripathy et al. (2015) stated that CMD suction measurements of compacted samples correspond to the wetting SWRC of a soil.

Otter (2011) determined the SWRC in terms of matric suction for Material B using a combination of two suction measurement methods. The methods include the filter paper method (in direct contact) and the pressure plate technique. Commercial laboratory measurements using a Ridley high-capacity tensiometer were also reported (Otter et al., 2015). The measurements made using the filter paper technique are presented and discussed in Section 5.3.1 together with the SWRC. The air entry value and residual water content was not distinctive and resulted in difficulty defining the inflection point

of the SWRC. The SWRC was fitted using the Fredlund and Xing (1994) equation and subsequent iterative process.

4.2.1 The Chilled-Mirror Dew-Point Potentiometer

The Chilled-mirror dew-point potentiometer (also known as a Chilled Mirror Psychrometer (ASTM D6836-02:, 2003)) (Figure 4.5a) measures the dew-point temperature of the water vapour in equilibrium with the soil sample. The relative humidity (water vapour) of the air above the sample relates to the water activity (a_w). Water activity, defined as the vapour pressure of water in the soil divided by vapour pressure of pure water at the same temperature, is converted to total suction using the Kelvin equation (Equation 4.2) as included in the ASTM D6836-02 standard test method for determining the SWRC (ASTM D6836-02:, 2003).

$$\psi = \frac{RT}{M} ln(a_w) \tag{4.2}$$

Where:
ψ = total suction;
a_w = water activity;
R = universal gas constant;
M = molecular mass of water;
$\frac{R}{M}$ = 461 kPa/K;
T = laboratory temperature, K.

This method is an indirect method of measuring total suction in the range of 0.1 MPa to 300 MPa and is often used to measure larger suctions (>1000 kPa) (Tarantino et al., 2011).

A WP4C Dewpoint PotentiaMeter (Decagon Devices, Inc.), at Cardiff University Geo-environmental Laboratory, was used to investigate the total suction of compacted samples of Material B. A schematic diagram of the chilled mirror technique is shown in Figure 4.5b. The specimen is placed in a sealed chamber and held at constant temperature. A small fan circulates the air within the sealed chamber. A small mirror with high thermal conductivity is located above the sample. The temperature of the mirror is reduced by means of a Peltier thermoelectric unit until condensation occurs. A light emitting diode (LED) illuminates the mirror and the reflected light is received by a photodiode. The presence of condensation on the mirror is determined by measuring a change in reflected light from the mirror. The temperature of the mirror is controlled to achieve equilibrium of water mass on the mirror, thus a rate of condensation equal to the rate of evaporation. This equilibrium point is measured as the dew-point temperature of the ambient water vapour.

The accuracy of measurement is $\pm 50\ kPa$ for the suction range of 0-5 MPa and 1% for the range of 5-300 MPa (Leong et al., 2003). The test is thus of particular value for the high suction ranges and as a quick check. The device is calibrated, according to the manufacturer's instructions, using a potassium chloride (KCl) solution of known concentration (thus allowing calculation of the total suction).

4.2.2 Sampling and testing

A range of Material B specimens at different water contents was prepared in the laboratory at the University of Southampton and transported to Cardiff University for soil suction testing. Material prepared according to the method described in Section 4.1.3 was compacted using the adapted compaction method described in Section 4.1.4. A single layer of material (approximately 40 mm thick) was compacted, levelled and sealed in an air-tight bag to equilibrate.

Samples for testing in the chilled-mirror dew-point potentiometer (CMD) were trimmed from the compacted specimens as outlined below and illustrated in Figure 4.6.

- The compacted specimen (or part thereof) was trimmed using a serrated knife to a thickness of approximately 5 mm (Figure 4.6a).
- A sharp edged ring (Figure 4.6b) was used to aid trimming of sample diameter to fit in the sample cup of 37 mm. A trimmed sample is shown in Figure 4.6c.
- The sample was lightly pressed into the sample cup to ensure contact with the base of the cup as shown in Figure 4.6d. Care was taken not to fill the sample cup more than half full as this could cause the mirror to become contaminated with soil resulting in measurement errors.
- The sample was sealed and placed on a temperature equilibration plate before testing (Figure 4.6e). The temperature of the specimen was brought within close range of the chamber temperature to reduce testing time (optional).

A sample is placed in the sample chamber of the CMD and testing commences when the sample temperature is equal or less than the temperature of the cup base and chamber. The device was set to determine the dew-point temperature for several cooling cycles and produced a reading once the measurement is the same for three consecutive cycles (accurate mode). The sample is removed and weighed immediately. The sample (in the sample cup) is oven dried to determine the water content corresponding to the suction measured. The results obtained for the samples of Material B tested are summarised in Table 4.5.

Table 4.5 includes information on the gravimetric water content and approximate dry density for the compacted specimens from which the Chilled mirror samples were trimmed.

The gravimetric water content for each sample was determined after testing. Some variation in the water content of the compacted specimen and the tested samples were observed. It is expected that the sample's gravimetric water content will be lower than the original specimen's water content due to evaporation during trimming. An increase in gravimetric water content is probably due to variation in the original specimens. A number of the compacted specimens were left for 6 days before samples were trimmed and resulted in some variation of water content across the specimen. The volumetric water content was calculated assuming no significant changes in density occurred during sample preparation.

Two samples trimmed from the specimen compacted near optimum water content (w = 7.11%) were used to determine further points on a drying curve. The two samples were incrementally dried by leaving the samples open to atmosphere. After being left open to atmosphere, the samples were sealed and left for a minimum of 1 hour to equilibrate before suction testing and subsequent weighing (to obtain the wet mass). After several drying steps were completed, the samples were oven-dried to determine their dry mass and subsequently the gravimetric water content back-calculated along the drying steps. The results are included in Table 4.5 and further discussed in Section 5.3.1 in relation to suction measurements made by Otter (2011).

4.3 Determination of stiffness by cyclic triaxial testing

The cyclic triaxial test, CTX, is used in some advanced railway formation design and maintenance strategies (Heath et al., 1972; Li and Selig, 1998a; Shahu et al., 2000; Network Rail, 2005) discussed in Section 2.3.2. In highway pavement design the cyclic triaxial test, CTX, is used to determine the resilient modulus, M_R, for design (Brown, 1996; Harrigan, 2004) as discussed in Chapter 2. The CTX has also been used in research to understand the influence of water content or matric suction on the resilient modulus of pavement materials as discussed in Sections 3.1.4 and 3.3.3.

The apparatus and methodology used in this investigation on railway formation material is further described in this section. The system components, technical description and software package are summarised (Section 4.3.1). The instrumentation used and transducer calibrations are briefly described in Sections 4.3.2 and 4.3.3. The method of CTX specimen preparation is presented in Section 4.3.4 followed by the CTX test set-up (Section 4.3.5). The loading and stress distribution in a CTX specimen are discussed in Section 4.3.6 with the test stress path details in Section 4.3.7. Typical CTX test results are included in Section 4.3.8.

4.3.1 The cyclic triaxial apparatus

The system components, technical description and a summary of the control software of the cyclic triaxial apparatus used in this study are described in the following sections. The GDS Advanced Dynamic Triaxial Testing System (DYNTTS) manufactured by GDS Instruments Ltd. was used for this study (GDS Instruments Ltd, 2014). The GDS DYNTTS is also referred to as the cyclic triaxial apparatus, CTX.

4.3.1.1 System components

The CTX applies the axial force and deformation through the base of the cell by means of a screw-driven ram. An internal submersible load transducer measures the axial load at the top of the specimen.

A high speed data acquisition and control card (HSDAC card) is used for high speed data transmission, logging and control of the axial force and axial displacement. Two GDS pressure/volume controllers, one for the cell pressure and the other for the back pressure, are computer controlled.

A schematic diagram of the CTX system is shown in Figure 4.7 with Figure 4.8 showing a photograph of the CTX apparatus with GDS pressure controllers.

4.3.1.2 Technical description

Axial load: The CTX has an electromechanical actuator and is fitted with a 10 kN axial load cell. The axial strain or forces are applied through the actuator in the base of the cell. The system is displacement controlled with a direct closed-loop communication between axial displacement and axial force to allow accurate control in either displacement or force mode. The maximum frequency for cyclic loading is (5 Hz), however testing was only conducted at 0.5 Hz. The apparatus is equipped with an internal submersible load transducer at the top of the specimen.

Loading ram: The CTX apparatus has an in-built balanced ram to allow for control during dynamic loading.

Cell fluid: De-aired water was used as cell fluid. Water was de-aired using a Nold DeAerator and the cell chamber was filled from the de-aired water tank under gravity. After testing the water was drained from the base of the cell under gravity.

Pressure controller: The CTX system includes two GDS advanced hydraulic actuators which digitally regulate and measure the cell and pore fluid pressure and volume change. The pore fluid pressure (back pressure) controller was closed off from the system as testing was carried out on unsaturated specimens drained (open) to atmosphere. The

controllers each have a 200 cc volumetric capacity and are rated for a maximum pressure of 2 MPa.

Specimen dimensions: Test specimens had an external diameter of 100 mm and a height of 204 mm. The CTX was designed for testing specimens up to 150 mm diameter (300 mm high). The enlarged chamber volume gave more space for fitting local instrumentation. The larger chamber volume allows for significantly reduced contact of the LVDT cabling with the cell wall, which could influence results when relative movement during docking and testing occurs.

4.3.1.3 Software description

The commercially available software package GDSLAB by GDS Instruments Ltd. was used to control the CTX system and also to acquire and store the accumulated test data. The GDSLAB CTX software module not only controls the pressure controllers, but also has the following axial control options:

- axial displacement, mm;
- axial load, kN; and
- axial stress, kPa.

The software enables strain- as well as stress-controlled testing by specifying target values or loading sequences. The two pressure control parameters (cell pressure and back pressure) and one axial control parameter (displacement, load or stress) can be specified. These parameters can be controlled by means of the following options:

- a constant target, e.g. 30 kPa axial stress;
- a target value and ramp time, e.g. 50 kPa cell pressure in 10 minutes;
- a sinusoidal cyclic target with specific datum, amplitude and period, e.g. cyclic axial force with datum of 30 kPa, an amplitude of 15 kPa and frequency of 0.5 Hz; and
- A continuous hold on the volume, of a saturated specimen, measured with the pressure controllers.

A test consists of several individual test stages as required (e.g. cyclic loading, rest periods, etc.) The test stages can be terminated manually or by using a set of automatic trigger criteria. The automatic test stage termination criteria are

- maximum axial load;

- test length or maximum time;
- maximum deviator stress; and
- maximum stress ratio.

The end of the stage command can be specified by the user as one of

- hold pressure at end of test;
- hold volumes at end of test; and
- continue to next stage automatically; or
- wait for user interaction.

4.3.2 Instrumentation

A selection of instrumentation was used to measure stresses and strains during testing. Instruments used for taking measurements over the mid-third or at the mid-height of the specimen are referred to as local instrumentation. Measurements referencing the top and bottom faces of the test specimen are referred to as global measurements.

4.3.2.1 Measurement of load and stress

An internal, submersible, load transducer or load cell was used to measure the vertical force at the top of the test specimen. The 10 kN load transducer was calibrated over a range of 3 kN to achieve higher resolution and accuracy over the low testing stresses. Calibration of the instrumentation is discussed in Section 4.3.3

4.3.2.2 Measurement of deformation and strain

Global axial displacement was measured from the axial actuator motor shaft encoder. The accuracy of global strain measurements may be reduced significantly by a number of errors resulting from seating, alignment, bedding, end restraints and compliance (Baldi et al., 1988). Local strain measurement is invaluable and submersible linear variable differential transformers, LVDTs, were used in this study. LVDTs can accurately measure small strain increments and are relatively easy to use (Cuccovillo and Coop, 1997).

Two LVDTs were used for measuring local axial deformation on diametrically opposite sides of the specimen. These LVDTs were each held in position by two aluminium brackets (Figure 4.10) as shown in Figure 4.11a. The brackets were glued in place onto the membrane using rapid hardening glue. A variation in the set-up included the

addition of rubber bands around the brackets. The rubber bands, which was left on, ensured good contact with the specimen (Figure 4.11b).

Change in the specimen diameter was measured using a submersible LVDT connected to the specimen by means of a radial caliper as shown in Figure 4.11c. The light-weight caliper used in the CTX was made from perspex (Figure 4.10) and was based on the design by Bishop and Henkel (1957). Rapid hardening glue was used to attach the radial caliper onto the membrane, at two diametrically opposite points, to the specimen at mid-height. The caliper is hinged on the one side and the LVDT measurement, made on the opposite side, is twice the magnitude of the change in diameter as illustrated in Figure 4.12.

Volumetric strain was calculated from the local axial and radial strain measurements, assuming the specimen stayed cylindrical. This assumption is reasonable as axial strain was limited to 5% with most tests having strain levels well below the strain limit. The calculated vertical and volumetric strain before and after each cyclic stage (cumulative strains) are included for each test in Appendix C.

4.3.2.3 Measurement of pressures

The cell pressure was measured and controlled by the digital pressure controller (with a 2000 kPa range and 2 kPa accuracy). A pressure transducer was used in-line at the base of the cell for accurate measurement of the pressure applied. The pressure transducer accuracy was better than 0.8 kPa for the 900 kPa calibration range.

Neither the pore air pressure nor the pore water pressure were measured during CTX testing. Instead, the average matric suction was estimated from the soil-water retention curve, SWRC, by relating it to the water content. The specimen is allowed to drain externally, to air (i.e. at atmospheric pressure). The testing strategy is similar to that used by Sauer and Monismith (1968) and others in order to gain a qualitative understanding of the effects of suction.

4.3.3 Transducer calibration

The load cell and pressure transducers were calibrated using a dead-weight calibration system (DH Brudenberg Ltd., 580-series hydraulic dead-weight tester) (Figure B.2). The LVDTs were calibrated using a micrometer (Mitutoyo series 152-348) (Figure B.1), which had a range of 25 mm and a resolution of 1 μm. All the instrumentation was logged using the GDSLAB software and a GDS Ltd data logging system (16 bit data acquisition).

The instruments were calibrated at the start of the testing programme and at intervals over the six month testing period. Typical calibration results are included in Appendix B. The calibration range of the LVDTs was reduced to improve the resolution to the very small displacements of the high stiffness specimens. The resolution was improved from 0.00536 mm/mV for a 10 mm/1000 mV range to 0.00156 mm/mV for a 3 mm/1000 mV range (values for LVDT1).

4.3.4 Cyclic triaxial specimens

The CTX specimen preparation method is discussed below followed by the properties of the tested specimens.

4.3.4.1 Specimen preparation

The CTX specimens were compacted using the 2.5 kg rammer as discussed in Section 4.1.4. Prepared material was compacted using the adjusted number of blows to achieve the target dry density (Section 4.1.3).

A 3-part-split mould, with a compaction base and collar, of 100 mm diameter and 204 mm height was used as a compaction mould. Before compaction commenced the mould was sprayed with RS494-736 PTFE lubricant to reduce friction on the side walls and allow easy removal of the specimen. Specimens compacted and tested wet of optimum (w=8%) could not be removed easily from the mould. Each part of the mould was removed in turn by applying a small force parallel to the axis as suggested by Bishop and Henkel (1957). A comparison specimen (at w=8%) was compacted with the mould lined by a membrane to aid removal after compaction.

A membrane was placed around the specimen immediately after removal from the mould to reduce moisture loss. Cling film was used to cover the top and bottom surfaces during set-up.

4.3.4.2 Test specimen properties

For each test conducted, the test name reflects the test type (CTX), the water content relative to optimum water content (w_{opt} = 7%, thus +1 refers to w=8%) and the variant of the test loading path (e.g. v1). The variant on the test loading path (staging) is discussed in Section 4.3.7. The specimen properties for all the CTX tests are summarised in Table 4.6. Included in the table is the compaction gravimetric water content, w_i, determined from a sample of the material used for compaction. The dry density, initial volumetric water content, void ratio and degree of saturation were determined using the compaction water content, w_i (Equation 4.3 - 4.7). The volumetric water content is the

volume of water, V_w, divided by the total volume, V_t, and often considered better for use in unsaturated soil mechanics as it reflects the degree of saturation (Fredlund et al., 2012).

$$\rho_d = \frac{m_s}{V_t} \tag{4.3}$$

$$w = \frac{100 m_w}{m_s} \tag{4.4}$$

$$\theta_w = \frac{100 V_w}{V_t} \tag{4.5}$$

$$e = \frac{V_v}{V_s} \tag{4.6}$$

$$S_r = \frac{100 V_w}{V_v} \tag{4.7}$$

Where:
ρ_d = Dry density, kg/m^3;
w = Gravimetric water content, %;
θ_w = Volumetric water content, % (Fredlund et al., 2012);
e = Void ratio, unitless;
S_r = Degree of saturation, %;
m = Mass, kg;
V = Volume, m^3;
Subscripts: w = water; s = solids; v = voids; t = total.

The gravimetric water content was measured after testing for the whole specimen, w_f, and locally at three different levels (top, middle and bottom). The w_f reported in Table 4.7 is the water content measured for the whole specimen at the end of the test. The gravimetric water content at approximately mid-height of the specimen is denoted as w_{f_m}. The corresponding matric suction was estimated from the soil water retention curve, SWRC, taking w_f as representative (Bishop and Henkel, 1957). This assumes that the SWRC is valid for the specimens after some volumetric strain during testing. Specimens tested wet of optimum (CTX+1) showed significant strains (more than the allowable 5%) and matric suction was taken as zero to reflect the saturation of the specimen during testing.

4.3.5 Cyclic triaxial specimen set-up

The CTX base pedestal was prepared by clearing the back pressure lines of any water using a vacuum pump. An air-dried porous stone was placed on top of the base pedestal and two O-rings placed around the base pedestal ready for use. This enabled the specimen set-up to commence without delay. Specimen preparation, set-up and testing took place in a temperature controlled environment at 20^oC.

The specimen set-up procedure was as follows.

- The specimen was lowered onto the base pedestal fitted with with air-dried porous stone (coarse stone, low air entry).
- The three-part split-mould was removed and a new membrane fitted.
- An air-dried porous stone and top cap (Figure 4.9) was positioned on top of the specimen. The dimple in the top cap was covered to reduce the error in global measurements resulting from any lack of alignment between the specimen and the loading ram.
- The membrane was sealed using two O-rings each around the base pedestal and the top cap.
- The top pore water pressure tube was connected. All pore pressure connections were open to atmosphere.
- Local strain measurement devices were fitted. A radial calliper (Figure 4.10) was glued onto the specimen at mid-height for radial strain measurement using a Linear Variable Differential Transformer, LVDT (Figure 4.11c).
- Two LVDTs were fitted to the mid-third of the specimen for axial strain measurement. The two pairs of brackets were glued onto the membrane (Figure 4.11a), diametrically opposite each other.
- The cell chamber was lifted onto the base using a mobile crane and screwed down to create a watertight seal. The chamber was filled with de-aired water after the specimen was docked.
- After filling, testing commenced.

4.3.6 Loading and stress distribution in cyclic triaxial specimens

The cyclic triaxial apparatus enables the application of a radial confining pressure or cell pressure, p_o, and an axial load, W, or axial displacement as illustrated in Figure 4.13. The stress condition is controlled by the applied axial load and radial pressure on the cylindrical specimen (Kramer, 1996).

4.3.6.1 Stress distribution in triaxial specimens

Triaxial test results are interpreted assuming the specimen is a single element and maintains its cylindrical shape. Calculations of stresses and strains are presented by Equations 4.8 to 4.11 with reference to Figure 4.13.

$$\overline{\sigma}_z = \frac{W}{\pi r_o^2} + p_o \tag{4.8}$$

$$\overline{\sigma}_r = p_o \tag{4.9}$$

$$\overline{\epsilon}_z = \frac{\Delta h}{h} \tag{4.10}$$

$$\overline{\epsilon}_r = \frac{\Delta r}{r_o} \tag{4.11}$$

Where:
$\overline{\sigma}_z$ = average vertical stress, Pa,
$\overline{\sigma}_r$ = average radial stress, Pa,
$\overline{\epsilon}_z$ = average axial strain,
$\overline{\epsilon}_r$ = average radial strain from local measurements,
W = axial (vertical) load, N,
r_o = outer radius, m,
Δr = radial displacement, m,
p_o = cell pressure, Pa,
h = height, m,
Δh = vertical displacement, m.

4.3.6.2 Test parameters and principal stresses

The three principal stresses are known when using the triaxial test. For testing conducted under triaxial compression (TC) the intermediate principal stress, σ_2, is equal to the minor principal stress, σ_3, which in turn is equal to the cell pressure, p_o. The major principal stress, σ_1, is equal to the average vertical stress, $\overline{\sigma}_z$.

The three dimensional stress invariants namely deviator stress, q (Equations 4.12), and mean or average principal stress, p (Equation 4.13), are used to describe the stress state when the intermediate principal stress is known (Powrie, 2014b).

$$q = \left(\frac{1}{\sqrt{2}}\right)\sqrt{(\sigma_1 - \sigma_2)^2 + (\sigma_1 - \sigma_3)^2 + (\sigma_2 - \sigma_3)^2} \tag{4.12}$$

$$p = \left(\frac{1}{3}\right)(\sigma_1 + \sigma_2 + \sigma_3) \tag{4.13}$$

Where:
q = deviator stress, kPa,
p = mean principal stress, kPa,
σ_1 = major principal stress, kPa,
σ_2 = intermediate principal stress, kPa,
σ_3 = minor principal stress, kPa.

The expression for deviator stress, q, reduces to Equation 4.14 for axisymmetric conditions in the triaxial test as the intermediate principal stress is equal to either the minor or the major principal stress. For railway formation applications specimens are tested in triaxial compression (TC) where $\sigma_2 = \sigma_3$. Under these conditions Equation 4.12 simplifies to:

$$q = \sigma_1 - \sigma_3 \tag{4.14}$$

The intermediate principal stress, σ_2, can be related to the major and minor principal stresses, σ_1 and σ_3, by the parameter b (Bishop, 1966) (Equation 4.15). The intermediate principal stress is generally not considered as a major factor in the mechanical behaviour of soils when compared to the major and minor principal stresses (Kramer, 1996). In the CTX the intermediate principal stress cannot be independently controlled.

$$b = \frac{\sigma_2 - \sigma_3}{\sigma_1 - \sigma_3} \tag{4.15}$$

As summarised in Figure 4.14 originally presented by Jamiolkowski et al. (1985), the triaxial apparatus can only apply conditions where b=0 and $\alpha = 0^o$ (triaxial compression, TC) or b=1 and $\alpha = 90^o$ (triaxial extension, TE). Alpha, α, is the angle between the direction of the major principal stress and the vertical. Even though the true triaxial (TT) is able to vary b, continuous principal stress rotation, PSR, is not possible (Saada, 1988).

4.3.7 Stress paths applied

Specimens were tested according to the loading sequences suggested in the Harmonized Test Methods for Laboratory Determination of Resilient Modulus for Flexible Pavement Design (NCHRP Project 1-28A) for granular pavement subgrade material (Harrigan, 2004). Testing was carried out drained (air and water) by allowing the top and bottom pore pressure lines to drain to atmosphere. It was assumed that the pore-air pressure remained at atmospheric pressure ($u_a = 0$), therefore giving a net normal stress, $\sigma_n = \sigma - u_a$, equal to the applied total stresses. Variations in matric suction during cyclic loading were not considered. Specimens were compacted at different water contents and related to the matric suction by means of the SWRC.

Each test consisted of 20 loading sequences as given in Table 4.8. The stress path for each loading sequence is compared in Figure 4.15 and numbered according to the relevant loading sequence. Each loading sequence is conducted at one of five selected cell pressures (15; 30; 40; 55; or 85 kPa). One of four applied stress ratios, calculated as the cyclic deviator stress, q_{cyc}, divided by the cell pressure, p_o is used (0.5; 1.0; 2.0; or

3.0) resulting in four loading sets. The cell pressures used span the range of confining stresses used by Miller et al. (2000) (14-35 kPa) and Shahu et al. (2000) (20-40 kPa) for railway formation testing. The higher confining stresses (55 and 85 kPa) represent elements at a greater depth within the formation and enable evaluation of the effect of confining stress influence on resilient modulus (discussed in Chapter 3). Gräbe (2002) tested at p_o of 30 kPa and an applied stress ratio of 1.0 following finite element modelling of the stresses in the formation, which is the same as that prescribed by Network Rail (2005) for subgrade soils (see Section 4.3.6).

During a loading sequence the cell pressure, p_o, was held constant while applying the cyclic deviator stress. The cyclic deviator stress was applied using a sine-wave load-form representative of the applied vertical stress from a passing train bogie as discussed in Chapter 2. 100 cycles per sequence were applied at a frequency of 0.5 Hz.

A contact stress, q_{min}, having a magnitude of 20% of the confining pressure was maintained to ensure good contact between the specimen and the load transducer. No pre-conditioning phase was applied as this is considered unnecessary when local strain measurements are made (Nazarian et al., 1996), and was found to result in the underestimation of M_R (Cerni et al., 2015) The maximum principal total stress ratio, η, is calculated as the maximum deviator stress, q_{max}, divided by the average principal total stress, p. q_{max} and the corresponding p were calculated according to Equation 4.14 and 4.13. The maximum principal total stress ratios, η, corresponding to the applied stress ratios (q_{cyc}/p_o=0.5, 1.0, 2.0 and 3.0), are 0.78, 1.13, 1.57 and 1.85 respectively.

The time required between sequences is not prescribed in the NCHRP Project 1-28A. Initially, testing was conducted allowing pause periods of 5 minutes following a cell pressure increase and 10 minutes following a cell pressure decrease (from 85 kPa to 15 kPa). The deviator stress datum ($q_{min} + \left(\frac{1}{2}\right) q_{cyc}$) was changed to the next deviator stress datum (for the next loading sequence) over a period of 2 minutes. This test variant is referred to as variant #0 in Table 4.9. The test plan was adjusted after the times for pore pressure dissipation were identified as being insufficient. Test variant #1 allows for cell pressure change at a rate of 2 kPa/minute.

To evaluate the influence of test staging the order of the dynamic test stages was changed. Test variant #2 (Table 4.9) incrementally applied the loading sequences in Table 4.8 at the same confining pressure, from the lowest (15 kPa) to the highest (85 kPa). Thus applying sequence 1, 6, 11, 16 ($p_o = 15\ kPa$) then sequence 2, 7, 12, 17 ($p_o = 30\ kPa$) and so forth. The impact of the test staging is further discussed in Section 5.4.2.

4.3.8 Typical test results

Stresses and strains were calculated from the test data using the equations presented in Section 4.3.6. Typical test results are shown in Figure 4.16. The results are for one test

sequence (sequence 7) from CTX+0v0. Figure 4.16a shows the development of global and average local vertical strain over 100 cycles at 0.5 Hz. The deviator stress is plotted against vertical strain for cycles 1-5 and cycles 95-100 in Figure 4.16b. A straight line is indicated between the minimum and maximum points of cycle 100 to illustrate the calculation of resilient modulus, M_R, which is the slope of the line. The stress path (in terms of net normal stresses) for a cycle in sequence 7 is also plotted (Figure 4.16c).

The resilient modulus, M_R is calculated using the average recoverable local strain measurements made on diametrically opposite sides of the specimen. A difference in local vertical strain measurement (hence local M_R) on diametrically opposite sides of the specimen (ϵ_{zL1} and ϵ_{zL2}) is considered to be due to uneven loading resulting from slight misalignment of the specimen and the ram. $\epsilon_{z^{max}}$ and $\epsilon_{z^{min}}$ should be less than 1.1 for an acceptable test (Harrigan, 2004). Measurements on less stiff specimens tested at higher water content (including optimum water content specimens as tested in general practice) had an acceptable variation in local strain measurement ($0.91 < \epsilon_{zL1}/\epsilon_{zL2} < 1.1$). The stiff specimens (at low water content) showed greater variation in the local strain measurements (Figure 4.17), but the data were not discarded as repeated tests at the same water content gave similar averaged results.

For most test sequences, M_R tends to level off towards the end of 100 cycles as shown in Figure 4.18 for sequence 6-10 with an applied stress ratio $q_{cyc}/p_o = 1$ in CTX+0v0. The reported M_R for a particular test sequence is calculated as the average M_R over the last 5 cycles (96-100). The influence of number of cycles is discussed in Section 5.4.1.

For the first set of CTX tests (tests 1 to 7), the measured cell pressure was corrected to a datum value of zero at the mid-height of the specimen after testing. The magnitude of p_o for these tests (including CTX+0v0) is therefore higher than the target values in the test plan (Table 4.8), because the target value was initially for the top of the cell.

Figure 4.19 and 4.20 show M_R against confining pressure, p_o, and cyclic deviator stress, q_{cyc}, respectively for test CTX+0v0. In Figure 4.19 the results are grouped together (as sets) for sequences with the same applied stress ratio (0.5, 1.0, 2.0 or 3.0). From the two figures it is evident that the results at low testing stresses (sequence 1: p_o=15 kPa and q_{cyc}=7.5 kPa) are outliers. The exclusion of sequence 1 from most of the tests conducted is further discussed with the M_R regression analysis in Section 5.6. The last entry (sequence 20: p_o=85 kPa and q_{cyc}=255 kPa) should also be discounted as the accumulated vertical strain is more than 5% (Harrigan, 2004). The results from all of the CTX tests are tabulated in Appendix C.

4.4 Determination of stiffness by cyclic hollow cylinder testing

Saada (1988) summarised the historical development of the hollow cylinder apparatus, HCA, for soil testing and its use in studying the effects of anisotropy, liquefaction and principal stress rotation, PSR, on soil. Gräbe and Clayton (2009) suggested the use of a railway subgrade testing method that can induce PSR. This recommendation followed HCA testing on saturated subgrade materials, some of which indicated a significant influence of PSR on the stiffness and permanent deformation of rail track foundations (Gräbe and Clayton, 2014).

The HCA is recognised as one of the laboratory tools that can be used to investigate the influence of complex load conditions in soil (Hight et al., 1983; Brown, 1996; Hight and Leroueil, 2003). This section includes the details relating to the HCA system (Section 4.4.1), instrumentation and calibration (Sections 4.4.2 and 4.4.3), specimen preparation (Section 4.4.4) and test set-up (Section 4.4.5). The stress distribution in a hollow cylinder specimen is discussed in Section 4.4.6 and the testing stress paths applied summarised in Section 4.4.7. The section concludes with some typical results in Section 4.4.8.

4.4.1 The hollow cylinder apparatus

The GDS Small Strain Hollow Cylinder Apparatus II, SS-HCA II, developed by GDS Instruments Ltd and described and used by Gräbe (2002) was used in this research. The hollow cylinder apparatus is also referred to as the HCA. The system components, technical description and control software are described in the following section.

4.4.1.1 System components

The HCA has two servo motors for separate control of the axial and torsional movements. A single actuator in the base of the cell imposes both the torque and the vertical force. An internal, submersible, combined load and torque transducer measures the axial load and torque at the top of the specimen.

Direct, closed-loop servo control of the axial force and displacement, and the torque and angular rotation is achieved with two high speed data acquisition and control cards (HSDAC cards). Three GDS pressure/volume controllers, for external cell pressure, internal cell pressure and back pressure, are computer controlled. A schematic diagram of the HCA system is given in Figure 4.21. Figure 4.22 shows a photograph of the HCA apparatus with GDS pressure controllers. A closer view of the HCA apparatus is shown in Figure 4.23.

4.4.1.2 Technical description

Axial load and torque: The HCA was designed for a maximum axial load and torque of 10 kN and 100 Nm respectively. The deformations or forces are applied through the actuator in the base of the cell. The system is displacement controlled with a direct closed loop of displacement and force to allow for accurate control in either displacement or force mode. The maximum frequency for cyclic loading of axial and torsional deformation is 1 Hz. The apparatus is equipped with an internal submersible load/torque transducer at the top of the specimen.

Loading ram: A tight tolerance ram with a light pressure seal is used in the base instead of an in-built balanced ram to achieve lower friction on the ram. Because of this, a more viscous fluid, silicone oil, is used for the cell fluid instead instead of water as used for triaxial testing.

Cell fluid: Silicone oil (Dow Corning 200 fluid) was used for the cell fluid. The oil has a viscosity of 50 cSt at 25 ^oC, is electrically inert and has no effect on latex membranes. The oil reservoir is at floor level and a pump is used to fill the cell and cell pressure controllers. The oil was drained from the base of the cell under gravity. Under the low cell pressure used during testing (less than 50 kPa) no noticeable weeping of oil from the low friction seal at the bottom of the cell occurred.

Pressure controller: The HCA is equipped with three GDS advanced hydraulic actuators, which digitally regulate and measure the inner cell, outer cell and pore fluid pressures and volume changes. The pore pressure controller was closed off from the system since testing was conducted on unsaturated specimens drained (open) to atmosphere. The controllers each have a 200 cc volumetric capacity and are rated for a maximum pressure of 1 MPa. The accuracy and resolution of the pressure was better than 0.1% of the full range. The accuracy of volume change measurement was better than 0.25% of the nominal volumetric capacity of the controller. The resolution of the volume change measurement was 0.5 mm^3.

System compliance: With regard to system stiffness, the apparatus was designed to have a maximum system compliance of 10 $\mu m/kN$ under applied axial load (Gräbe, 2002). The designed maximum system compliance under applied torque was 0.0015 ^{o}/Nm. Three high-stiffness reaction bars were attached to the base of the cell and to a circular steel plate at the top. The load/torque transducer was in turn attached to the steel plate, as seen in Figure 4.23a.

Specimen dimensions: Test specimens had an external diameter of 100 mm, an internal diameter of 60 mm and a height of 204 mm. The specimen geometry affects the uniformity of the stress distribution in hollow cylindrical specimens as discussed in section 4.4.6. The inner and outer cell pressures, p_i and p_o, were equal ($p_i = p_o = p$)

for all the HCA tests, so that there would be no variation in the radial stress, σ_r, across the specimen wall and that $\sigma_r = p = \sigma_\theta$.

4.4.1.3 Software description

The commercially available software package GDSLAB (GDS Instruments Ltd) was used to control the HCA system and also to acquire and store the test data. The same software controls discussed in Section 4.3.1.3 for the CTX were used for the HCA. The GDSLAB HCA software module is an extension of the GDSLAB CTX software module. In addition to controlling the three pressure controllers and the axial displacement or load as previously described (Section 4.3.1.3), the options for torque control are:

- rotational displacement, degrees;
- rotational (torque) load, Nm; and
- rotational (shear) stress, kPa.

The software enables strain- as well as stress-controlled testing by means of target values or loading sequence specification. The three pressure control parameters (external cell pressure, internal cell pressure and back pressure), one axial control parameter (displacement, load or stress) and one torque control parameter (rotational displacement, torque or shear stress) can be specified similarly to the CTX control conditions (Section 4.3.1.3). The software aims to provide a simple and reliable code that allows the user flexibility to perform stress path, as well as standard laboratory tests (Gräbe, 2002).

4.4.2 Instrumentation

A selection of instrumentation was used to measure stresses and strains during HCA testing. To distinguish between measurements on the inner and outer faces of the hollow test specimens, the terms internal and external are used. Instruments used for taking measurements over the mid-third or at the mid-height of the specimen are referred to as local. Measurements with reference to the top and bottom faces of the test specimen are referred to as global.

4.4.2.1 Measurement of load and stress

An internal, submersible, combined load and toque transducer was used to measure the vertical force and torque at the top of the test specimen. The 10 kN/100 Nm transducer was calibrated over ranges of 3 kN and 30 Nm to achieve higher resolution over the low testing stresses used. Calibration of the instrumentation is discussed in Section 4.4.3.

4.4.2.2 Measurement of deformation and strain

Global axial displacement was measured from the axial actuator motor shaft encoder as in the CTX (see Section 4.3.2). The accuracy of global strain measurements may be reduced significantly by a number of errors as previously discussed and therefore, local strain measurements were made. Similar to the CTX instrumentation, two LVDTs were used to measure axial deformation on diametrically opposite sides of the specimen (Figure 4.29a) further discussed in Section 4.4.5. The mid-height radial displacement of the external diameter was made using a radial caliper as shown in Figure 4.28c. The light weight caliper used in the HCA is made from stainless steel with the two brackets able to pivot to aid fitting onto the specimen.

A simple set-up for measuring the angular rotation locally was designed by Gräbe (2002) and is shown in Figure 4.29b. Two submersible LVDTs are attached to the reaction bars at one third and two thirds of the specimen height, to measure the relative rotation over the mid-third. Two thin stainless steel rings are attached to the specimen at four equidistant points. The LVDT pins are fixed to the steel rings, which rotate with the specimen, while the LVDT bodies are stationary. The difference in measured rotation over the mid-third of the specimen is taken as the segment length relating to the angle of rotation of a circle of known radius (i.e., that of the stainless steel rings). This assumes that the angle is small and the segment length is represented linearly. The shear strain can then be calculated using Equation 4.23 given in Section 4.4.6. The local measurements were compared with the angular rotation measured on the radial actuator shaft encoder (global measurement).

Determining the volumetric strain of specimens tested in the HCA requires measurement not only of local axial and radial deformations (of the external radius), but also of the change in the internal radius. Measurements of the change in the cell fluid volume in the inner chamber were made by the internal cell pressure digital controller. It is assumed that the cell fluid is incompressible and extreme care was taken to ensure that the chambers and connections between the controllers and the cell were completely de-aired, prior to testing, to ensure accuracy in these volume measurements.

4.4.2.3 Measurement of pressures

The internal and external cell pressures were measured and controlled by seperate GDS digital pressure controllers, with a range of 1000 kPa. Pressure transducers were used in-line, at the base of the cell, for accurate measurement of the pressures applied. The internal and external cell pressures were held equal throughout testing and were used to calculate the radial stress, σ_r, acting on the specimen.

Several specimens were compacted each at different water content and tested in the unsaturated state. No pore pressure measurements were made during testing (see Section 4.3.2.3).

4.4.3 Transducer calibration

The load/torque transducer in axial load and the pressure transducers were calibrated using a dead-weight calibration system (DH Brudenberg Ltd., 580-series hydraulic dead-weight tester) (Figure B.2), similar to the CTX transducer calibration. The LVDTs were calibrated using a micrometer (Mitutoyo series 152-348) (Figure B.1), which had a range of 25 mm and a resolution of 1 μm.

The load/torque transducer was calibrated for torque using a purpose-built calibration frame (Gräbe, 2002) as developed by Rust (2003). The load/torque transducer is subjected to a couple using the dead weight system as shown in Figure B.3.

Instruments were calibrated before use and at intervals over the two year testing period. For all the instruments, the calibration varied by less than 1%. Typical calibration results are included in Appendix B.

4.4.4 Hollow cylinder specimens

The HCA specimen preparation technique is described below followed by a summary of the test specimen properties.

4.4.4.1 Specimen preparation

The HCA specimen preparation technique is an extended version of the method used for preparing a CTX specimen (Section 4.3.4). Prepared material (Section 4.1.3) was compacted into the 100 mm diameter split mould using the BS1377-4:1990 standard 2.5 kg rammer (Figure 4.24a) as discussed in section 4.1.4. A membrane was initially used to line the compaction mould for easy removal of the specimen, but was later substituted by spraying the mould walls with RS494-736 PTFE lubricant to reduce friction on the side walls. A membrane was placed over the specimen as soon as compaction was complete.

The inner diameter of the specimen (60 mm) was cored from the bottom up using a wood drill. A split mould (taller than the compaction split mould) was used to support and protect the specimen and to align it with the ends of the wood drill (Figure 4.24b). The specimen was cored in two stages, starting with a smaller diameter of approximately

30 mm, to reduce disturbance (Figure 4.24c). The finished specimen, within a split mould for protection, was carefully removed from the wood drill.

The top and bottom ends of the specimen were prepared for fitting onto the finned porous discs. The fin positions were marked and cut into the specimen (Figure 4.25), using a Stanley knife, to prevent cracking of the specimen during set-up and initial loading. This was particularly important for lower water content specimens, which were very stiff and less pliable. Pre-cutting aided the bedding of the fins into the specimen end surfaces to reduce errors associated with gaps between the specimen and the top and bottom platens.

4.4.4.2 Test specimen properties

For each test reported, the test name reflects the test type (HCA), the water content relative to the optimum water content (w_{opt}=7%), and the relevant stress path variant used for testing. The stress path variants are discussed in Section 4.4.7. The specimen properties for all the HCA tests are summarised in Table 4.11 for the initial condition before testing. The initial specimen properties in Table 4.11 include the water content of the compacted material (initial water content), dry density, volumetric water content, void ratio and degree of saturation. Calculation of these parameters using the initial gravimetric water content were for the specimen before drilling, using Equations 4.4 - 4.7 as for the CTX specimens (Section 4.3.4).

The gravimetric water content of each specimen was determined for diametrically opposite points at the top, middle and bottom of the specimen after testing. These results are reported in Table 4.12 as well as the water content of the whole specimen (w_f). The initial water content for HCA-1.7v1 was used, as no final water content could be measured due to unforeseen test termination. A loss in communication between the control software and the apparatus during testing resulted in the uncontrolled rotation of the specimen and subsequent entry of cell fluid (silicon oil) into the specimen.

As with the CTX specimens, the matric suction was estimated from the SWRC determined by Otter (2011) using the water content of the whole specimen (bulk water content). Khoury and Zaman (2004) reported that the influence of the bulk water content is the important parameter when assessing the influence of the water content (suction) on the modulus even if some variation across the specimen exist. The values of matric suction were adjusted for wet of optimum specimens that were close, or at, saturation due to large volumetric strains by using the water content that corresponds to the degree of saturation.

4.4.5 Hollow cylinder specimen set-up

Prior to specimen preparation, the base pedestal and top cap were prepared, ready for specimen set-up. This enabled the specimen to be fitted into the apparatus without delay. Moisture loss from the specimen was reduced as much as reasonably possible using cling film to cover the top and bottom surfaces where exposed. Specimen preparation, set-up and testing took place in a temperature controlled environment at 20^oC.

4.4.5.1 Base pedestal and top cap preparation

The base pedestal and inner membrane were prepared according to the following steps as illustrated in Figure 4.26.

- The inner edge of the base pedestal was lubricated with a silicone-based grease and the lower membrane holder inserted as shown in (Figure 4.26a).
- An O-ring was fitted to the upper membrane holder and inserted into one end of the inner membrane (Figure 4.26b). All membranes were checked for leaks before use by filling them with water (held closed either end).
- The inner membrane, with its upper membrane holder and O-ring, was lowered into place. Care was taken to prevent folds in the membrane. The upper membrane holder was screwed down into the base pedestal, using four screws, compressing the O-ring to create a good seal (Figure 4.26c). The membrane was kept upright using a thin rod.
- A sintered bronze porous disc with fine pores (fitted with six fins) was fixed in place (Figure 4.26d). Two O-rings were placed around the outside of the base pedestal for later use.

The top cap components were prepared and partly assembled as shown in Figure 4.27.

- A second sintered bronze porous disc with fins was fixed to the underside of the lower top cap. Two O-rings (for the outer membrane) placed around the top cap for later use (Figure 4.27a).
- The upper top cap was cleaned and the O-ring seal greased (Figure 4.27b).
- The 60 mm O-ring (for the inner membrane), and bolts for connecting the lower and upper top cap components were set aside for use (Figure 4.27c&d).

4.4.5.2 Specimen set-up

The specimen set-up procedure is outlined below as illustrated by Figures 4.28 and 4.29.

- The specimen was lowered onto the base pedestal with the porous disc, and the inner membrane threaded through.
- The three-part split-mould was removed and the specimen enclosed in a new outer membrane.
- The lower top cap was placed on the specimen. A three-part split-mould was positioned around the specimen, including parts of the base pedestal and top cap, to protect the specimen during the remainder of the test set-up process (Figure 4.28a) and to ensure correct alignment.
- The inner membrane was secured in place using the 60 mm O-ring.
- After filling the inner chamber with as much silicon oil as possible, the upper top cap was screwed onto the lower top cap.
- Once the specimen had been transferred and secured in the HCA, the outer membrane was sealed using two O-rings each around the base pedestal and the top cap.
- The pore water and inner cell fluid tubes were connected to the base pedestal and the split mould removed (Figure 4.28b).
- Local strain measurement devices were fitted. A radial caliper was glued onto the specimen at mid-height for the radial measurement using a LVDT (Figure 4.28c).
- Two LVDTs were fitted to span the mid-third of the specimen, for axial strain measurement. Two pairs of brackets were glued onto the membrane (Figure 4.29a) at diametrically opposite sides.
- Two circumferential displacement LVDTs were fitted to measure the rotation of the mid-third using brackets fitted to the reaction bars and special circular rings (Section 4.4.2) glued to the membrane at four equidistant points (Figure 4.29b).
- After connecting the pore and cell fluid tubes to the top cap the pressure cell chamber was lowered, sealed and filled with silicon oil (Figure 4.29c). The inner chamber was also supplied with silicon oil to complete the filling.
- After filling, testing commenced.

4.4.6 Loading and stress distribution in hollow cylinder specimens

Both the normal and shear stress can be controlled in the HCA to better represent the in-situ load condition (Brown, 1996). The shear stresses on the vertical and horizontal planes are applied by means of a torque load, M_T, applied at the top of the specimen shown in Figure 4.30. The axial load, W, and lateral stresses (internal, p_i, and external, p_o, radial cell pressures) are controlled in order to create the desired vertical and radial stresses (Hight et al., 1983).

A gradient of radial stress, σ_r, will exist if p_o and p_i are not equal (Hight et al., 1983). Saada (1988) suggest that a difference in p_o and p_i (in order to vary b) results in almost the same amount of non-uniformities as in the direct simple shear device. Assuming no shear stresses act on the vertical (circumferential) faces of the specimen, σ_r will always be a principal stress (Hight et al., 1983). This assumption is recognised to only be valid if the end restraint effects are negligible.

The ratio of the inner and outer diameter of the specimen will influence the radial uniformity of shear strains (Hight et al., 1983; Kramer, 1996). The main critique of the HCA is that non-uniformities develop across the wall of the specimen (Saada et al., 1985). Therefore, the geometry of the specimen is very important if the effects thereof are to be reduced (Hight et al., 1983; Jardine, 2011). The need for local measurements of displacements, rotations and pore pressures has been recognised by Hight et al. (1983) to account for variations, but this does not necessarily improve accuracy (Saada et al., 1985).

Specimen dimensions adopted by Hight et al. (1983) include an outer diameter of 254 mm, inner diameter of 203 mm and height of 254 mm. These dimensions were selected to reduce the influence of non-uniformities, within practical limits. HCA tests reported by a number of researchers were conducted on a range of specimen sizes summarised in Table 4.10. Although a range of specimen sizes are used in the literature, the potential effect of the specimen size has not been accounted for.

4.4.6.1 Stress distribution in hollow cylinder specimens

HCA test results were interpreted assuming the specimen as a single element. Calculations of stresses and strains are presented by Equations 4.16 to 4.23 presented by (Hight et al., 1983; Saada, 1988) with reference to Figure 4.30.

$$\overline{\sigma}_z = \frac{W}{\pi(r_o^2 - r_i^2)} + \frac{p_o r_o^2 - p_i r_i^2}{r_o^2 - r_i^2} \tag{4.16}$$

$$\overline{\sigma}_r = \frac{p_o r_o + p_i r_i}{r_o + r_i} \tag{4.17}$$

$$\overline{\sigma}_\theta = \frac{p_o r_o - p_i r_i}{r_o - r_i} \tag{4.18}$$

$$\overline{\tau}_{\theta,z} = \frac{3M_T}{2\pi(r_o^3 - r_i^3)} \tag{4.19}$$

$$\bar{\epsilon}_z = \frac{\Delta h}{h} \tag{4.20}$$

$$\bar{\epsilon}_r = -\frac{u_o - u_i}{r_o - r_i} \tag{4.21}$$

$$\bar{\epsilon}_\theta = -\frac{u_o + u_i}{r_o - r_i} \tag{4.22}$$

$$\overline{\gamma}_{\theta,z} = \frac{2\theta(r_o^3 - r_i^3)}{3h(r_o^2 - r_i^2)} \tag{4.23}$$

Where:
$\overline{\sigma}_z$ = average vertical stress, Pa,
$\overline{\sigma}_r$ = average radial stress, Pa,
$\overline{\sigma}_\theta$ = average circumferential stress, Pa,
$\overline{\tau}_{\theta,z}$ = average shear stress, Pa,
$\bar{\epsilon}_z$ = average axial strain,
$\bar{\epsilon}_r$ = average radial strain,
$\bar{\epsilon}_\theta$ = average circumferential strain,
$\overline{\gamma}_{\theta,z}$ = average shear strain,
θ = angular circumferential displacement, radians,
W = axial (vertical) load, N,
r_o = outer radius, m,
r_i = inner radius, m,
p_o = external (outer) cell pressure, Pa,
p_i = internal (inner) cell pressure, Pa,
M_T = torque, Nm,
h = height, m,
Δh = vertical displacement, mm,
u = radial movement of specimen wall, mm.

When equal external and internal cell pressures are applied, then $p_i = p_o = \overline{p}$ reducing Equations 4.16, 4.17 and 4.18 to:

$$\overline{\sigma}_z = \frac{W}{\pi(r_o^2 - r_i^2)} + \overline{p} \tag{4.24}$$

$$\overline{\sigma}_r = \overline{p} \tag{4.25}$$

$$\overline{\sigma}_\theta = \overline{p} \tag{4.26}$$

4.4.6.2 Test parameters and principal stresses

The principal stresses can be calculated from the hollow cylinder test parameters using Equations 4.27, 4.28 and 4.29 as given by Hight et al. (1983).

$$\sigma_1 = \frac{\sigma_z + \sigma_\theta}{2} + \sqrt{\left(\frac{\sigma_z - \sigma_\theta}{2}\right)^2 + \tau_{\theta,z}^2} \tag{4.27}$$

$$\sigma_2 = \sigma_r \tag{4.28}$$

$$\sigma_3 = \frac{\sigma_z + \sigma_\theta}{2} - \sqrt{\left(\frac{\sigma_z - \sigma_\theta}{2}\right)^2 + \tau_{\theta,z}^2} \tag{4.29}$$

The stress path used, together with the specimen geometry, need careful consideration (Jardine, 2011). Due to the complexities associated with the HCA it has mainly been used as research tool (Hight and Leroueil, 2003). The Hollow Cylinder is used in practice for testing of dynamic load influence on foundations such as for earthquake design. The specimen preparation, set-up and stress path testing are presented in Chapter 4.

4.4.7 Stress paths applied

The stress path approach described by Lambe (1967) was used in the laboratory testing of the compacted railway formation material. The expected (total) stress path experienced by a specific soil element in the track foundation due to a passing train was applied. The matric suction was not controlled or measured during testing and was related to the water content of the specimen before and after testing using the soil-water retention curve, SWRC.

Specimens compacted at a range of water contents were used to investigate the effect of matric suction. Testing was conducted drained (for both air and water) by allowing the top and bottom pore pressure lines, connected to the specimen, to drain freely to atmosphere. It was assumed that the pore-air pressure remained at atmospheric pressure ($u_a = 0$). Therefore, the net normal stress, $\sigma_n = \sigma - u_a$, was equated to the applied total stresses. Variation in matric suction during cyclic loading was not considered.

The effect of principal stress rotation, PSR, on the resilient modulus was investigated by applying stages of loading with and without PSR. The magnitude of cyclic stresses employed by Gräbe (2002), to simulate the train induced stresses, were used during this study. Figure 4.31 indicates the two cyclic stress paths in terms of the applied stresses.

- Stress path 1 (SP1): The specimen was subject to a cyclic deviator (axial) stress while the cell pressure was held constant with no rotational stress. This was equivalent to a cyclic triaxial test as no principal stress rotation occured.

- Stress path 2 (SP2): The specimen was subject to both cyclic deviator (axial) stress and rotational loading to induce PSR. The rotational loading was 90^o out of phase with the deviator stress. A constant cell pressure was maintained

The inner and outer cell pressures, p_i and p_o, were held equal and constant during the HCA testing. A constant ratio of the cyclic deviator stress, q_{cyc}, to the confining stress, $p_o = \sigma_{nc}$, equal to 1.0 was adopted (similar to sequence 7 of the CTX stress path). The resulting maximum principal stress ratio ($\eta_n^* = \sigma_{n1}/\sigma_{n3}$) given in terms of net normal stresses) achieved when $q_{cyc}/\sigma_{nc} = 1.0$ is $\eta_n^* = 2.0$. It is expected that this stress ratio is well below the failure stress ratio in a well-designed pavement (Gräbe, 2002). An average confining pressure, σ_c, of 30 kPa was selected for a typical railway formation element by Gräbe (2002) following finite element modelling. This value is in the same range as used by Miller et al. (2000) (14-35 kPa) and Shahu et al. (2000) (20-40 kPa) for CTX testing (Section 4.3.7).

The period of cycling, T, was 1 minute (0.017Hz). This rate is low in comparison to expected field loading rates such as 0.5 Hz (Heath et al., 1972). Limitations in control software and data logging prevent faster loading in the HCA (Gräbe, 2002). However, the slower rate is likely to reduce any pore-air pressure build-up and consequent changes in net normal stress and matric suction. The influence of the slower testing rate on the measured resilient modulus was considered by comparing it to results from the CTX testing (Section 5.4.3).

Each of the HCA tests consisted of three dynamic phases. Prior to applying any cyclic stress path phases an isotropic confining stress was applied (30 kPa) to allow equilibration of the specimen under the in-situ stress condition. Phase one, two and three were the cyclic phases with and without PSR. Phases one and three used the same stress path, normally 500 cycles of SP2. Phase two consisted of 1000 cycles of SP1, except for test HCA+0v2 for which the stress path order was changed. This approach was adopted to evaluate the effect of the load staging and any changes in water content (matric suction) during testing of a particular specimen. It also enabled testing and monitoring of the SP2 phases and the change-over stages between test phases during the day. Table 4.13 summarises the HCA tests conducted and indicates the sequence of stress paths.

4.4.8 Typical test results

Stresses and strain were calculated from the HCA test data using the equations presented in Section 4.4.6. Typical test results from HCA+0v1 are presented in Figure 4.32 and 4.33.

Calculation of M_R was the same as discussed in Section 4.3.8 and illustrated in Figure 4.16b for the CTX tests (M_R=q_{cyc}/ϵ_R). Figure 4.32a presents M_R for all three test

phases with (SP2) and without PSR (SP1). An increase in M_R is noted as the number of SP1 cycles increases (without PSR). This effect is less evident for SP2 conditions (with PSR). The local axial strain accumulation since the start of the test is shown in Figure 4.32b. Stress paths (total stress) for cycles of SP1 (without PSR) and SP2 (with PSR) are plotted in Figure 4.32c.

The minimum and maximum deviator stresses (q_{min} and q_{max}) used to calculate q_{cyc} (= q_{max}-q_{min}) are marked on Figure 4.32c. These points are the same for SP1 and SP2. q_{min} and q_{max} correspond to the points in the stress cycle at which the vertical stress is a minimum and maximum respectively for both SP1 and SP2, because the applied shear stress for SP2 goes through zero at these points (refer to Figure 4.31). The corresponding vertical strains used to calculate the recoverable strain, ϵ_R, were taken as illustrated by Figure 2.5. M_R was subsequently calculated per cycle as defined by Equation 2.2, as illustrated for a CTX test in Figure 4.16b.

The values of M_R reported in Table 4.14 are calculated as the average over 5 cycles. Values from global and average local measurements are included for cycle 100, 500 and 1000. Table 4.15 summarises the modulus ratios of interest including MR_{PSR} and MR_s to evaluate the effect of PSR and matric suction respectively. MR_{PSR} is calculated per test as the M_R measured under cyclic triaxial conditions (SP1, no PSR) divided by M_R for SP2 conditions (including PSR), as discussed in Section 5.2.3. The effect of the degree of saturation or matric suction is evaluated using the ratio of M_R measured for a particular water content relative to M_R measured for saturated conditions (MR_s=$M_R/M_{R^{sat}}$). Results from HCA+1v1 were used to represent the saturated condition and the influence of matric suction on M_R is further discussed in Section 5.3.

The measured local and global shear strains for HCA+0v1 phase 1 (SP2) are plotted over time in Figure 4.33a (1 minute = 1 cycle). During each cycle, as the shear stress moves through zero (stresses controlled), significant strain occurred as seen in Figure 4.33b suggesting a lag in the rotation mechanism or slip of the specimen on the platen. The local circumferential strain measurements are thus important for the accurate determination of the cyclic shear modulus, especially for stiff specimens. The cyclic or resilient shear modulus, G_R, was calculated as the shear stress difference divided by the shear strain difference per cycle, i.e. the slope of the line plotted in Figure 4.33b. G_R for HCA+0v1 phase 1 is plotted in Figure 4.33c. Results are summarised in Table 4.16 for all of the HCA tests.

Fine cracking was observed during specimen preparation of HCA-3iv1 after difficulties in removing the specimen from the split mould due to expansion of the split mould inside the compaction collar during compaction. The test at w=4% was subsequently repeated (HCA-3iiv1). The local M_R measured on diametrically opposite sides in HCA-2v1 was

significantly different ($M_{R,L1}/M_{R,L2} > 1.3$). After comparison with results from CTX-2v1$_r$, the local M_R reported for HCA-2v1 is as measured on one side of the specimen only ($M_{R,L2}$) instead of the average local M_R from both sides.

Table 4.1: Particle size distribution and quantities of constituent materials for Material B (as used by Gräbe (2002))

Particle size	Sand			Silt	Clay
% by mass		73		16	11
Material	Leighton Buzzard sand fraction B	Leighton Buzzard sand fraction C	Leighton Buzzard sand fraction D	HPF4 silt	Hymod Prima clay
% by mass	47	10	10	21	13

Table 4.2: Atterberg limits of the representative railway subballast material, Material B, compared to previous results by Gräbe (2002) and Otter (2011) for the same material

Material	Plastic limit (%)	Liquid limit (%)	Plasticity Index (%)	Clay content (%)	Activity, A
Material B	14	27	13	11	1.2
Gräbe (2002)	14	28	14	11	1.3
Otter (2011)	14	29	15	11	1.4

Table 4.3: Compaction energy (kJ/m^3) for different manual compaction test methods using the 2.5 kg and 4.5 kg rammers

	TMH1 Method A7 SA [1]	BS1377-4:1990 UK [2]	ASTM D1557-07 USA [3]	AASHTO Method A USA [4]
2.5 kg rammer		596		585
4.5 kg rammer	2415	2682	2697	2697

1 Lockyer (1986)
2 British Standards Institution (2012)
3 ASTM D1557-07: (2007)

Table 4.4: Required number of blows per layer (2.5 kg rammer) to achieve the aimed dry density of 2.10 Mg/m^3 for Material B - determined by trial and error

Gravimetric water content (%)	Blows per layer	Energy input kJ/m^3
4	90	2066
5	65	1492
6	27	620
7	23	528
8	27	620

Table 4.5: Chilled mirror hygrometer test sample properties and total suction measurements. Suction measured at the compacted state unless marked as dried

Compaction grav. water content, w_i (%)	Dry density achieved Mg/m^3	Void ratio, e	Sample grav. water content, w_f (%)	Sample vol. water content, θ_{w_f} (%)	Total suction ψ (kPa)
7.94	2.119	0.246	7.60	16.10	350
			7.32	15.52	430
			7.32	15.51	310
			7.86	16.66	290
			7.94	16.82	230
7.11	2.113	0.249	7.19	15.20	230
			5.26^{dried}	11.11	1200
			3.34^{dried}	7.06	4180
			2.37^{dried}	5.00	6190
			0.96^{dried}	2.04	26130
			7.00	14.79	290
			5.64^{dried}	11.92	860
			4.78^{dried}	10.10	1700
6.06	2.111	0.251	6.37	13.45	340
			6.21	13.11	340
			6.02	12.71	290
5.01	2.086	0.266	5.09	10.61	580
			5.10	10.63	530
			4.93	10.29	430
			4.88	10.18	410
4.05	2.070	0.275	4.40	9.12	820
			4.44	9.19	820
			4.14	8.57	810

Table 4.6: Cyclic triaxial (CTX) specimen properties - initial condition

Test number	Test name	Compaction grav. water content, w_i (%)	Dry density achieved ρ_d (Mg/m^3)	Deviation from target density, (%)	Void ratio, e	Volumetric water content, θ_{wi} (%)	Degree of saturation, S_r (%)
3	CTX+0v0	7.04	2.113	0.62	0.249	14.81	74.2
4	CTX+0v0$_p$	6.88	2.146	2.19	0.230	14.79	79.1
10	CTX+0v2	7.04	2.135	1.67	0.237	15.03	78.6
17	CTX+0v1$_c$	7.04	2.142	2.00	0.232	15.08	79.9
5	CTX-1v0	5.91	2.079	-1.00	0.270	12.28	57.8
7	CTX-2v0	4.91	2.117	0.81	0.247	10.38	52.4
12	CTX-2v1$_r$	4.90	2.111	0.52	0.251	10.34	51.6
6	CTX-3v0	4.19	2.113	0.62	0.249	8.86	44.4
8	CTX-3v1	4.15	2.104	0.19	0.255	8.74	43.0
11	CTX-3v1$_r$	4.08	2.099	-0.05	0.258	8.56	41.8
9	CTX+1v1	8.02	2.095	-0.24	0.260	16.80	81.4
13	CTX+1v2$_i$	8.09	2.099	-0.05	0.257	16.97	82.9
14	CTX+1v2$_{ii}$	7.92	2.109	0.43	0.252	16.70	83.1
15	CTX+1v2$_{iii}$	8.05	2.101	0.05	0.257	16.91	82.8
16	CTX+1v2$_{iii^m}$	7.86	2.079	-1.00	0.270	16.33	76.9

Table 4.7: Cyclic triaxial (CTX) specimen properties - After testing

Test number	Test name	Total grav water content, w_f (%)	Top grav water content, w_{f_t} (%)	Mid height grav water content, w_{f_m} (%)	Bottom grav water content, w_{f_b} (%)	Dry density estimate after ρ_{dry}, (Mg/m^3)	Void ratio, e	Volumetric water content, θ_{wf} (%)	Degree of saturation, S_r (%)	Est. matric suction ψ_m (kPa)
3	CTX+0v0	7.10	-	-	-	2.178	0.226	15.47	88.4	62**
4	CTX+0v0$_p$	7.11	-	-	-	2.193	0.210	15.59	92.1	40**
10	CTX+0v2	7.03	6.85	6.83	7.02	2.181	0.224	15.33	88.1	62**
17	CTX+0v1$_c$	7.01	7.24	6.82	7.15	2.182	0.223	15.30	88.2	65**
5	CTX-1v0	5.90	5.76	5.86	5.92	2.109	0.258	12.43	61.9	298
7	CTX-2v0	5.03	4.92	4.92	4.86	2.143	0.245	10.77	57.2	452
12	CTX-2v1$_r$	5.16	4.83	5.05	4.84	2.138	0.248	11.02	58.0	424
6	CTX-3v0	4.10	-	4.07	4.01	2.130	0.245	8.73	45.2	739
8	CTX-3v1	4.08	4.05	4.10	4.11	2.121	0.229	8.66	44.1	747
11	CTX-3v1$_r$	4.01	4.02	4.04	4.02	2.132	0.252	8.55	44.4	778
9	CTX+1v1	7.97	7.81	8.08	7.61	2.171	0.229	17.3	97.5	0*
13	CTX+1v2$_i$	8.06	7.90	7.98	8.04	2.177	0.226	17.55	100	0*
14	CTX+1v2$_{ii}$	7.80	7.76	7.87	7.65	2.257	0.183	17.6	100	0*
15	CTX+1v2$_{iii}$	8.00	7.94	7.96	7.75	2.184	0.222	17.48	100	0*
16	CTX+1v2$_{iii^m}$	7.82	7.82	7.68	7.56	2.161	0.181	16.89	93.0	0*

* Assumed saturated, zero matric suction
** Reduced to reflect wetting due to densification

Table 4.8: CTX test loading sequences based on the NCHRP Project 1-28A granular subgrade material test plan

Loading sequence	Confining pressure, p_o (kPa)	Contact stress, q_{min} (kPa)	Cyclic stress, q_{cyc} (kPa)	Maximum stress q_{max} (kPa)	Number of cycles, N	Applied stress ratio q_{cyc}/p_o
1	15	3	7.5	10.5	100	0.5
2	30	6	15	21	100	0.5
3	40	8	20	28	100	0.5
4	55	11	27.5	38.5	100	0.5
5	85	17	42.5	59.5	100	0.5
6	15	3	15	18	100	1.0
7	30	6	30	36	100	1.0
8	40	8	40	48	100	1.0
9	55	11	55	66	100	1.0
10	85	17	85	102	100	1.0
11	15	3	30	33	100	2.0
12	30	6	60	66	100	2.0
13	40	8	80	88	100	2.0
14	55	11	110	121	100	2.0
15	85	17	170	187	100	2.0
16	15	3	45	48	100	3.0
17	30	6	90	96	100	3.0
18	40	8	120	128	100	3.0
19	55	11	165	176	100	3.0
20	85	17	255	272	100	3.0

Table 4.9: CTX test variants

Test variant	Test sequence order	Additional information
v0	sequence 1-20	+Δp=5min; -Δp=10min
v1	sequence 1-20	Δ p=2 kPa/min thus -Δ p=35min
v2	p=15kPa (1,6,11,16); p=30kPa (2,7,12,17); p=40kPa (3,8,13,18); p=50kPa (4,9,14,19); p=85kPa (5,10,15,20)	Δ p=2 kPa/min

Table 4.10: Various HCA specimen dimensions reported in the literature

Authors	Outer diameter, mm	Inner diameter, mm	Height, mm
Hight et al. (1983)	254	203	254
Gräbe (2002)	100	60	200
Nishimura et al. (2007)	100	60	200
	70	30	170-190
Jafarian et al. (2012)	50	30	180

Table 4.11: Hollow cylinder (HCA) specimen properties - initial condition

Test number	Test name	Compaction grav. water content, w_i (%)	Dry density achieved ρ_{dry} (Mg/m^3)	Deviation from target density, (%)	Void ratio, e	Volumetric water content, θ_{wi} (%)	Degree of saturation, S_r (%)	Air voids, A (%)
8	HCA+0v1	6.97	2.140	1.89	0.234	14.92	78.7	4.0
9	HCA+0v2	7.03	2.130	1.45	0.239	14.98	77.6	4.3
5	HCA-1v1	6.13	2.086	-0.66	0.265	12.80	61.0	8.2
3	HCA-1.7v1	5.31	2.117	0.83	0.247	11.25	56.8	8.5
11	HCA-2v1	5.01	2.126	1.26	0.242	10.66	54.8	8.8
6	HCA-3iv1	4.07	2.109	0.41	0.252	8.58	42.6	11.5
10	HCA-3iiv1	4.10	2.123	1.10	0.243	8.71	44.5	10.9
7	HCA+1v1	8.04	2.116	0.78	0.247	17.01	85.8	2.8

Table 4.12: Hollow cylinder (HCA) specimen properties - After testing

Test number	Test name	Total grav water content, w_f (%)	Top grav water content, w_{f_t} (%)	Mid height grav water content, w_{f_m} (%)	Bottom grav water content, w_{f_b} (%)	Dry density estimate after ρ_{dry}, (Mg/m^3)	Void ratio, e	Volumetric water content, θ_{wf} (%)	Degree of saturation, S_r (%)	Est. matric suction ψ_m (kPa)
8	HCA+0v1	7.04	7.27, 7.31	6.94, 6.98	6.91, 6.95	2.149	0.210	15.1	81.5	62**
9	HCA+0v2	6.98	6.78, 6.82	6.74, 6.89	6.82, 6.83	2.212	0.194	15.4	95.3	40**
5	HCA-1v1	5.82	5.73, 5.74	5.77, 5.76	5.91, 6.00	2.135	0.244	12.4	65.0	318
3	HCA-1.7v1	-	-	-	-	2.195	0.204	11.6	68.8	394
11	HCA-2v1	4.80	4.77, 4.59	5.03, 4.67	4.64, 4.67	2.120	0.223	10.2	51.6	495
6	HCA-3iv1	4.53	4.87, 4.11	4.16, 4.13	5.32, 5.50	2.120	0.241	9.6	48.7	722
10	HCA-3iiv1	4.14	4.20, -	3.96, -	4.22, -	2.135	0.237	8.8	46.2	735
7	HCA+1v1	8.08	8.26, 8.41	7.90, 7.86	8.11, 8.34	2.278	0.195	18.4	97.8	0*

* Assumed saturated, zero matric suction
** Reduced to reflect wetting due to densification

Table 4.13: HCA testing summary

Test number	Test name	Confining pressure	Test Phase	Stress path	No. cycles
8	HCA+0v1	30	1	SP2	500
			2	SP1	1000
			3	SP2	500
9	HCA+0v2	30	1	SP1	500
			2	SP2	1000
			3	SP1	500
5	HCA-1v1	30	1	SP2	500
			2	SP1	1000
			3	SP2	500
3	HCA-1.7v1	30	1	SP2	500
			2	SP1	540*
11	HCA-2v1	30	1	SP2	500
			2	SP1	1000
			3	SP2	120*
6	HCA-3iv1	30	1	SP2	500
			2	SP1	1000
			3	SP2	500
10	HCA-3iiv1	30	1	SP2	500
			2	SP1	1000
			3	SP2	500
7	HCA+1v1	30	1	SP2	500
			2	SP1	1000
			3	SP2	500

* Interrupted testing

Table 4.14: HCA global and average local resilient modulus values for SP1 and SP2 cycles 100, 500 and 1000 in MPa

Test name	Global M_R						Average Local M_R					
	SP1 c100	SP1 c500	SP1 c1000	SP2 c100	SP2 c500	SP2 c1000	SP1 c100	SP1 c500	SP1 c1000	SP2 c100	SP2 c500	SP2 c1000
HCA+0v1	103.2	105.6	109.4	85.4	91.3	93.5	138.4	144.1	150.5	117.0	126.0	128.1
HCA+0v2	90.0	96.9	100.8	87.6	89.2	90.4	111.2	124.0	128.0	110.2	110.3	111.3
HCA-1v1	127.9	134.9	140.5	113.8	120.5	128.0	234.3	262.3	268.3	206.5	225.4	248.1
HCA-1.7v1	194.2	199.9	-	182.8	182.3	-	357.1	385.6	-	341.4	350.5	-
HCA-2v1	221.5	230.0	234.1	194.0	198.4	208.7*	467.0	499.0	526.9	475.2	499.5	502.0*
HCA-3iv1	122.5	125.5	127.8	109.3	112.5	115.4	386.4	387.9	418.7	330.5	337.5	321.9
HCA-3iiv1	214.6	224.7	225.9	181.5	188.2	206.6	461.6	480.8	503.5	491.5	500.3	477.0
HCA+1v1	75.6	81.1	83.0	51.0	64.5	70.2	78.0	85.5	83.0	48.8	66.1	70.2
Grabe**	62.2	70.3	65.2	52.9	50.5	50.8	65.7	75.2	69.2	54.8	53.2	53.8

* cycle 600
**Gräbe (2002)

Table 4.15: Resilient modulus ratios from HCA results: MR_{PSR}, MR_s and M_R/G_R

Test name	$MR_{PSR} = M_{R^{SP1}}/M_{R^{SP2}}$			$MR_s = M_R/M_{R^{sat}}$ (SP1)			$M_{R^{SP2}}/G_R$		
	c100	c500	c1000	c100	c500	c1000	c100	c500	c1000
HCA+0v1	1.18	1.14	1.18	1.77	1.69	1.81	4.83	4.60	4.54
HCA+0v2	1.01	1.12	1.15	1.43	1.45	1.54	4.84	4.53	4.54
HCA-1v1	1.13	1.16	1.08	3.00	3.07	3.23	4.64	3.99	3.90
HCA-1.7v1	1.05	1.10	-	4.58	4.51	-	-	-	-
HCA-2v1	0.98	1.00	1.05	5.99	5.84	6.35	5.46	3.81	4.39
HCA-3iv1	1.17	1.15	1.30	4.96	4.54	5.04	2.06	2.10	2.46
HCA-3iiv1	0.94	0.96	1.06	5.92	5.62	6.07	3.55	3.29	
HCA+1v1	1.60	1.29	1.18	1.00	1.00	1.00	4.99	4.30	3.82
Grabe**	1.20	1.41	1.29	0.84	0.88	0.83	-	-	-

**Gräbe (2002)

Table 4.16: Adjusted global resilient modulus and local resilient modulus measured in the HCA in MPa

Test	Test name	Adjusted G_{R^G} c500	SP2 G_{R^L} c100	SP2 G_{R^L} c500	SP2 G_{R^L} c1000
8	HCA+0v1	11.0	24.2	27.4	28.2
9	HCA+0v2	12.3	22.8	24.3	24.5
5	HCA-1v1*	14.3	44.5	56.4	63.6
3	HCA-1.7v1	25.7	-	-	-
11	HCA-2v1	16.5	87.0	131.1	114.4
6	HCA-3iv1	12.6	160.7	161.0	131.1
10	HCA-3iiv1*	17.8	138.5	152.0	-
7	HCA+1v1	9.3	9.8	15.4	18.4
	Grabe**	6.1	-	-	-

* Local circumferential strain over top 2/3 specimen height
**Gräbe (2002)

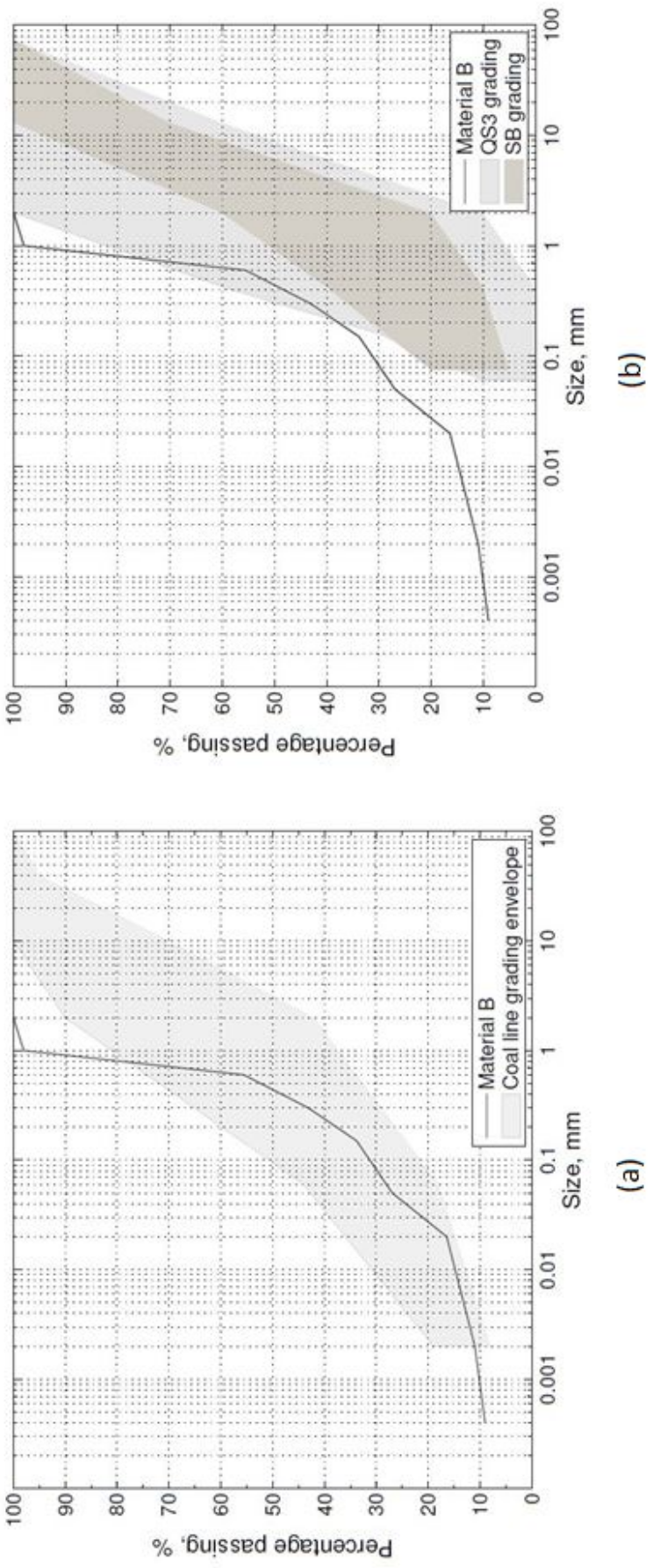

Figure 4.1: Particle size grading by percentage of mass (a) Material B particle size distribution and Coal Line material grading envelope (data from Gräbe (2002)); (b) Design grading envelopes - subballast material (SB) (Spoornet, 2006) and soil quality class 3 material (QS3) (International Union of Railways, 2008)

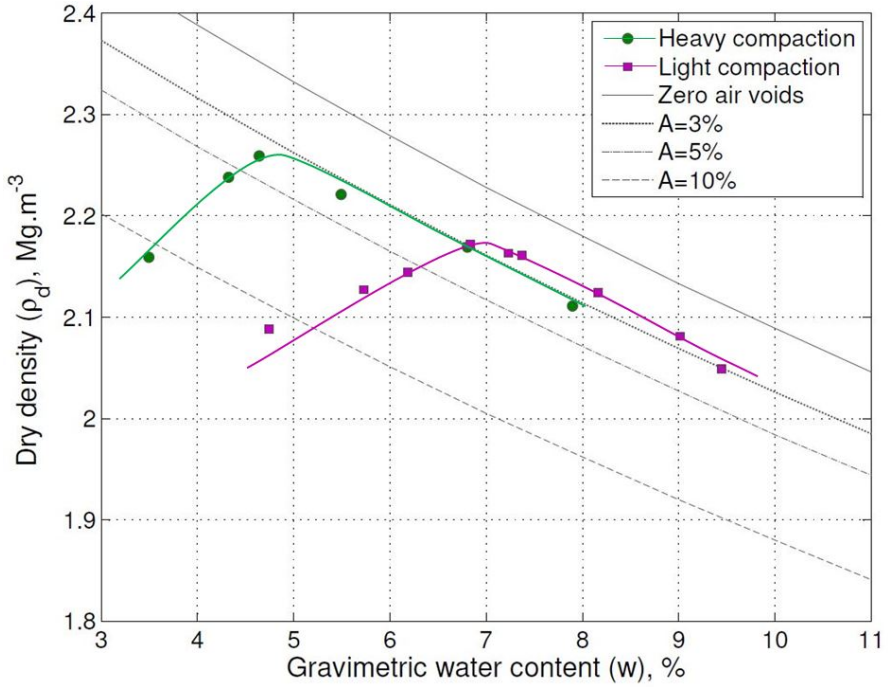

Figure 4.2: BS1377-4:1990 heavy (4.5 kg/ 27 blows/ 5 layers) and light compaction curves (2.5 kg/ 27 blows/ 3 layers) for Material B with lines of constant air void ratio (A) indicated

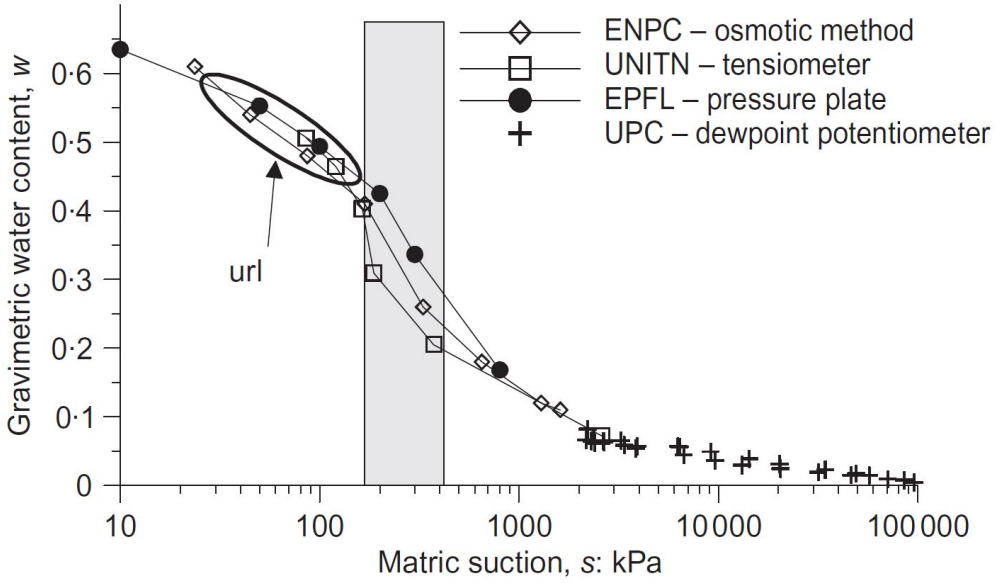

Figure 4.3: Suction measurement results by various research teams using pressure plate, osmotic method, high-capacity tensiometer, and chilled-mirror dewpoint techniques, in terms of water content presented by Tarantino et al. (2011) showing the unloading reloading line (url) and intermediate suction range

ENPC: *É*cole des Ponts ParisTech, France.

UNITN: Universit*à* di Trento, Italy.

EPFL: *É*cole Polytechnique F*é*d*é*rale de Lausanne, Switzerland.

UPC: Universutat Polit*é*cnica da Catalunya, Spain.

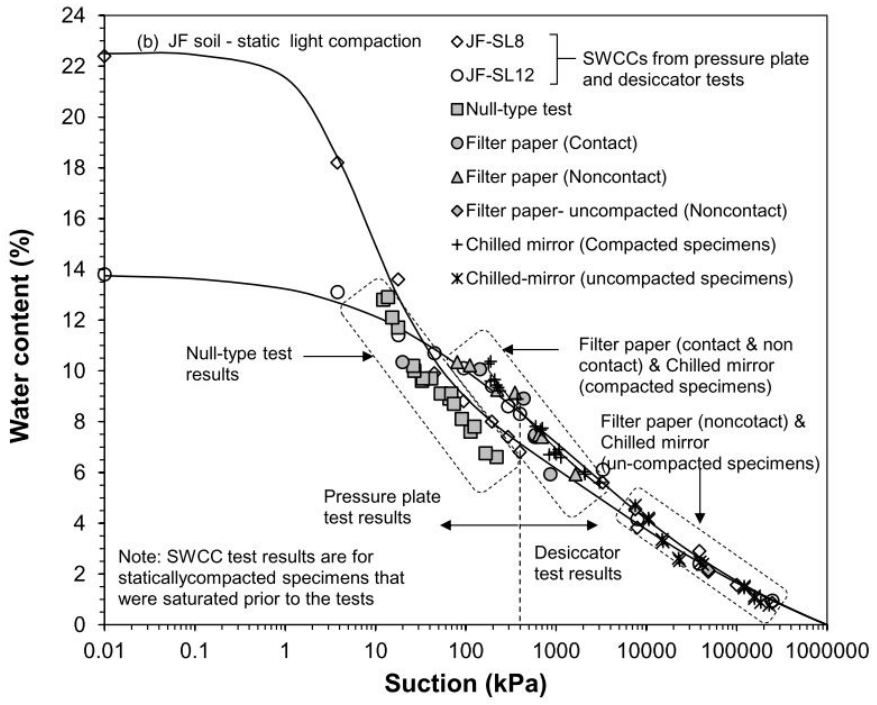

Figure 4.4: Comparison of measured suctions by null-type, filter paper, and chilled-mirror dew-point tests with SWRC/SWCC (pressure plate) for statically compacted JF (silty sand) soil (equivalent BS light compaction, maximum dry density ρ_d=1.99 Mg/m^3)

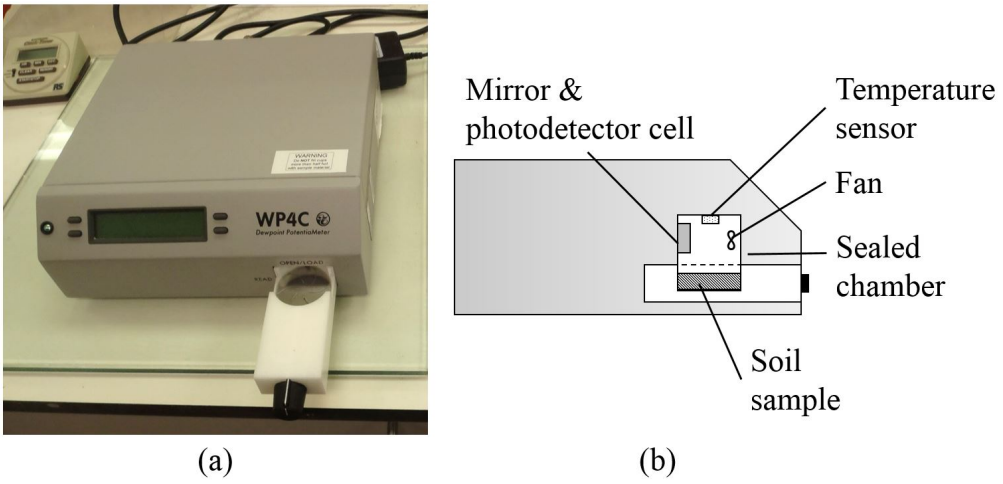

Figure 4.5: (a) WP4C Dewpoint PotentiaMeter at Cardiff University and (b) a diagrammatic view of the Chilled-Mirror Dew-Point Potentiometer

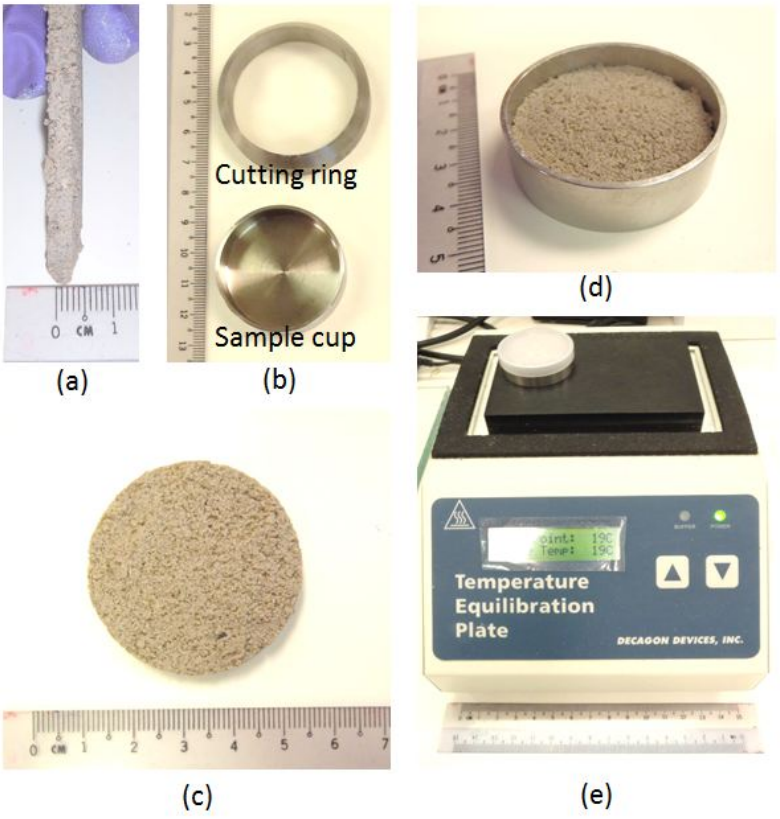

Figure 4.6: Preparation of a chilled mirror sample (a) Trimming to a suitable thickness ($\leq 5\ mm$), (b) Sharp edge cutting ring for trimming to sample cup diameter, (c) Trimmed sample, (d) Sample lightly pressed into sample cup, (e) Sealed sample placed on a temperature equilibration plate

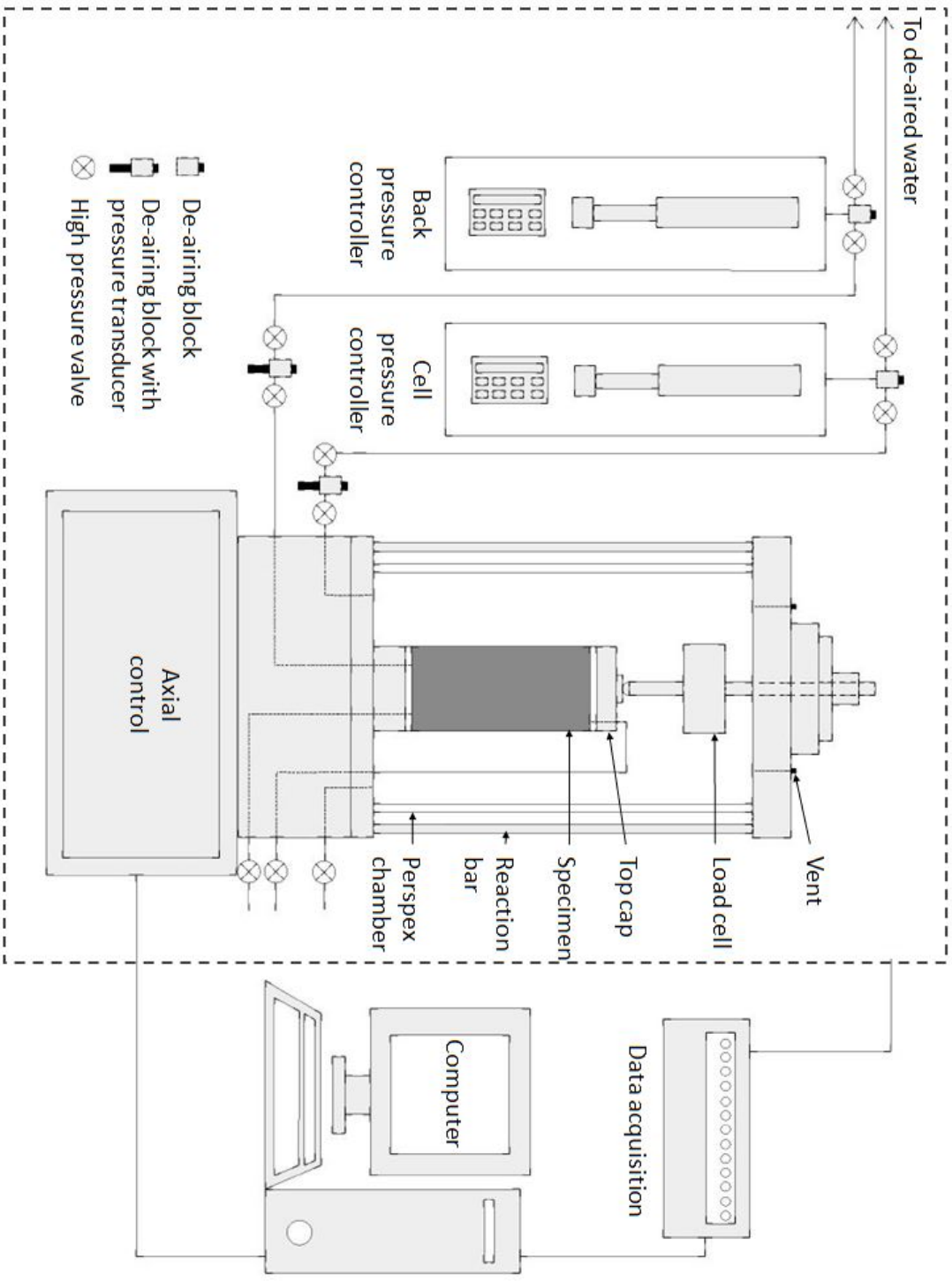

Figure 4.7: Schematic presentation of the cyclic triaxial apparatus (GDS DYNTTS)

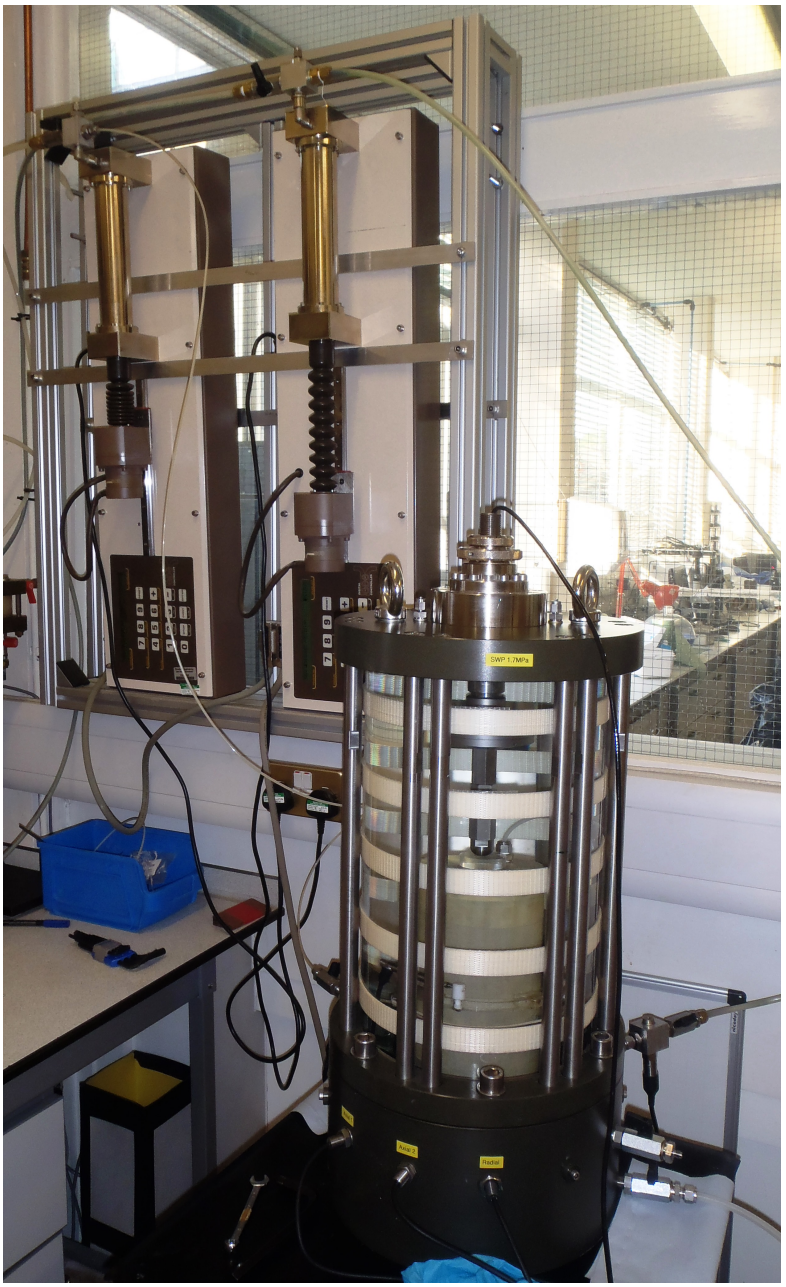

Figure 4.8: A picture of the GDS Advanced Triaxial Testing System (DYNTTS) also referred to as the cyclic triaxial apparatus, CTX

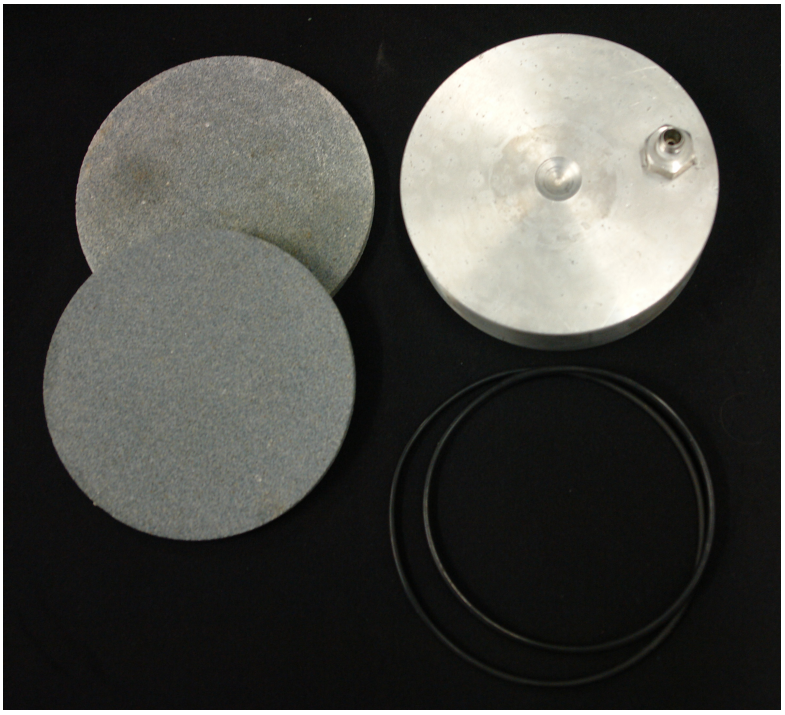

Figure 4.9: A picture of the porous stones, top cap and O-rings used in the CTX

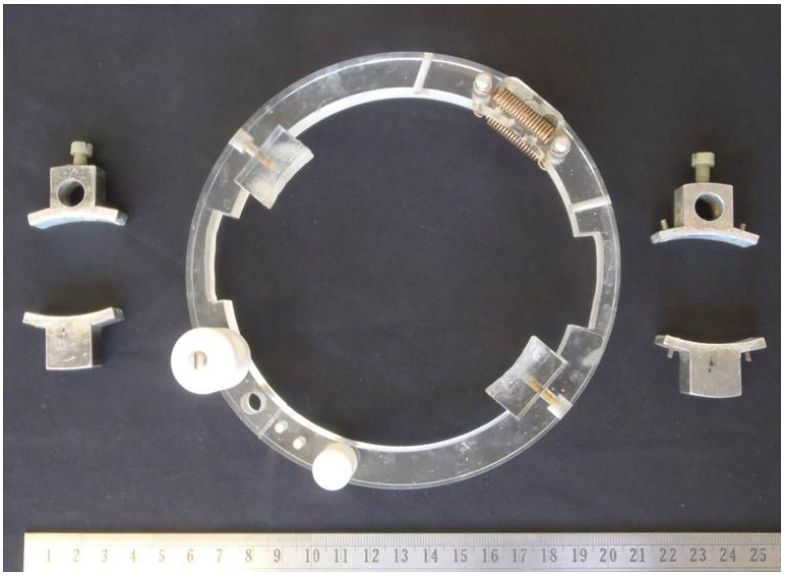

Figure 4.10: A picture showing the two sets of axial LVDT brackets and the radial caliper used in CTX testing

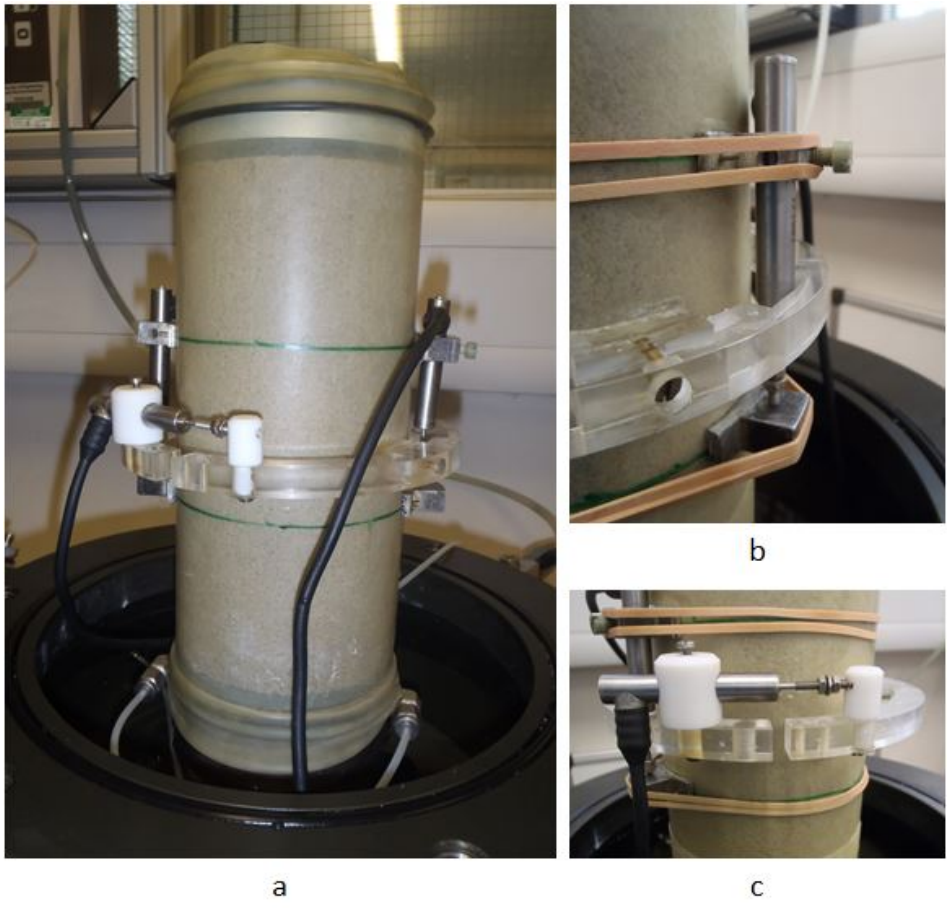

Figure 4.11: Picture of (a) the local instrumentation fitted to the CTX specimen, (b) variation including rubber bands, and (c) the radial LVDT fitted

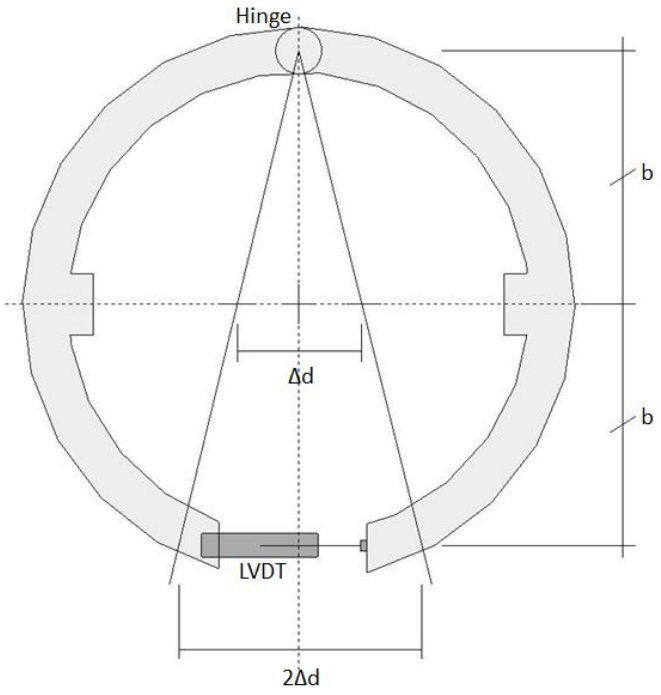

Figure 4.12: Diagram of a radial caliper mechanism used to measure change in specimen diameter at mid-height

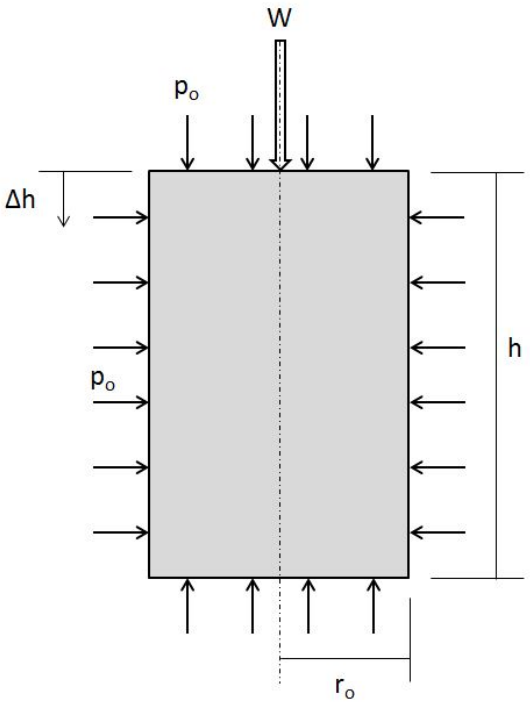

Figure 4.13: Loading on a triaxial specimen

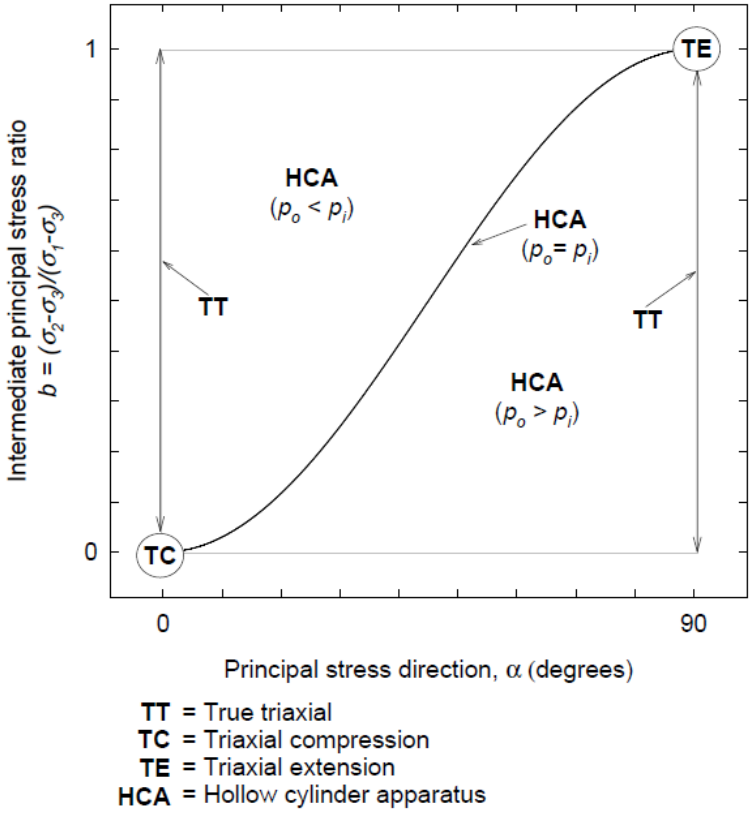

Figure 4.14: Summary of laboratory testing capabilities (redrawn by Gräbe (2002))

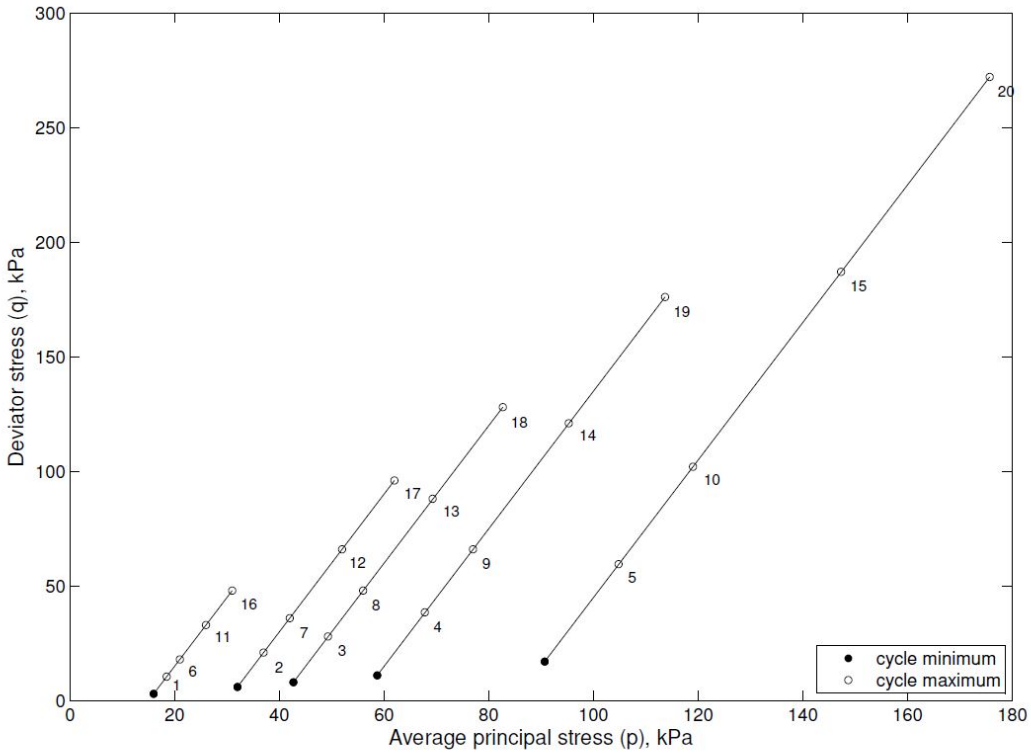

Figure 4.15: Stress paths for each of the CTX test loading sequences used and numbered accordingly (See Table 4.8). The stress cycles between the minimum and the maximum points indicated

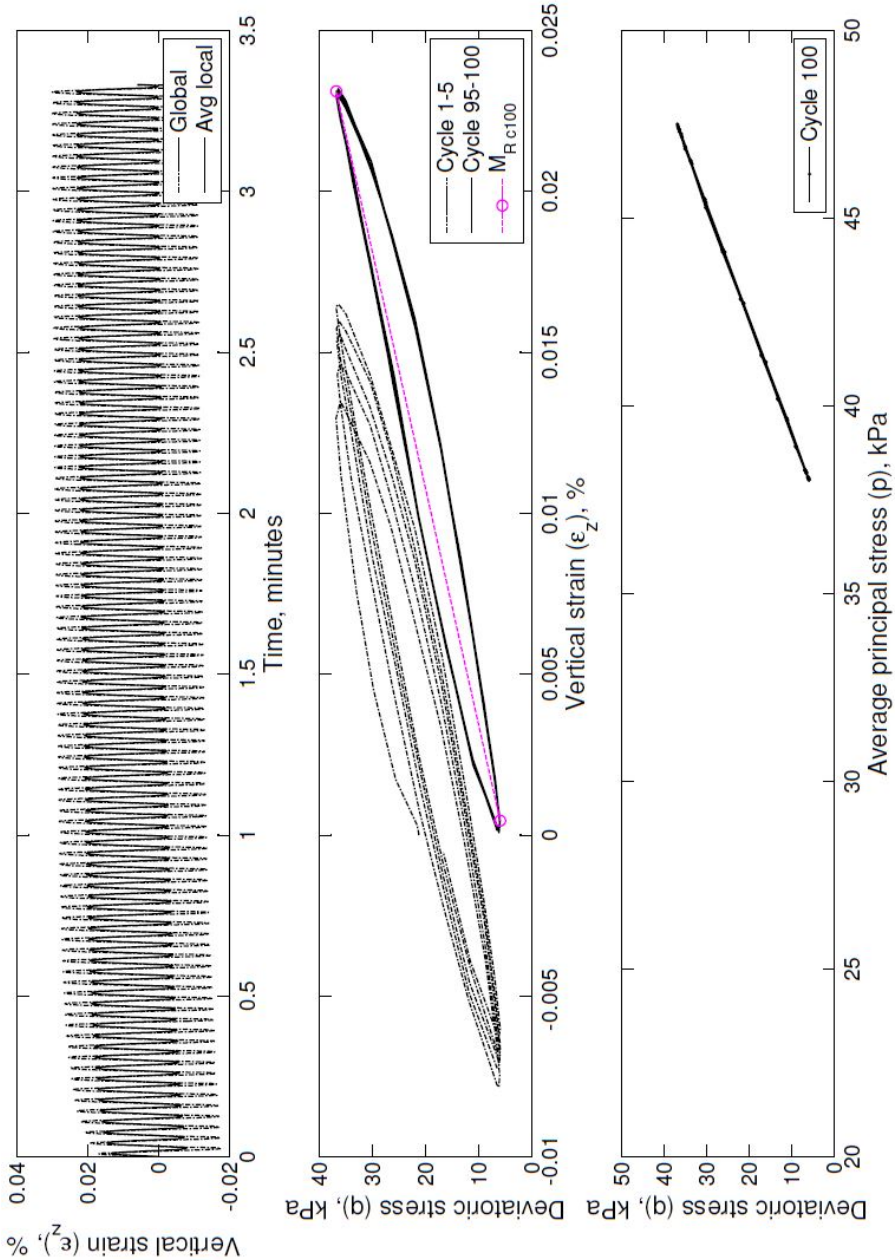

Figure 4.16: Typical CTX results taken from CTX+0v0 sequence 7 (a) Development of vertical strain, ϵ_z with time (30 cycles per minute), (b) Deviator stress, q, versus average local vertical strain for selected cycles, and (c) Net normal stresses: Deviator stress, q, versus average principal stress, p

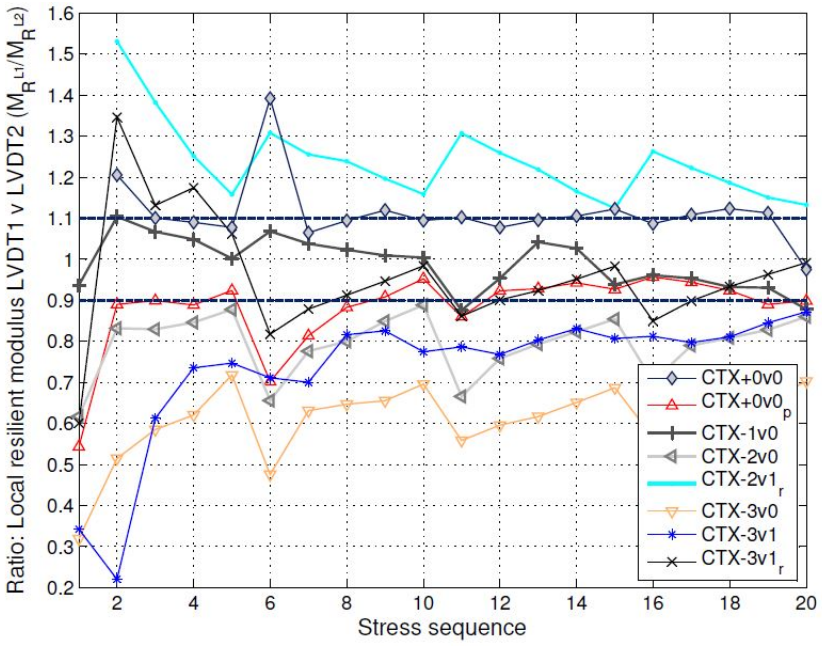

Figure 4.17: Ratio of local resilient modulus measured on diametrically opposite sides (M_R^{L1}/M_R^{L2}) using LVDT1 and LVDT2 all CTX tests

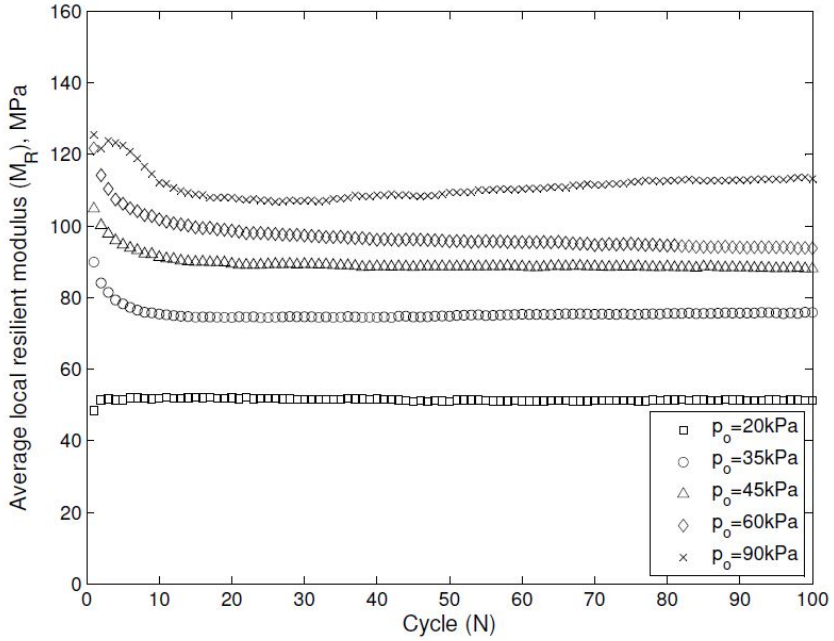

Figure 4.18: Average local resilient modulus, M_R, per cycle, N, for CTX+0v0 sequence 6-10 with applied stress ratio $q_{cyc}/p_o = 1.0$

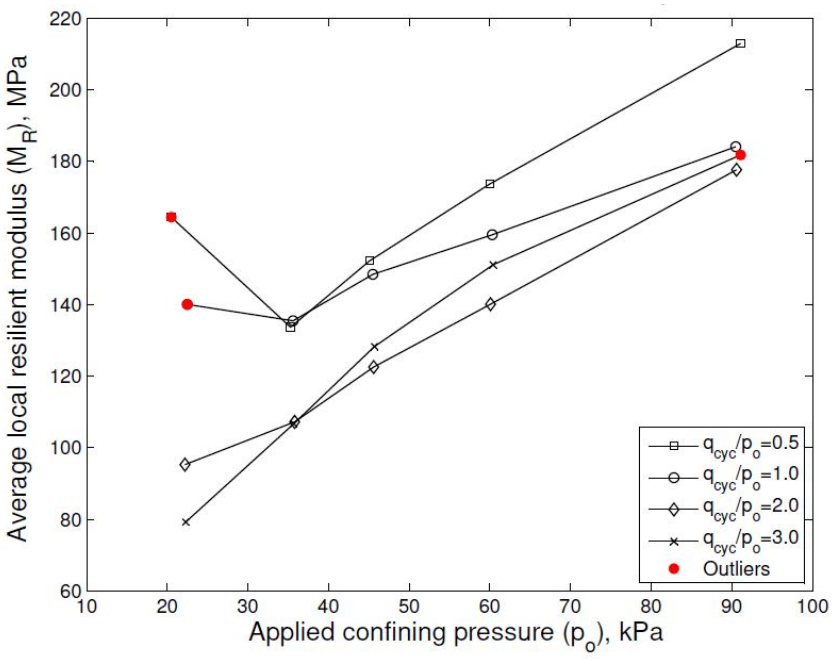

Figure 4.19: Average local resilient modulus, M_R, relative to applied confining pressure, p_o for the range of applied stress ratios (CTX+0v0)

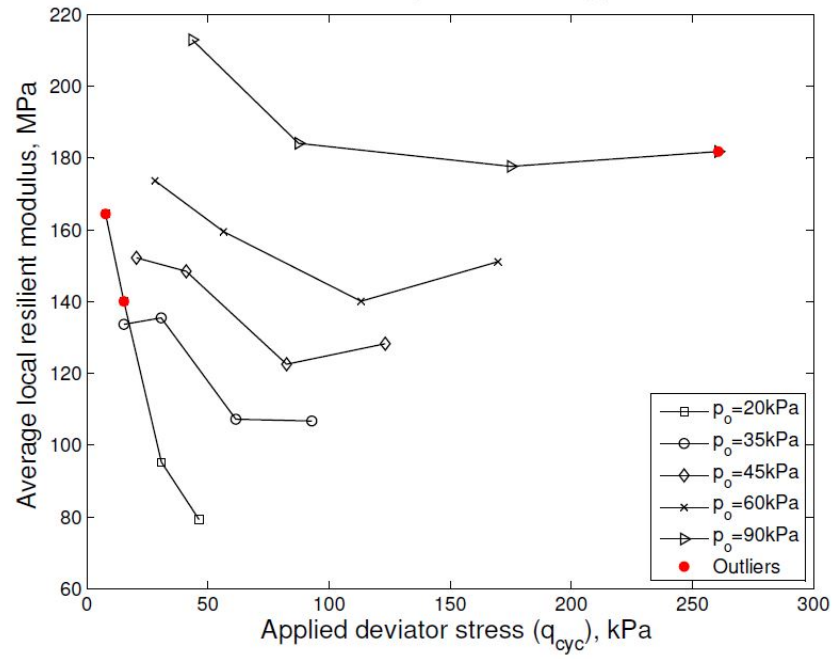

Figure 4.20: Average local resilient modulus, M_R, relative to applied cyclic deviator stress q_{cyc} for the range of confining pressures tested (CTX+0v0)

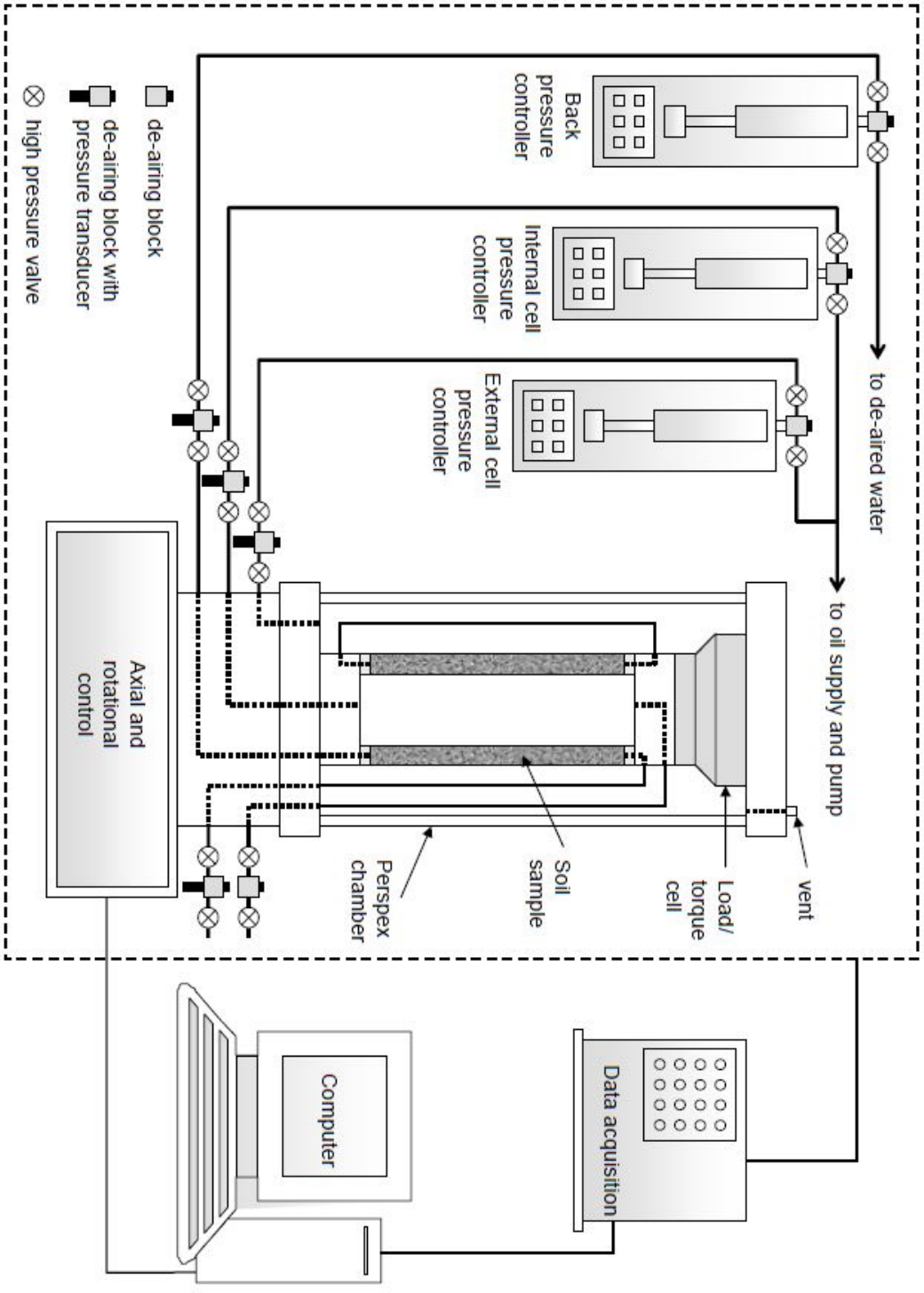

Figure 4.21: Schematic presentation of the Hollow Cylinder Apparatus drawn by Gräbe (2002)

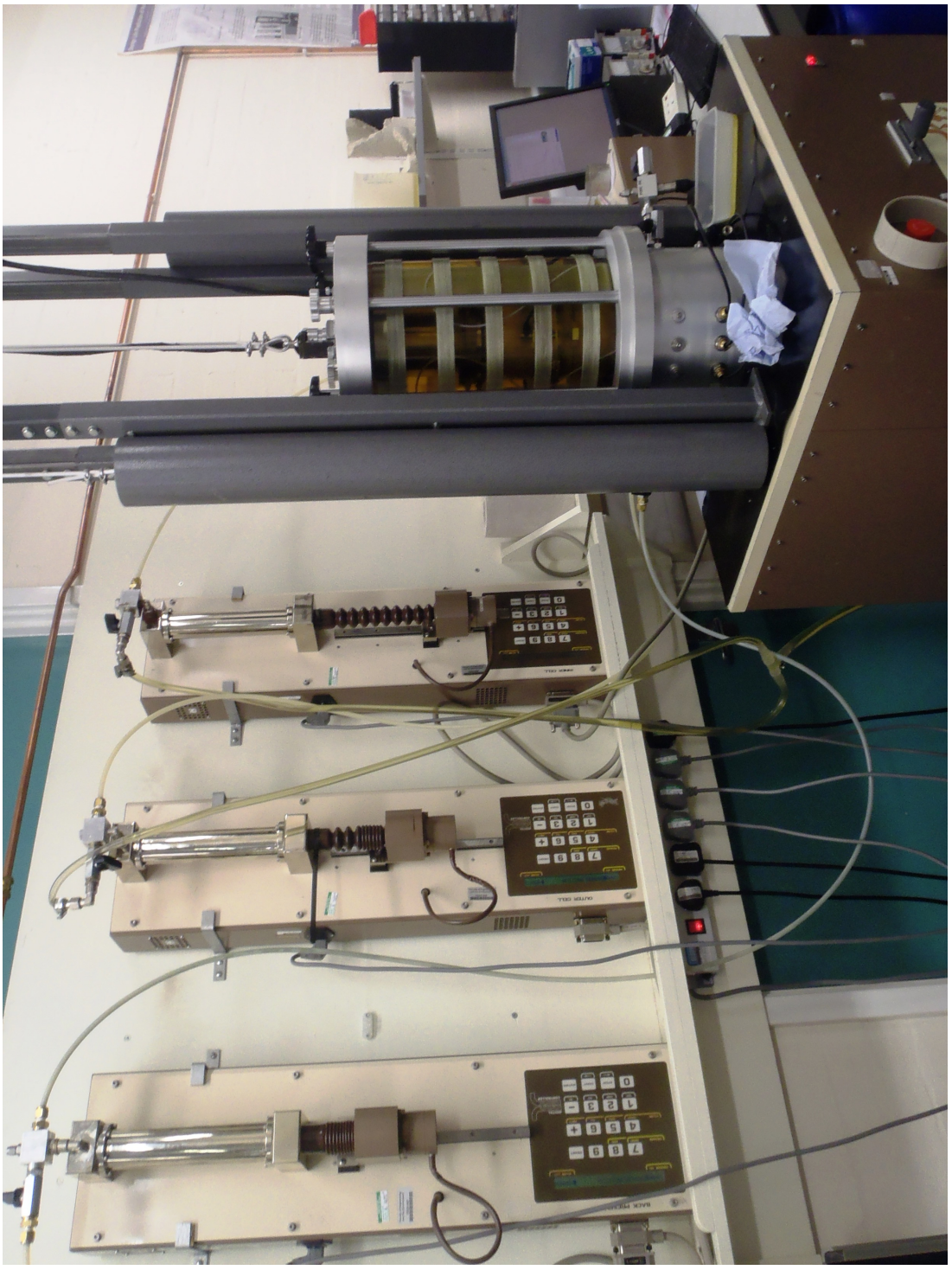

Figure 4.22: A picture of the GDS Small Strain Hollow Cylinder Apparatus

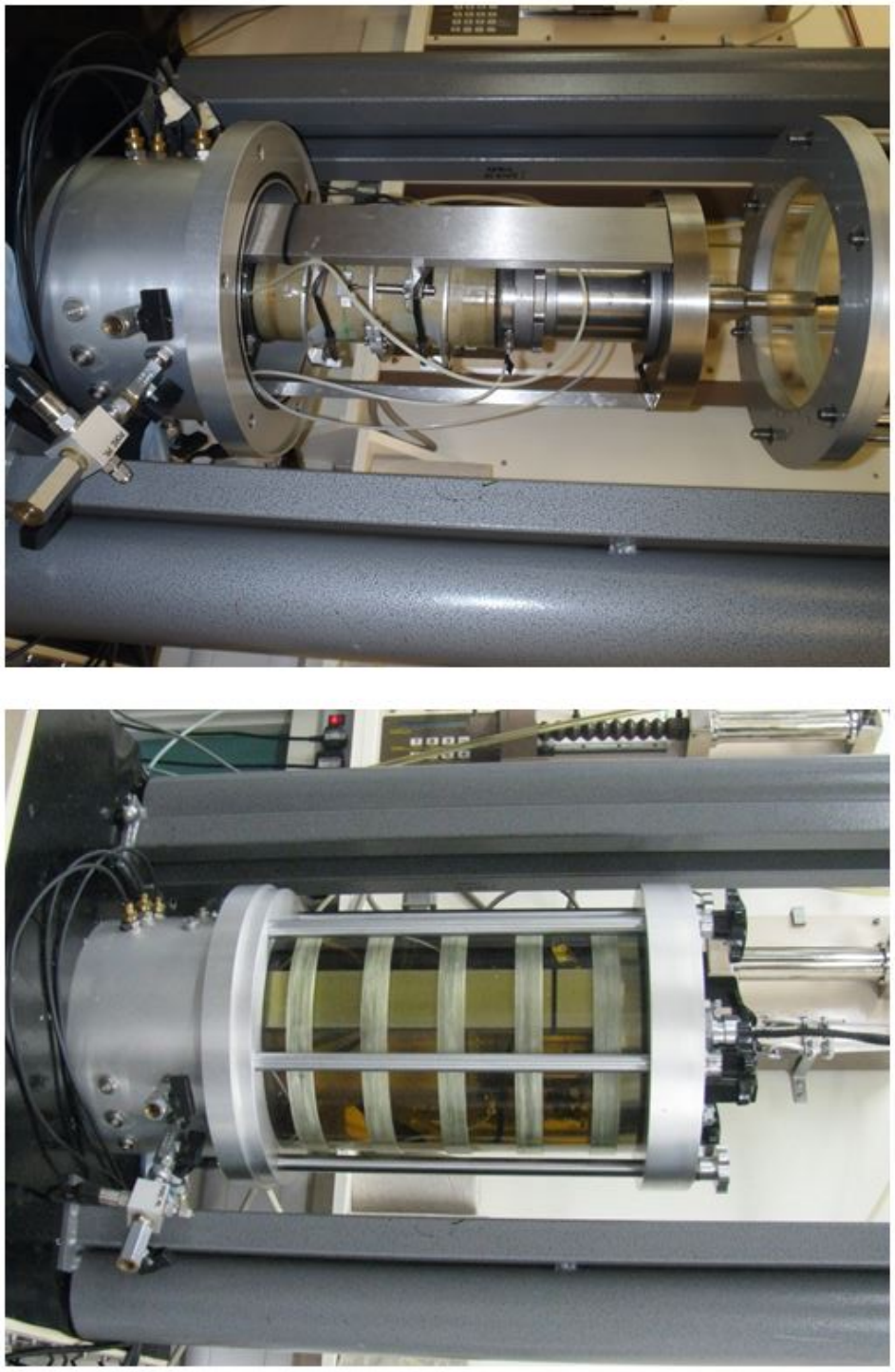

Figure 4.23: A closer view of the HCA apparatus (a) open showing the internal reaction bars and (b) closed

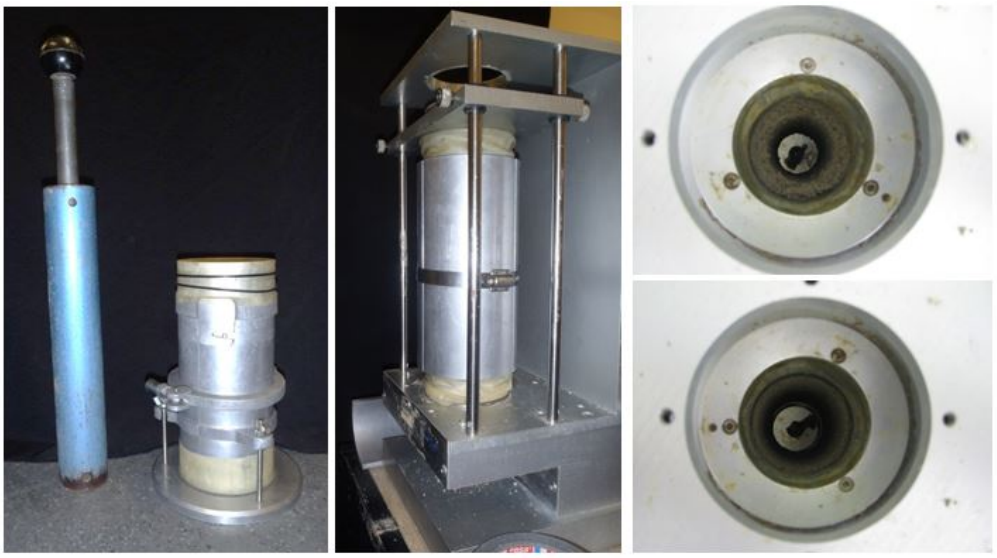

Figure 4.24: HCA sample preparation (a) compaction mould and standard 2.5 kg compaction rammer, (b) wood drill with sample contained in a split mould (c) incremental drilling of inner diameter

Figure 4.25: Cuts made into the top surface (similar for the bottom) of the HCA specimen at the positions of the porous disc fins

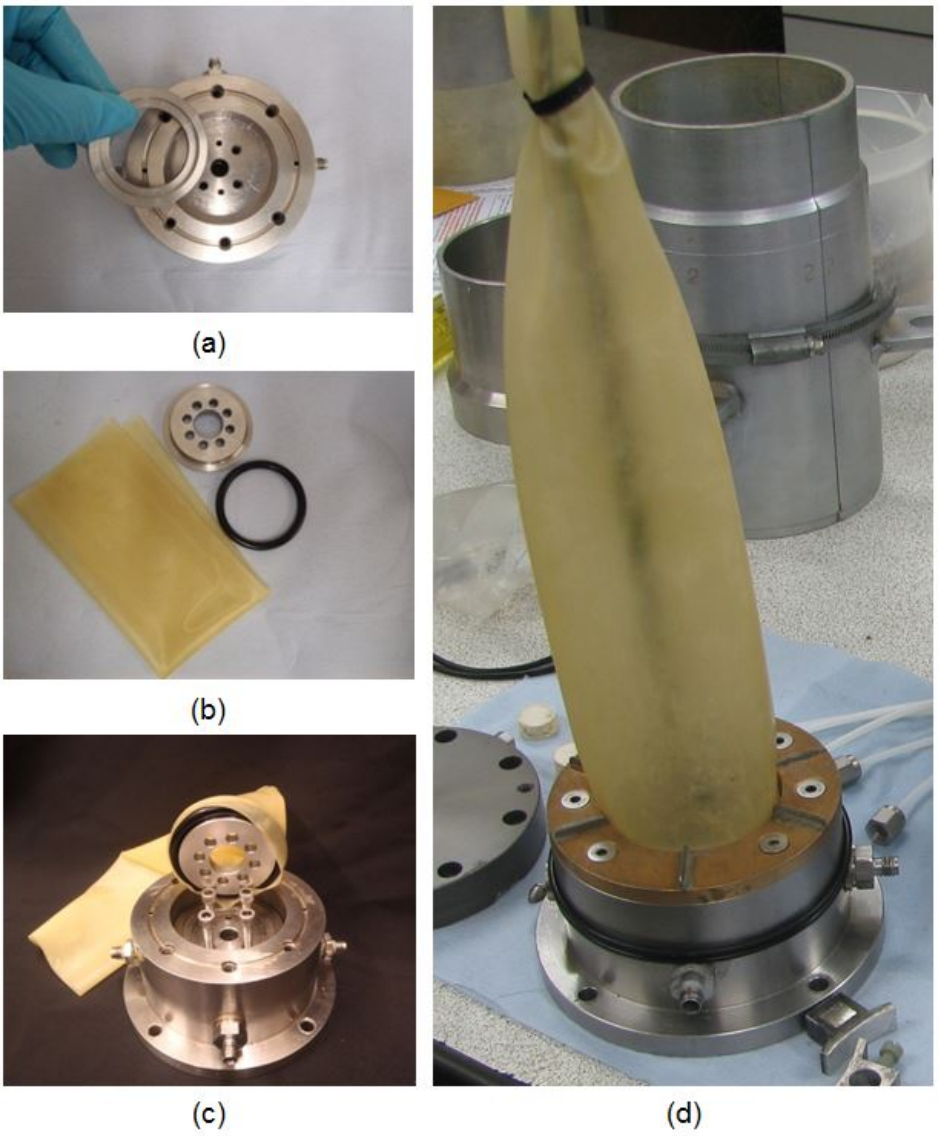

Figure 4.26: HCA base pedestal preparation (a) lower membrane holder placed into base pedestal, (b) upper membrane holder, O-ring and inner membrane, (c) fitting of inner membrane, (d) prepared base pedestal with porous disc

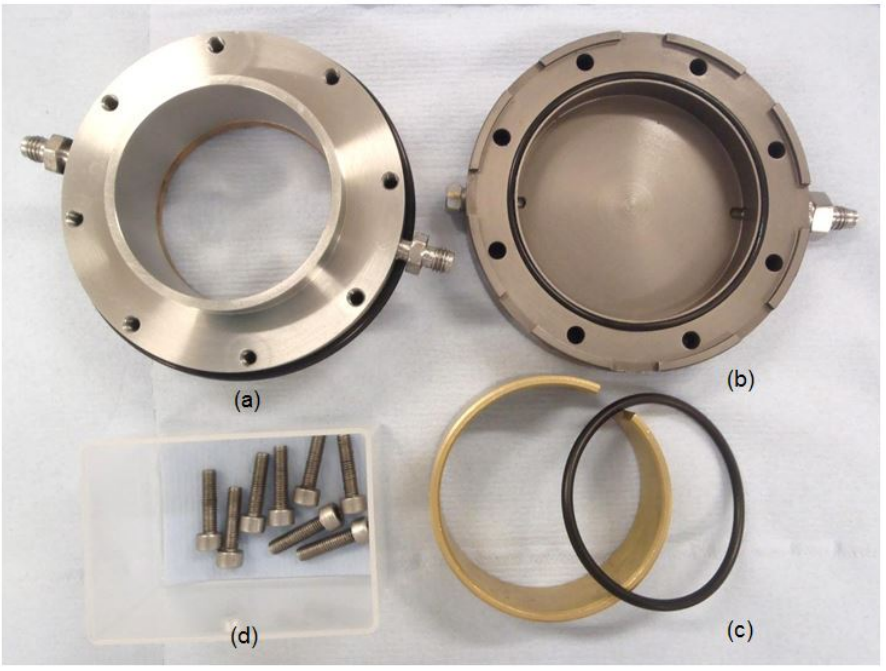

Figure 4.27: HCA top platen preparation (a) lower top cap fitted with finned porous disc and two 100 mm O-rings (for the outer membrane), (b) lower top cap with greased O-ring seal, (c) 60 mm O-ring with O-ring stretcher (for the inner membrane), (d) bolts to connect lower and upper top cap

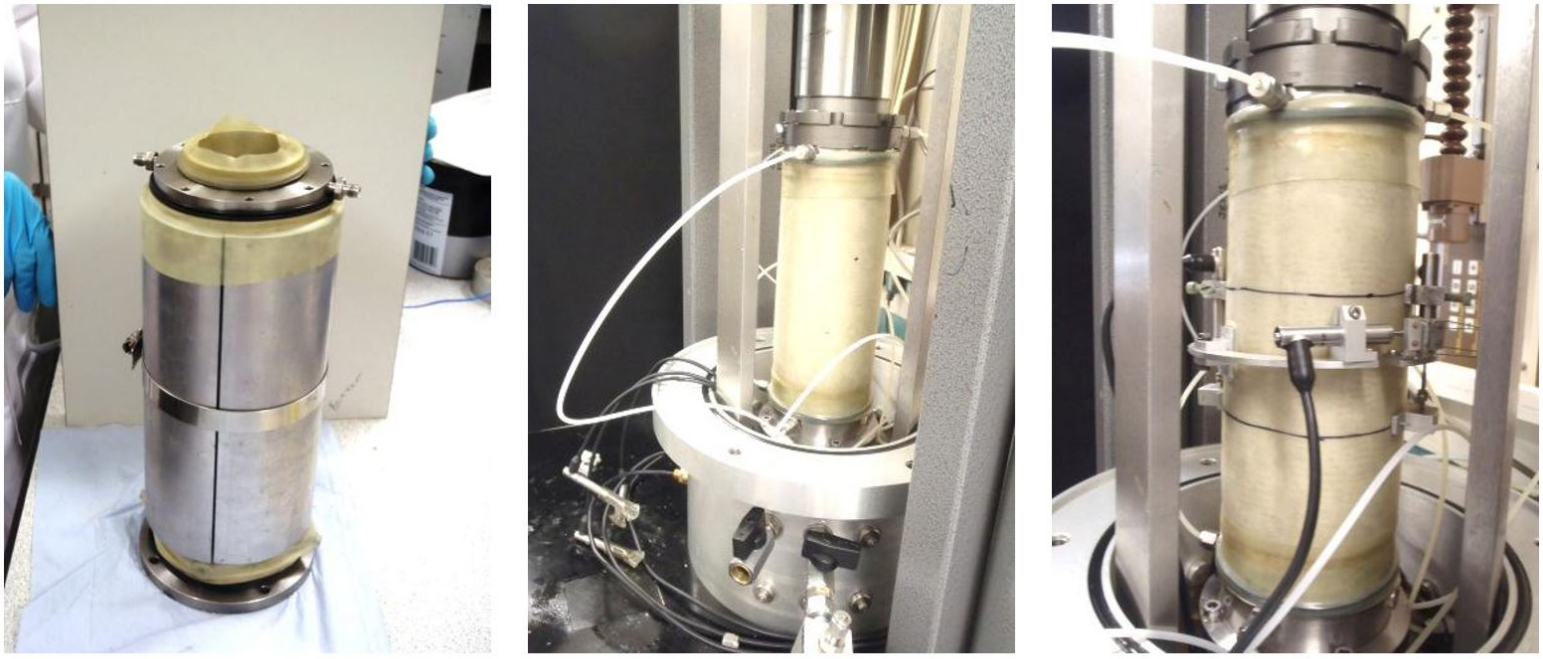

Figure 4.28: HCA specimen set-up (a) specimen, base pedestal and top cap enclosed by a split mould, (b) specimen docked in the HCA, (c) radial caliper and LVDT fitted

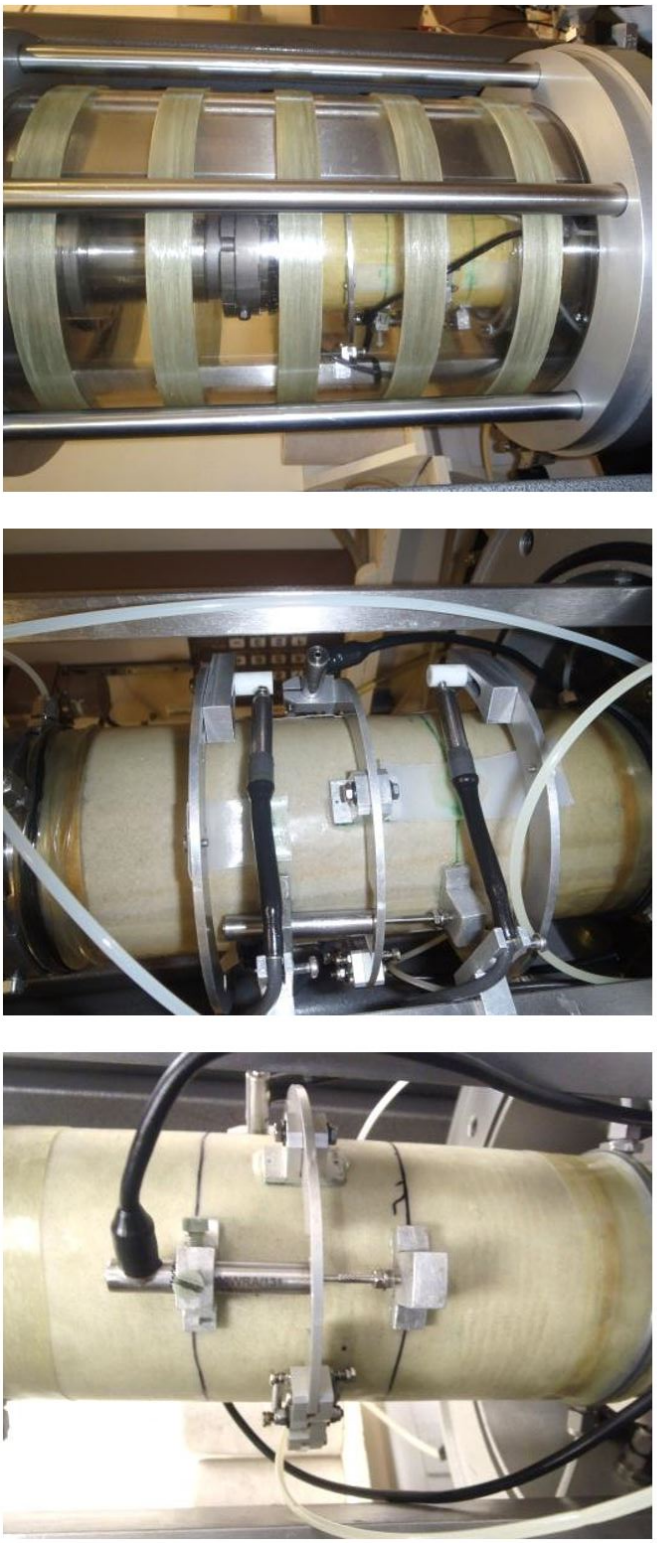

(c)

(b)

(a)

Figure 4.29: HCA specimen set-up (continued) (a) local axial displacement LVDT fitted, (b) local circumferential LVDTs fitted, and (c) cell closed and chambers filled with silicon oil

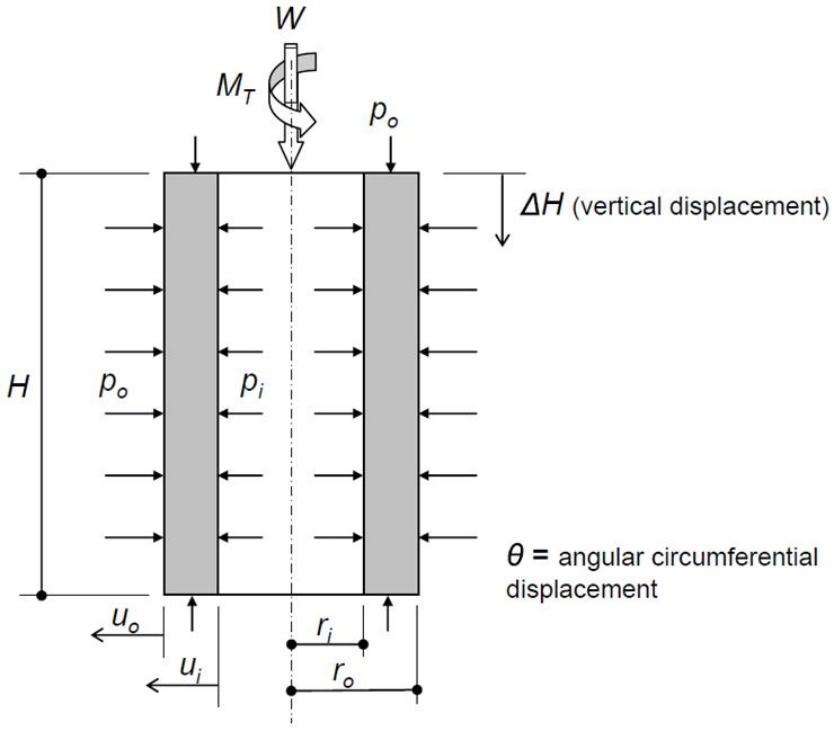

Figure 4.30: Loading on a hollow, cylindrical specimen (redrawn by Gräbe (2002) after Hight et al. (1983))

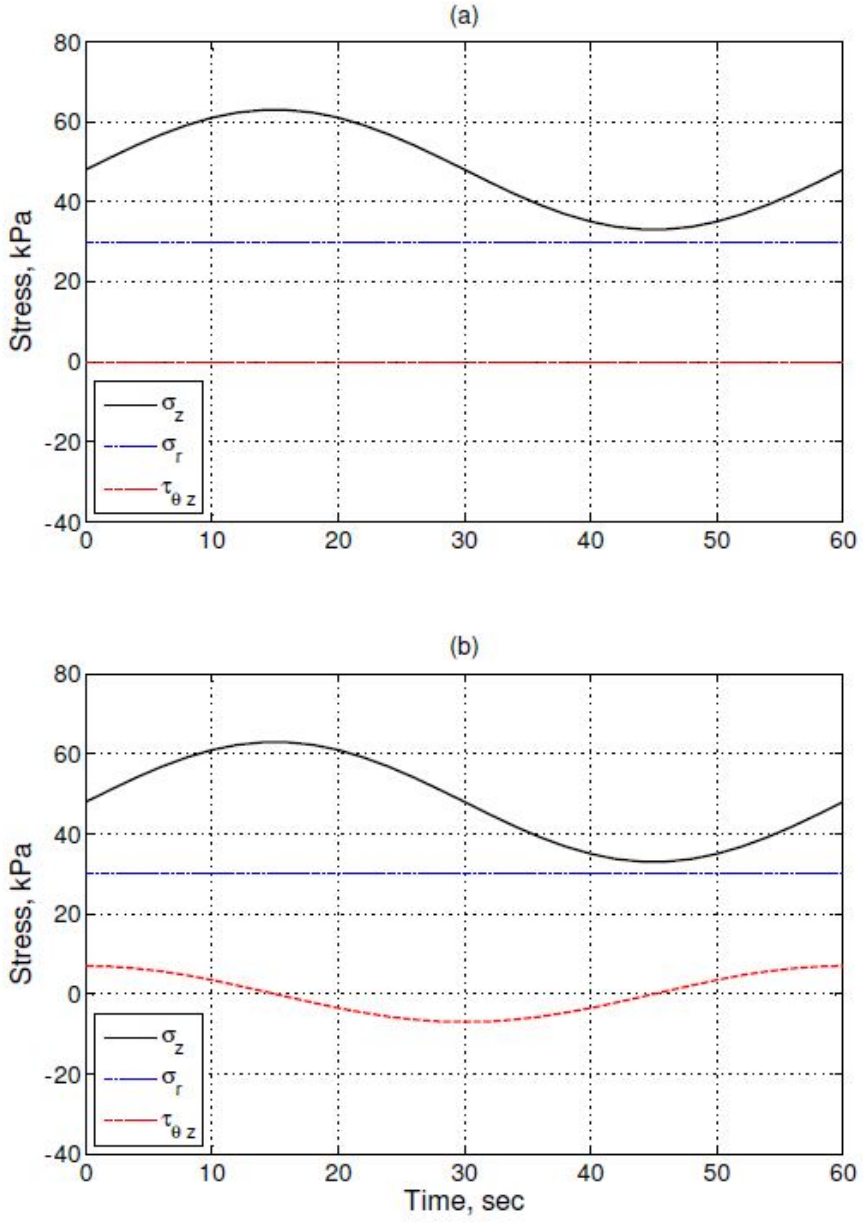

Figure 4.31: Cyclic stress paths in terms of the applied stresses σ_z, $\sigma_r = \sigma_\theta$ and $\tau_{\theta,z}$ (redrawn from Gräbe (2002)) (a) SP1 without PSR and (b) SP2 with PSR

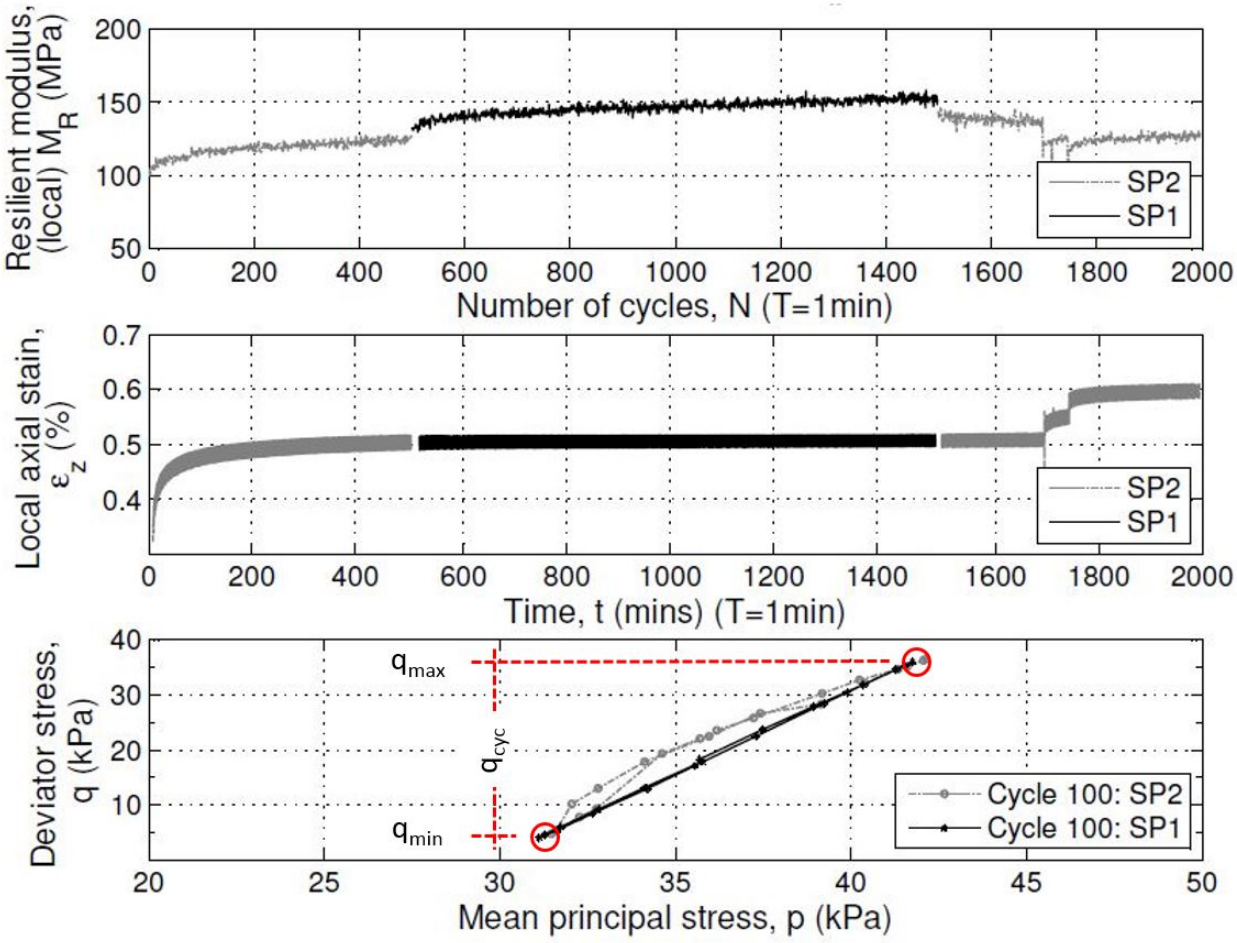

Figure 4.32: Typical open-to-drain HCA cyclic test results for HCA+0v1 including SP1 and SP2 phases measurements of (a) Average local resilient modulus and (b) local axial strain versus number of cycles (1 cycle = 1 minute); (c) Deviator stress versus mean principal total stress with q_{max} and q_{min} indicated

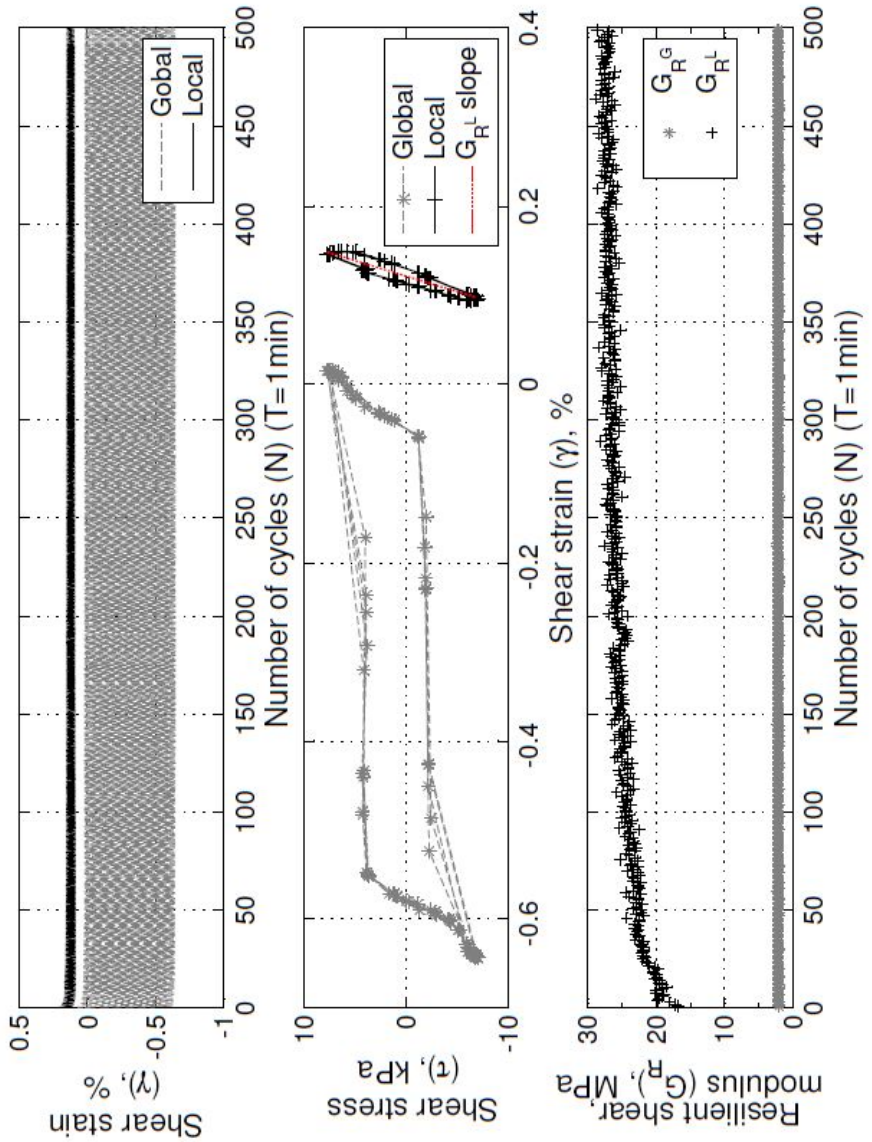

Figure 4.33: Typical test results for HCA+0v1 measurements of (a) Local shear strain for SP2 (cycle 1 to 500), (b) Shear stress versus global and local shear strain for c495-500 indicating the calculation of G_R (slope of the line) for one cycle, and (c) Resilient shear modulus per cycle for phase 1

Chapter 5

Discussion of results

A representative railway formation material has been selected (Section 4.1) and tested to evaluate the influence of some factors on its resilient modulus, M_R. The main investigation focussed on the influence of matric suction and train induced net normal stresses with principal stress rotation. M_R was measured using a cyclic triaxial, CTX, and hollow cylinder apparatus, HCA. Details of the selected material, specimen preparation, calculation of stresses and strains, as well as testing methods were discussed in Chapter 4.

In this chapter the results of testing are described under six main headings. The results obtained from the tests conducted on the railway formation material are compared with previous stiffness determinations in Section 5.1. The effects of the applied stresses (including confining stress, cyclic deviator stress and shear stress - causing principal stress rotation) on resilient modulus are discussed in Section 5.2. This is followed in Section 5.3 by an evaluation of the effect of matric suction (estimated from the soil water retention curve, SWRC) on the resilient modulus. The effects of the laboratory testing method are considered in Section 5.4. A comparison and summary of the effects of the different factors on M_R is included in Section 5.5. Finally, Section 5.6 evaluates the data using some existing resilient modulus models for flexible highway pavements.

5.1 Comparison of data with previous stiffness determinations

Gräbe and Clayton (2014) reported the saturated resilient Young's modulus as 72 MPa for the clayey sand formation material subject to cyclic triaxial conditions (p_o=30 kPa and q_{cyc}=30 kPa, no PSR). The addition of PSR (τ_{cyc}=14 kPa, 90^o out of phase) reduced M_R by approximately 23% to 58 MPa, as measured after 1000 cycles. In this work the measured M_R values of the wettest specimen (w=8%), tested under the same stresses

in the HCA, were slightly higher (78 MPa and 70 MPa respectively) perhaps due to different specimen preparation techniques and a small lack of saturation.

M_R values measured for saturated specimens have been found to be significantly lower than those back figured from the in-situ measurements made by Shaw (2005) and Priest et al. (2010) on the formation layer of the CoalLine near Vryheid (which the laboratory material was designed to represent). The in-situ stiffnesses calculated from displacements measured under a passing train (26 tonne axle) were between 113 MPa and 143 MPa for the formation layer (layer A), approximately 0.5 m below the sleeper soffit (Priest et al., 2010). The in-situ formation stiffness values are equivalent to M_R measured in the laboratory for specimens at optimum water content, reported in this thesis as ranging between 110 MPa and 150 MPa with and without PSR. The results emphasize the likely, beneficial influence of drainage to prevent the formation from becoming saturated for prolonged periods.

Comparison of results for the clayey sand formation material tested in this work was made with those from unsaturated subgrade pavement materials with low plasticity reported in the literature. Khoury and Zaman (2004) and Ng et al. (2013) tested a sandy soil (A-4) and silt (ML or A-7-6) respectively. The sandy soil tested by Khoury and Zaman (2004) showed a significant (3.1 times) increase in M_R due to lack of saturation. Specimens were compacted and tested saturated (w=16.5% or opt+4%) and dry of optimum (w=8.5% or opt-4%). The average M_R values were approximately 37 MPa and 115 MPa. Results reported were for one net normal stress sequence only, with p_o=41 kPa and q_{cyc}=28 kPa, and load and displacement measurements made externally. The significant change in M_R is similar for the clayey sand material tested here, approximately 70 MPa when saturated (w=8% or opt+1%) and 250 MPa when dry of optimum (w=6% or opt-1%).

Ng et al. (2013) showed a decrease in M_R of approximately 30% due to the increase in q_{cyc} from 30 kPa to 70 kPa (with p_o=30 kPa) for a specimen close to optimum water content. The influence of q_{cyc} was similar to that for the formation material tested here (approximately 25% reduction), when subject to this same net normal stress sequence, also at optimum water content. The influence of q_{cyc} was shown to reduce for higher suction conditions for the silt tested by Ng and his co-workers, as also found for the sandy clay formation material tests reported in this thesis. M_R measured by Ng et al. (2013) increased up to 8 times due to lack of saturation (increase in matric suction) depending on the q_{cyc} applied to the silt specimens. Similar trends were measured for a clay subgrade (A-6, 39% clay and PI=15) by Yang et al. (2005) for wet of optimum tests.

5.2 Effect of applied stresses on the resilient modulus of railway formation material

The total stresses applied to the external surfaces (boundaries) of each specimen were used to calculate the net normal stresses (Section 3.1.3). The CTX and HCA testing were conducted drained (water and air open to atmosphere) in order to be representative of a rail formation. The pore air pressure within the specimens was assumed to be atmospheric, thus $u_a = 0$. The total stresses applied to the specimen were therefore equated to the net normal stresses on the unsaturated specimens ($u_w < u_a$).

The CTX is routinely used to determine the resilient modulus, M_R, used in mechanistic-empirical highway design strategies. The material is tested drained at the expected physical state (water content and dry density). As discussed in Section 2.3, railway formation layers are compacted to achieve the maximum dry density at the optimum water content determined from laboratory compaction tests. In this work laboratory tests were conducted on specimens compacted to a target dry density of 2.1 Mg/m^3 close to the maximum dry density determined using the BS1377-4:1990 dynamic compaction method (2.5 kg rammer). Specimens were tested at a range of water contents and were named to reflect the test type (CTX or HCA), water content relative to the optimum water content (OMC=7%), with the variant of the test (v1 or v2) indicating the loading sequence (see below). A specimen compacted at 6% water content tested in the CTX using the test variant #1 would, for example, be named CTX-1v1.

CTX tests were conducted according to the test plan discussed in Section 4.3.7 used for coarse flexible pavement subgrade materials as summarised in NCHRP Project 1-28A (Harrigan, 2004). The 20 stress sequences, as given in Table 4.8, can be divided into 4 sets, each set containing a stress sequence at each of the five specified confining pressures (p_o = 15 kPa, 30 kPa, 40 kPa, 55 kPa or 85 kPa). In each set of stress sequences the cyclic deviator stress (q_{cyc}) magnitudes were proportional to p_o with q_{cyc}/p_o equal to 0.5 (set 1, sequence 1-5), 1.0 (set 2, sequence 6-10), 2.0 (set 3, sequence 11-15) or 3.0 (set 4, sequence 16-20). The majority of CTX tests (denoted v0 or v1 in the test name) were conducted by applying the stress sequences in order from 1 to 20. The difference between v0 and v1 relates only to the rate of stress change when switching between stress sequences (see Table 4.9) Exceptions to the v0 / v1 test sequences were denoted as v2 in the test name, and relate to CTX tests for which the sequence order was changed (see Table 4.9).

Additional footnotes are used to distinguish between different tests at the same water content, for example CTX+1v2$_i$ and CTX+1v2$_{ii}$. The footnote p used for CTX+0v0$_p$ indicates that the test was prepared, docked and, with initial confining pressure applied (15 kPa), left for 12 hours (over-night) before cyclic testing commenced. Footnote c (as in CTX+0v1$_c$) is used to specify that the specimen was compacted in 8 layers (instead

of 5 layers). When rubber bands were used around LVDT brackets the footnote r (CTX-2v1$_r$) was included in the test name.

M_R results from the CTX tests conducted on the sandy clay formation material are tabulated in Appendix C and include the strain levels before and after each cyclic loading stage. All the M_R results from the CTX testing, for all the stress sequences, are plotted in Figure 5.1 relative to p_o and q_{cyc} (test control parameters). The results are grouped in terms of the approximate gravimetric water content of the specimens tested. This section discusses the influences of the applied stresses including:

- Confining stress,
- Cyclic deviator stress, and
- Principal stress rotation.

5.2.1 Confining stress

The influence of p_o on M_R for specimens tested at optimum water content, CTX+0v0 and CTX+0v0$_p$, is shown in Figure 5.2. As discussed in Section 4.3.7 the highest p_o values used are unlikely to be relevant for the shallow formation layer under consideration, but have been included to show the trend of the p_o influence on M_R. The increase in M_R relative to p_o depended on the applied stress ratio as shown by the results of loading sequence sets 2 to 4 which ranged between approximately 1.35 and 1.9. The results have been normalised by M_R measured for the second stress sequence in each set of sequences (thus sequence 7, 12, or 17) for comparison of the relative p_o influence in the different stress sequence sets.

The second sequence in each set was used to normalise the results because a confining stress of 30 kPa is used by Network Rail (2005) during CTX testing to determine cyclic stiffness of subgrade materials. The value of p_o for CTX+0v0 and CTX+0v0$_p$ is approximately 7 kPa higher than the target confining stress for a particular stress sequence. This is due to the adjustment of the soft-zero point of the confining pressure, to be at mid-height of the specimen, which was originally set to be at the top of the cell chamber during tests set-up (soft-zeroed once filled) as discussed in Section 4.3.8. This applied to the first set of CTX tests conducted (test numbers 1 to 7).

An increase in M_R is expected with an increase in the minor principal net normal stress, σ_{n3} ($= p_o$) as the stress state moves further from the failure envelope. A 40% increase in M_R was observed for the increase in confining stress of 55 kPa (from 37 kPa to 92 kPa) for set 2 with q_{cyc}/p_o of 1.0 (Figure 5.2). The results for the clayey sand railway formation material are in general agreement with results reported by Salour et al. (2014) and Cary and Zapata (2011) for silty sand and clayey sand (flexible pavement) subgrades

respectively. Further comparisons are made in Section 5.6 as the combined influence of net normal stress and matric suction on M_R needs to be considered.

The likely range of p_o as found in literature (Miller et al., 2000; Shahu et al., 2000; Network Rail, 2005; Gräbe and Clayton, 2014) is between 14 kPa and 40 kPa as discussed in Section 4.3.7. To assess the influence of p_o, for this range, the results for optimum water content specimen tests CTX+0v0 and CTX+0v0$_p$ are considered (data tabulated in Appendix C). Considering a linear relationship between M_R and p_o, the average M_R for $q_{cyc} = p_o$ conditions at the lower and upper end of the likely p_o range (15 kPa to 40 kPa) is 98.8 MPa and 127.6 MPa respectively. With $q_{cyc} = 2p_o$ the average M_R is 78.8 MPa when p_o is 15 kPa and 110.4 MPa when p_o is 40 kPa. Thus, a change in p_o from 15 kPa to 40 kPa results in an increase in M_R of 30% and 40% depending on the applied deviator stress ($q_{cyc} = p_o$ and $q_{cyc} = 2p_o$ respectively). The same change in p_o when $q_{cyc} = 3p_o$ resulted in a 90% increase in M_R from 59.9 MPa to 113.4 MPa, however the deviator stresses are not expected to be three times the confining stress (Powrie et al., 2007).

An increase in p_o particularly influences M_R for CTX specimens at higher water contents, including optimum and wet of optimum conditions. The relative increase in the intergranular stress (or equivalent effective stress) for the same change in p_o is smaller for lower water content specimens due to the higher matric suction, further discussed in Section 5.3.2. The influence of p_o on M_R is smaller for CTX specimens tested dry of optimum, as shown in Figure 5.3. The effect of p_o reduced as the water content reduced, and thus as matric suction increased. M_R increased by approximately 45%, 23% and 17% for reducing water content specimens CTX-1v0, CTX-2v1$_r$ and CTX-3v1$_r$ respectively for set 4 ($q_{cyc}/p_o = 3.0$) compared to approximately 70% for CTX+0v0 seen in Figure 5.2 Both Figure 5.2 and Figure 5.3 indicate that the effect of p_o was most significant when high q_{cyc} (and thus high shear stress) was applied.

Figure 5.4 shows the change in M_R for set 2 ($q_{cyc}/p_o = 1.0$; sequence 6-10) relative to sequence 6 ($p_o = q_{cyc} = 15$ kPa) resulting from an increase in p_o. The change, ΔM_R, was similar for the different water content specimens CTX+0v0, CTX-1v0 and CTX-2v1$_r$. The vertical strains for these tests were less than 1% up to this point in the test and the density change was not considered significant. ΔM_R for optimum water content specimens measured for set 3 ($q_{cyc}/p_o = 2.0$; sequence 11-15) was larger than for the drier specimens (Figure 5.5). The stiffening of the material resulted from significant volumetric strain (densification) for the optimum water content specimens and the onset of dilation due to the applied deviator stress further discussed in Section 5.2.2.

The magnitude of p_o chosen for laboratory evaluation of M_R requires assumptions regarding K_0 and the inclusion of an average horizontal stress for the loaded track. Assuming K_0 of 1.0 for compacted material (discussed in Section 2.2) the stress ratio is approximately 1.0 for a subballast layer 0.5 m below the sleeper soffit. The increase

in M_R for $q_{cyc}/p_o = 1.0$ (set 2) was approximately 40%, 20%, 16% and 10% as p_o increased by 55 kPa (comparing sequence 7 and sequence 10; with $p_o = 30$ kPa versus $p_o = 85$ kPa), the influence of p_o reducing as the water contents reduced as seen in Figure 5.2 and Figure 5.3.

The in-situ confining stress for the subballast layer under consideration is low and approximately 20 to 30 kPa (at 0.5 m below sleeper soffit) with approximately 20 kPa increase per meter depth. The increase in ballast depth by half a meter would thus increase p_o by 10 kPa (say from 30 kPa to 40 kPa). This could result in a 10% increase in M_R (Figure 5.2, $q_{cyc}/p_o = 1.0$) for the sandy clay formation at optimum water content. As the depth increases, the train load applied would be spread over a larger area, thus reducing q_{cyc} and consequently q_{cyc}/p_o. As q_{cyc}/p_o reduces, the benefit of an increase in p_o would reduce (Figure 5.2 and 5.3). The influence of p_o and q_{cyc} should therefore be simultaneously assessed to prevent costly increases in ballast depth with reducing benefit. This is in agreement with the limit in benefit of increased ballast depth (beyond an upper limit) suggested by Li and Selig (1998b). The influence of the cyclic deviator stress magnitude, q_{cyc}, on M_R is discussed next.

5.2.2 Cyclic deviator stress

The resilient modulus, M_R, for dry of optimum specimens reduced as q_{cyc} increased, as shown in Figure 5.6 for CTX-2v0 and CTX-2v1$_r$ under different confining stresses. M_R was normalised with respect to M_R measured in set 2 ($q_{cyc}/p_o = 1.0$) and plotted in Figure 5.7 to compare the influence of q_{cyc} on specimens at different water contents, and thus different matric suctions. The relative influence of q_{cyc} on M_R was similar irrespective of the water content for dry of optimum specimens and specimens at optimum water content (CTX+0v0) before large volumetric strains (ϵ_V) occurred (>1.5%) which resulted in densification and the onset of dilation.

The cumulative vertical strains for CTX+0v0$_p$ are plotted in Figure 5.8 for stress sequences 2, 7, 12, and 17 for which p_o=37 kPa. The increase in deviator stress resulted in permanent strain accumulation; therefore a reduction in M_R is expected due to non-linear soil stiffness (Atkinson, 2000). The increase in M_R seen for Sequence 17 is due to a small amount of dilation as the material starts to shear (Figure 5.9).

For specimens compacted and tested wet of optimum, M_R increased as q_{cyc} increased as shown in Figure 5.10. Wet of optimum specimens (CTX+1; $w = 8\%$) experienced large vertical strains, even for low confining stress and q_{cyc}, preventing the full range of sequences from being tested. CTX+1v2$_i$, v2$_{ii}$, v2$_{iii}$ results (Table C.13) are combined as CTX+1v2 to evaluate the influence of q_{cyc} and p_o. A difference in mechanical behaviour could be expected for a change in the soil fabric for cohesive material from flocculated (when dry) to dispersed when compacted wet (Seed et al., 1967). An increase in M_R due

to an increase in q_{cyc} was measured by Hicks and Monismith (1971) and Brown et al. (1975) for granular highway base materials as discussed in Section 3.1.3. The response of CTX+1v2 is thus suggested to be controlled by the coarse sand particles with the clay fractions dispersed.

CTX+0v1$_c$ showed the same trend of increasing M_R with increasing q_{cyc} as for the wet of optimum specimens (Figure 5.10). The CTX+0v1$_c$ specimen was compacted in 8 layers instead of 5 layers to evaluate the influence of specimen preparation. Although the bulk dry density of the specimen is the same as for the other optimum water content specimens, less variation in density across each compacted layer is likely, thus resulting in a more uniform pore distribution. The increase in number of layers could have resulted in a change in soil fabric.

The effect on M_R of the principal stress ratio (in terms of net normal stress ratio) is shown by Figure 5.11 for dry of optimum specimens. The mean principal net normal stress (p_n) was calculated as the average of the three principal net normal stresses with $\sigma_{n3} = p_o$ and $\sigma_{n2} = \sigma_{n3}$. The maximum value of σ_{n1} per cycle was used. The maximum deviator stress, q_{max}, per cycle (rather than q_{cyc}) was used as this is the most critical stress point in each loading sequence. M_R was normalised with the modulus measured for set 2 ($p_o = q_{cyc}$) for each applied confining pressure. It is clear that the relationship between the principal net normal stress ratio (q_{max}/p_n) and M_R is non-linear with M_R reducing as the ratio increases.

5.2.3 Principal stress rotation

CTX testing is used to determine M_R for mechanistic-empirical highway pavement design strategies and its use has been suggested for railway formation design by Li and Selig (1998a). The CTX is used to simulate the expected stress cycles in a pavement as it readily allows for a large number of tests (Brown, 1996). But the CTX test applies a simplified stress path with a constant confining pressure and cyclic vertical stress. The continuous shear stress reversal induced by a moving wheel cannot be recreated in a CTX test.

The hollow cylinder apparatus, HCA, was used to investigate the effect of shear stress reversal or principal stress rotation, PSR, expected for a 26 tonne axle load freight train running at constant speed as determined by Gräbe (2002). The stresses applied in the HCA included cycles with no PSR (SP1; equivalent to CTX stress sequence 7 with $p_o = q_{cyc} = 30$ kPa) and with PSR (SP2; includes $\Delta\tau = 14$ kPa, 90^o out of phase) as discussed in Section 4.4.7. The M_R results from the CTX equivalent stress path (SP1) conducted in the HCA were compared with results from CTX testing (Figure 5.12). There is good agreement for the range of specimen water contents tested.

Gräbe (2002) defined the modulus ratio MR_{PSR}, originally denoted as PSR_{res}, to evaluate the influence of principal stress rotation. MR_{PSR} is defined as $M_{R,SP1}$ measured for cycles without PSR divided by $M_{R,SP2}$ measured for cycles with PSR ($MR_{PSR} = M_{R,SP1}/M_{R,SP2}$). The influence of PSR was investigated for a range of water contents specimens using the stress paths (SP1 and SP2) discussed in Section 4.4.7. MR_{PSR} values for cycles 100, 500 and 1000 are given in Table 4.15. The HCA tests (variant #1) were conducted by applying 500 cycles of SP2 (with PSR), followed by 1000 cycles of SP1 (no PSR), and a further 500 cycles of SP2 (with PSR). One test was conducted for which SP1 and SP2 were switched around (variant #2), HCA+0v2.

MR_{PSR} measured for specimens at different water contents (in terms of bulk water content after testing, w_f) are plotted in Figure 5.13. It can be seen that the influence of PSR reduces as water content is reduced and matric suction increases. Shear resistance increases with matric suction (Tarantino and Tombolato, 2005) and reduces the influence of PSR caused by a moving wheel load.

MR_{PSR} at optimum water content ($w = 7\%$) was found to be approximately 1.15, thus giving a 13% reduction in measured M_R when PSR was included. M_R will thus be overestimated somewhat when using the CTX, because PSR cannot be applied.

The results from saturated tests conducted by Gräbe (2002) are also included in Figure 5.13, for w= 9.5%. The 5 cycle average of M_R was calculated, after the data provided by Gräbe were re-analysed, and PSR was found to reduce M_R by approximately 25%. The reduction in M_R due to PSR was previously reported by Gräbe as 20% when using the value of the final cycle (c1000) only. Although the specimens tested by Gräbe were consolidated from a slurry, rather than being compacted the trend of MR_{PSR} is consistent. For the wet of optimum specimen (material compacted at $w = 8\%$) MR_{PSR} was approximately 1.2.

Resilient modulus values for HCA+0v1 and HCA+0v2 are plotted in Figure 5.14. The order in which the SP1 (no PSR) and SP2 (with PSR) phases were applied was reversed as summarised in Table 4.13. The development of M_R with number of cycles, N, did not show a significant difference for the first 500 cycles (phase one) with the same increase in M_R for both SP1 and SP2 cycles (Figure 5.14a). The influence PSR had on the development of M_R with N is seen in Figure 5.14b and 5.14c for phase two and three of testing. M_R increased for SP1 conditions, while M_R did not change significantly for SP2 conditions (with PSR) in phase 2 shown in Figure 5.14b. In phase three (Figure 5.14c) the higher M_R, which resulted from SP1 cycles in phase two for HCA+0v1, was reduced when shear stress reversal was included, resulting in particle rearrangement.

The trend of M_R relative to N can be related to the accumulation of vertical strain, ϵ_z. In the first phase (500 cycles) ϵ_z was similar for HCA+0v1 (with PSR) and HCA+0v2 (without PSR) as shown in Figure 5.15a. The minimum vertical strain per cycle (the permanent strain) is plotted. The strain for the first cycle of each test was disregarded.

Figure 5.15b shows how the application of shear stress reversal (SP2) resulted in the continued increase in plastic strain. The continuous increase in strain for SP2 cycles prevented the increase in M_R as seen in Figure 5.14b. For HCA+0v1 subject to CTX stress conditions (SP1, without PSR) in phase two the plastic strain plateaued (Figure 5.15b) for which a corresponding increase in M_R was seen (Figure 5.14b).

The sudden increase in vertical strain, shown in Figure 5.15c, suggests particle rearrangement due to the applied shear stress which caused a corresponding reduction in M_R (Figure 5.14c). PSR increased permanent strain accumulation, as previously reported by Gräbe and Clayton (2009) for saturated formation material, and also seen by Chan and Brown (1994) for an unbound road base material (crushed dolomitic limestone) tested dry. The data suggest that the lack of PSR in CTX testing could thus lead to plastic strain accumulation during the life of the track being underestimated.

5.3 Effect of water content on the resilient modulus of formation

The influence of matric suction on M_R was indirectly assessed by changing the water content of the compacted specimens tested in the CTX and HCA. The matric suction was estimated using the soil water retention curve, SWRC, determined by Otter (2011); Otter et al. (2015) for the representative formation material. The suction stress relating to the water content was determined using the effective degree of saturation, S_e, as Bishop$'$s χ factor. This was compared with the suction stress back-calculated from measured CTX results. The effect of matric suction on the resilient Young$'$s modulus is compared with the effect of suction on small strain shear modulus measured by Otter et al. (2015). This section covers the following four topics:

- The soil water retention curve.
- The effect of matric suction on M_R.
- The suction stress characteristic curve.
- Comparison of the matric suction effect on M_R and on very small strain shear stiffness.

5.3.1 The soil water retention curve

The soil water retention curve, SWRC, defines the relationship between suction (matric suction or total suction) and water content (gravimetric or volumetric) or degree of saturation. The shape of the SWRC is dependent on the material type and the dry

density or porosity as these influence the pore space and thus matric suction. Properties of the SWRC have been discussed in Section 3.3.

Otter (2011) determined the SWRC for the representative formation material (Material B, 11% clay) used in this study, compacted to a target dry density of 2.1 Mg/m^3. Otter reported measurements made using several techniques to determine the matric suction/water content relationship, including the filter paper technique, the pressure plate and a high-capacity tensiometer (Ridley tensiometer (Ridley and Burland, 1993)). The matric suction measurements made by Otter on specimens dried from different initial water contents using the filter paper technique (in direct contact) are plotted in Figure 5.16 for reference.

The SWRC was calculated by Otter using the Fredlund and Xing (1994) equation on the combined matric suction results from all the techniques used. Otter found the residual water content and inflection point difficult to determine, possibly due to the bi-modal response of the material due to the clay content. The residual matric suction was estimated to be 1500 kPa which corresponds with a gravimetric water content of 3% on the SWRC.

In this research a Chilled Mirror Dew-point Potentiometer, at Cardiff University, was used to measure the total suction of the compacted material, as described in Section 4.2. The samples tested were cut from specimens prepared and compacted in the same way as the CTX and HCA specimens, at a range of water contents. However, two samples cut from the specimen compacted at optimum water content (w =7%) were incrementally dried and tested to allow measurement of suction at low water content, to compare the trend with the SWRC determined by Otter. The results of total suction measurement have been given in Table 4.5 and are plotted against gravimetric water content in Figure 5.17 with the SWRC determined by Otter for reference. Gravimetric water content was used as engineers are most familiar with this parameter. Compared to the SWRC based on matric suction determined by Otter the total suction values are expected to plot slightly higher as they include a component of osmotic suction.

The SWRC is not a unique function of gravimetric water content but varies due to the process of wetting and drying (scanning curves) resulting from the ink bottle effect as discussed in Section 3.3. It can be seen in Figure 5.17 that the total suctions measured for dried samples were higher than for samples tested at the compacted state. This could be due to some variation in microstructure (Alonso 2013), but it could also be due to some disturbance of the material when samples are cut, especially when cut from dry and brittle specimens (at low water content). Samples compacted dry of optimum are likely to have a more open microstructure (larger void spaces) or bimodal void structure due to the forming of clay aggregates during material mixing (Jennings and Burland, 1962), although this is more prominent in cohesive materials. Larger void spaces may result in lower matric suctions for the same water content. The method of specimen

preparation, by dynamic compaction, could to some degree be viewed as an incremental wetting process as density increases incrementally with applied blows, which could result in lower suction measurements.

Suction measurements using different techniques are known to vary (Tarantino et al., 2011). A Chilled-Mirror Dew-point Potentiometer is generally used for measurements in the high suction range (>1000 kPa) and the equipment is unable to accurately measure suctions below 200 kPa (Ahmed, 2014). The results obtained by the chilled-mirror dew-point technique suggest that further refinement of the SWRC is necessary. However, Leong et al. (2003) found total suction measured using a Chilled-Mirror Dew-Point Potentiometer to be larger than the sum of the components matric suction and osmotic suction measured using other methods. The chilled-mirror dew-point technique is thus expected to overestimate total suction. As the measured total suctions for the samples at their compacted state were just above the SWRC suggested by Otter, the Otter curve was regarded as suitable for estimating the matric suction of CTX and HCA specimens to assess the effect of matric suction on M_R.

5.3.2 Effect of matric suction on resilient modulus

The bulk water content at the end of each CTX and HCA test was used to estimate the matric suction using the SWRC determined by Otter (2011). However, significant volumetric compression occurred during testing of specimens compacted at and above optimum water content (w = 7% and w = 8%). The degree of saturation was used to adjust (lower) the matric suction estimates for these specimens subjected to wetting due to densification. For example, the degree of saturation for HCA+1v1 (specimen compacted wet of optimum (w = 8%, S_r=86%) was calculated as 98% after testing due to densification. This significant increase in degree of saturation, also seen for similar CTX specimens, is not reflected in the measured gravimetric water content. The matric suction was subsequently assumed equal to zero for all wet of optimum specimens. The matric suction estimates are reported in Tables 4.7 and 4.12 for CTX and HCA specimens respectively.

The influence of matric suction on M_R was evaluated using results for the CTX stress condition of $p_o = q_{cyc}$ = 30 kPa, used as representative of in-situ formation stresses (Network Rail, 2005; Gräbe and Clayton, 2014). This is the stress applied during stress sequence 7 in the CTX test and SP1 used in the HCA testing. M_R values measured for CTX and HCA specimens with different water contents are plotted in Figure 5.12 relative to final gravimetric water content and in Figure 5.18 relative to final degree of saturation. The increase in M_R as the degree of saturation reduced was considerable with M_R ranging between 36.4 MPa and 467.0 MPa.

The effect of matric suction was evaluated by normalising M_R with the resilient modulus when saturated, $M_{R,sat}$. The ratio ($M_R/M_{R,sat}$) is denoted as the modulus ratio of suction (MR_s) with the calculated ratios included in Table 4.15. HCA+1v1 was taken to represent the saturated condition for the compacted material with S_r >97% measured after testing. M_R measured for HCA+1v1 (78 MPa for SP1 c100) was chosen, however Gräbe measured M_R to be 16% lower for fully saturated conditions (66 MPa for SP1 c100).

M_R for CTX+1v2 specimens at w_f approximately 8% (close to saturation due to densification) was 46% lower than HCA+1v1 used as $M_{R,sat}$ (Figure 5.19). However, this large variation in results between CTX and HCA measurements was ascribed to the higher cyclic frequency used during CTX testing (0.5 Hz versus 0.0167 Hz in the HCA). The CTX cyclic frequency may have resulted in the build-up of positive pore water pressure ($u_w > 0$) in the near saturated specimens, resulting in the reduction of effective stress. No pore-water pressure measurements were made to confirm this hypothesis. The cyclic frequency did not have a significant effect on the dry of optimum specimens possibly due to the compressibility of air (Marinho et al., 2008). The strain accumulation in the CTX prior to sequence 7 could also be a contributing factor.

MR_s plotted in Figure 5.19 shows an increase in M_R of up to six times as the water content reduced and thus matric suction increased. A significant increase in M_R occurred for slight changes in water content as previously reported by Sauer and Monismith (1968). M_R for optimum water content specimens (S_r approximately 90%) was approximately 1.5 times the near saturated value ($M_{R,sat}$).

The significant increase in M_R for low water content conditions resulted not only from the direct effect of matric suction on M_R, but also from the lower permanent strain levels. The vertical strain accumulation during the first phase of HCA testing (500 cycles of SP2) is shown in Figure 5.20. The plotted vertical strain, ϵ_z, is the minimum value per cycle representative of the permanent strain. The permanent strain after 500 cycles for low water content specimens were considerably smaller (approximately 0.002% for $w = 4\%$ and $w = 5\%$) than at higher water content (0.17% for OMC).

5.3.3 Suction stress characteristic curve for formation material

Although very high suctions can be present in the material micro-pores (for water content below the residual water content) these are not representative of the bulk of the material and its behaviour. The effective degree of saturation, S_e, representing the degree of saturation of the macro-pores is expected to play a role on the mechanical behaviour of the material (Alonso et al., 2013). S_e is calculated using the water content range above the residual water content. Otter identified the residual matric suction as 1500 kPa which corresponds to $w = 3\%$ on the SWRC.

The estimated suction stress (σ_s) was calculated by multiplying the estimated matric suction (from the SWRC) by the effective degree of saturation, S_e (Equation 3.16) to obtain the suction stress characteristic curve (SSCC). Due to the uncertainty around the residual water content used by Otter (2011) ($w_r = 3\%$) two additional SSCC curves were calculated with residual water contents assumed as 2% and 1.5% respectively. The SSCC curves for Material B ($\rho_{dry} = 2.1$ Mg/m^3) are plotted in Figure 5.21 together with the SWRC by Otter. A reduction in suction stress at low water contents is expected for granular materials (Lu and Likos, 2006), as seen for the clayey sand formation material with only 11% clay. σ_s for each CTX specimen was calculated and is included in Table 5.4.

The suction stress (σ_s) is added to the net normal stress (σ_n) to calculate the intergranular stress (σ_i) or equivalent effective stress for unsaturated materials as discussed in Section 3.1.2. The advantage of such a simplified, but debated approach, for unsaturated soils is the use of existing effective stress analyses as for saturated soils (Lu and Likos, 2006). The true effective stress for unsaturated soils is an ongoing research topic.

M_R results from CTX tests (stress set 2; $p_o = q_{cyc}$) on specimens compacted at optimum or dry of optimum water contents are plotted in Figure 5.22 against the minor principal intergranular stress ($\sigma_{i3} = \sigma_{n3} + \sigma_s$) calculated with $w_r = 3\%$, as selected by Otter (2011) for Material B, and $u_a = 0$. An increase in M_R with σ_{i3} is expected as the stress state moves further from the failure envelope. The step changes in M_R for σ_{i3} between 150 kPa and 200 kPa can be due to errors in the calculation of σ_s. If a lower value for w_r is selected, σ_s will increase for specimens at lower water contents ($w = 4\%$ and $w = 5\%$ as seen in Table 5.4) with a corresponding increase in σ_{i3}. However, the increase in M_R for the same intergranular stress could also be due to the lower strain levels measured for the low water content specimens as shown in Figure 5.20 for HCA specimens.

Additional tests for σ_{i3} between 100 kPa and 150 kPa (specimens below OMC; $6\% < w < 7\%$) could aid evaluation of the trend. The suction stress estimated from the SWRC is compared with the suction stress back-calculated using M_R in Section 5.6.

5.3.4 Comparison of the effect of water content on resilient modulus and on very small strain stiffness

Otter et al. (2015) previously used the Stokoe resonant column apparatus, RCA, to determine very small strain shear modulus, G_0, as a surrogate for resilient modulus, M_R. Tests were carried out under isotropic loading conditions. They found that the stiffness of the typical railway formation material could be increased by a factor of three (relative to saturated) for a confining stress of 20 kPa depending on the water content and thus matric suction (Figure 5.23). The maximum G_0 for the clayey sand, compacted

to a dry density of approximately 2.1 Mg/m^3, occurred at approximately 5% gravimetric water content.

Peak M_R was therefore expected to be at approximately $w = 5\%$ corresponding to the maximum G_0 measured by Otter (2011). The maximum increase in M_R was in fact up to six times relative the near saturated $M_{R,sat}$, as discussed in Section 5.3.2, at approximately 5% water content. M_R was not measured for specimens with water content lower than 4%, therefore no assessment can be made regarding the reduction of M_R for low water contents ($w < 4\%$). The water content was limited by the ability to obtain specimens for testing. At water content lower than 4% the compacted specimens became too brittle for handling, especially when coring for HCA specimens.

Values of M_R measured in the HCA and CTX for sequence 7 ($p_o = q_{cyc} = 30$ kPa) are plotted on the primary y-axis in Figure 5.23 while G_0 measured by Otter is plotted on the secondary y-axis for which the scale was increased by a factor of 2.5. For an isotropic linear elastic material the resilient Young′s modulus would be expected to be about 2-3 times the shear modulus depending on Poisson′s ratio. At $w = 4\%$ and $w = 5\%$ the ratio of M_R to G_0 is approximately 2.5 but, for higher water content specimens M_R divided by G_0 was approximately 1.5. However, comparison of M_R and G_0 for higher water content specimens is probably affected by larger strains occurring during CTX and HCA testing at higher water contents.

The values of (resilient) shear modulus, G_R, determined from the HCA tests reported in this thesis (from SP2 cycles, with PSR), were lower than would be expected for an isotropic elastic material on the basis of the measured (resilient) Young′s modulus, E ($= M_R$). The resilient Young′s modulus measured in the HCA was approximately 4 times the shear modulus (Figure 5.25). This suggests that compaction produces an anisotropic material. Further investigation of the potential anisotropy induced by material compaction should be considered.

5.4 Effect of laboratory testing method on measured stiffness

A number of factors affecting measured resilient modulus, M_R, relating to the method of testing, have been evaluated. These factors, discussed in the following section, include:

- Number of load cycles;
- Loading sequence;
- Rate of testing;
- Global and local strain measurement; and

- Conformance and resolution of the measurement equipment.

5.4.1 Number of load cycles

The HCA test results were used to assess the influence of the number of load cycles, N, on M_R for cycles with and without PSR. M_R has been normalised with the value of the second cycle, M_{R2} in order to evaluate the influence of N as plotted in Figure 5.26. The first vertical stress cycle does not include a full shear stress cycle as it is 90 degrees out of phase (resulting in a staggered start during testing); therefore the first cycle was discounted. A moving average of 20 was used to reduce scatter and to aid visual evaluation of the trend.

Phase one and three consisted of SP2 cycles which included PSR and phase two consisted of SP1 cycles which did not include PSR, as in a CTX test. A continued increase in M_R with N is seen for CTX conditions (SP1) (Figure 5.26b) which is not seen when PSR is included (Figure 5.26c). The continued increase in M_R with N under CTX conditions was observed for all HCA with the relative increase less for higher suction conditions, also observed by Ng et al. (2013). However, Ng and his co-workers did not use more than 100 cycles to evaluate the development of M_R. The reduced stiffening caused by N for lower water content specimens (higher suction) could explain the reducing effect of PSR as water content reduces (Figure 5.13). The use of 100 cycles per stress sequence in the CTX is therefore considered adequate for evaluating M_R without overestimation resulting from the lack of PSR.

5.4.2 Loading sequence

The stress history of soil is known to influence its stress-strain behaviour. Gräbe (2002) evaluated the influence of the over consolidation ratio, OCR, on saturated formation material. He found that whilst M_R increased by 20% when the OCR changed from 15 to 25, only a small difference due to the influence of principal stress rotation ($MR_{PSR} =$ 1.23 versus 1.20) was measured. An OCR of 15 was used by Gräbe to obtain specimens thought to be representative of a compacted formation layer, made from slurry, before cyclic testing.

In the testing reported here material was dynamically compacted to simulate construction of a formation layer to obtain representative specimens (Section 4.1.4). No consolidation or pre-conditioning phase was included in the test programme, in order to preserve the as-compacted void structure (target dry density of 2.1 Mg/m^3). The main objective of a pre-conditioning phase in flexible pavement testing protocol (Nazarian et al., 1996) is to reduce global strain measurement errors due to bedding; therefore in this research local strain measurements were made (see Section 5.4.4).

The mechanistic-empirical CTX testing strategy is based on the assumption that the loading sequence or staging does not significantly influence measured M_R which is considered an elastic response (Nazarian et al., 1996). The effect of CTX staging on the measured M_R was investigated by changing the order of the loading sequences. CTX tests conducted with the stress sequences in order from 1 to 20 denoted as variant v0 or v1, with the difference in v0 and v1 only relating to small differences in test stages when changing between stress sequences. CTX test variant v2 indicates the change in the order of stress sequences as summarised in Table 4.9; conducting the loading sequences in the following order: 1, 6, 11, 16 (p_o =15 kPa); 2, 7, 12, 17 (p_o =30 kPa); 3, 8, 13, 18 (p_o =40 kPa); 4, 9, 14, 19 (p_o =55 kPa); 5, 10, 15 and 20 (p_o =85 kPa).

M_R measured for specimens at optimum water content (w =7%) CTX+0v0, CTX+0v0$_p$, and CTX+0v2 are plotted in Figure 5.27 relative to q_{cyc} for the five confining stresses used. The most significant influence of the loading sequence (staging) on M_R relates to the measurements made at low p_o; sequence 1, 6, 11 and 16 where p_o =15 kPa. The consistently higher M_R measured for CTX+0v0 and CTX+0v1$_p$ is due to the 7 kPa higher applied p_o than the target p_o as discussed in Section 5.2.1; with the highest influence for the low p_o sequences (22 kPa/15 kPa=1.47 increase in p_o). CTX+0v0, CTX+0v0$_p$, and CTX+0v2 have similar trends irrespective of the loading sequence (Figure 5.27) and it was therefore concluded that the sequence of loading stages did not significantly influence measured M_R while vertical strains remained below the 5% maximum limit.

5.4.3 Rate of testing

An in depth investigation of cyclic frequency effects on measured M_R was not conducted. Some observations are discussed as the cycles in the CTX and HCA tests were conducted at two different frequencies. The cyclic frequency used in the CTX tests was 0.5 Hz in line with NCHRP Project 1-28A testing protocols. The HCA testing was conducted at a lower frequency of 0.0167 Hz (1 cycle/min) due to apparatus and data acquisition limitations (Gräbe, 2002). M_R results from the CTX and HCA testing have been plotted together in Figure 5.12. Comparable results were obtained for the unsaturated specimens as measured after 100 cycles where p_o = q_{cyc} =30kPa without PSR (CTX sequence 7 and HCA SP1).

Assessing the results for the specimens wet of optimum (w =8%), close to saturation (S_r > 95%), the results from CTX tests were considerably lower than measured using the HCA. Due to the higher cyclic frequency used in the CTX a build-up of positive pore water pressure is probable due to partly drained conditions which would reduce the effective stress (assuming saturated conditions). No pore-water pressure measurements were made and further testing is required to validate this hypothesis. A full investigation is needed if the effects of faster trains (thus higher cyclic frequency) are to be evaluated.

This is especially true for weak subgrade where the loading frequency is close to natural material frequency.

5.4.4 Global and local strain measurement

Local strain measurement made over the mid third of the specimen reduces the likely influence of end restraints and bedding (Bishop and Henkel, 1957). The importance of local strain measurement for determining M_R of the railway formation material was assessed by comparing it with the global M_R values. Figure 5.28 shows M_R calculated using local and global (external) strain measurements from CTX sequence 7 and HCA SP1. The calculated M_R values have been tabulated in Appendix C and Table 4.14 for CTX and HCA tests respectively.

It is evident from Figure 5.28 that CTX global measurements were unable to capture the increase in M_R as the water content reduced. The relationship between local and global M_R is plotted in Figure 5.29. In the HCA local M_R measurements were approximately twice the global M_R for dry of optimum specimens while the ratio was up to seven for CTX measurements. The global M_R measurements at optimum water content (w =7%) were approximately half the local M_R for CTX tests and approximately two thirds for HCA tests; reducing for wet specimens. Global measurements are thus likely to underestimate M_R and local strain measurements are particularly important for high stiffness specimens.

CTX global strain measurements were particularly unrepresentative and unable to capture the increase in M_R as water content reduced. Several apparatus and specimen set-up details could contribute to global strain measurement errors (Baldi et al., 1988). The main difference between the CTX apparatus and the HCA apparatus is the location of the tie bars (or reaction bars). The CTX has external tie bars (Figure 4.8) while the HCA has internal tie bars (Figure 4.23a). This difference in arrangement changes the connection between the loading ram (fitted with an internal load cell) and the top cap.

The equipment alignment and seating can be checked and corrected when using an apparatus with internal tie bars (Baldi et al., 1988) such as the HCA apparatus. A system with external tie bars (such as the CTX apparatus) is more prone to misalignment, because of non-parallel load platen and specimen surfaces, with consequences (as summarised by Baldi et al. (1988)) which are difficult to correct.

Further details thought to contribute to larger global strain measurement errors in the CTX are the type of porous disc used and system compliance due the loading ram arrangement. An extension piece is used between the load cell and the top cap of the CTX in order to reach the 200 mm high specimen within the large cell chamber that can accommodate a 300 mm high specimen. Potential relative movement and bending of the extension is possible, although probably small. The coarse stone porous discs used

in the CTX is thought to result in larger bedding errors compared to the finer sintered bronze porous discs used in the HCA. Although, fins included on the HCA porous discs to prevent slip between platens and specimen could result in larger vertical bedding errors if not seated fully into the specimen.

Cutting of the HCA specimen top and bottom surfaces at the porous disc fin positions was required to prevent cracking of the stiff unsaturated specimens. Visual observations are particularly important when using finned porous discs to identify cracking due to localised loading at fin positions. The benefit of the fins can be debated as higher vertical bedding errors can result especially for brittle specimens. Jumps in the global shear strain as shear stress cycled through zero (from positive to negative) were observed, as seen in Figure 4.33. This could result from slip of the specimen on the porous disc (thus bedding) or due to slip of the servo-motor.

Local shear strain measurements were regarded as unnecessary by Mamou (2013) and Gräbe (2002), both of whom tested saturated specimens. The local and global shear moduli measured for HCA+1v1 (wet specimen, w=8%) were within 50% measuring as 18.4 MPa and 9.3 MPa respectively. An increased ratio of local to global shear modulus was seen as water content reduced (Table 4.16). Therefore, this research has shown that external (global) measurement systems are unable to measure shear modulus for reducing water content specimens (Figure 5.30) with high stiffness.

5.4.5 Conformance and resolution of measurement equipment

Consideration of measurement resolution is important as very stiff specimens require the ability to measure very small increments of displacements, especially for low applied stresses. In addition to slight misalignment of the specimen, which can cause unequal displacements on diametrically opposite sides of the specimen, movement of the LVDTs and fixings separately from the specimen can also influence the measurement accuracy. The LVDT brackets are glued to the membrane and some movement of the membrane with respect to the specimen is possible due to the pull from cables, or due to LVDT mass. However, most likely only for very dry specimens under low confining stresses as shown for CTX-3v0 in Figure 5.31 during set-up, as the membrane does not stick to the dry specimen surface as with wetter specimens. The cabling of the LVDT could also inhibit movement when pressing against the cell chamber especially when docking (CTX) requires more than 5 mm movement, however this is of less concern when testing 100 mm diameter specimens in the large CTX apparatus (which is able to test 150 mm diameter specimens).

The local recoverable strain per cycle used to calculate M_R for the lowest water content specimens tested (w =4%) are plotted in Figure 5.32 as tested in the HCA apparatus (SP1, cycle 1-100) and CTX apparatus (sequence 7) with $p_o = q_{cyc} = 30$ kPa. The

LVDTs were calibrated over the full range of ±5 mm except for CTX-3v1$_r$ for which the calibration range was smaller (±1.5 mm) to assess the effect of resolution. As an additional measure, rubber bands were placed around the LVDT brackets (Figure 4.11b) for CTX-3v1$_r$ to prevent any potential movement of the brackets relative to the specimen which could result in non-conformance. The recoverable strains measured for CTX-3v1$_r$ with the use of the rubber bands were most constant (less scatter) and similar for diametrically opposite local measurements.

More variation in the HCA recoverable strain measured for consecutive cycles can be seen in Figure 5.32. This is attributed to very small rotations of the base platen under stress control even for SP1 cycles with no PSR. Therefore, it is considered good practise to use the average M_R of five cycles as prescribed in CTX protocols. Rubber bands were not used during HCA testing. Their use is suggested for future testing of stiff materials.

5.5 Comparison of factors affecting formation stiffness

In this work it has been assumed that the resilient modulus, M_R, of any unsaturated soil is controlled by applied net normal stresses $(\sigma - u_a)$ and matric suction $(u_a - u_w)$ as reflected by Figure 3.2. The CTX and HCA were used to evaluate the influence of net normal stresses. The applied stresses included confining stress, deviator stress and shear stress (inHCA only) which influences the stress path in the net normal stress plane (principal net normal stresses) analogous to effective stress for saturated materials. The CTX stress sequences applied were based on the NCHRP Project 1-28A granular subgrade material test plan (Harrigan, 2004) as it includes the range of expected net normal stresses (cyclic vertical stress and confinement) proposed for railway formations by Miller et al. (2000); Shahu et al. (2000) and Powrie et al. (2007). Additional tests were conducted in the HCA to investigate the effect of shear stress cycles (PSR) due to the moving wheel load. The effect of matric suction was evaluated indirectly using the SWRC and testing specimens compacted at different water contents. Specimens were allowed to drain to atmosphere and u$_a$ taken as zero.

The effect of applied applied confining stress, cyclic deviator stress, and applied shear stresses (PSR) has been individually discussed in Section 5.2. The effect of water content has been discussed in Section 5.3, while the influence of laboratory testing is considered in Section 5.4. A comparison of the effects of these factors is given in Table 5.1. These are average M_R values extracted from the data tables provided in Appendix C, for CTX tests, and Table 4.14, for HCA tests.

The normalised M_R values or ratios, as discussed and plotted in the previous sections, have been used to compare the relative effect of the various factors on the cyclic stiffness. The normalised values summarised in Table 5.2 are approximated values as obtained from the various plots indicated on the table. However, when the average M_R values

summarised in Table 5.1 are normalised similar ratios are obtained. The base values (divisors) or condition used for comparison are highlighted in the tables. The left side of Table 5.2 reflects the deviator stress influence for different confining stress conditions, while the middle part of the table shows the influence of confining stress. The right side of the table summarises the influence of water content, PSR and strain measurement location (testing method).

Table 5.2 shows that the most important factor influencing measured M_R is water content. The second most important factor controlling measured M_R is the method of strain measurements. The influence of cyclic deviator stress magnitude seems to be higher than the effect of confining stress and PSR, however it is dependent on the water content or suction of the specimen. Therefore, when conducting resilient modulus testing on formation material, such as the clayey sand tested, it is recommended that the impact of the water content and changes thereof is considered. Local strain measurements are important to obtain accurate results, especially for stiff, unsaturated soils. The expected cyclic deviator stress and confining stress is also important when selecting test conditions to obtain reasonable design input stiffness values. An assessment of the influence of PSR (HCA testing) is suggested as advanced consideration for high induced shear stress zones such as for braking and acceleration zones (not tested in this research), or for problematic subgrade sections saturated for prolonged periods.

A brief summary of the importance of the individual factors is given below. As seen in the summary Table 5.2, the effect of the various factors on M_R are interdependent and some existing resilient modulus models have been applied in Section 5.6.

5.5.1 Effect of testing and measurement technique

Global strain measurement is still often used in practice when obtaining data to calculate M_R for design purposes. In the tests reported in this thesis the global M_R measured in the HCA was approximately half the measured local M_R for dry of optimum specimens (Section 5.4.4). The ratio of local to global M_R was 1.3 at optimum water content and was close to one for wetter material. M_R values determined using the global CTX strain measurement did not reflect the true values, determined using local strain measurement. It is concluded that M_R can only be determined accurately when using local strain measurement.

Consideration of measurement resolution is important as very stiff specimens, such as those tested in this work, require the ability to measure very small displacements, especially for small stress excursions. Measurements were improved by reducing the calibration range (increasing resolution) and using rubber bands around the LVDT brackets (improving conformance), as discussed in Section 5.4.5.

The CTX and HCA (under CTX conditions) determinations of M_R were comparable for unsaturated specimens, irrespective of the lower cyclic frequency used in the HCA (0.0167 Hz) (see Section 5.4.3). The CTX frequency of 0.5 Hz resulted in significantly lower M_R for wet specimens ($S_r > 90\%$, w=8%) probably due to the development of positive excess pore water pressure.

The influence of loading sequence on measured M_R has generally been neglected or regarded as insignificant, in the existing literature. It was found in these tests that the loading sequence influenced the M_R value measured at low confining stresses (p_o=15 kPa, sequence 6, 11, 16) as a result of the densification at higher confining stresses (Section 5.4.2). For the limited testing carried out in this study, a change in loading sequence for HCA testing did not appear to significantly influence measured results. Some variation was noted due to the stiffening effect under SP1 stress cycles (no PSR) that was not seen for SP2 cycles (with PSR) (see Section 5.4.1).

5.5.2 Effect of confining stress

The confining stress, p_o, is often considered to be the most significant factor to influence M_R when assessing standard laboratory results of specimens at optimum water content. For the clayey sand tested, Material B, a change in confining pressure from 30 kPa to 85 kPa (55 kPa increase) resulted in a relative change in M_R of 1.4 (40% increase) for the applied stress ratio (q_{cyc}/p_o) of 1.0 (refer to Section 5.2.1). The increase in M_R was dependent on the stress ratio and was 1.4, 1.7 and 1.8 for q_{cyc}/p_o equal to 1.0, 2.0 and 3.0 respectively.

An increase in p_o significantly influenced CTX specimens at high water contents resulting in densification of the material, which in turn increased M_R. The relative effect of p_o on M_R was less significant for CTX specimens tested dry of optimum, where volumetric strain is small, and prevented by the matric suction or equivalent confinement. The magnitude of p_o chosen for laboratory evaluation of M_R requires assumptions regarding K_0 and whether to include an average horizontal stress for the loaded track.

Although the influence of p_o is significant, the range of in-situ confining stresses for shallow foundations is very low. For the likely range of p_o between 15 kPa and 40 kPa (Miller et al., 2000; Shahu et al., 2000) M_R for optimum water content specimens increased by 30% and 40% when $q_{cyc} = p_o$ and $q_{cyc} = 2p_o$ respectively. The importance of the confining stress increased when applied shear stress increased and reduced as matric suction increased.

5.5.3 Effect of deviator stress

The influence of the confining stress and the cyclic deviator stress (q_{cyc}) should be simultaneously assessed. The CTX test results showed that the cyclic deviator stress, q_{cyc}, and principal stress ratio significantly influence M_R. The effect of q_{cyc} changes depending on whether material is wet of optimum or dry of optimum. M_R increased due to q_{cyc} when wet, while decreasing when dry (refer to Section 5.2.2). Wet CTX specimens experienced large permanent deformation under the applied stresses and the increase in M_R has been ascribed to densification. The difference in behaviour could also potentially link to the difference in micro-structure produced when the material is compacted wet or dry of optimum respectively. Densification of CTX specimens compacted at optimum water content resulted in an increase in the degree of saturation of the material, and a subsequent change in response to q_{cyc}.

A trend of M_R decrease due to an increase in the principal stress ratio (in terms of net normal stress) was observed for dry of optimum CTX specimens at various confining stresses. A reduction in M_R of approximately 20% was observed when q_{max}/p_n increased from approximately 0.8 (q_{cyc}/p_o of 1.0) to 1.5 (q_{cyc}/p_o of 3.0), but was influenced by the water content of the material. This same trend was observed for CTX specimens at optimum water content until larger strains resulted in in an onset of dilation.

5.5.4 Effect of degree of saturation

Otter et al. (2015) has previously used the Stokoe resonant column apparatus to determine very small strain modulus, G_0, as a surrogate for resilient modulus. Tests were carried out under isotropic loading conditions. They found that the stiffness of the typical rail formation material could be increased by a factor of three for a confining stress of 20 kPa, depending on the water content (and hence degree of saturation) at which it was compacted and tested (refer to Section 5.3.4).

The results of unsaturated hollow cylinder and triaxial testing reported here in general confirm the large effect of degree of saturation on stiffness, in this case on resilient (Young's) modulus, M_R. The modulus was found to increase up to six times when compared to measurements made near saturated condition (see Section 5.3.2). This significant increase in M_R resulted not only from the direct effect of matric suction, but also from the lower permanent strain levels produced under this loading. The permanent strain for low water content specimens were significantly smaller (0.002% for w=4 and 5%) than at higher water content (0.17% at optimum w=7%) after 500 cycles.

Material tested saturated was found to give unrealistically low stiffnesses when compared with those used for pavement design; a significant increase in M_R occurs even for slight changes in water content as concluded by Sauer and Monismith (1968). M_R nearly

doubled when degree of saturation changed from 98% to approximately 85% (at optimum water content, w=7%).

5.5.5 Effect of principal stress rotation

Previous laboratory testing on typical rail formation material in a saturated state (approx. w=9.5%) was conducted by Gräbe (2002) using the HCA. His results suggested that the selected combination of cyclic vertical and shear stress (90^o out of phase) for a typical rail formation reduced M_R by approximately 30% compared with M_R measured without PSR (i.e. under cyclic triaxial conditions).

In this work, the reduction in M_R (approximately 15% at optimum water content) caused by PSR for the stress path applied was small compared with the measured increase of up to six times due to lack of saturation. As discussed in Section 5.2.3, this research found that the influence of PSR reduced for low water content (high suction) conditions and increased when the material was saturated. The matric suction appeared to stabilise the structure of the material, resulting in higher resistance to relative particle slippage (Tarantino and Tombolato, 2005) caused by the relatively low shear stress applied.

PSR (applied in the HCA) was also found to reduce the stiffening effect observed due to repeated load cycles, N, discussed in Section 5.4.1 under CTX conditions. This could be linked to the continuous strain increase due to PSR cyclic conditions. Gräbe and Clayton (2009) also reported an increase in the rate of strain accumulation due to PSR for saturated specimens. The rate of permanent strain accumulation for unsaturated specimens tested in the HCA was found to reduce as the degree of saturation or water content reduced.

The values of shear modulus (G_R) determined from the HCA, based on data from Gräbe (2002) and tests reported in this thesis, were lower than would be expected for an isotropic elastic material on the basis of the measured resilient moduli. This suggests that compaction produces an anisotropic material. For an isotropic linear elastic material the resilient Youngs modulus would be expected to be about 2-3 times the shear modulus depending on Poissons ratio. The resilient Youngs modulus measured in the HCA was approximately 4 times the shear modulus (see Section 5.3.4).

5.6 Application of existing resilient modulus models to data

A number of constitutive models have been developed to predict the resilient response of unbound granular pavement materials in terms of total stress, as reviewed by Lekarp et al. (2000). However, these models do not explicitly incorporate the effect of matric

suction resulting from changes in water content. Salour and Erlingsson (2015) investigated the modelling of M_R for unsaturated subgrade soils. They reviewed several predictive models (Parreira and Goncalves, 2000; Yang et al., 2005; Liang et al., 2008; Sawangsuriya et al., 2009; Cary and Zapata, 2011; Ng et al., 2013) developed to include the influence of matric suction as a stress state variable. This section is not intended to validate and compare the available models, but as an initial assessment of the application of such models to the CTX data. The multiple linear regression analyses reported here were carried out using Microsoft Excel.

5.6.1 Total stress model

The $k-\Theta$ (Bulk Stress Model) developed by Hicks and Monismith (1971) is often used for unbound granular materials due to its simplicity (Lekarp et al., 2000). The Bulk Stress Model (Equation 3.11) was extended by Uzan (1985) to include the influence of deviator stress, which is especially important for finer grained subgrade materials. Uzan's model has been adapted in the mechanistic-empirical pavement design approach as given in Equation 3.12 and is referred to as the Universal Model (Salour and Erlingsson, 2015).

The model parameters for the individual CTX tests at a range of water contents were determined and are summarised in Table 5.3. The bulk stress model was unable to capture the resilient behaviour of the dry of optimum specimens (OMC-1%, OMC-2%, and OMC-3%), with R^2 less than 0.25 due to these test being insensitive to the minor principal total stress (net normal confining stress for $u_a = 0$) for higher matric suction conditions as discussed in Section 5.2.1. Combining all the CTX results in one analysis resulted in R^2 of 0.013. The predicted M_R, using the Bulk Stress Model in terms of total stress, is plotted relative to the measured M_R in Figure 5.33a.

The coefficient of determination (R^2) for the Universal model ranged between 0.54 and 0.98 for individual CTX tests. However, when combining all CTX test data (optimum and dry of optimum specimens) R^2 was 0.04 (Table 5.5) as the total stress analysis does not capture the influence of matric suction and thus environmental factors such as rainfall and temperature. The predicted M_R, using the Universal Model in terms of total stress, is plotted relative to the measured M_R in Figure 5.33b.

5.6.2 Matric suction models

Salour and Erlingsson (2015) summarise the advanced constitutive M_R models developed over recent years to include the influence of matric suction on the resilient modulus of unbound granular pavement material (Section 3.1.4). The Advanced Model (Equation 3.13), suggested by Cary and Zapata (2011) as an extension of the Universal Model to include for pore pressure conditions (positive more water pressure in saturated material or matric suction in unsaturated material), was used in this study to assess the

M_R data. When including the matric suction in the constitutive model, the coefficient of determination (R^2) was 0.87 which is considered good as data scatter is common in unbound granular pavement material testing (Salour et al., 2014). The regression coefficients are given in Table 5.5. It can be seen that, for the representative railway formation material (clayey sand), M_R was most sensitive to the octahedral shear stress, followed by the matric suction. The predicted M_R, using the Advanced Model by Cary and Zapata (2011), is plotted relative to the measured M_R in Figure 5.34.

5.6.3 Intergranular stress method to normalise stiffness

The proposed advantage of assessing unsaturated pavement material stiffness in terms of intergranular stress ($\sigma_i = \sigma_n + \sigma_s$) is the use of existing total stress models, as proposed by Heath et al. (2004) and Liang et al. (2008). The suction stress (σ_s) was estimated from the soil water retention curve, SWRC, using the effective degree of saturation (S_e), as discussed in Section 5.3.3. S_e is taken as zero below the residual water content and as 100% for fully saturated conditions. Otter (2011) selected the residual (gravimetric) water content (w_r) to be at 3%. Due to some uncertainty related to the residual water content and the fitting of the SWRC, a second, lower, w_r equal to 2% was considered when estimating σ_s (Table 5.4). The intergranular bulk stress was subsequently calculated for both cases for use in the two total stress models considered.

The regression coefficients for the Bulk Stress Model and the Universal Model were calculated using the intergranular stress, for the two separate cases (w_r=3% and w_r=2%), as given in Table 5.5. The intergranular stress approach led to coefficients of determination (R^2) of 0.61 and 0.78 for the Bulk Stress Model, and 0.84 and 0.90 for the Universal Model respectively. The higher R^2 value for the w_r=2% case, for both the applied models, suggest that the selected w_r (=3%) for the SWRC (Otter, 2011), is too high. Refinement of the SWRC should be carried out, with focus on establishing the residual water content.

The suction stress (σ_s) was back calculated from the M_R results for specimens at different water contents, as suggested by Heath et al. (2004), using CTX+0v0 as the base test. The calculated σ_s values are compared to the estimated σ_s from the SSCC plotted in Figure 5.21. The results obtained when back-calculating σ_s are similar to σ_s estimated for the SSCC if w =2% (rather than 3%) as seen in Figure 5.35. However, care should be taken when determining the suction stress from stiffness results, due to the non-linear stress-strain behaviour of soil. A reduction in matric suction is also possible due to localised dilation on the shear plane (leading to increased void space) as well as relative movement of particles (Heath et al., 2004). Further assessment of the ability to predict M_R using different constitutive models and the intergranular stress approaches should be considered.

Table 5.1: Average M_R values for selected test conditions for comparison, calculated from CTX results (tabulated in Appendix C) and HCA results (Table 4.14)

Gravimetric water content (w), % (approx.)		Average M_R (CTX) $q_{cyc} = 0.5p_o$	Average M_R (CTX) $q_{cyc} = p_o$	Average M_R (CTX) $q_{cyc} = 2p_o$	Average M_R (CTX) $q_{cyc} = 3p_o$
4	p_o = 30kPa	568	481	439	396
5		450	421	357	313
6		298	245	196	172
7 (OMC)		145	126	103	105
	p_o				
OMC	40kPa	156	140	118	127
	55kPa	172	152	136	151
	85kPa	204	176	175	187

Gravimetric water content (w), % (approx.)		Average M_R (CTX) p_o = 15kPa	Average M_R (CTX) p_o = 30kPa	Average M_R (CTX) p_o = 40kPa	Average M_R (CTX) p_o = 55kPa	Average M_R (CTX) p_o = 85kPa
4	$q_{cyc} = p_o$	461	481	501	514	551
5		417	421	426	435	460
6		250	245	253	266	292
7 (OMC)		108	126	140	152	176
	q_{cyc}					
OMC	$2p_o$	89	103	118	136	175
	$3p_o$	77	105	127	151	187

Degree of Saturation (S_R), % (approx.)	Gravimetric water content (w), % (approx.)		Average $M_{R,w}$ (= $M_{R,SP1}$), MPa (CTX and HCA)	$M_{R,SP2}$ (c500), MPa	Global M_R (HCA)	Global M_R (CTX)
45	4	$p_o = q_{cyc}$ = 30kPa	466	419	169	69
58	5		431	500	222	64
63	6		241	225	128	83
88 (OMC)	7 (OMC)		126	118	97	72
98 (sat)	8		78	66	76	62

Table 5.2: Normalised M_R and calculated ratios to assess the relative impact of the different factors considered (conditions used for normalisation highlighted). Values estimated from respective figures as noted

Fig. 5.7

Gravimetric water content (w), % (approx.)		Normalised M_R $q_{cyc} = 0.5p_o$	Normalised M_R $q_{cyc} = p_o$	Normalised M_R $q_{cyc} = 2p_o$	Normalised M_R $q_{cyc} = 3p_o$
4	p_o = 30kPa	1.25	1.0	0.9	0.85
5		1.3	1.0	0.85	0.75
6		1.2	1.0	0.8	0.7
7 (OMC)		1.25	1.0	0.8	0.7

Fig. 5.7

	p_o				
OMC	55kPa	1.2	1.0	0.85	0.8
	85kPa	1.15	1.0	0.9	0.85

Figs. 5.2 & 5.3

Gravimetric water content (w), % (approx.)		Normalised M_R p_o = 15kPa	Normalised M_R p_o = 30kPa	Normalised M_R p_o = 40kPa	Normalised M_R p_o = 55kPa	Normalised M_R p_o = 85kPa
4	$q_{cyc} = p_o$	0.95	1.0	1.0	1.1	1.15
5		1.0	1.0	1.0	1.05	1.1
6		1.0	1.0	1.05	1.1	1.2
7 (OMC)		1.0	1.0	1.1	1.2	1.4

Fig. 5.2

	q_{cyc}					
OMC	$2p_o$	0.85	1.0	1.15	1.3	1.65
	$3p_o$	0.75	1.0	1.2	1.4	1.8

Degree of Saturation (S_R), % (approx.)	Gravimetric water content (w), % (approx.)		Fig. 5.19 MR_S ($M_{R,w}/M_{R,sat}$)	Fig. 5.13 MR_{PSR} ($M_{R,SP1}/M_{R,SP2}$)	Fig. 5.29 Local/Global (HCA)	Fig. 5.29 Local/Global (CTX)
45	4	$p_o = q_{cyc}$ = 30kPa	6.0	1.02	2.1	7.0
58	5		5.0	1.05	1.9	6.5
63	6		3.0	1.1	1.8	3.0
88 (OMC)	7 (OMC)		1.5	1.15	1.3	2.0
98 (sat)	8		1.0	1.35	1.0	1.0

Table 5.3: Regression coefficients for individual cyclic triaxial tests (CTX) for two frequently used constitutive M_R models (1) the Bulk stress model (Equation 3.11) and (2) the Universal model (Equation 3.12)

Test number	Test name	(1) k_1	k-Θ k_2	model R^2	(2) k_1	Universal k_2	model k_3	R^2
3	CTX+0v0	1023	0.405	0.491	1167	0.921	-1.647	0.875
4	CTX+0v0$_p$	1011	0.361	0.452	1045	0.754	-1.105	0.651
10	CTX+0v2	704	0.699	0.757	846	1.105	-1.503	0.864
17	CTX+0v1$_c$	0780	0.558	0.978	775	0.617	-0.174	0.984
5	CTX-1v0	2246	0.091	0.045	2380	0.645	-1.563	0.617
7	CTX-2v0	4079	-0.020	0.005	4388	0.359	-1.140	0.589
12	CTX-2v1$_r$	3893	-0.011	0.001	4650	0.339	-1.240	0.542
6	CTX-3v0	5620	-0.081	0.091	5914	0.278	-1.028	0.693
8	CTX-3v1	3983	0.169	0.234	4926	0.575	-1.435	0.817
11	CTX-3v1$_r$	4455	0.022	0.007	5034	0.360	-1.101	0.665

Table 5.4: Suction stress, σ_s (kPa), calculated from SWRC with different residual water contents and back calculated from CTX M_R results fitting regression curves from CTX+0v0

Test name	ψ_m (kPa) (avg w_f)	σ_s ($w_r = 3\%$)	σ_s ($w_r = 2\%$)	σ_s ($w_r = 1.5\%$)	σ_s CTX+0v0
CTX+0v0	-62*	40	43	44	0
CTX+0v0$_p$	-40*	26	28	29	-4
CTX+0v2	-62*	40	43	44	-5
CTX+0v1$_c$	-65*	42	45	46	-4
CTX-1v0	-298	129	151	160	61
CTX-2v0	-452	132	174	191	165
CTX-2v1$_r$	-424	122	162	178	165
CTX-3v0	-739	135	214	246	261
CTX-3v1	-747	139	218	250	224
CTX-3v1$_r$	-778	127	212	246	211
HCA+0v1	-62*	39	42	43	
HCA+0v2	-40*	26	28	29	
HCA-1v1	-318	138	162	171	
HCA-1.7v1	-394	149	181	194	
HCA-2v1	-495	136	183	202	
HCA-3iiv1	-735	133	211	243	

*adjusted for higher saturation due to large volumetric compression

Table 5.5: Regression coefficients from linear regression analyses on all CTX tests combined excluding wet of optimum specimens. Assessed before and after adjusting for estimated suction stress (1) the Bulk stress model (Equation 3.11) and (2) the Universal model (Equation 3.12); or including matric suction as in (3) the Advanced universal model (Equation 3.13)

	(1) k-Θ model			(2) Universal model				(3) Advanced Universal model				
	k_1	k_2	R^2	k_1	k_2	k_3	R^2	k_1	k_2	k_3	k_4	R^2
Θ (no suction)	2661	0.13	0.013	2940	0.401	-0.912	0.037	883	0.565	-1.314	0.823	0.874
Θ_i (σ_s=f(SWRC, w_r=3%))	360	1.293	0.610	278	1.802	-1.839	0.843					
Θ_i (σ_s=f(SWRC, w_r=2%))	328	1.206	0.776	331	1.410	-1.240	0.903					

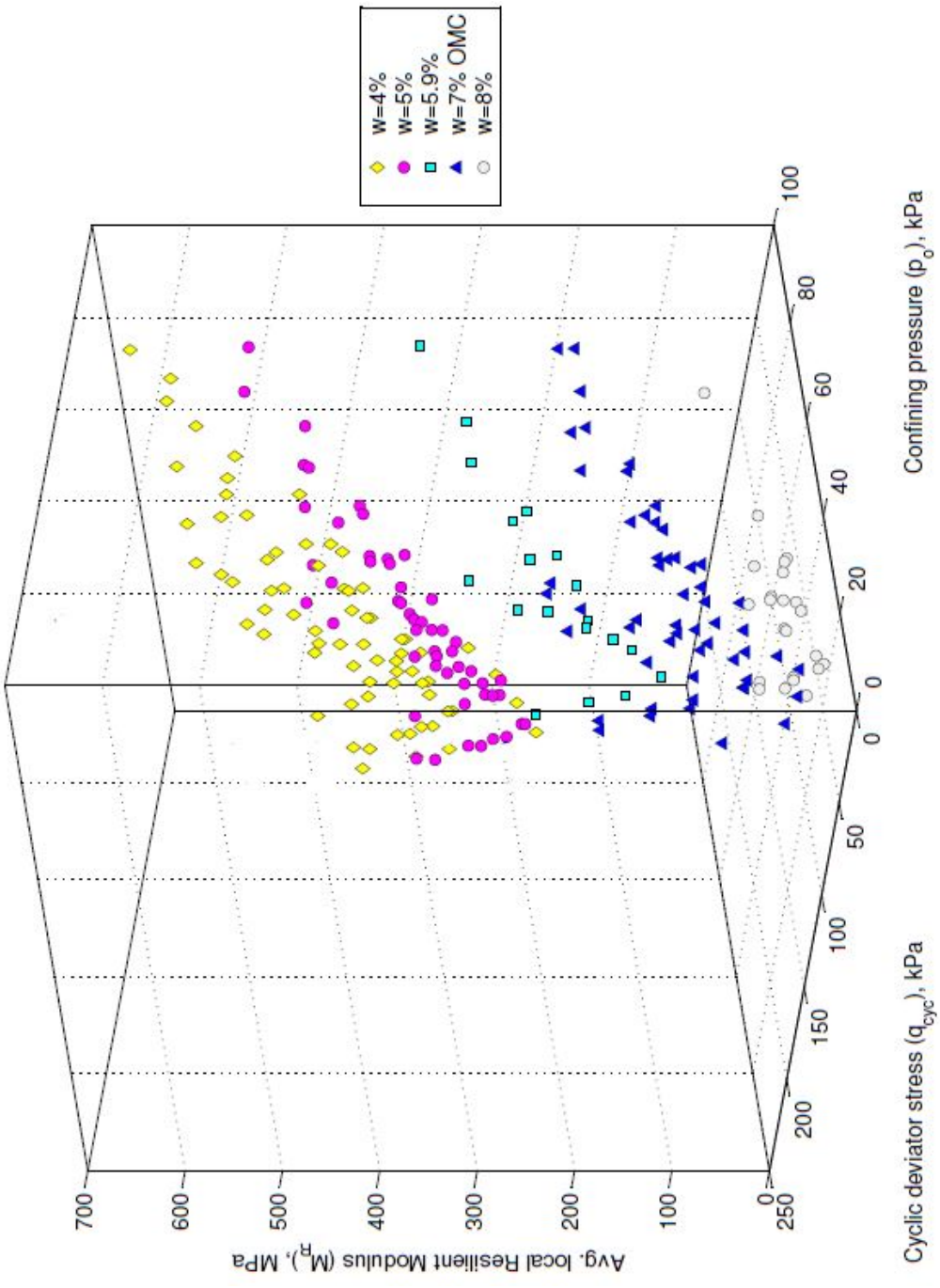

Figure 5.1: M_R measured in the CTX from all tests on different water content specimens relative to confining stress, $p_o = \sigma_{n3}$, and cyclic deviator stress, q_{cyc}

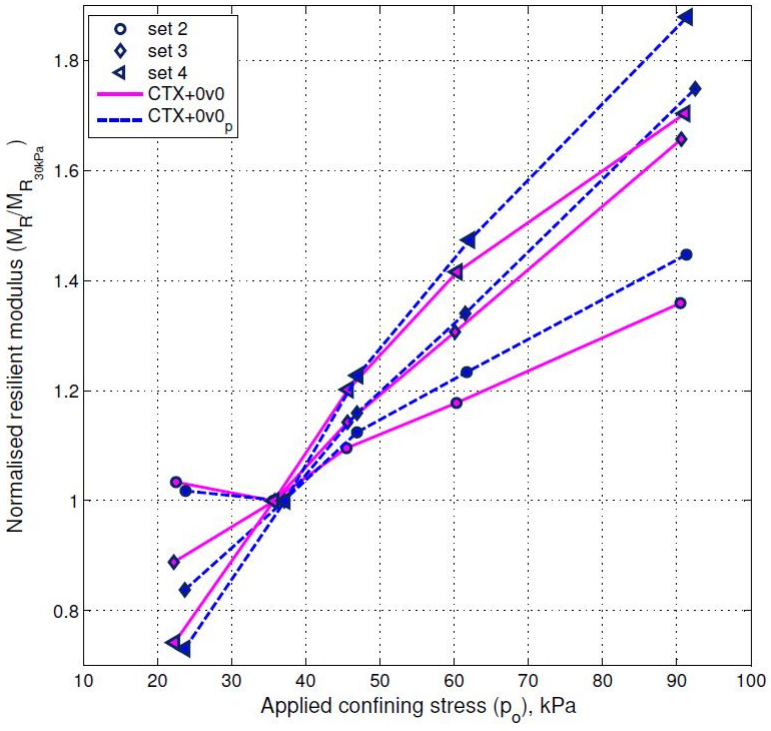

Figure 5.2: Normalised M_R for each stress sequence set (normalised by the M_R of the second sequence in each set) for specimens at OMC (w=7%); CTX+0v0 and CTX+0v0$_p$ relative to confining stress equal to the minor net normal stress, $p_o = \sigma_{n3}$

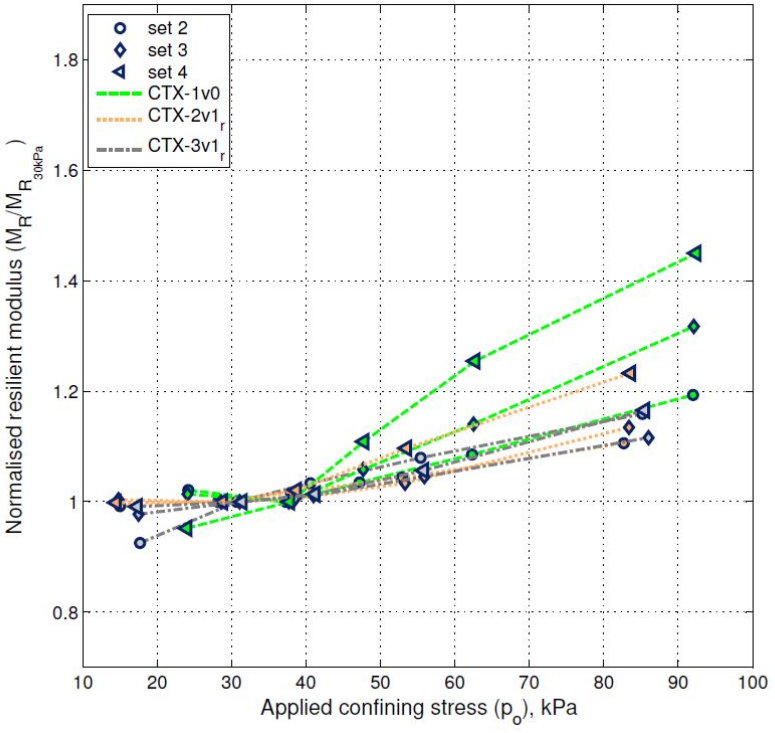

Figure 5.3: Normalised M_R for each stress sequence set (normalised by the M_R of the second sequence in each set) for specimens dry of OMC; CTX-1v0, CTX-2v1$_r$ and CTX-2v1$_r$ relative to confining stress, $p_o = \sigma_{n3}$

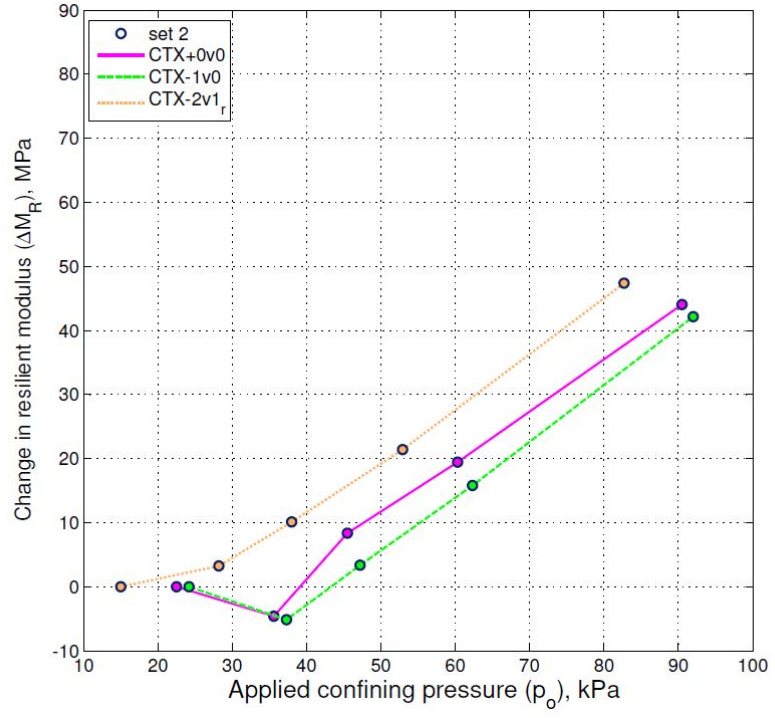

Figure 5.4: Change in resilient modulus, $\Delta\ M_R$, due to p_o for set 1 ($q_{cyc}/p_o = 1$) with cumulative vertical strain for CTX+0v0 less than 1%

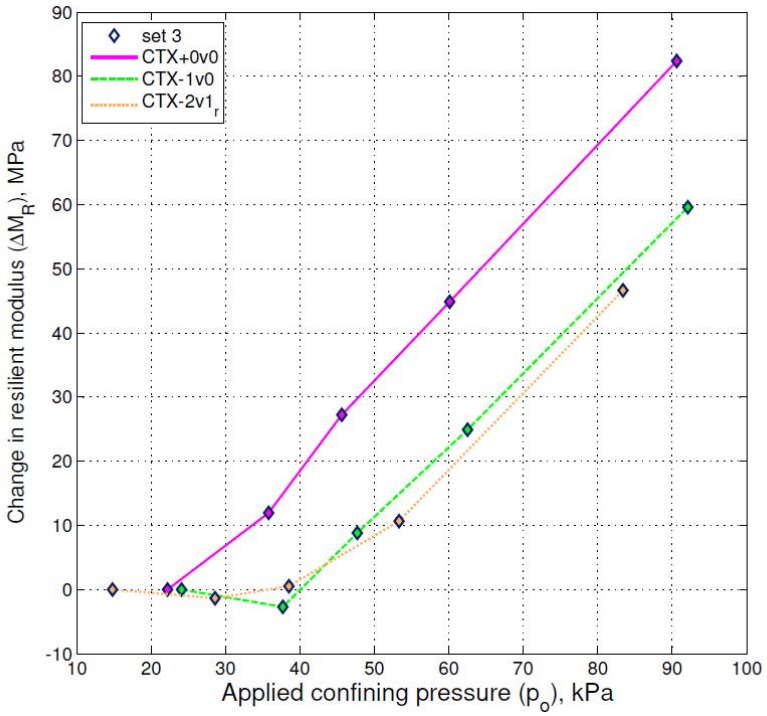

Figure 5.5: Change in M_R due to p_o for set 2 ($q_{cyc}/p_o = 2$) with cumulative vertical strain for CTX+0v0 up to 2.4%

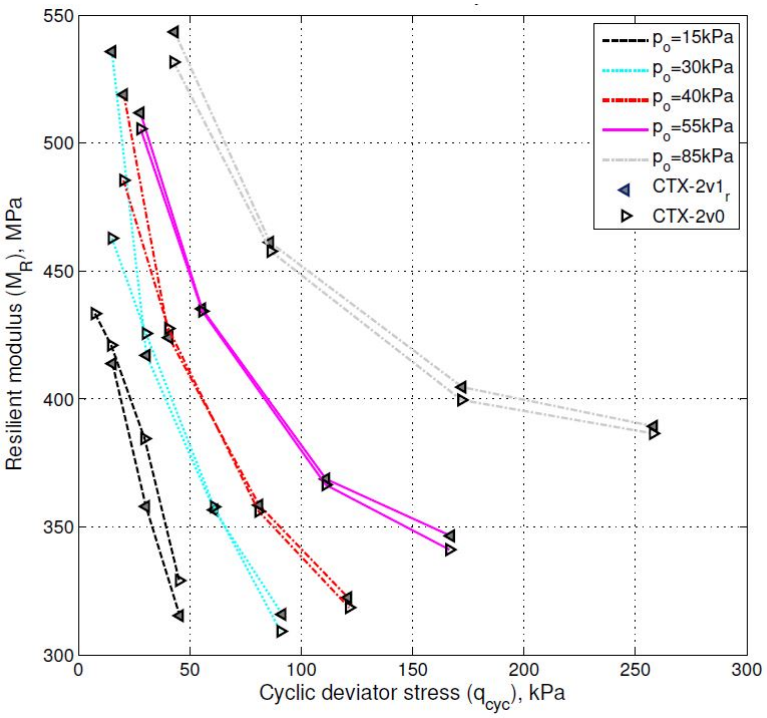

Figure 5.6: M_R at different p_o relative to q_{cyc} for dry of optimum specimens at w=5% (CTX-2v1$_r$ and CTX-2v0)

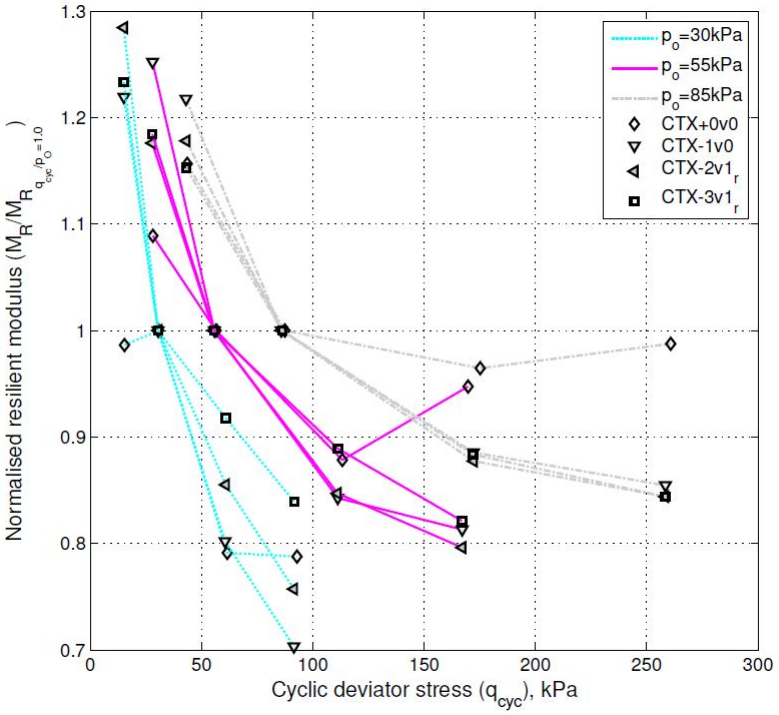

Figure 5.7: Normalised M_R versus q_{cyc} at three different p_o conditions (Normalised with M_R measured in set 2, $q_{cyc} = p_o$) for specimens at different water contents

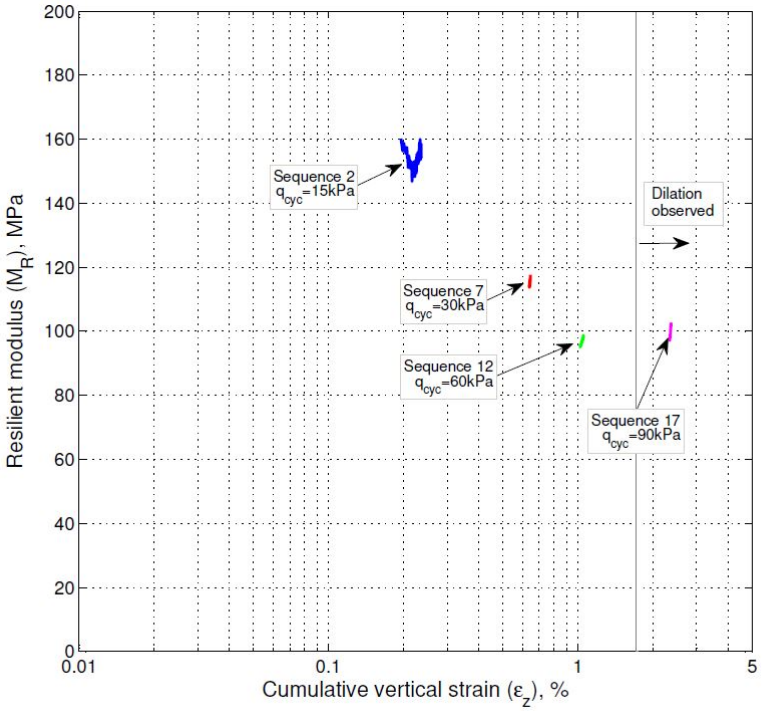

Figure 5.8: M_R relative to cumulative vertical strain since the start of the test for CTX+0v0$_p$ sequence 2, 7, 12 and 17 (with p_o=37 kPa)

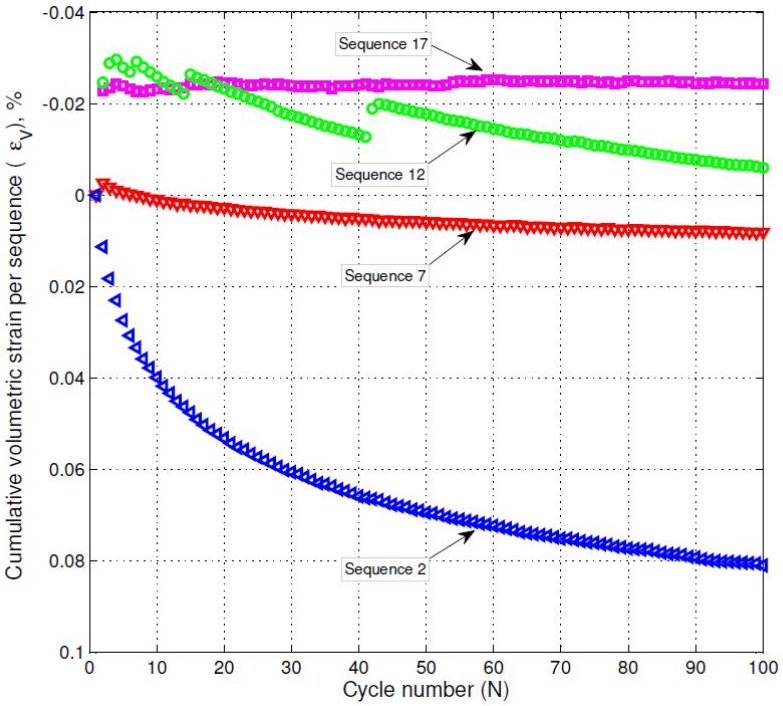

Figure 5.9: Cumulative volumetric strain for CTX+0v0$_p$ sequence 2, 7, 12 and 17 (with p_o=37 kPa)

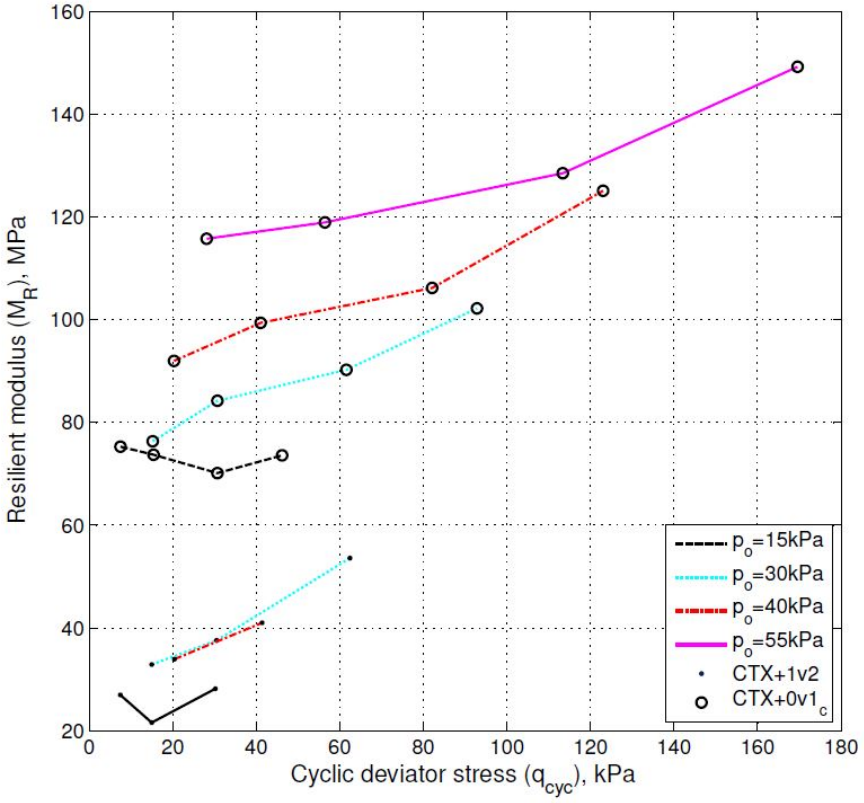

Figure 5.10: M_R at different p_o versus q_{cyc} for wet of optimum specimens (CTX+1v2) and OMC specimen CTX+0v1$_c$ compacted in 8 layers

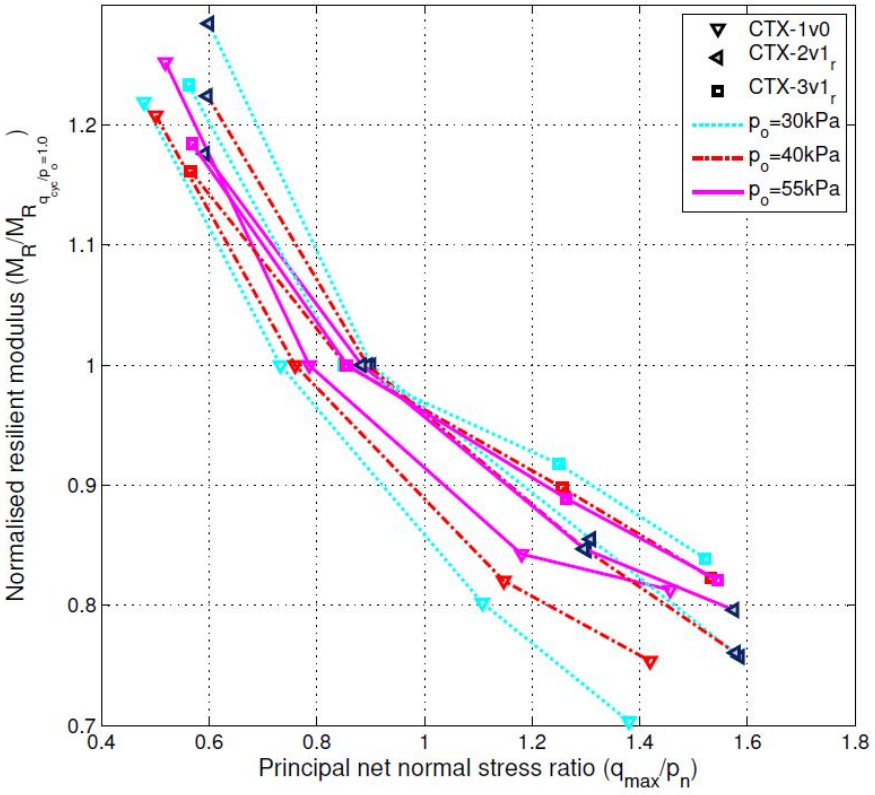

Figure 5.11: Normalised M_R, by M_R of set 2 ($q_{cyc} = p_o$) for dry of optimum specimens versus principal net normal stress ratio (q_{max}/p_n)

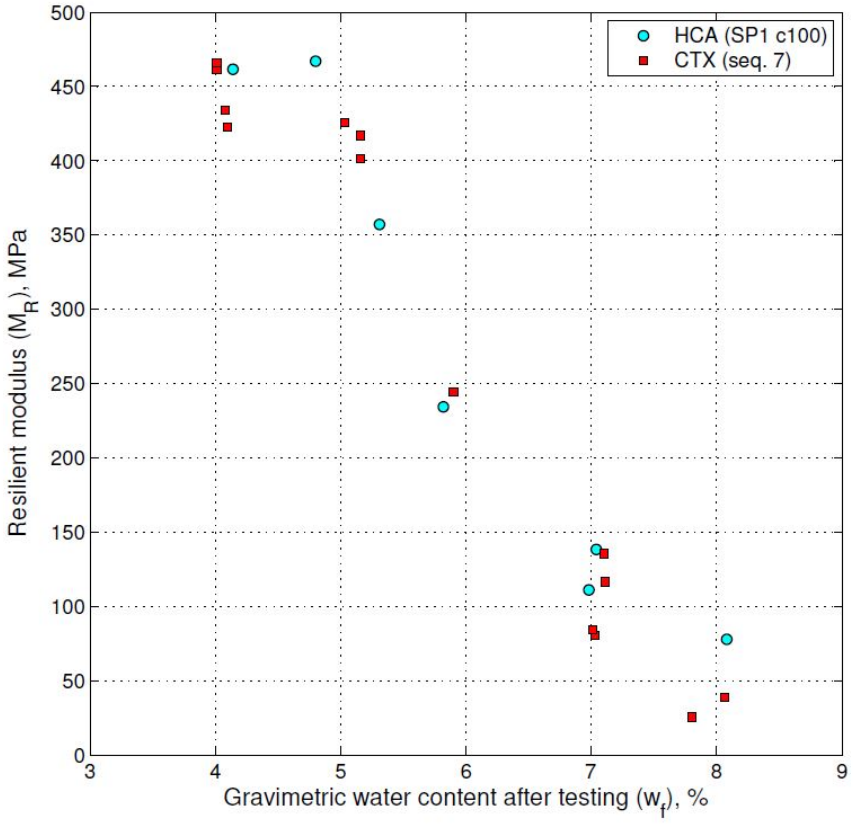

Figure 5.12: M_R measured in the HCA under CTX conditions (SP1, c100) compared to M_R measured in the CTX for different water content specimens

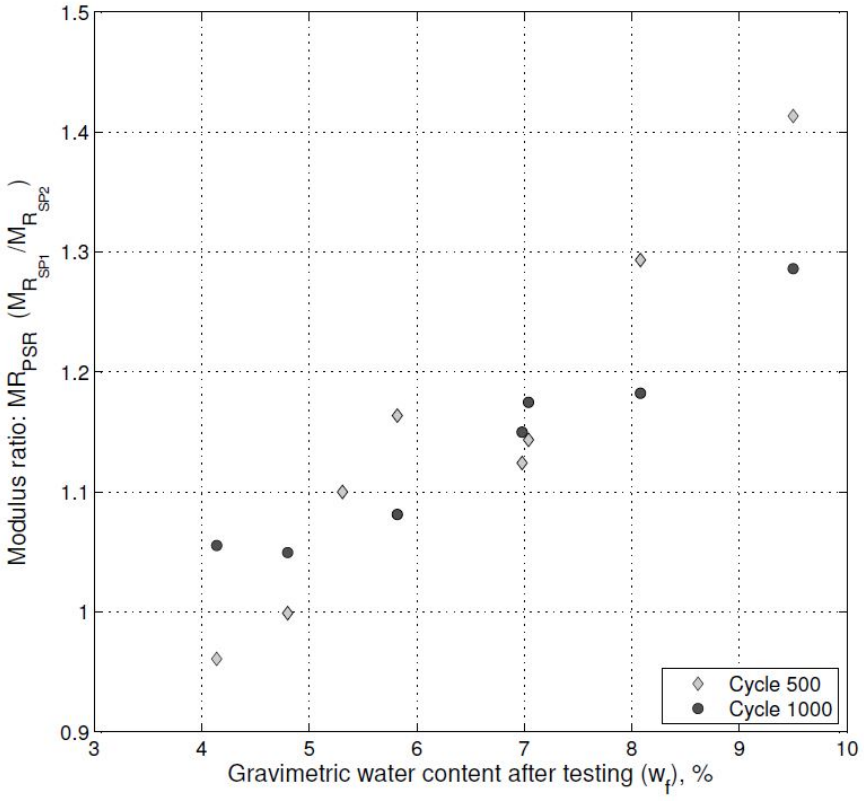

Figure 5.13: MR_{PSR}: M_R due to SP1 (no PSR) divided by M_R due to SP2 (with PSR) for specimens at different water contents tested in the HCA

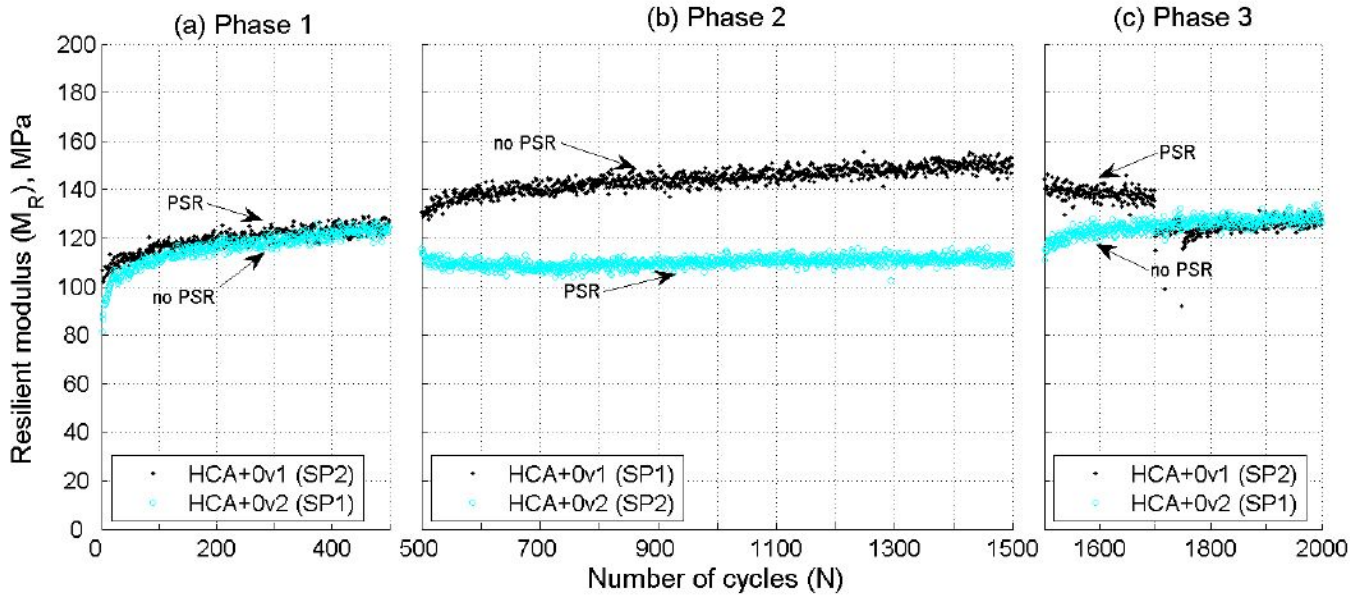

Figure 5.14: M_R development due to stress cycles with and without PSR measured for OMC specimens; HCA+0v1 and HCA+0v2 (a) Phase 1 (500 cycles); (b) Phase 2 (1000 cycles); and (c) Phase 3 (500 cycles)

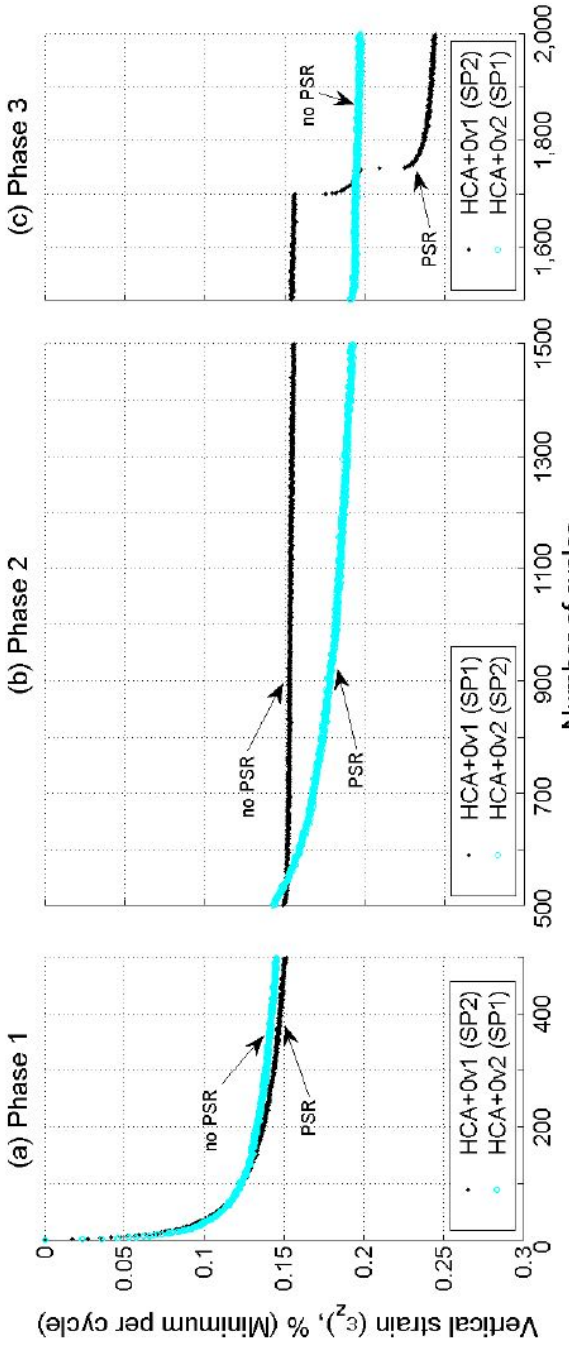

Figure 5.15: Vertical strain accumulation since the start of the test (excluding cycle 1) due to stress cycles with and without PSR measured for OMC specimens; HCA+0v1 and HCA+0v2 (a) Phase 1 (500 cycles); (b) Phase 2 (1000 cycles); and (c) Phase 3 (500 cycles)

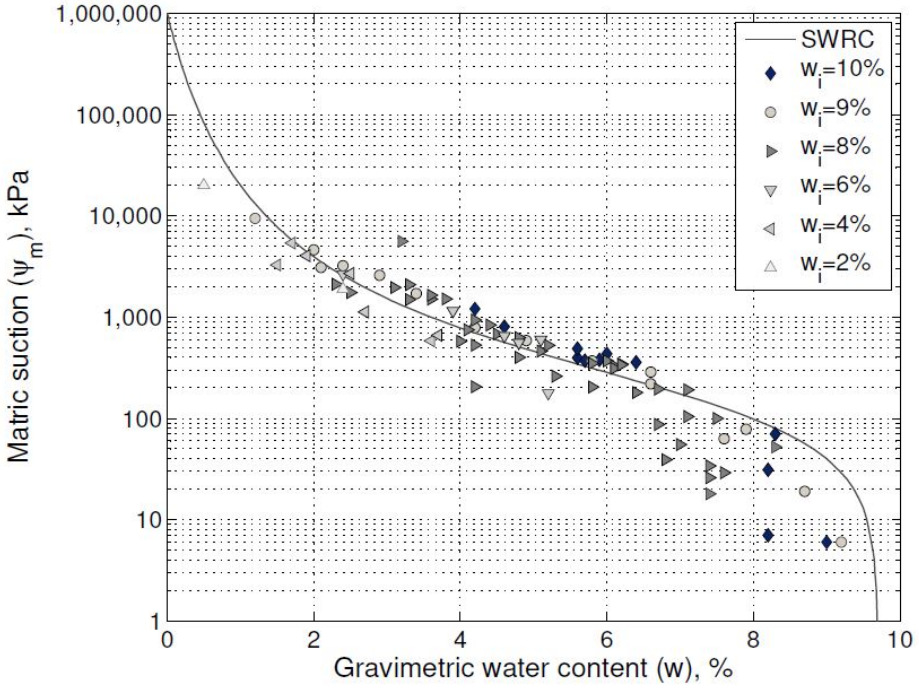

Figure 5.16: Matric suction measured by Otter (2011) using the direct contact filter paper technique. Material B specimens compacted and dried from different initial water contents

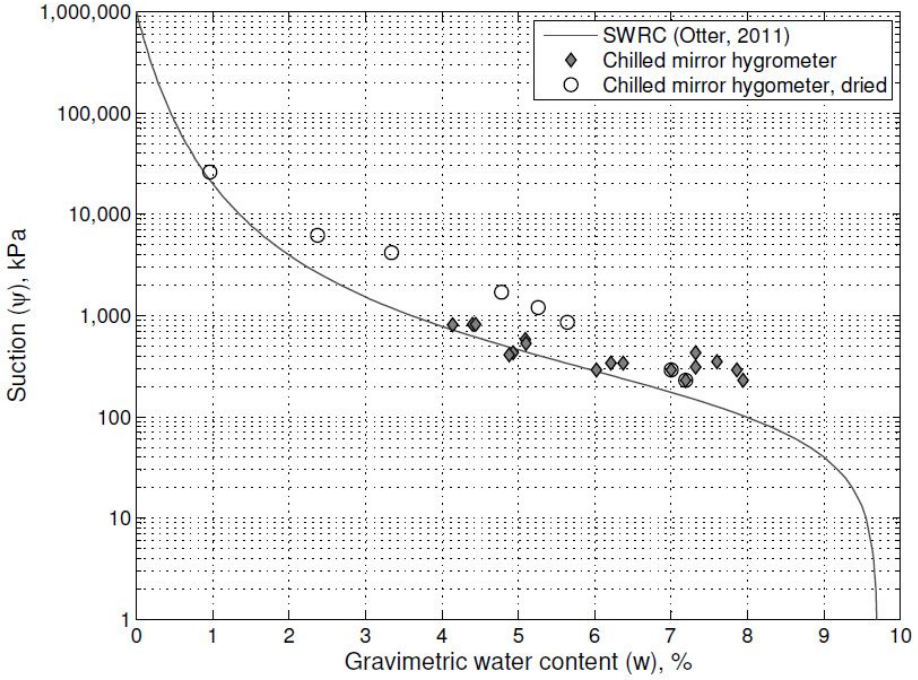

Figure 5.17: Total suction measured for Material B using the Chilled Mirror Dew-point Hygrometer at Cardiff University. Material tested at the compacted water content unless indicated as dried (from w=7%)

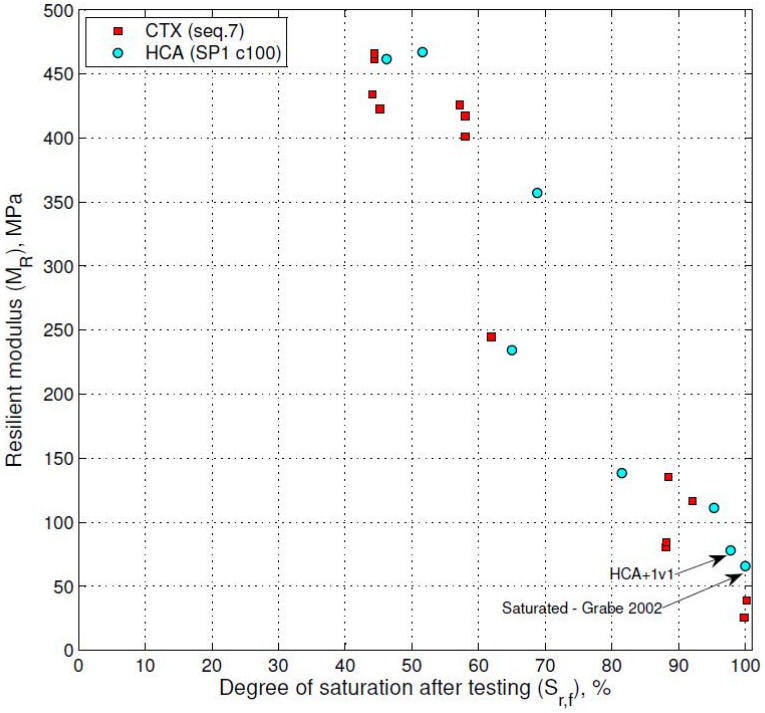

Figure 5.18: M_R measured in the HCA under CTX conditions (SP1, c100) compared to M_R measured in the CTX for different water content specimens relative to degree of saturation after testing

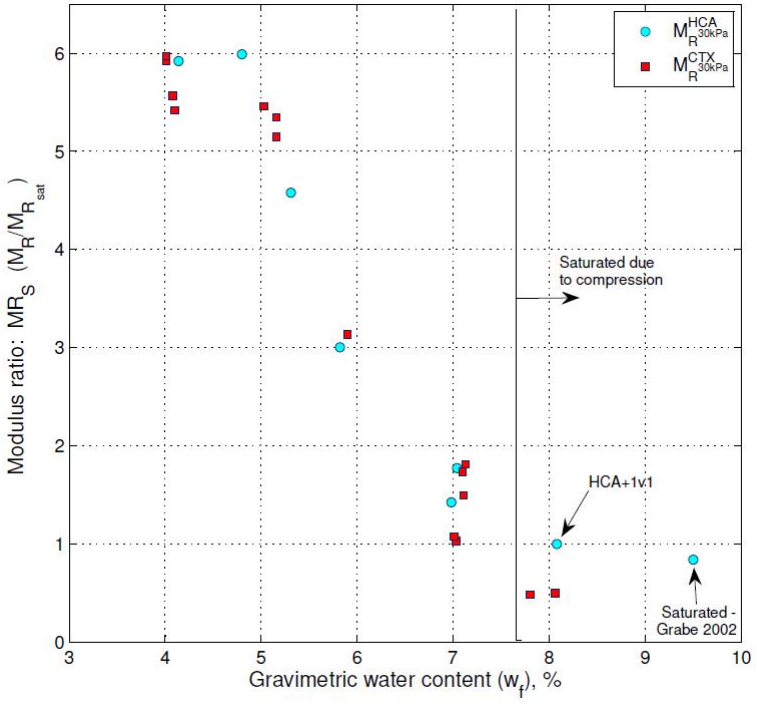

Figure 5.19: Suction modulus ratio, MR_s: HCA and CTX M_R normalised by $M_{R,sat}$ (HCA+1v1)

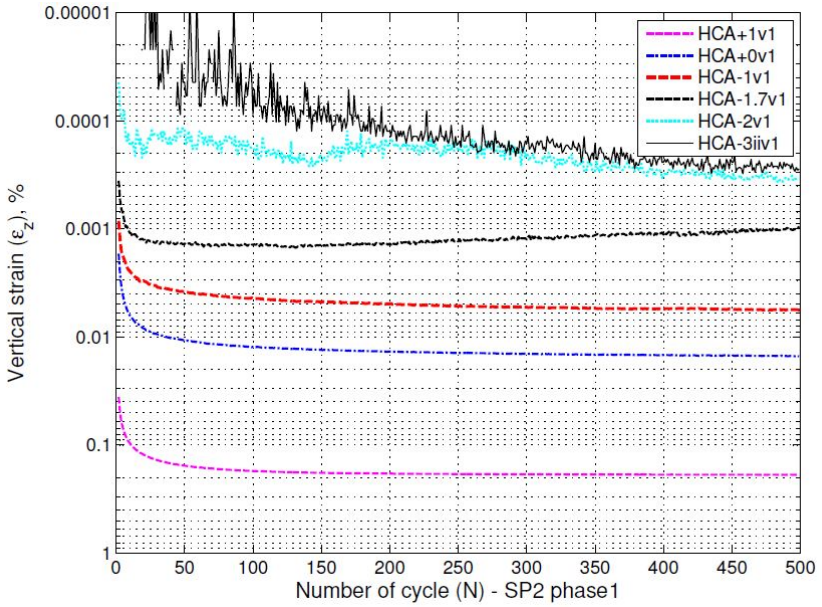

Figure 5.20: Permanent vertical strain accumulation for HCA phase 1 (500 cycles of SP2 including PSR) for different water content specimens

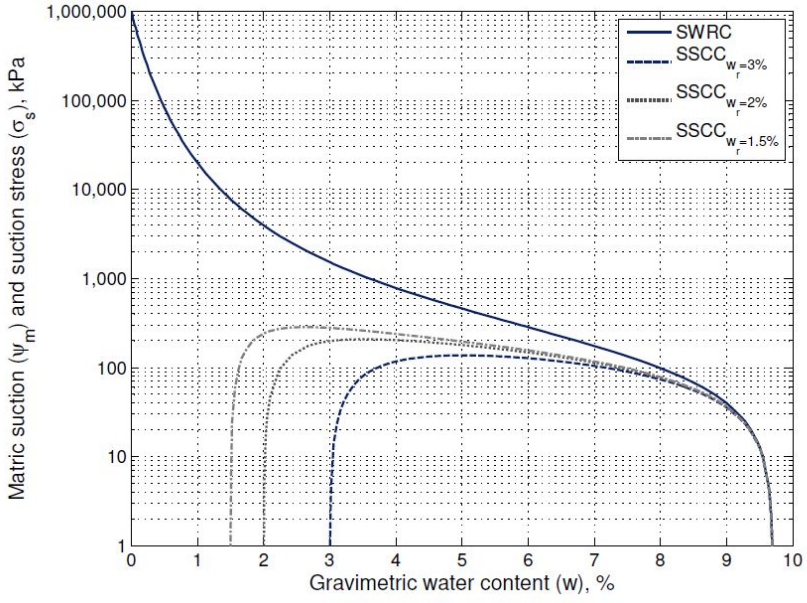

Figure 5.21: SWRC determined by Otter (2011) and calculated SSCC based on three different residual water contents w_r=3%, w_r=2%, and w_r=1.5%

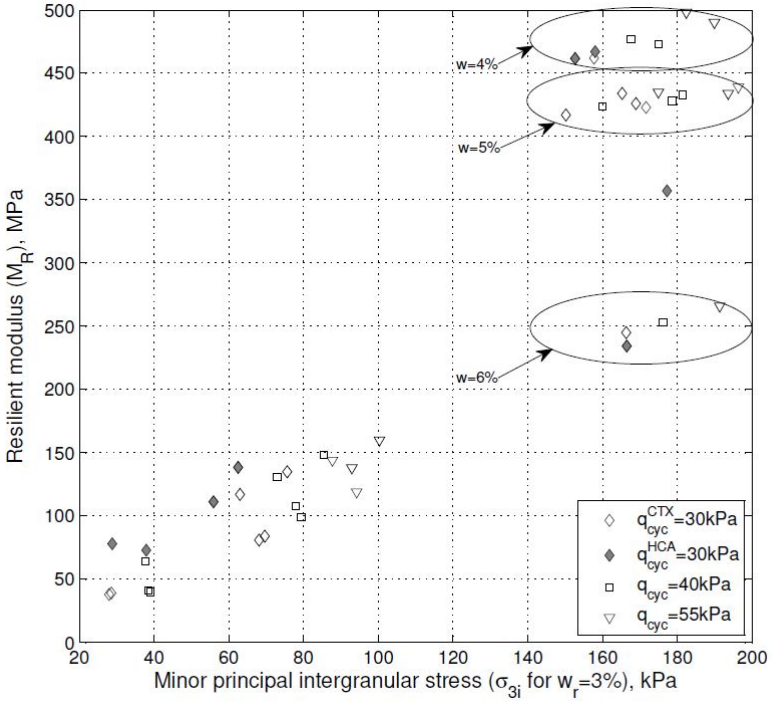

Figure 5.22: M_R for HCA and CTX sequence 7 (q_{cyc}=30 kPa); CTX sequence 8 (q_{cyc}=40 kPa) and sequence 9 (q_{cyc}=55 kPa) versus minor principal intergranular stress (σ_{i3}) calculated with suction stress (σ_s) for w_r=3%

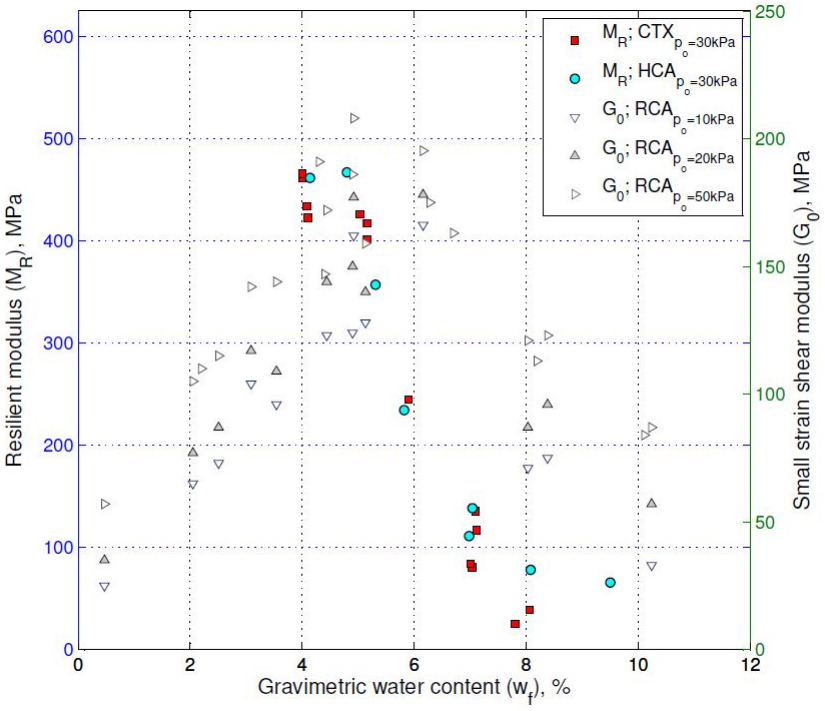

Figure 5.23: M_R measured for CTX and HCA test with p_o=30 kPa and small strain shear modulus, G_0, determined by Otter (2011) using the resonant column

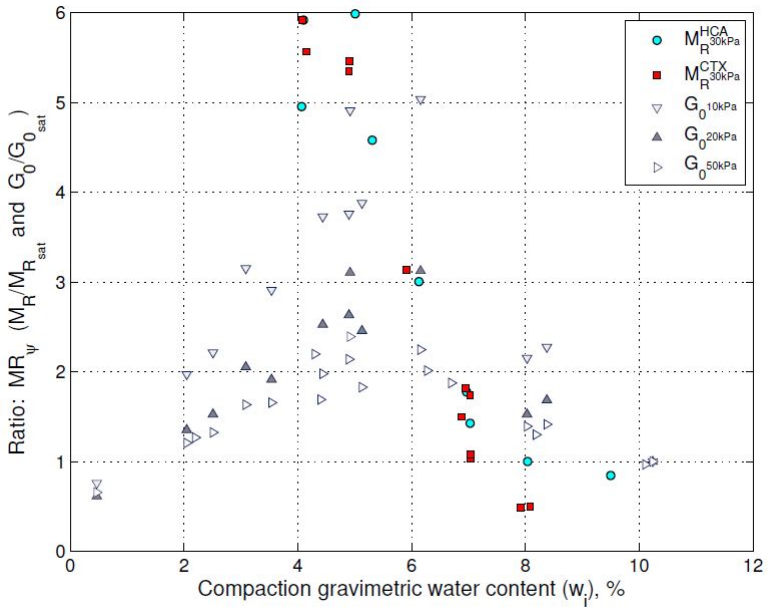

Figure 5.24: MR_s calculated for M_R measured using the CTX and HCA; and G_0 measured by Otter (2011) using the RCA (divided by $G_{0,sat}$)

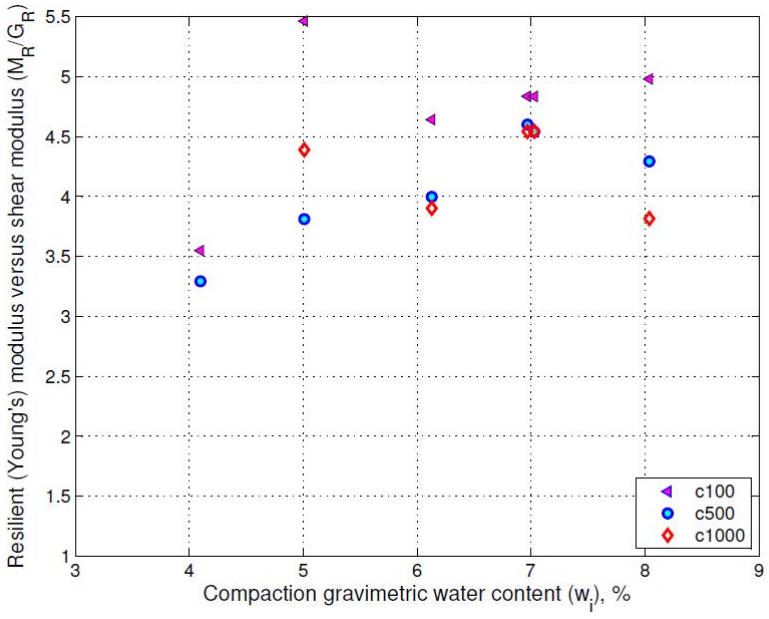

Figure 5.25: HCA: M_R (resilient Young's modulus) for SP2 relative to resilient shear modulus, G_R, measured for the same cycle ($\Delta\tau_{cyc}$=14 kPa) as after 100, 500 and 1000 cycles)

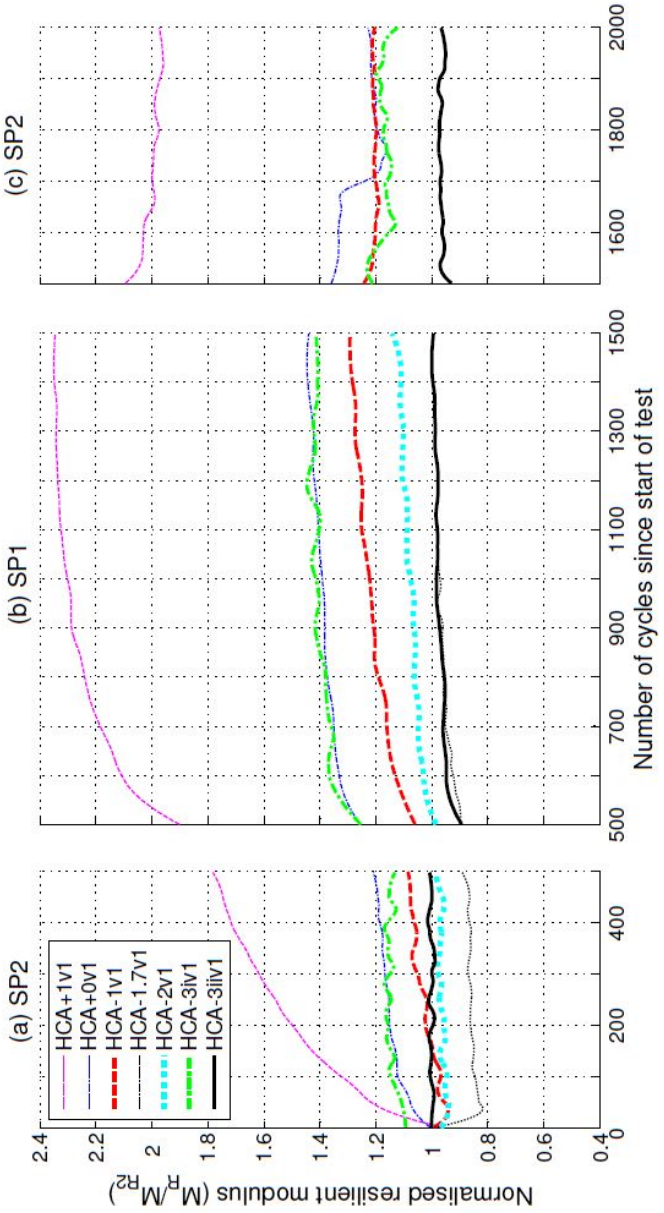

Figure 5.26: Normalised M_R (with M_R of cycle 2) for different water content tests using the HCA, (a) phase 1, SP2 with PSR; (b) phase 2, SP1 without PSR; and (c) phase 3, SP2 with PSR

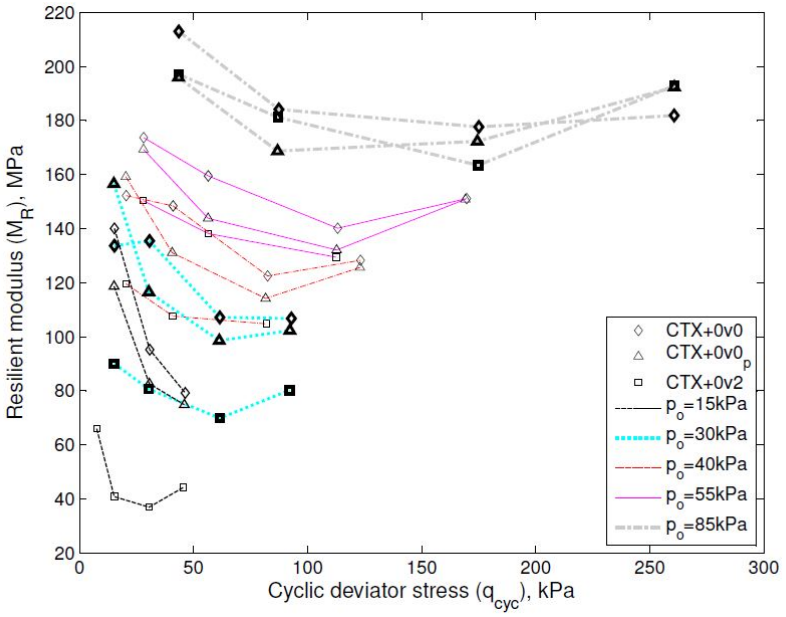

Figure 5.27: Resilient modulus, M_R, versus cyclic deviator stress, q_{cyc} for CTX+0v0, CTX+0v1$_p$ and CTX+0v2 (with change loading sequence)

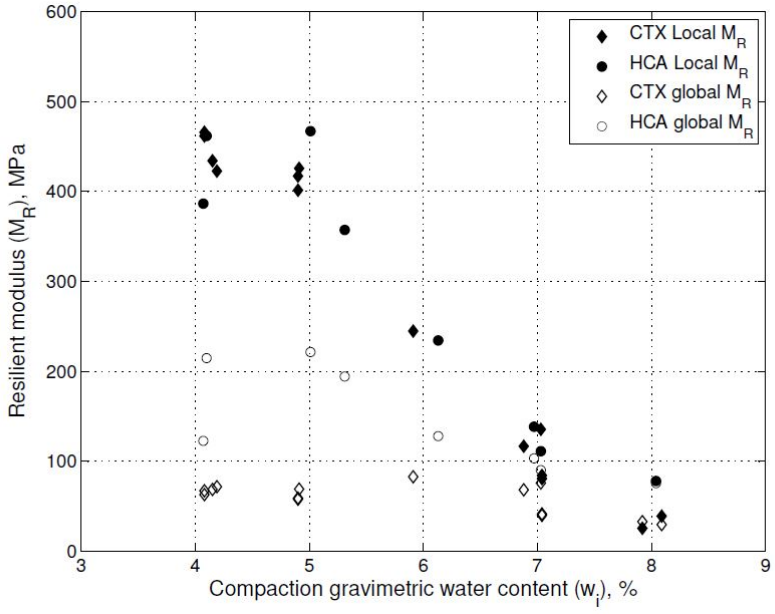

Figure 5.28: Local and global resilient modulus for cycle 100, M_{Rc100}, of HCA SP1 (no PSR) at 0.0167 Hz frequency and CTX sequence 7 (p_o=30 kPa; q_{cyc}=30 kPa) at 0.5 Hz frequency for different water content specimens

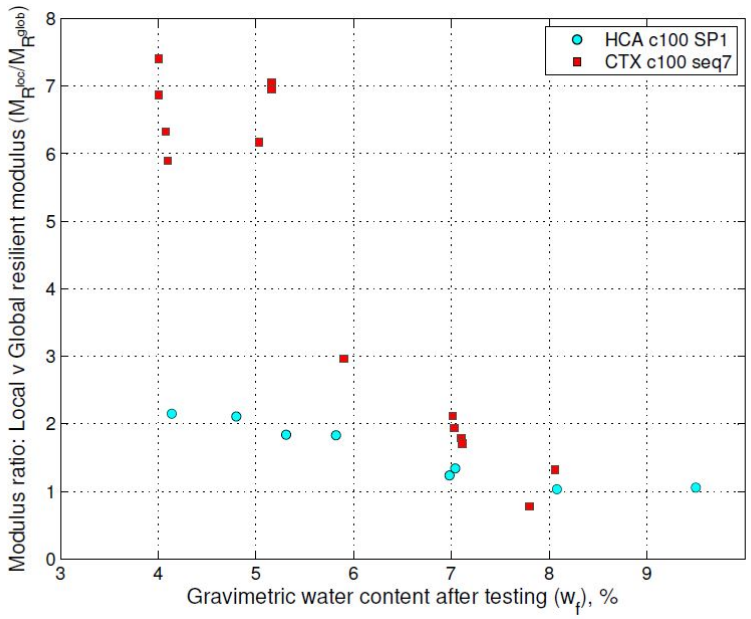

Figure 5.29: Ratio of local resilient modulus over global resilient modulus for CTX (sequence 7) and HCA (SP1, c100) tests

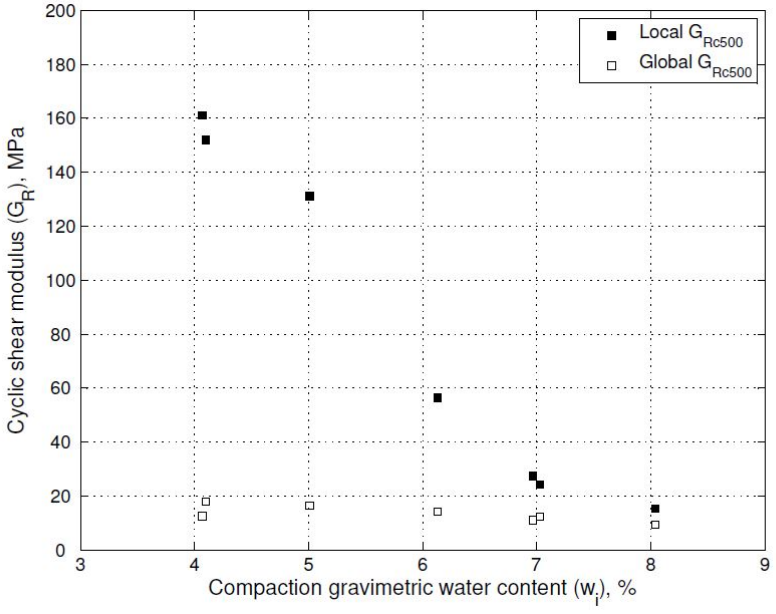

Figure 5.30: Local and global resilient shear modulus for cycle 500, G_{Rc500}, of HCA SP2 (with PSR) stress phase 1 at 0.0167 Hz frequency for different water content specimens

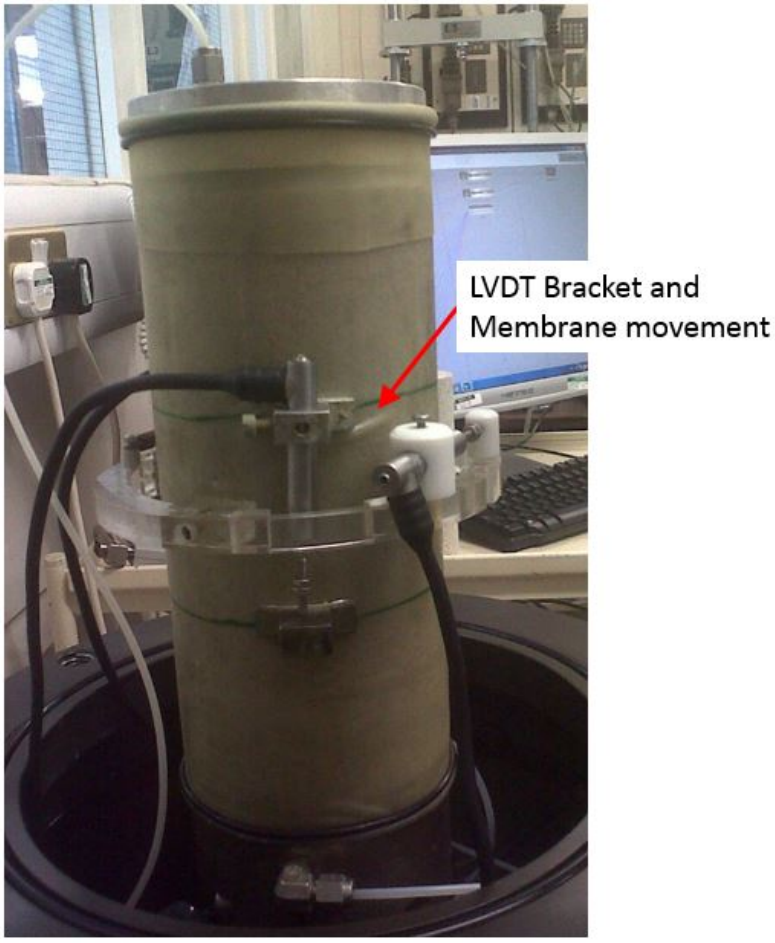

Figure 5.31: Movement of LVDT bracket during set-up as a result of LVDT mass and cable position, resulting in membrane movement relative to the very dry specimens (w=4%) for CTX-3v0

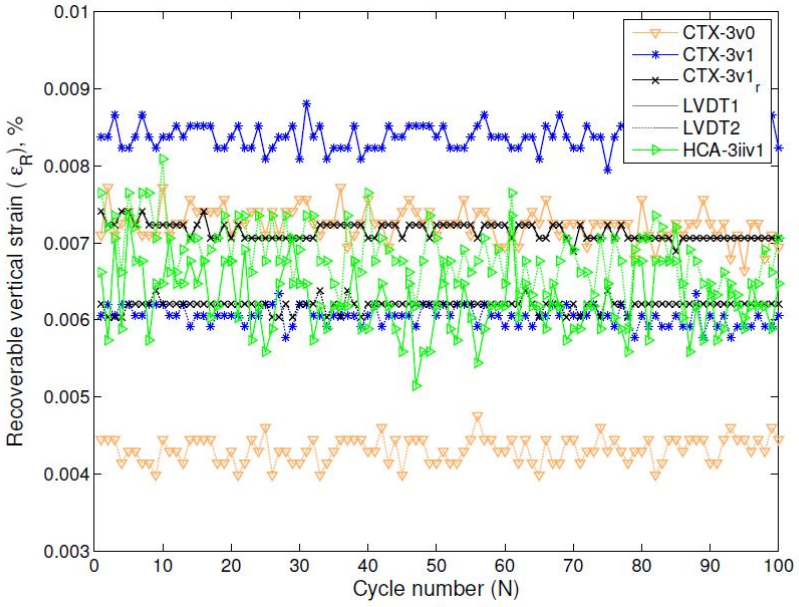

Figure 5.32: Recoverable strain, ϵ_R, measured for sequence 7 (p_o = 30 kPa, q_{cyc} = 30 kPa for very dry, stiff specimens (w=4%) for CTX-3v0, CTX-3v1, CTX-3v1$_r$ and HCA-3iiv1

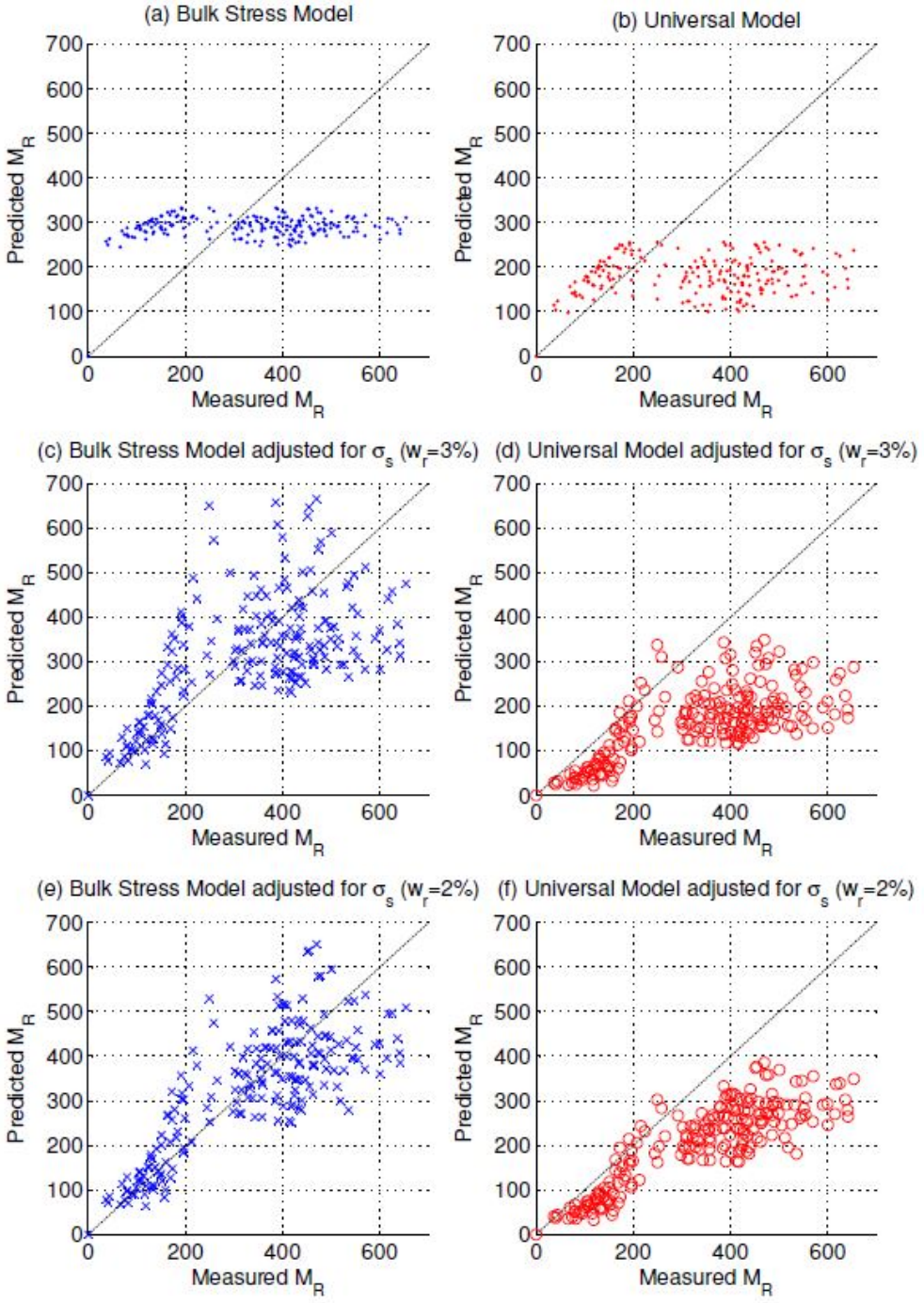

Figure 5.33: Measured vs. predicted M_R using the Bulk Stress Model and the Universal Model: (a) and (b) in terms of total stress; (c) and (d) in terms of intergranular stress, σ_s estimated from SWRC with w_r=3%; (e) and (f) in terms of intergranular stress, σ_s estimated from SWRC with w_r=2%

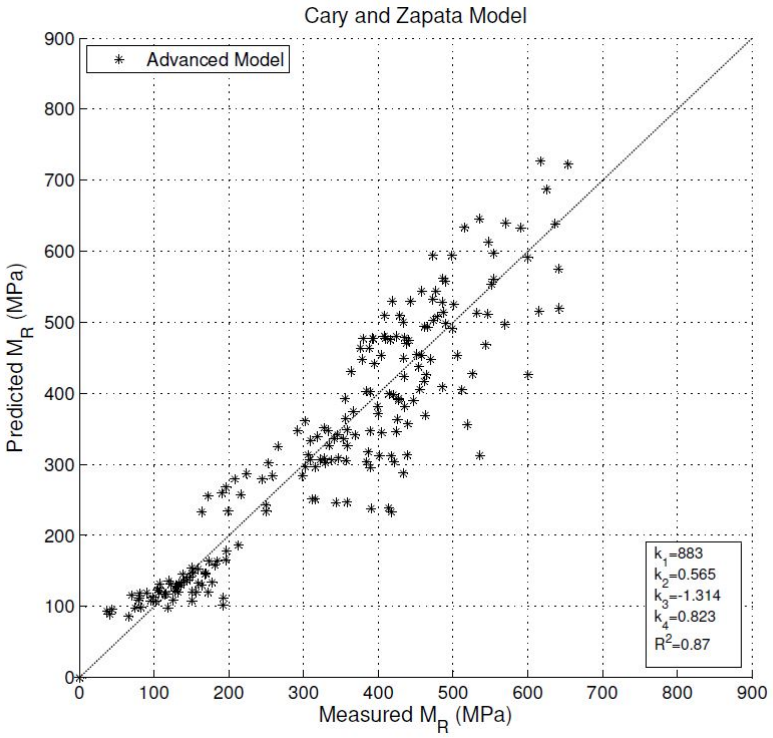

Figure 5.34: Measured vs. predicted M_R using the Advanced Model by Cary and Zapata (2011)

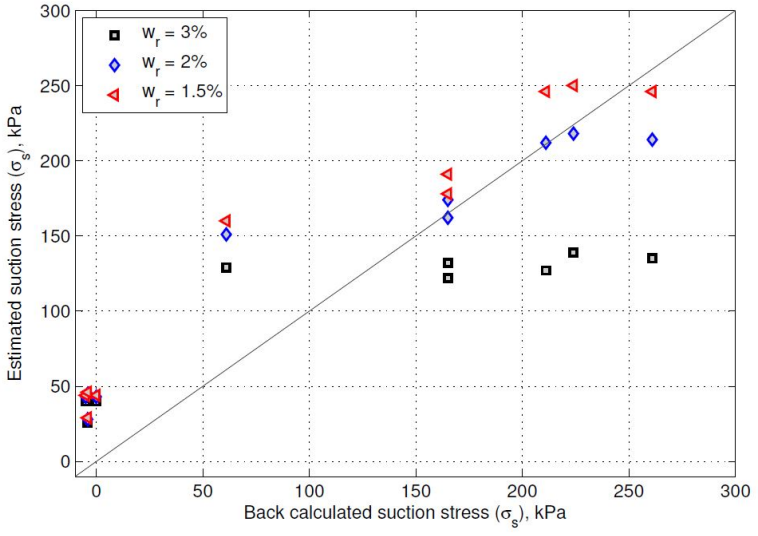

Figure 5.35: Suction stress estimated from the SWRC for different residual water contents (w_r=3%, 2% and 1.5%) versus the back-calculated suction stress from the M_R results of the CTX tests using CTX+0v0 as base test

Chapter 6

Conclusions and future work

The study set out to explore the relative importance of some factors that affect the measured cyclic stiffness of railway formation material. The main aim of the laboratory test program was to assess not only the influence of lack of saturation, but also that of principal stress rotation due to train loading on the resilient modulus.

Several methods of track foundation design have been reviewed to identify input parameters used in practice (Chapter 2). Design methods currently used, including the Spoornet (2006); NSW Transport RailCorp (2010); International Union of Railways (2008) designs, are mainly empirical, based on material properties such as particle size distribution, Atterberg limits and CBR values. Empirical design methods do not accommodate changing operational conditions, such as heavier, faster and more frequent trains (Priest et al., 2010), and changing environmental conditions including temperature and rainfall. Li and Selig (1998b) suggested a mechanistic-empirical approach similar to that used for flexible highway pavement design (AASHTO 1993) based on strain accumulation and resilient modulus. A similar approach was used in the past by British Rail (Heath et al., 1972). A more scientific understanding of railway substructure behaviour is required for safe, economic and sustainable track design and maintenance strategies for the future.

Despite the fact that rail formation materials are placed unsaturated, little is known of the effect of matric suction on the mechanical behaviour of track formation. The strength and stiffness of granular material is affected by the water content (degree of saturation) related to an intergranular stress in unsaturated soil mechanics by incorporating soil suction (Chapter 3).

Cyclic triaxial testing (CTX) is widely used to determine resilient modulus as part of modern mechanistic-empirical pavement design. In this study not only cyclic triaxial but also cyclic hollow cylinder (HCA) tests have been conducted to assess the effect of net normal stresses, principal stress rotation and matric suction on measured resilient

modulus of unsaturated specimens of a clayey sand formation material. The influence of net normal stresses or skeletal forces assessed include the confining stress, cyclic deviator stress and shear stress reversal.

HCA tests were conducted to determine resilient modulus M_R with and without PSR, on unsaturated specimens, to compare with values obtained on saturated specimens by Gräbe (2002); Gräbe and Clayton (2014) and at very small strain levels, on unsaturated material, by Otter (2011); Otter et al. (2015). Complex loading conditions under a moving wheel load which includes continuous principal stress rotation (PSR) have not previously been investigated for unsaturated formation materials.

The CTX was used to evaluate the effect of load staging and cyclic deviator stress excursions on measured M_R. The laboratory test results were used to assess the effects of stress level, strain level, PSR and cyclic excursions on measured stiffness for a range of water content.

The soil suctions for samples from a range of soil-water mixes of the clayey sand formation material were measured using the chilled-mirror dew-point technique. The soil suctions were compared with the soil water retention curve (SWRC) for the same material determined previously by Otter (2011) using the pressure plate apparatus, a high-capacity tensiometer and the filter paper technique (in direct contact). The use of matric suction and suction stress for analysing the measured resilient modulus of the unsaturated formation material was assessed. The results from the CTX tests were used in a preliminary assessment of the advanced resilient modulus models suggested for use in flexible pavement design.

The main conclusions from this work are presented in the following sections:

- Comparison of data with previous stiffness determinations.
- Effect of applied stresses on the resilient modulus.
- Effect of water content on the resilient modulus.
- Effect of laboratory testing method on measured stiffness.
- Comparison of factors affecting formation stiffness.
- Application of existing resilient modulus models.

6.1 Comparison of data with previous stiffness determinations

M_R values obtained from CTX and HCA tests on the unsaturated clayey sand reported in this thesis are broadly in line with the relatively few reported in the literature for

low plasticity soils. M_R measured at optimum water content (w = 7%),was between 110 MPa and 150 MPa, similar to values back-figured from field monitoring in South Africa reported by Priest et al. (2010) and Shaw (2005).

HCA and CTX results in general confirm the large effect of degree of saturation on stiffness (M_R) also seen by Otter (2011) at very small strain (G_0) from resonant column testing. Otter measured an increase in G_0 of approximately 3 times when degree of saturation reduced from near saturated to approximately 55% (w = 5%). The increased matric suction resulted in up to 6 times increase in M_R measured in this study, however in the HCA and CTX strain levels also influenced the results.

The resilient Young$'$s modulus measured in the HCA was approximately 4 times the shear modulus (from local shear strain measurements in the HCA), thus indicating that compaction produces an anisotropic material. Further investigations are needed to explore this.

6.2 Effect of applied stresses on the resilient modulus

Confining stress

The effect of increased confining stress, p_o, on M_R was dependent on the stress ratio and increased by a factor of 1.4, 1.7 and 1.8 for q_{cyc}/p_o equal to 1.0, 2.0 and 3.0 respectively (Δp_o = 55 kPa, from 30 kPa to 85 kPa) for optimum water content conditions. The influence of p_o was most significant for high water content specimens, reducing as water content reduced (and thus as matric suction increased). However, confining stress levels are low for the shallow foundation (estimated between 14 kPa and 40 kPa) and variable with depth. For this expected range of confining stress, the change in M_R is relatively small (c. 98-127 MPa for $q_{cyc} = p_o$; at optimum water content).

Cyclic deviator stress

Cyclic deviator stress, q_{cyc}, significantly influenced M_R. However, the effect of increasing q_{cyc} depended on the compacted water content and confining stress. For wet of optimum material M_R increased due to an increase in q_{cyc} (ascribed to densification due to large permanent deformation and subsequent dilation), while M_R decreased for dry of optimum material (which might be expected due to non-linear soil behaviour).

For wet of optimum conditions, M_R was very low and increased (from 32 kPa to 54 kPa) as a result of significant volumetric strain (ϵ_V up to 5.4%, ϵ_z 5% - test terminated) due to vertical stress cycling (for q_{cyc} = 15 kPa and q_{cyc} = 60 kPa, p_o = 30 kPa). For dry of optimum specimens M_R reduced between 20% and 40% as q_{max}/p_n increased from approximately 0.8 to 1.4, depending on the water content of the specimen.

Principal stress rotation

M_R was found to decrease by approximately 15% at optimum water content (w = 7%, S_R = 85%) due to the inclusion of shear stress reversal or PSR for the stress path applied in the HCA testing. The effect of PSR increased when the material was wet of optimum. Gräbe and Clayton (2014) previously reported approximately a 25% reduction in M_R due to PSR for saturated specimens. In this research the influence of PSR decreased as water content reduced and matric suction increased (MR_{PSR} = 1.05 at w = 5%, S_R = 55%), because stiffness and strength increased with increasing matric suction. The matric suction appeared to stabilise the structure of the material, resulting in higher resistance to relative particle slippage (Tarantino and Tombolato, 2005) caused by the relatively low shear stresses applied (estimated for constant speed running track).

The increase in M_R with number of load cycles seen in CTX testing was not significant for HCA testing with PSR. This may be the result of the continuous permanent strain accumulation due to shear stress reversal. Permanent strain accumulation due to PSR was influenced by the degree of saturation.

6.3 Effect of water content on the resilient modulus

The soil suction measured using the chilled-mirror dew-point potentiometer was higher, especially at low water content, than that reported for the other methods used by Otter (2011), but was in general agreement.

M_R increased considerably, from 36.4 MPa to 467 MPa, as the degree of saturation decreased, from 95% to 45%, when measured for CTX and equivalent HCA (SP1) tests carried out with $p_o = q_{cyc}$ = 30 kPa at different water contents (between w = 8% and w = 4%). M_R at optimum (w = 7%) was approximately 1.5 times the near saturated value (w = 8%). M_R at the driest state tested (w = 4%) was approximately six times the value measured for the near saturated specimen.

An increase in M_R with decreasing water content may to some extent be further influenced by lower permanent strain levels. The permanent strains, measured after 500 cycles on low water content specimens were significantly smaller (approx. 0.002% for w = 4% and w = 5%) than at higher water content (0.17% at optimum water content w = 7%).

M_R measured for near saturated conditions will significantly underestimate the field values after placement at optimum water content (S_R approximately 85%) and maximum dry density, and for long term performance, unless drainage of the formation layers are poor or due to prolonged rainfall.

The suction stress characteristic curve for the formation material was estimated from the SWRC. The suction stress estimations were based on the effective degree of saturation which is dependent on the residual water content. The variation in M_R at higher suction stress values may be linked to permanent strain level differences and the selected residual water content. Additional tests between w = 6% and w = 7% could aid evaluation of the trend.

6.4 Effect of laboratory testing method on measured stiffness

Based on the results of the laboratory tests reported in this thesis, the use of 100 cycles per stress combination in the CTX is considered adequate for evaluating M_R without overestimation resulting from lack of PSR.

The loading sequence did not significantly affect measured M_R provided vertical strains remained below 5%. However, load staging may influence M_R measured at low confining stresses (p_o=15 kPa) as a result of the densification during stages at higher confining stresses.

M_R values measured during CTX tests (at 0.5 Hz) for high water content specimens (w=8%) were lower (approximately half) those from HCA tests (at 0.0167 Hz), probably due to lack of time for excess pore water pressure to dissipate due to the faster loading rate. Test results for specimens with water contents at or below optimum (w≤7%) were comparable regardless the difference in cyclic frequency.

Local vertical strain measurements from CTX and HCA tests were comparable. The ratio of local M_R divided by global M_R increased as water content decreased, due to bedding. Local M_R was approximately twice the global M_R for dry of optimum HCA specimens, and up to 7 times higher for CTX specimens. Data from the HCA tests also showed that external (global) shear strain measurement was inaccurate.

Lack of conformance (for example, caused by stiff LVDT cabling), and resolution are significant issues that must be addressed in tests such as these, where effective stress levels are low, and stiffness is high. Some improvement was seen when including rubber bands around LVDT brackets to reduce potential movement.

6.5 Comparison of factors affecting formation stiffness

Test results from the CTX and HCA tests conducted on Material B, a clayey sand representative of a designed railway formation material (Spoornet S410, A-layer) was

compared. The effect of several factors on the measured resilient modulus, M_R, is listed in descending order of significance.

- Water content (matric suction).
- Method of strain measurement (local strain measurements).
- Cyclic deviator stress magnitude.
- Confining stress.
- Shear stress reversal, PSR, due to trains traveling at constant speed.

It was shown (Section 5.5) that the most important factor influencing measured M_R is water content. The second most important factor controlling measured M_R is the method of strain measurements. The influence of cyclic deviator stress magnitude seems to be higher than the effect of confining stress and PSR, however it is dependent on the water content or suction of the specimen. Therefore, when conducting resilient modulus testing on formation material, such as the clayey sand tested, it is recommended that the impact of the water content and change thereof is considered. Local strain measurements are important to obtain accurate results, especially for stiff, unsaturated soils. The expected cyclic deviator stress and confining stress is also important when selecting test conditions to obtain reasonable design input stiffness values. An assessment of the influence of PSR (HCA testing) is suggested as advanced consideration for high induced shear stress zones such as for braking and acceleration zones (not tested in this research), or for problematic subgrade sections saturated for prolonged periods.

6.6 Application of existing resilient modulus models to data

The various factors controlling M_R are interlinked and their significance was therefore further assessed using some existing resilient modulus regression models.

Total stress models

For individual test results M_R could not be modelled accurately ($R^2 < 0.1$) using the Bulk Stress model, while the Universal model, including not only bulk stress but also octahedral shear stress, achieved $R^2 > 0.5$ for the various, individual tests. These total stress models were unable to represent the combined results for the range of water content specimens tested as they do not capture the effects of soil suction.

Matric suction models

The ′Advanced model′ by Cary and Zapata (2011), which includes matric suction as an enhancement of the Universal model, achieved the best fit between predicted and measured M_R (R^2=0.87) for the combined set of CTX results, for the range of water contents. The model predicted M_R as most sensitive to octahedral shear stress, followed by matric suction and bulk (total) stress. This model includes matric suction and bulk stress as two separate parameters, while an intergranular stress approach combines matric suction into the bulk intergranular stress (thus compounding the influence).

Intergranular stress method to normalise stiffness

Adapting the Bulk Stress model and Universal model by using the intergranular stress (suction stress, σ_s estimated using the effective degree of saturation and the SWRC) instead of total stress achieved R^2 of 0.61 and 0.84 respectively. The Universal model with intergranular stress ($\sigma_n + \sigma_s$) parameters indicated a similar importance of bulk intergranular stress and octahedral shear stress on M_R.

The suction stress when back-calculated from the M_R results for specimens at different water contents, as suggested by Heath et al. (2004), produced similar values as calculated from the SWRC using the S_e for w_r = 2%, which is lower than the proposed residual water content value used by Otter (2011). However, care should be taken when determining the suction stress characteristic curve from stiffness results, due to the non-linear stress-strain behaviour of soil.

6.7 Future work

The CTX and HCA laboratory testing of a representative formation material conducted in this study was done to assess the effect of train induced stresses (including PSR) and matric suction, related to water content, on M_R. Specimens of the clayey sand material were compacted to the same target dry density at a range of water contents to create different matric suctions. However, further work is needed

- to assess the effect of PSR on a wider range of unsaturated formation material types;
- to assess a broader range of test load conditions, such as increased shear stresses in breaking or acceleration zones;
- to assess the influence of PSR on permanent strain accumulation;

- to assess the impact of in-situ changes in water content and suction after construction due to wetting and drying cycles;
- to assess and compare the ability of available M_R models to represent the measured M_R of the unsaturated formation material; and
- to assess stresses and strains in the railway substructure using computer modelling.

References

AASHTO (1993). *AASHTO guide for design of pavement structures*. American Association of State Highway and Transportation Officials, Online, 4th editio edition.

Ahmed, K. I. (2014). *Effect of gypsum on the hydro-mechanical characteristics of partially saturated sandy soil*. PhD thesis, Cardiff University.

Aitchison, G. D. (1960). Relationships of moisture stress and effective stress functions in unsaturated soils. In *Conference on Pre Pressures*, Butterworths, London.

Alonso, E. E., Gens, A., and Josa, A. (1990). A constitutive model for partially saturated soils. *Géotechnique*, 40(3):405–430.

Alonso, E. E., Pereira, J. M., Vaunat, J., and Olivella, S. (2010). A microstructurally based effective stress for unsaturated soils. *Géotechnique*, 60(12):913–925.

Alonso, E. E., Pinyol, N. M., and Gens, A. (2013). Compacted soil behaviour: initial state, structure and constitutive modelling. *Géotechnique*, 63(6):463–478.

Andrei, D., Witczak, M. W., Schwartz, C. W., and Uzan, J. (2004). Harmonized resilient modulus test method for unbound pavement materials. *Transportation research record: Journal of the transportation research board*, 1874:29–37.

ASTM D1557-07: (2007). Standard test method for laboratory compaction characteristics of soil using modified effort.

ASTM D5311-11: (2011). Standard test method for load controlled cyclic triaxial strength of soil.

ASTM D6836-02: (2003). Standard test method for determination of the soil water characteristic curve for desorption using a hanging column, pressure extractor, chilled mirror hygrometer, and/or centrifuge.

Atkinson, J. H. (2000). Non-linear soil stiffness in routine design. *Géotechnique*, 50(5):487–508.

Azam, A. M., Cameron, D. A., and Rahman, M. M. (2013). Model for prediction of resilient modulus incorporating matric suction for recycled unbound granular materials. *Canadian Geotechnical Journal*, 50:1143–1158.

Baille, W., Tripathy, S., and Schanz, T. (2013). Effective stress in clays of various mineralogy. *Vardose Zone Journal*.

Baldi, G., Hight, D. W., and Thomas, G. E. (1988). A reevaluation of conventional triaxial test methods. In Donaghe, R. T., Chaney, R. C., and Silver, M. L., editors, *Advanced triaxial testing of soil and rock, ASTM STP 977*, pages 219–263, Philadelphia. American Society for Testing and Materials.

Bishop, A. W. (1959). The principle of effective stress. *Teknick Ukeblad*, 39:859–863.

Bishop, A. W. (1966). The strength of soils as engineering materials. *Géotechnique*, 16(2):91–130.

Bishop, A. W. and Blight, G. E. (1963). Some aspects of effective stress in saturated and partly saturated soils. *Geotechnique*, 13(3)(No. 3):177–197.

Bishop, A. W. and Henkel, D. J. (1957). *The measurement of soil properties in the triaxial test*. William Clowes and Sons Limited, London and Beccles.

Brandl, H. (2001). The importance of optimum compaction of soil and other granular material. In Correia, A. G. and Brandl, H., editors, *Geotechnics for roads, rail tracks and earth structures*, pages 47–66. A.A. Balkema publishers, Lisse, The Netherlands.

British Standards Institution (2012). BS 1377 Methods of test for Soils for civil engineering purposes.

Brown, S. F. (1996). Soil mechanics in pavement engineering. *Géotechnique*, 46(3):383–426.

Brown, S. F. and Hyde, A. F. L. (1975). Significance of cyclic confining stress in repeated-load triaxial testing of granular material. *Transportation Research Record*, 537:49–58.

Brown, S. F., Lashine, A. K. F., and Hyde, A. F. L. (1975). Repeated load triaxial testing of a silty clay. *Géotechnique*, 25(1):95–114.

Brown, S. F. and Selig, E. T. (1991). The design of pavement and rail track foundations. In O'Reilly, M. P. and Brown, S. F., editors, *Cyclic loading of soils: From theory to design*, chapter 6, pages 249–305. Van Nostrand Reinhold, New York.

Bui, M. T. (2009). *Influence of some particle characteristics on the small strain response of granular materials*. PhD thesis, University of Southampton.

Burrow, M. P. N., Bowness, D., and Ghataora, G. S. (2007). A comparison of railway track foundation design methods. *Proc. IMechE*, 221 Part F(Special issue paper):1–12.

Cary, C. E. and Zapata, C. E. (2011). Resilient Modulus for Unsaturated Unbound Materials. *Road Materials and Pavement Design*, 12(3):615–638.

Ceratti, J. A., Gehling, W. Y. Y., and Nunez, W. P. (2004). Seasonal variations of a subgrade soil resilient modulus in southern Brazil. *Transportation research record: Journal of the transportation research board*, 1874:165–173.

Cerni, G., Corradini, A., Pasquini, E., and Cardone, F. (2015). Resilient behaviour of unbound granular materials through repeated load triaxial test: influence of the conditioning stress. *Road Materials and Pavement Design*, 16(1):70–88.

Chan, F. W. K. and Brown, S. F. (1994). Significance of principal stress rotation in pavements. In *XIII Internation Conference on soil mechanics and foundation engineering (ICSMFE)*, pages 1823–1826, New Delhi, India. A.A. Balkema publishers.

Chang, C. S., Adegoke, C., and Selig, E. T. (1980). GEOTRACK Model for Railroad Track Performance. *Journal of the geotechnical engineering division-ASCE*, 106(11):1201–1218.

Corey, A. T. (1994). *Mechanics of immerscible fluids in porous medi.* Water resource publications, Highlands Ranch, CO.

Craciun, O. (2009). *Matric suction response of unbound granular base materials subject to cyclic loading.* PhD thesis, University of New South Wales.

Craciun, O. and Lo, S. (2010). Matric Suction Measurement in Stress Path Cyclic Triaxial Testing of Unbound Granular Base Materials. *ASTM geotechnical testing journal*, 33(1):33–44.

Craig, R. F. (2004). *Craig's soil mechanics.* Spon Press, Taylor & Francis Group, London and New York, 7 edition.

Croney, D. and Coleman, J. D. (1961). Pore pressure and suction. In *Pore pressure and suction in soils*, pages 31–37, London, UK. Butterworths.

Croney, D., Coleman, J. D., and Black, W. P. M. (1958). Movement and distribution of water in soil in relation to highway design and performance. Technical report, Highway Research board.

Cuccovillo, T. and Coop, M. R. (1997). Technical note: The measurement of local axial strains in triaxial tests using LVDTs. *Géotechnique*, 47(1):167–171.

Dehlen, G. L. (1969). *The effects of non-linear material response on the behaviour of pavements subjected to traffic loads.* PhD thesis, University of California, Berkeley, Calif.

Escario, V. (1980). Suction controlled shear and penetration tests. In *Proceedings of the 4th International Conference on Expansive soils.*, pages 781–797, Denver.

Esveld, C. (2001). *Modern Railway Track.* MRT-Productions, Zaltbommel.

Fredlund, D. G. (1979). Second Canadian Geotechnical Colloquium: Appropriate concepts and technology for unsaturated soils. *Canadian Geotechnical Journal*, 16:121–139.

Fredlund, D. G. and Morgenstern, N. (1977). Stress state variables for unsaturated soils. *Journal of the geotechnical engineering division-ASCE*, 103(GT5):447–466.

Fredlund, D. G. and Rahardjo, H. (1993). *Soil mechanics for unsaturated soils.* John Wiley & Sons Inc., New York.

Fredlund, D. G., Rahardjo, H., and Fredlund, M. D. (2012). *Unsaturated soil mechanics in engineering practice.* Wiley, Somerset, NJ, USA.

Fredlund, D. G., Rahardjo, H., and Gan, J. K. M. (1987). Non-linearity of strength envelope for unsaturated soils. In *Proceedings of the 6th International Conference on Expansive Soils, New Delhi*, pages 49–54, Rotterdam:Balkema.

GDS Instruments Ltd (2014). Systems Elements & Options.

Gräbe, P. J. (2002). *Resilient and permanent deformation of railway foundations under principal stress rotation.* PhD thesis, University of Southampton.

Gräbe, P. J. and Clayton, C. R. I. (2009). Effects of principal stress rotation on permanent deformation in rail track foundations. *Journal of Geotechnical and Geoenvironmental Engineering*, 135(4):555–565.

Gräbe, P. J. and Clayton, C. R. I. (2014). Effects of Principal Stress Rotation on Resilient Behavior in Rail Track Foundations. *Journal of Geotechnical and Geoenvironmental Engineering*, 140(2):1–10.

Gräbe, P. J., Clayton, C. R. I., and Shaw, F. J. (2005). Deformation measurement on a heavy haul track formation. In *Proceedings of the 8th International Heavy Haul Conference*, pages 287–295, Rio se Janeiro, Brazil.

Greening, J. (2012). Reforming our railways: Putting the customer first. Technical report, Department for transport, UK, London, UK.

Harrigan, E. T. (2004). Laboratory determination of resilient modulus for flexible pavement design. *Research results digest*, Number285:1–52.

Heath, A. C., Pestana, J. M., Harvey, J. T., and Bejerano, M. O. (2004). Normalizing behavior of unsaturated granular pavement materials. *Journal of Geotechnical and Geoenvironmental Engineering*, 130(9):896–904.

Heath, D. L., Shenton, M. J., Sparrow, R. W., and Waters, J. M. (1972). Design of conventional rail track foundations. *Proceedings - Original meeting 7 March 1972, British Railways Board Research Department*, Part 2(7468).

Hendry, M., Hughes, D. A., and Barbour, L. (2010). Track displacement and energy loss in a railway embankment. *Proceedings of the Institution of Civil Engineers*, 163(GE1):3–12.

Hicks, R. G. and Monismith, C. L. (1971). Factors influencing the resilient response of granular materials. *Highway research record*, 345(15-31).

Hight, D. W., Gens, A., and Symes, M. J. (1983). The development of a new cylinder apparatus for investigating the effects of principal stress rotation in soils. *Géotechnique*, 33(4):355–383.

Hight, D. W. and Leroueil, S. (2003). Characterisation of soils for engineering purposes. In Tan, T. S., Phoon, K. K., Hight, D. W., and Leroueil, S., editors, *Natural soils Conference*, page 255. A.A. Balkema publishers.

Houlsby, G. T. (1997). Technical note: The work input to an unsaturated granular material. *Géotechnique*, 47(1):193–196.

Indraratna, B. and Salim, W. (2005). *Mechanics of Ballasted Rail Tracks*. Taylor & Francis Group, London, UK.

International Union of Railways (1988). UIC Code 714R: Classification of lines for the purpose of track maintenance.

International Union of Railways (2008). UIC code 719R: Earthworks and track bed for railway lines.

Jafarian, Y., Towhata, I., Baziar, M. H., Noorzad, A., and Bahmanpour, A. (2012). Strain energy based evaluation of liquefaction and residual pore water pressure in sands using cyclic torsional shear experiments. *Soil Dynamics and Eartquake Engineering*, 35:13–28.

Jamiolkowski, M., Ladd, C. C., Germaine, J. T., and Lancellotta, R. (1985). New developments in field and laboratory testing of soils. In *11th International conference on soil mechanics and foundation engineering*, pages 57–153, San Francisco.

Jardine, R. J. (2011). Characterization of mudrocks: a practical application of advanced laboratory testing. *Journal of Zhejiang University Science A*, 12(1):1–14.

Jennings, J. E. B. (1957). Discussion on M.S. Youssef's paper. In *Proceedings of the 4th International Conference on Soil Mechanics.*, page 3:168.

Jennings, J. E. B. and Burland, J. B. (1962). Limitations to the use of effective stress in partly saturated soils. *Geotechnique*, 12(2):125–144.

Jin, M. S., Lee, K. W., and Kovacs, W. D. (1994). Seasonal variation of resilient modulus of subgrade soils. *Journal of Transportation Engineering - ASCE*, 120(4):603–616.

Karasahin, M. and Dawson, A. R. (1994). Resilient behaviour of cohesionless soil. In *XIII Internation Conference on soil mechanics and foundation engineering (ICSMFE)*, page 1827.

Khedr, S. (1985). Deformation characteristics of granular base course in flexible pavement. *Transportation Research Record*, 1043:131–138.

Khoury, N. N. and Zaman, M. M. (2004). Correlation between resilient modulus, moisture variation, and soil suction for subgrade soils. *Transportation research record: Journal of the transportation research board*, 1874:99–107.

Kramer, S. L. (1996). *Geotechnical Earthquake Engineering*. Prentice-Hall Inc., Upper Saddle River, USA.

Lambe, T. (1967). Stress path method. *Journal of the soil mechanics and foundations division, Proceedings of the ASCE*, 93(SM6):309–331.

Lekarp, F., Isacsson, U., and Dawson, A. (2000). State of the Art. II: Permanent strain response of unbound aggregates. *Journal of Transportation Engineering - ASCE*, 126(1)(No. 1):76–83.

Leong, E. C., Tripathy, S., and Rahardjo, H. (2003). Total suction measurement of unsaturated soils with a device using the chilled-mirror dew-point technique. *Geotechnique*, 53(2):173–182.

Li, D. and Davis, D. (2005). Transition of railroad bridge approaches. *Journal of Geotechnical Engineering - ASCE*, 131(11):1392–1398.

Li, D. and Selig, E. T. (1994). Resilient modulus for fine-grained subgrade soils. *Journal of Geotechnical and Geoenvironmental Engineering*, 120(6):939–957.

Li, D. and Selig, E. T. (1996). Cumulative plastic deformation for fine-grained subgrade soils. *Journal of geotechnical engineering*, 122(12):1006–1013.

Li, D. and Selig, E. T. (1998a). Method for railroad track foundation design. I: Development. *Journal of Geotechnical and Geoenvironmental Engineering*, 124(4):316–322.

Li, D. and Selig, E. T. (1998b). Method for railroad track foundation design. II: Applications. *Journal of Geotechnical and Geoenvironmental Engineering*, 124(4):323–329.

Liang, R. Y., Al-Akhras, K., and Rabab'ah, S. (2006). Field Monitoring of Moisture Variations Under Flexible Pavement. *Transportation research record: Journal of the transportation research board*, 1967(1):160–172.

Liang, R. Y., Rabab'ah, S., and Khasawneh, M. (2008). Predicting moisture-dependent resilient modulus of cohesive soils using soil suction concept. *Journal of Transportation Engineering - ASCE*, 134(1):34–40.

Lockyer (1986). TMH1 Method A7: The determination of the maximum dry density and optimum moisture content of gravel, soil and sand.

Lu, N., Godt, J. W., and Wu, D. T. (2010). A closed-form equation for effective stress in unsaturated soil. *Water Resources Research*, 46(W05515).

Lu, N. and Likos, W. J. (2006). Suction Stress Characteristic Curve for Unsaturated Soil. *Journal of Geotechnical and Geoenvironmental Engineering*, 132(2):131–142.

Mamou, A. (2013). *Effects of Principal Stress Rotation and Drainage on the Resilient Stiffness of Railway Foundations.* PhD thesis, University of Southampton.

Mancuso, C., Vassallo, R., and D'Onofrio, A. (2002). Small strain behavior of a silty sand in controlled-suction resonant column torsional shear tests. *Canadian Geotechnical Journal*, 39:22–31.

Marinho, F. A. M., Take, A., and Tarantino, A. (2008). Tensiometeric and axis translation technique for suction measurement. *Geotechnical and Geological Engineering*, 26(6):615–631.

Mayne, P. W. and Kilhawy, F. H. (1982). K0-OCR relationships in soil. *Journal of Geotechnical Engineering-Asce*, 108(GT6):851–887.

McCartney, J. S. and Khosravi, A. (2013). Field-Monitoring System for Suction and Temperature Profiles under Pavements. *Journal of Performance of Constructed Facilities - ASCE*, 27:818–825.

Miller, G. A., Li, D., and Zaman, M. M. (2000). Cyclic Shear Strength of Soft Railroad subgrade. *Journal of Geotechnical and Geoenvironmental Engineering*, 126(2):139–147.

Mishra, D., Tutumluer, E., Stark, T. D., Hyslip, J. P., Chrismer, S. M., and Tomas, M. (2012). Investigation of differential movement at railroad bridge approaches through geotechnical instrumentation. *Journal of Zhejiang University Science A*, 13(11):814–824.

Mitchell, J. K. and Soga, K. (2005). *Fundamentals of soil behavior.* John Wiley & Sons Inc., New Jersey, 3 edition.

Moco Ferreira, T., Fonseca Teixeira, P., and Cardoso, R. (2011). Technical note: Impact of bituminous subballast on railroad track deformation considering atmospheric actions. *Journal of Geotechnical and Geoenvironmental Engineering*, 137(3):288–292.

Muhlhaus, H. B. and Vardoulakis, I. (1987). The thickness of shear bands in granular materials. *Geotechnique*, 37(3):271–283.

Nazarian, S., Pezo, R., and Picornell, M. (1996). Testing methodology for resilient modulus of base materials. Technical report, The center for geotechnical and highway materials research, Texas.

Network Rail (2005). Business Process document NR/SP/TRK/9039.

Network Rail (2010). NR/L3/CIV/140/52C - Earthworks.

Network Rail (2012). Planning ahead. Control Period 5 and beyond: Britain's railway from 2014.

Ng, C. W. W., Zhou, C., Yuan, Q., and Xu, J. (2013). Resilient modulus of unsaturated subgrade soil : experimental and theoretical investigations. *Canadian Geotechnical Journal*, 50:223–232.

Nishimura, S., Minh, N. A., and Jardine, R. J. (2007). Shear strength anisotropy of natural London Clay. *Géotechnique*, 57(1):49–62.

NSW Transport RailCorp (2010). Engineering standards - Geotechnical.

NSW Transport RailCorp (2012). ESC200: Track system v4.3.

O'Brien, A. S. (2007). Rehabilitation of urban railway embankments - investigation, analysis and stabilisation. In Cueller, V. and Dapena, E., editors, *14th International Conference on Soil Mechanics and Geotechnical Engineering*, pages (1) 125–143, Madrid. Millpress, Rotterdam.

Oda, M. and Kazama, H. (1998). Microstructure of shear bands and its relation to the mechanisms of dilatancy and failure of dense granular soils. *Geotechnique*, 48(4):465–481.

Oh, S., Lu, N., Kim, T.-k., and Lee, Y. H. (2013). Experimental Validation of Suction Stress Characteristic Curve from Nonfailure Triaxial K0 Consolidation Tests. *Journal of Geotechnical and Geoenvironmental Engineering*, 139(9):1490–1503.

Ooi, P. S., Archilla, A. R., and Sandefur, K. G. (2004). Resilient modulus models for compacted cohesive soils. *Transportation research record: Journal of the transportation research board*, 1874:115–124.

O'Reilly, M. P. and Brown, S. F. (1991). *Cyclic loading of soils: from theory to design.* Blackie and Son Ltd, London.

Otter, L. (2011). *The influence of suction changes on the stiffness of railway formation.* PhD thesis, University of Southampton.

Otter, L., Clayton, C. R. I., Priest, J. A., and Gräbe, P. J. (2015). The stiffness of unsaturated railway formations. *Proceedings of the Institution of Mechanical Engineers Part F-Journal of Rail and Rapid Transit*, 0(0):1–13.

Parreira, A. B. and Goncalves, R. F. (2000). The influence of moisture content and soil suction on the resilient modulus of a lateritic subgrade soil. In *GeoEng - An international conference on geotechnical and geological engineering*, Melbourne, Australia.

Powrie, W. (2014a). On track: the future for rail infrastructure systems. *Civil Engineering, ICE Proceedings*, 167(CE4).

Powrie, W. (2014b). *Soil mechanics concepts and application*. CRC Press, Taylor & Francis Group, London, UK, third edition.

Powrie, W., Yang, L. A., and Clayton, C. R. I. (2007). Stress changes in the ground below ballasted railway track during train passage. *Proc. IMechE*, 221 Part F:247–261.

Priest, J. A., Powrie, W., Yang, L. A., Gräbe, P. J., and Clayton, C. R. I. (2010). Measurements of transient ground movements below a ballasted railway line. *Géotechnique*, 60(9):667–677.

Puppala, A. J., Manosuthkij, T., Nazarian, S., Hoyos, L. R., and Chittoori, B. (2012). In Situ Matric Suction and Moisture Content Measurements in Expansive Clay during Seasonal Fluctuations. *Geotechnical Testing Journal*, 35(1):74–82.

Read, D. and Li, D. (2006). Design of track transitions. *Transit Cooperative Research Program: Research Digest*, 79(Federal Transit Administration).

Rhind, D. M. (1997). *Heavy Haul in South Africa*. Prolink, Randburg, South Africa.

Ridley, A. M. and Burland, J. B. (1993). Technical note: A new instrument for the measurement of soil moisture suction. *Géotechnique*, 43(2):321–324.

Road Research Laboratory (1952). *Soil Mechanics for Road Engineers*. Her Majesty's stationary office, London.

Roscoe, K. H. (1970). The influence of strains in soil mechanics. *Geotechnique*, 20(2):129–170.

Rust, M. (2003). *Mechanics of continuous flight augers*. PhD thesis, University of Southampton.

Saada, A. (1988). Hollow cylinder torsional devices: their advantages and limitations. In Donaghe, R. T., Chaney, R. C., and Marshall, L. S., editors, *Advanced triaxial testing of soil and rock, ASTM STP 977*, pages 766–795. Philadelphia.

Saada, A., Puccini, P., and Jamal, A. K. (1985). Discussion of: The development of a new hollow cylinder apparatus for investigating the effects of principal stress rotation in soils and Undrained anisotropy and principal stress rotation in saturated sand. *Géotechnique*, pages 78–85.

Salour, F. and Erlingsson, S. (2015). Resilient modulus modelling of unsaturated subgrade soils: laboratory investigation of silty sand subgrade. *Road Materials and Pavement Design*, 16(3):553–568.

Salour, F., Erlingsson, S., and Zapata, C. E. (2014). Modelling resilient modulus seasonal variation of silty sand subgrade soils with matric suction control. *Canadian Geotechnical Journal*, 51(12):1413–1422.

Santamarina, J. C. (2003). Soil behaviour: the role of particle shape. In Germaine, J. T., Sheahan, T. C., and Whitman, R. V., editors, *Soil behavior and soft ground construction.*, pages 25–56. ASCE, Reston, VA, asce geote edition.

Sauer, E. K. and Monismith, C. L. (1968). Influence of soil suction on behavior of a glacial till subjected to repeated loading. *Highway research board*, 215:8–23.

Sawangsuriya, A., Edil, T. B., and Benson, C. H. (2009). Effect of Suction on Resilient Modulus of Compacted Fine-Grained Subgrade Soils. *Transportation Research Record*, (2101):82–87.

Seed, H. B., Chan, C. K., and Lee, C. E. (1962). Resilience characteristics of subgrade soils and their relation to fatigue failures in asphalt pavements. In *International Conference on Structural Design of Asphalt Pavements*, volume 1, pages 1–23, Ann Arbor, Michigan.

Seed, H. B., Mistry, F. G., Monismith, C. L., and Chan, C. K. (1967). Factors influencing the resilient deformations of untreated aggregate base in two-layer pavements subjected to repeated loading. *Highway research record*, 190:19–57.

Selig, E. T. and Li, D. (1994). Track modulus: Its meaning and factors influencing it. *Transportation research record: Journal of the transportation research board*, 1470:47–54.

Shahu, J. T., Yudhbir, and Kameswara, R. (2000). A rational method for design of railroad track foundation. *Soils and Foundations - Japanese Geotechnical Society*, 40(6):1–10.

Shahu, J. T., Yudhbir, and Kameswara Rao, N. S. V. (1999). A simple test methodology for soils under transportation routes. *Géotechnique*, 49(5):639–649.

Shaw, F. J. (2005). *Railway track formation stiffnesses*. PhD thesis, University of Pretoria, Pretoria, South Africa.

Sivakumar, V., Kodikara, J., O'Hagan, R., Hughes, D., Cairns, P., and McKinley, J. (2013). Effects of confining pressure and water content on performance of unsaturated compacted clay under repeated loading. *Géotechnique*, 63(8):628–640.

Soliman, H. and Shalaby, A. (2013). Characterising the elastic behaviour of fine-grained subgrade soils under traffic loading. *International Journal of Pavement Engineering*, 15(8):698–707.

Spoornet (2006). S410: Specification for railway earthworks. Transnet Limited, South Africa.

Steenbergen, M. J. M. M. (2013). Physics of railroad degradation : The role of a varying dynamic stiffness and transition radiation processes. *Computers and Structures*, 124:102–111.

Symes, M. J., Gens, A., and Hight, D. W. (1988). Drained principal stress rotation in saturated sand. *Géotechnique*, 38(1):59–81.

Tarantino, A., Gallipoli, D., Augarde, C. E., De Gennaro, V., Gomez, R., Laloui, L., Mancuso, C., El Mountassir, G., Munoz, J. J., Pereira, J. M., Peron, H., Pisoni, G., Romero, E., Raveendiraraj, A., Rojas, J. C., Toll, D. G., Tombolato, S., and Wheeler, S. J. (2011). Benchmark of experimental techniques for measuring and controlling suction. *Géotechnique*, 61(4):303–312.

Tarantino, A. and Tombolato, S. (2005). Coupling of hydraulic and mechanical behaviour in unsaturated compacted clay. *Géotechnique*, 55(4):307–317.

Terzaghi, K. (1936). The shearing resistance of saturated soils. In *Proceedings of the first international conference on soil mechanics. Volume 1*, pages 54–56, Cambridge, MA.

Thom, R., Sivakumar, V., Brown, J., and Hughes, D. (2008). A simple triaxial system for evaluating the performance of unsaturated soils under repeated loading. *Geotechnical Testing Journal*, 31(2):107–114.

Toll, D. G. (1990). A framework for unsaturated soil behaviour. *Geotechnique*, 40(1):31–44.

Tripathy, S., Elgabu, H., and Thomas, H. R. (2012). Matric Suction Measurement of Unsaturated Soils With Null-Type Axis-Translation Technique. *ASTM Geotechnical Testing Journal*, 35(1):91–102.

Tripathy, S., Elgabu, H., and Thomas, H. R. (2014). Soil-water characteristic curves from various laboratory techniques. In Khalili, N., Russell, A. R., and Khoshghalb, A., editors, *International Conference on Unsaturated Soils: Research and Applications (UNSAT2014)*, Sydney, Australia. CRC Press/Balkema, The Netherlands.

Tripathy, S., Thomas, H. R., and Bag, R. (2015). Geoenvironmental Application of Bentonites in Underground Disposal of Nuclear Waste : Characterization and Laboratory Tests. *Journal of Hazardous, Toxic, and Radioactive Waste -ASCE*, ISSN 2153-.

Uzan, J. (1985). Characterization of granular material. *Transportation Research Record*, 1022:52–59.

van Genuchten, M. T. (1980). A closed-form equation for predicting the hydraulic conductivity of unsaturated soils. *Soil Science Society of America Journal*, 44(5):892–898.

Vorster, D. J. (2016). Discussion: Continuing water content measurements in the University of Pretoria test track.

Vorster, D. J. and Gräbe, P. J. (2013). A new test track at the University of Pretoria. *SAICE Civil Engineering Magazine*, pages 35–39.

WAQTC (2011). Embankment and base in-place density. Technical Report October, Western Alliance for Quality Transportation Construction, Washington.

Wheeler, S. J. (1991). Technical note. An alternative framework for unsaturated soil behaviour. *Geotechnique*, 41(2):257–261.

Yang, H., Rahardjo, H., Leong, E. C., and Fredlund, D. G. (2004). Factors affecting drying and wetting soil-water characteristic curves of sandy soils. *Canadian Geotechnical Journal*, 41:908–920.

Yang, L. A., Powrie, W., and Priest, J. A. (2009). Dynamic Stress Analysis of a Ballasted Railway Track Bed during Train Passage. *Journal of Geotechnical and Geoenvironmental Engineering*, 135(5):680–689.

Yang, S. R., Huang, W. H., and Tai, Y. T. (2005). Variation of resilient modulus with soil suction for compacted subgrade soils. *Transportation Research Record*, 1913:99–106.

Yang, S. R., Lin, H. D., Kung, J. H. S., and Huang, W. H. (2008). Suction-controlled laboratory test on resilient modulus of unsaturated compacted subgrade soils. *Journal of Geotechnical and Geoenvironmental Engineering*, 134(9):1375–1384.

Yau, A. and Von Quintus, H. L. (2004). Predicting elastic response characteristics of unbound materials and soils. *Transportation research record: Journal of the transportation research board*, 1874:27–56.

Zapata, C. E. and Houston, W. N. (2008). *NCHRP Report 602: Calibration and Validation of the Enhanced Integrated Climatic Model for Pavement Design*. Transportation Research Board, Washington, DC.

Appendices

Appendix A

Subballast and formation design considerations

Design	Loading/ Categories	Foundation layers	Material properties	Density (compaction)	Strength/Stiffness	Drainage/ moisture
British Rail (Heath et al. 1972)	Design chart: max 24 tonne axle load (heaviest commonly occurring axle load) No traffic split t/a/design period.	Subballast (reduce ballast needed to min. 300mm).	Predominantly granular, little cohesive matter. Lower part, role of blanketing layer (filter grading).	Laboratory test to test suitability (not specified).	Above water table.	Water table assumed at the surface of the subgrade.
		Subgrade formation	In-situ material (tested London clay)	Threshold stress tested, based on drained cyclic triaxial compression test.	max 10% cumulative strain (10^6 cycles) threshold elastic strain 0.65% (1000 cycles)	

Design	Loading/ Categories	Foundation layers	Material properties	Density (compaction)	Strength/Stiffness	Drainage/ moisture
UIC 719 R (International Union of Railways 2008)	UIC Code 714 R (1988) classification. Tonnage; Axle load (highest category >22.5t); Speed (max 250km/h); Tractive tonnage; Superstructure dimensions 100year design life	Blanket layer	Particle size (well graded, filter/ compatibility criteria); Durability (Los Angeles (LA) abrasion or Microdeval).	ρ_d =100-103% (proctor); ρ_d =98-100% (mod. Proctor) Min. deformation modulus (plate load bearing test) $E_v \geq 120 MN/m^2$		Permeability ($\leq 10^{-6}$, >5-10^{-5}m/s); 80-85% surface water to run away in ballast and blanket; Frost susceptibility (Casagrande criterion).
		Prepared subgrade (subgrade & embankment fill)	Soil quality class based on: Particle size (%fines); Plasticity; Weathering susceptibility (eg.chalk ρ_d<1.7t/m^3, marl, shale).	ρ_d =100% (proctor), ρ_d =95% (mod. proctor); Min. deformation modulus (plate load bearing test) $E_v \geq 80 MN/m^2$.	Bearing capacity: min. CBR range 2-17%, tested on a wet remoulded sample compacted to design conditions.	Cross fall min. 3-5%; Ground water table depth min. 0.8m below rail; Critical fines % (frost).

Design	Loading/ Categories	Foundation layers	Material properties	Density (compaction)	Strength/Stiffness	Drainage/ moisture
ESC 410, SPC411 (NSW Transport RailCorp 2010; 2012)	Characteristic traffic on RailCorp lines (no high speed)	Capping & structural zone (subballast)	Particle size distribution; Atterberg limits (PI, liquid limit, plastic limit, linear shrinkage); Durability (LA abrasion test – rock material)	Max dry density (≥20kN/m^3 and ≥18kN/m^3)	Soaked CBR (min. 50% and min. 8%)	not overtopped by 1:100 design flood Free draining Sloped (1 in 30)
		General fill (& subgrade)	PI, dispersive potential, free swell index	Max dry density (≥95%)	Soaked CBR (min. 3%)	Sloped (1 in 30)

Design	Loading/ Categories	Foundation layers	Material properties	Density (compaction)	Strength/Stiffness	Drainage/ moisture
S410 Earthworks specifications (Spoornet 2006)	Axle load categories: 20t; 26t; 30t.	Subballast layers	Particle size distribution; Plastic and liquid limit; PI (3-10); Max CBR swell; Durability (for rock) 10%FACT (Fines Aggregate Crushing Test).	Min. compaction mod AASHTO density (95 or 98%); Min. no. roller passes; At optimum moisture content.	Min. compacted CBR value = 30 or 60%.	Effective drainage. Cross fall not specified in document, but min. value used in practice=3%.
		Subgrade formation	Particle size distribution; Plastic and liquid limit; PI (<12).	Min. compaction mod AASHTO density (93 or 95%); Min. no. roller passes; At optimum moisture content.	Min. compacted CBR value = 20%.	Effective drainage.

Design	Loading/ Categories	Foundation layers	Material properties	Density (compaction)	Strength/Stiffness	Drainage/ moisture
USA (Li & Selig 1998a; 1998b)	Geotrack – analytical, elastic, multilayer 3D-model of track system; Dynamic wheel loads (static axle & speed); Number of load cycles	Subgrade	Soil type parameters from repeated loading tests (or estimated for type e.g. fat clay). Influenced by clay content and plasticity (Li and Selig, 1996).	Dry density assumed to be represented indirectly in static strength test.	Resilient modulus (deviator stress recoverable axial strain); Compressive strength.	
Formation treatment, Earthworks (Network Rail 2005; 2010)	Track category (speed and usage), 25.4 tonne axle limit on UK lines Total trackbed stiffness indicator (not per layer) [kN/mm/sleeper end]	Blanket layer (min thickness) & Fill material Subgrade (natural material)	Particle size distribution; Plasticity PI	Max. dry density, Optimum moisture content. Soft spots removed and backfilled.	CBR (subgrade and capping >15%). Fill over hard rock $E_v \leq 130 MN/m^2$. Undrained subgrade modulus. (E_{secant} for 5th cycle from repeated load triaxial test (BS1377:Part7) σ_c=30kPa; q=30kPa) CBR≥15% (BS1377-9)	Cross fall Cross fall; assume NGWL above base of trackbed

Appendix B

Calibration

Figure B.1: Mitutoyo series 152-348 micrometer used for displacement calibration of LVDTs, 25 mm range and 1 μm resolution

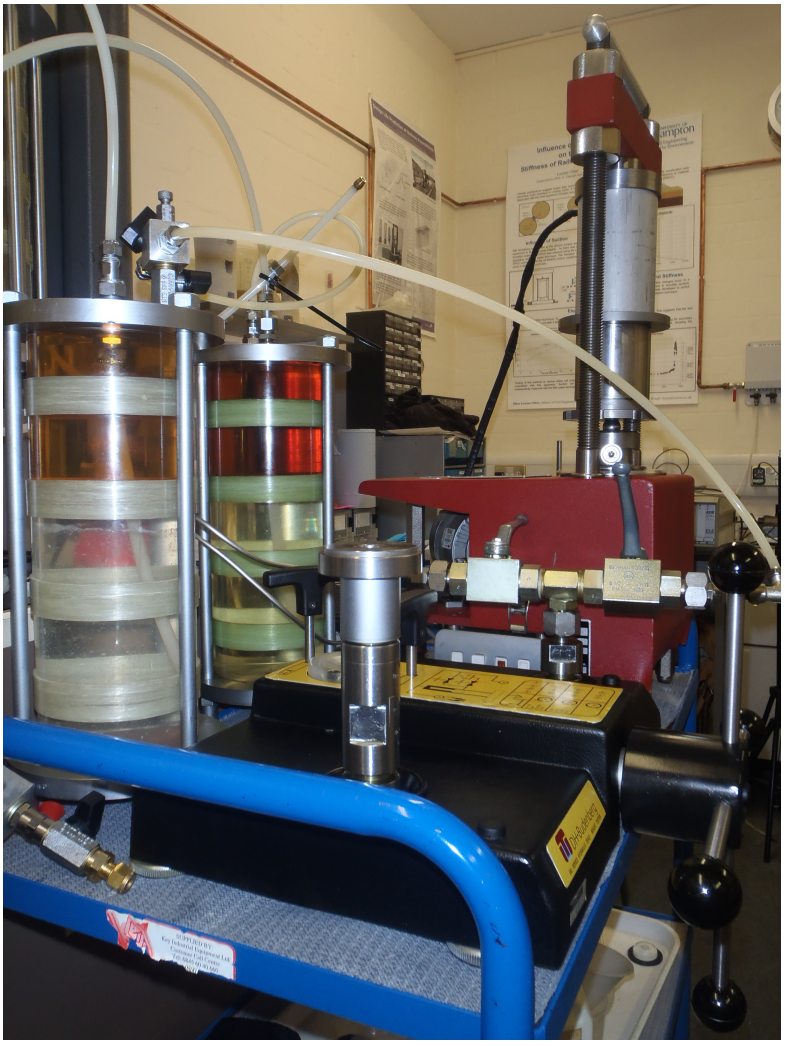

Figure B.2: DH Brudenberg Ltd., 580-series hydraulic dead-weight tester used for load transducers (axial) and the pressure transducers calibration. Set up for HCA axial load cell calibration using special extension piece

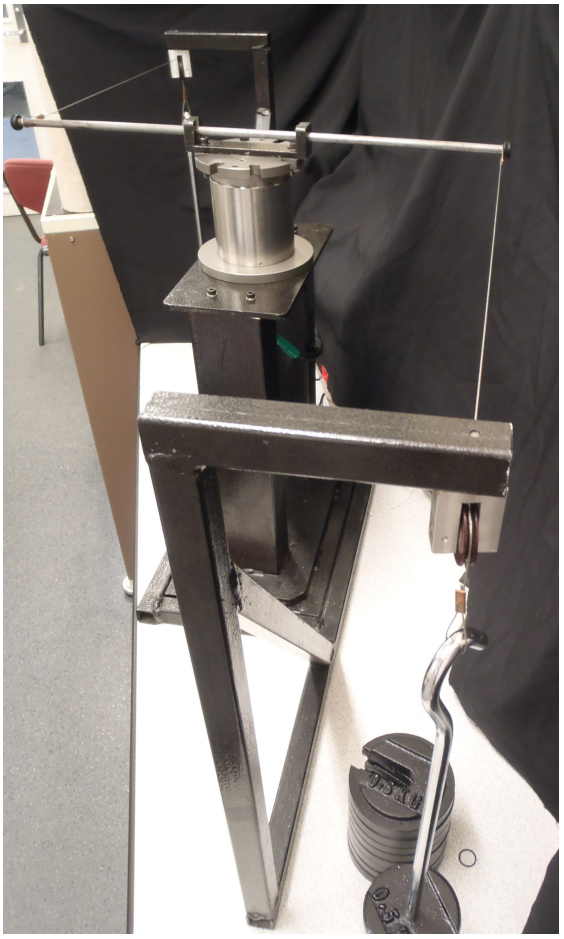

Figure B.3: Dead-weight calibration frame built by Gräbe (2002) used for the torque calibration of the HCA combined load&torque transducer

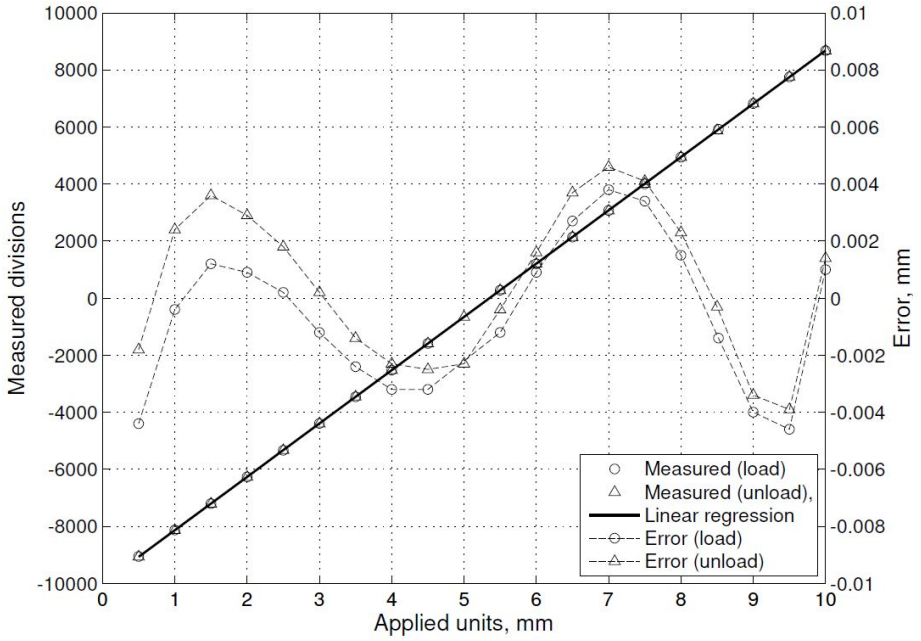

Figure B.4: Calibration graph of CTX LVDT1 used for local axial displacement measurement. Range: 10 mm, 1000 mV; sensitivity: 0.00536 mm/mV

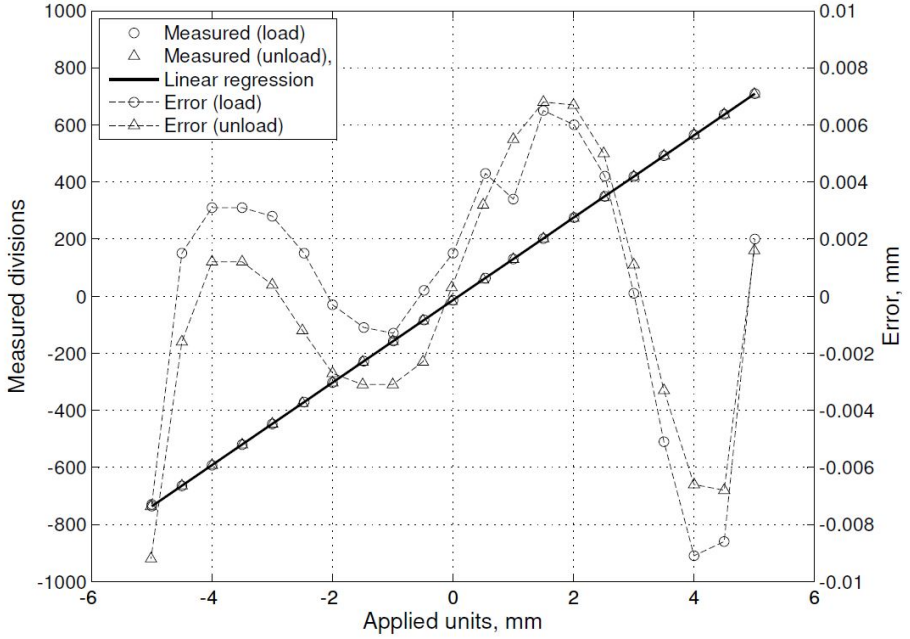

Figure B.5: Calibration graph of CTX LVDT2 used for local axial displacement measurement. Range: 10 mm, 1000 mV; sensitivity: 0.006939 mm/mV

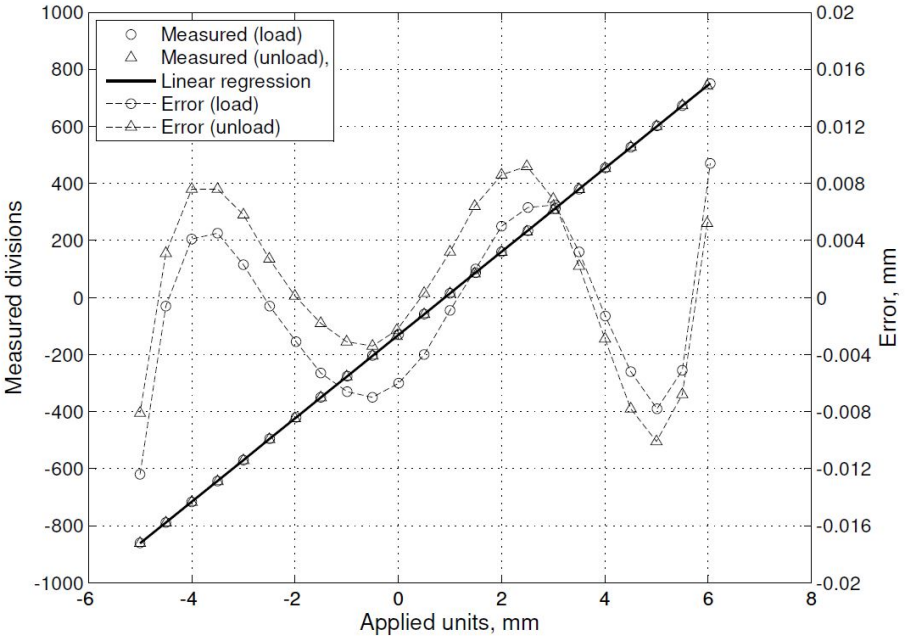

Figure B.6: Calibration graph of CTX LVDT3 used for local radial displacement measurement. Range: 10 mm, 1000 mV; sensitivity: 0.006847 mm/mV

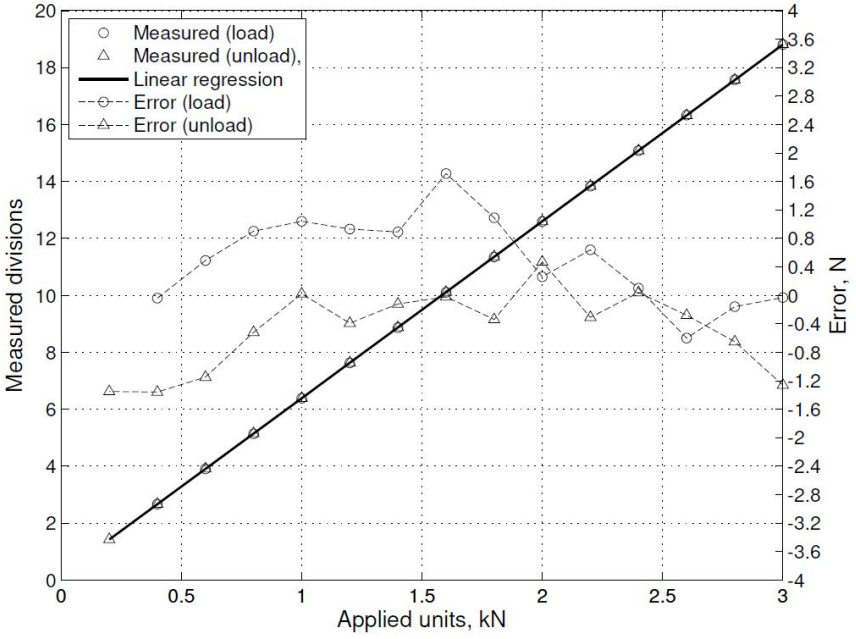

Figure B.7: Calibration graph of CTX load measurement of the 4 kN load transducer

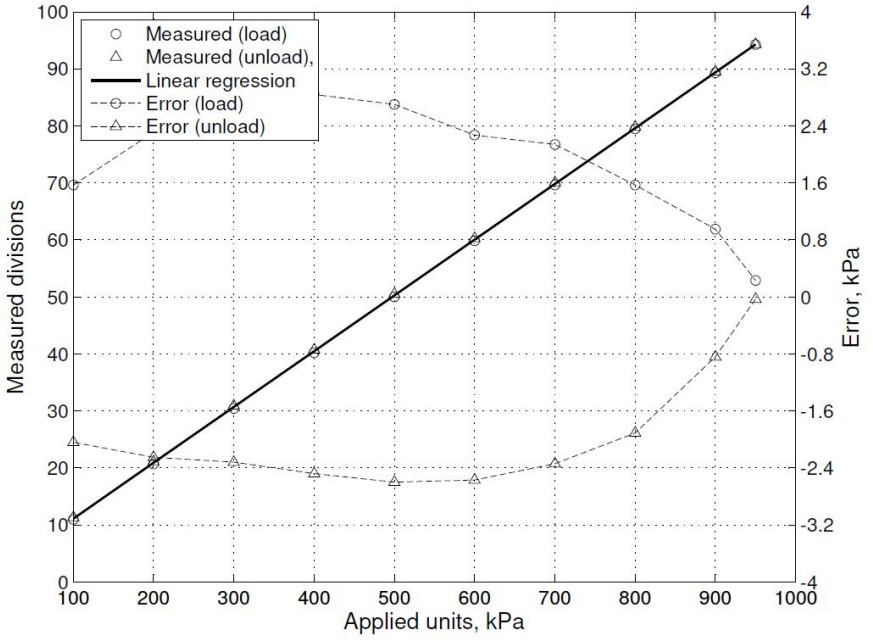

Figure B.8: Calibration graph of CTX pressure transducer (PDCR810, cell pressure)

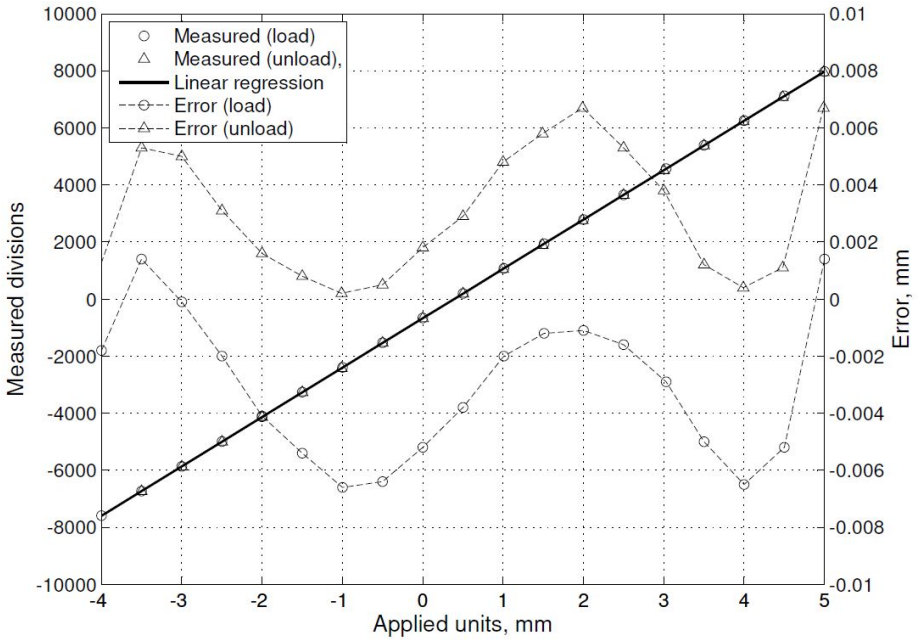

Figure B.9: Calibration graph of HCA LVDT1 used for local axial displacement measurement

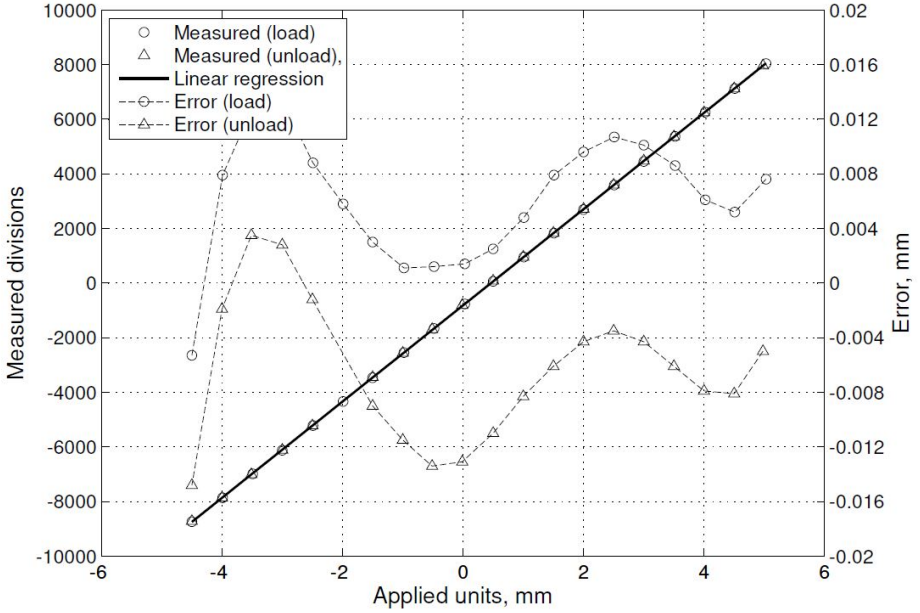

Figure B.10: Calibration graph of HCA LVDT2 used for local axial displacement measurement

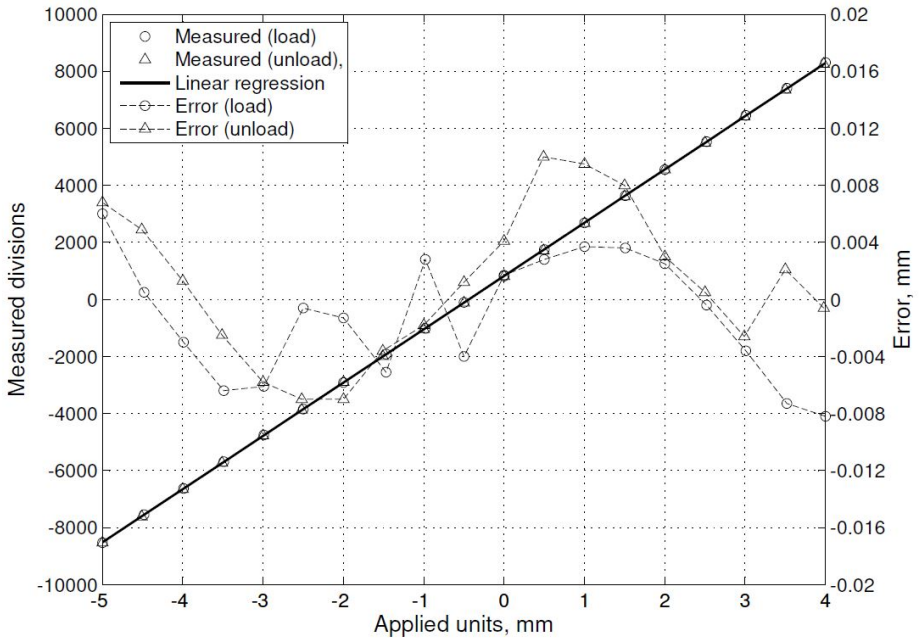

Figure B.11: Calibration graph of HCA LVDT3 used for local radial displacement measurement

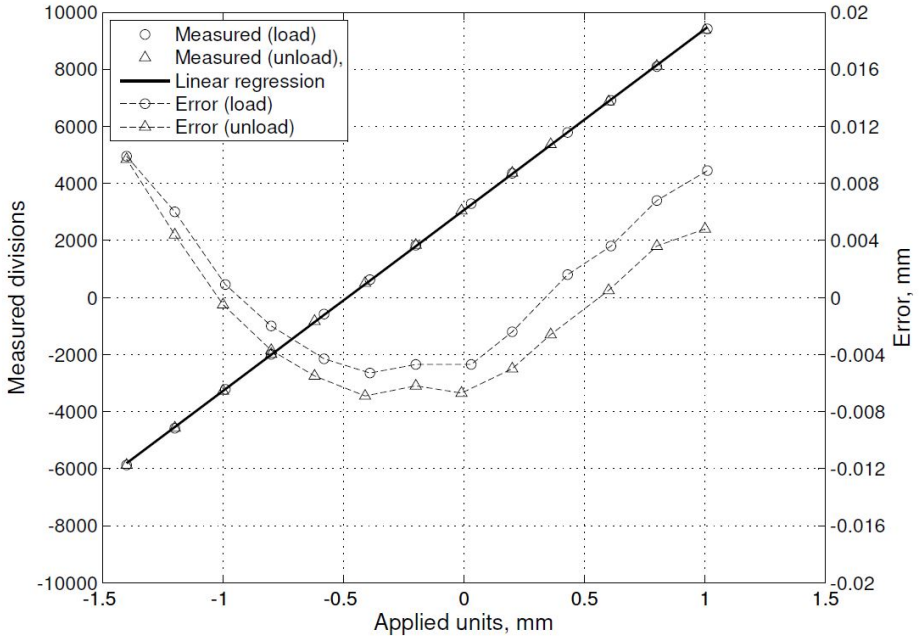

Figure B.12: Calibration graph of HCA LVDT4 used for local circumferential displacement measurement

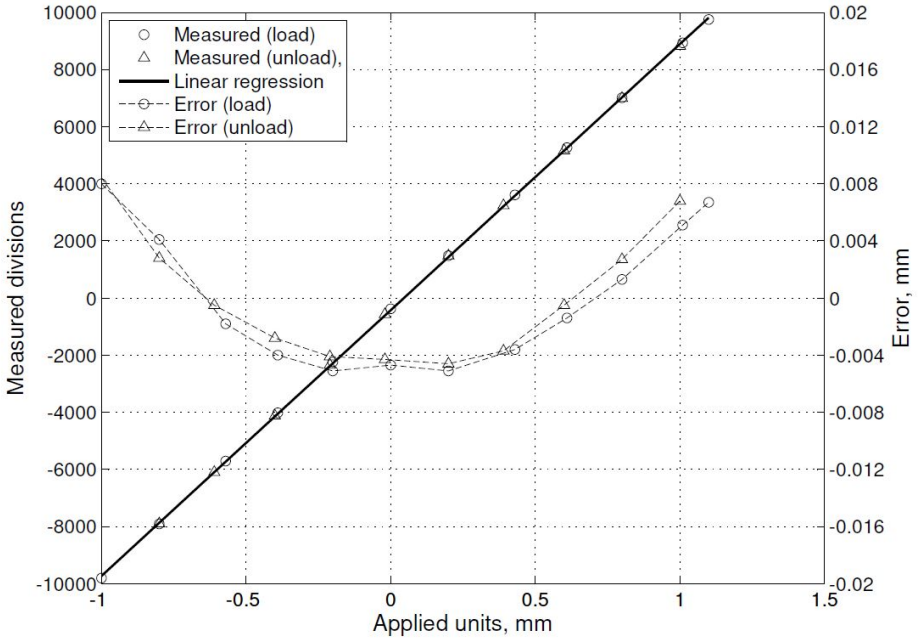

Figure B.13: Calibration graph of HCA LVDT5 used for local circumferential displacement measurement

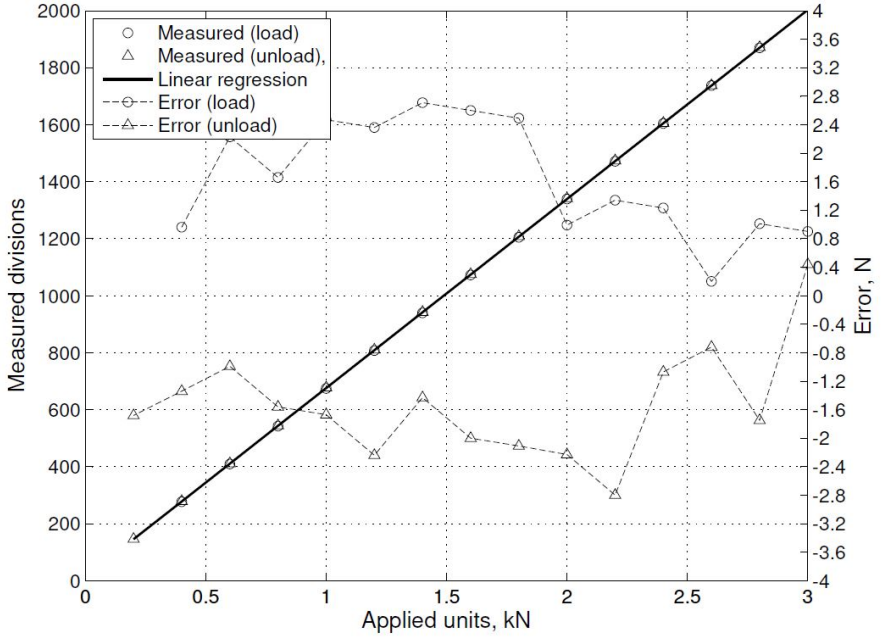

Figure B.14: Calibration graph of HCA axial load measurement of the 10kN/100Nm load/torque transducer

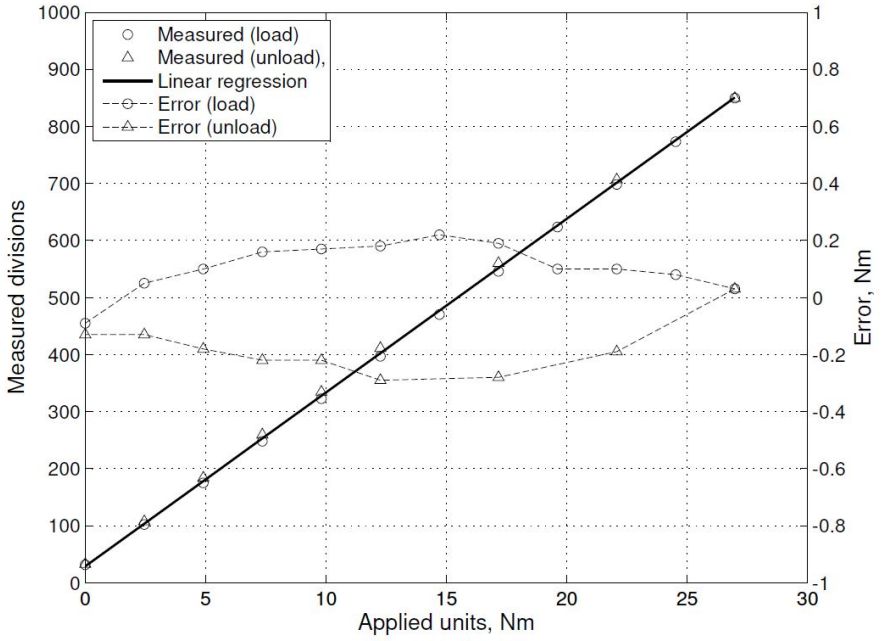

Figure B.15: Calibration graph of HCA torque measurement of the 10kN/100Nm load/torque transducer

Appendix C

Cyclic triaxial test results

Table C.1: CTX+0v0 test results

CTX+0v0 Stress sequence	Confining stress, p_o (kPa)	Min. deviator stress, q_{min} (kPa)	Max. deviator stress, q_{max} (kPa)	Global resilient modulus, M_{R^G} (MPa)	Local (1) resilient modulus, $M_{R^{L1}}$ (MPa)	Local (2) resilient modulus, $M_{R^{L2}}$ (MPa)	Avg. cyclic recoverable vert. strain, ϵ_R (local), (%)	Avg. local vertical strain initial, ϵ_{z_i}, (%)	Avg. local vertical strain final, ϵ_{z_f}, (%)	Avg. local volumetric strain initial, ϵ_{V_i}, (%)	Avg. local volumetric strain final, ϵ_{V_f}, (%)
1*	20.5	2.9	10.6	34.1	220.0	108.8	0.005	-0.05	-0.03	0.53	0.55
2	35.3	5.9	21.2	52.1	146.1	121.2	0.012	0.09	0.20	0.70	0.80
3	45.1	7.9	28.4	69.8	159.5	144.9	0.014	0.24	0.31	0.87	0.96
4	60.0	11.1	39.2	87.6	181.2	166.2	0.016	0.35	0.45	1.03	1.15
5	91.1	17.2	60.7	121.4	220.9	205.0	0.020	0.51	0.64	1.26	1.40
6*	22.5	3.0	18.3	51.3	163.0	117.1	0.011	0.59	0.57	1.41	1.40
7	35.6	6.0	36.7	75.7	139.7	131.2	0.023	0.60	0.60	1.41	1.41
8	45.5	7.9	49.0	88.2	155.1	141.7	0.028	0.62	0.63	1.43	1.43
9	60.3	10.9	67.4	93.9	168.5	150.5	0.036	0.65	0.70	1.45	1.49
10	90.5	17.1	104.5	113.3	192.4	175.8	0.048	0.73	0.97	1.51	1.75
11	22.2	3.0	33.8	51.3	99.9	90.6	0.032	0.91	0.89	1.73	1.71
12	35.8	5.9	67.5	69.2	111.2	103.2	0.058	0.93	0.97	1.74	1.76
13	45.6	7.7	90.3	84.7	128.1	116.9	0.068	1.00	1.07	1.79	1.84
14	60.1	11.0	124.3	96.4	147.1	133.1	0.081	1.11	1.44	1.86	1.89
15	90.6	16.9	192.1	116.3	187.9	167.4	0.099	1.50	2.41	1.93	1.97
16	22.3	2.9	49.3	53.8	82.5	75.9	0.059	2.35	2.30	1.95	1.82
17	35.7	5.6	98.5	75.8	112.2	101.2	0.087	2.36	2.38	1.86	1.78
18	45.7	8.0	131.3	89.2	135.7	120.8	0.096	2.43	2.48	1.82	1.78
19	60.4	10.8	180.5	106.2	159.2	143.0	0.113	2.52	2.92	1.82	1.75
20**	91.1	16.6	277.4	128.8	179.5	184.1	0.143	2.98	6.00	1.79	1.29

* Outlier ** $\epsilon_z > 5\%$

Table C.2: CTX+0v0$_p$ test results

CTX+0v0$_p$ Stress sequence	Confining stress, p_o (kPa)	Min. deviator stress, q_{min} (kPa)	Max. deviator stress, q_{max} (kPa)	Global resilient modulus, M_{R^G} (MPa)	Local (1) resilient modulus, $M_{R^{L1}}$ (MPa)	Local (2) resilient modulus, $M_{R^{L2}}$ (MPa)	Avg. cyclic recoverable vert. strain, ϵ_R (local), (%)	Avg. local vertical strain initial, ϵ_{z_i}, (%)	Avg. local vertical strain final, ϵ_{z_f}, (%)	Avg. local volumetric strain initial, ϵ_{V_i}, (%)	Avg. local volumetric strain final, ϵ_{V_f}, (%)
1*	23.8	3.0	10.6	32.7	182.5	335.8	0.003	0.12	0.12	0.33	0.33
2	36.9	6.0	21.1	60.9	147.5	165.7	0.010	0.15	0.23	0.35	0.43
3	46.5	7.9	28.3	65.1	150.8	167.7	0.013	0.25	0.34	0.45	0.53
4	61.5	10.8	39.0	79.0	159.4	179.3	0.017	0.37	0.48	0.55	0.67
5	91.1	17.0	60.4	100.9	188.2	203.7	0.022	0.53	0.67	0.73	0.89
6	23.8	3.0	18.2	43.5	97.9	139.4	0.013	0.61	0.63	0.88	0.89
7	37.0	6.0	36.4	68.3	104.6	128.5	0.026	0.63	0.64	0.89	0.90
8	46.9	7.9	48.6	75.3	122.9	139.2	0.031	0.66	0.67	0.91	0.92
9	61.7	10.7	67.1	85.0	136.9	150.7	0.039	0.69	0.76	0.93	0.99
10	91.3	17.0	104.0	99.6	164.6	172.8	0.052	0.79	1.05	1.01	1.22
11	23.7	2.9	33.6	47.5	76.4	88.8	0.037	1.00	0.98	1.22	1.16
12	37.1	5.8	67.1	61.3	94.6	102.5	0.062	1.02	1.06	1.18	1.18
13	46.9	8.0	89.7	75.0	110.0	118.5	0.072	1.09	1.17	1.20	1.22
14	61.5	10.7	123.5	90.5	128.2	136.0	0.085	1.21	1.52	1.24	1.35
15	92.5	16.9	191.3	115.9	165.8	178.9	0.101	1.57	2.40	1.39	1.62
16	23.7	3.1	49.0	51.7	73.2	76.5	0.061	2.35	2.30	1.60	1.46
17	37.2	5.9	98.2	76.1	99.4	105.3	0.090	2.36	2.39	1.50	1.48
18	47.0	7.9	130.9	82.6	120.7	130.6	0.098	2.43	2.47	1.51	1.51
19	62.1	10.7	179.9	100.7	142.1	159.6	0.113	2.51	2.80	1.53	1.50
20	91.4	16.5	277.3	122.8	182.1	202.6	0.136	2.86	5.16	1.52	1.21

* Outlier

Table C.3: CTX+0v2 test results

CTX+0v2 Stress sequence	Confining stress, p_o (kPa)	Min. deviator stress, q_{min} (kPa)	Max. deviator stress, q_{max} (kPa)	Global resilient modulus, M_{R^G} (MPa)	Local (1) resilient modulus, $M_{R^{L1}}$ (MPa)	Local (2) resilient modulus, $M_{R^{L2}}$ (MPa)	Avg. cyclic recoverable vert. strain, ϵ_R (local), (%)	Avg. local vertical strain initial, ϵ_{z_i}, (%)	Avg. local vertical strain final, ϵ_{z_f}, (%)	Avg. local volumetric strain initial, ϵ_{V_i}, (%)	Avg. local volumetric strain final, ϵ_{V_f}, (%)
1	14.1	2.9	10.5	19.9	68.3	63.7	0.012	0.12	0.14	0.10	0.12
6	14.3	2.9	18.2	24.2	40.5	41.1	0.038	0.15	0.35	0.14	0.33
11	14.5	2.9	33.5	25.7	38.2	35.7	0.083	0.40	0.99	0.37	0.66
16	14.6	3.1	48.7	29.4	46.6	41.8	0.104	1.05	1.57	0.72	0.78
2	28.0	5.9	21.2	35.1	96.6	83.5	0.017	1.60	1.57	0.80	0.81
7	28.1	6.0	36.4	41.5	86.6	74.7	0.038	1.59	1.59	0.83	0.85
12	28.1	5.5	67.1	44.1	75.2	64.5	0.089	1.62	1.82	0.87	1.04
17	28.3	5.4	97.6	49.0	86.7	73.7	0.116	1.86	2.75	1.08	1.13
3	37.9	7.9	28.4	46.8	129.1	110.0	0.017	2.76	2.73	1.13	1.13
8	38.0	7.9	48.9	54.5	115.9	99.3	0.038	2.74	2.73	1.14	1.14
13	38.1	7.5	89.5	57.5	113.5	96.0	0.079	2.76	2.77	1.17	1.19
4	52.8	11.2	39.1	56.6	163.6	137.2	0.019	2.78	2.76	1.19	1.21
9	52.9	10.7	67.3	62.9	149.4	127.0	0.041	2.77	2.77	1.23	1.24
14	52.6	10.8	123.3	68.0	141.4	117.5	0.088	2.79	2.89	1.27	1.36
5	82.3	17.2	60.7	73.7	212.2	182.0	0.022	2.89	2.87	1.35	1.40
10	82.5	17.1	104.2	79.2	194.6	167.8	0.048	2.88	2.88	1.41	1.44
15	82.7	16.6	191.4	83.4	177.5	149.4	0.108	2.91	3.61	1.47	1.65
20	83.4	16.4	277.3	91.1	205.6	180.1	0.136	3.66	6.63	1.69	1.03

Table C.4: CTX+0v1$_c$ test results

CTX+0v1$_c$ Stress sequence	Confining stress, p_o (kPa)	Min. deviator stress, q_{min} (kPa)	Max. deviator stress, q_{max} (kPa)	Global resilient modulus, M_{R^G} (MPa)	Local (1) resilient modulus, $M_{R^{L1}}$ (MPa)	Local (2) resilient modulus, $M_{R^{L2}}$ (MPa)	Avg. cyclic recoverable vert. strain, ϵ_R (local), (%)	Avg. local vertical strain initial, ϵ_{z_i}, (%)	Avg. local vertical strain final, ϵ_{z_f}, (%)	Avg. local volumetric strain initial, ϵ_{V_i}, (%)	Avg. local volumetric strain final, ϵ_{V_f}, (%)
1*	14.4	3.1	10.6	18.9	83.3	67.2	0.010	0.07	0.08	-0.01	0.01
2	27.1	5.8	21.0	31.3	90.4	62.2	0.021	0.18	0.28	0.10	0.22
3	37.1	7.9	28.2	39.4	109.7	74.2	0.023	0.31	0.38	0.26	0.35
4	51.7	10.9	39.0	47.3	141.0	90.5	0.026	0.42	0.50	0.43	0.55
5	82.6	17.1	60.5	63.6	195.2	124.8	0.028	0.56	0.65	0.71	0.84
6	14.8	2.9	18.3	27.9	85.0	62.4	0.021	0.56	0.58	0.81	0.83
7	27.6	6.1	36.8	39.7	98.2	70.2	0.037	0.60	0.62	0.83	0.85
8	37.4	8.0	49.0	47.4	115.4	83.3	0.042	0.64	0.66	0.87	0.89
9	52.2	11.0	67.4	55.7	137.8	100.0	0.049	0.69	0.76	0.91	0.98
10	82.5	17.0	104.4	71.9	181.0	131.4	0.057	0.80	1.00	1.01	1.20
11	15.0	3.0	33.7	34.1	76.9	63.4	0.044	0.94	0.91	1.19	1.10
12	27.8	5.9	67.5	47.5	98.9	81.6	0.069	0.97	1.02	1.14	1.11
13	37.6	7.8	89.9	57.3	117.2	95.2	0.078	1.06	1.15	1.14	1.12
14	52.3	10.6	123.9	70.0	143.2	113.7	0.089	1.19	1.46	1.15	1.16
15	82.3	17.1	191.7	88.8	192.4	149.6	0.104	1.52	2.18	1.20	1.25
16	15.1	2.9	49.1	37.1	78.6	68.5	0.063	2.12	2.08	1.24	1.10
17	27.8	5.3	98.1	58.2	110.5	93.9	0.091	2.14	2.16	1.14	1.07
18	37.6	7.9	131.0	68.3	136.3	113.8	0.099	2.20	2.24	1.11	1.07
19	52.5	10.3	179.9	76.9	163.1	135.4	0.115	2.29	2.52	1.11	1.04
20	82.3	16.7	277.3	97.3	208.8	179.5	0.135	2.58	3.92	1.09	0.72

* Outlier

Table C.5: CTX-1v0 test results

CTX-1v0 Stress sequence	Confining stress, p_o (kPa)	Min. deviator stress, q_{min} (kPa)	Max. deviator stress, q_{max} (kPa)	Global resilient modulus, M_{R^G} (MPa)	Local (1) resilient modulus, $M_{R^{L1}}$ (MPa)	Local (2) resilient modulus, $M_{R^{L2}}$ (MPa)	Avg. cyclic recoverable vert. strain, ϵ_R (local), (%)	Avg. local vertical strain initial, ϵ_{z_i}, (%)	Avg. local vertical strain final, ϵ_{z_f}, (%)	Avg. local volumetric strain initial, ϵ_{V_i}, (%)	Avg. local volumetric strain final, ϵ_{V_f}, (%)
1*	23.6	3.0	10.6	30.2	314.5	335.6	0.002	0.22	0.22	0.01	0.01
2	36.9	5.9	21.1	63.4	313.1	283.6	0.005	0.24	0.26	0.03	0.05
3	46.8	7.7	28.1	77.4	315.8	295.9	0.007	0.29	0.31	0.09	0.12
4	61.7	10.6	38.7	94.5	340.6	324.8	0.008	0.34	0.37	0.16	0.19
5	91.5	16.7	59.7	121.3	355.9	355.3	0.012	0.42	0.45	0.27	0.32
6	24.2	3.0	18.1	50.3	258.1	241.6	0.006	0.39	0.39	0.28	0.29
7	37.3	5.7	36.2	82.7	249.3	240.1	0.012	0.41	0.41	0.29	0.29
8	47.2	7.8	48.0	94.2	256.1	250.3	0.016	0.42	0.42	0.30	0.30
9	62.3	10.6	66.4	109.6	266.9	264.4	0.021	0.44	0.45	0.31	0.32
10	92.0	16.8	102.7	126.9	292.6	291.4	0.029	0.48	0.52	0.34	0.40
11	24.1	2.8	33.2	67.5	185.8	212.1	0.015	0.47	0.46	0.37	0.36
12	37.7	5.7	66.3	92.3	191.6	200.9	0.031	0.48	0.49	0.37	0.37
13	47.7	7.5	88.6	99.7	212.0	203.5	0.039	0.51	0.51	0.39	0.39
14	62.5	10.5	121.7	111.2	226.8	220.9	0.050	0.54	0.57	0.41	0.42
15	92.1	16.5	188.6	133.5	250.4	266.7	0.067	0.61	0.74	0.45	0.57
16	24.0	3.1	48.3	72.9	160.6	167.1	0.028	0.68	0.66	0.51	0.48
17	37.8	5.2	96.7	89.9	168.0	176.2	0.053	0.69	0.69	0.50	0.49
18	47.8	7.6	128.9	102.1	184.2	197.5	0.064	0.72	0.72	0.51	0.51
19	62.7	10.3	177.4	117.7	208.2	223.7	0.077	0.75	0.80	0.53	0.55
20	92.4	16.4	274.8	146.5	233.4	265.7	0.104	0.84	1.44	0.58	0.83

* Outlier

Table C.6: CTX-2v0 test results

CTX-2v0 Stress sequence	Confining stress, p_o (kPa)	Min. deviator stress, q_{min} (kPa)	Max. deviator stress, q_{max} (kPa)	Global resilient modulus, M_{R^G} (MPa)	Local (1) resilient modulus, $M_{R^{L1}}$ (MPa)	Local (2) resilient modulus, $M_{R^{L2}}$ (MPa)	Avg. cyclic recoverable vert. strain, ϵ_R (local), (%)	Avg. local vertical strain initial, ϵ_{z_i}, (%)	Avg. local vertical strain final, ϵ_{z_f}, (%)	Avg. local volumetric strain initial, ϵ_{V_i}, (%)	Avg. local volumetric strain final, ϵ_{V_f}, (%)
1	21.6	3.0	10.5	22.4	330.8	536.1	0.002	-0.01	-0.01	-0.07	-0.08
2	36.4	6.0	21.0	53.8	420.4	505.4	0.003	-0.01	-0.01	-0.09	-0.09
3	46.4	7.8	28.1	65.3	440.4	530.7	0.004	0.00	0.00	-0.09	-0.09
4	61.2	10.8	38.7	76.4	463.5	547.7	0.006	0.00	0.01	-0.09	-0.09
5	91.1	16.9	59.6	96.4	497.0	566.3	0.008	0.02	0.02	-0.09	-0.09
6	23.8	3.3	18.0	40.0	333.5	508.6	0.004	0.01	0.01	-0.06	-0.06
7	36.9	5.9	36.2	69.0	372.0	479.3	0.007	0.01	0.01	-0.07	-0.07
8	46.6	7.9	48.3	80.7	380.1	475.1	0.010	0.01	0.01	-0.07	-0.08
9	61.6	10.8	66.4	92.3	398.9	469.8	0.013	0.02	0.02	-0.08	-0.08
10	91.4	16.5	102.8	107.0	430.8	484.7	0.019	0.03	0.03	-0.08	-0.08
11	23.5	3.4	33.2	58.2	307.5	461.6	0.008	0.02	0.02	-0.05	-0.05
12	37.2	5.4	66.3	81.6	308.7	407.0	0.017	0.02	0.02	-0.06	-0.06
13	47.2	7.5	88.3	89.5	315.1	397.2	0.023	0.03	0.03	-0.06	-0.06
14	62.0	10.7	121.7	102.1	331.0	401.9	0.031	0.04	0.04	-0.06	-0.06
15	91.6	16.5	188.4	122.9	368.3	431.0	0.043	0.06	0.07	-0.05	-0.04
16	23.4	3.2	48.4	62.0	271.4	386.8	0.014	0.05	0.05	-0.02	-0.02
17	37.5	5.8	96.5	87.8	272.9	345.5	0.030	0.06	0.05	-0.02	-0.03
18	47.5	7.3	128.9	97.6	284.8	352.2	0.039	0.06	0.06	-0.02	-0.03
19	62.1	10.5	177.0	111.2	309.1	373.2	0.049	0.08	0.07	-0.02	-0.02
20	92.4	16.3	274.3	130.6	357.5	415.6	0.067	0.10	0.14	-0.01	0.02

Table C.7: CTX-2v1$_r$ test results

CTX-2v1$_r$ Stress sequence	Confining stress, p_o (kPa)	Min. deviator stress, q_{min} (kPa)	Max. deviator stress, q_{max} (kPa)	Global resilient modulus, M_{R^G} (MPa)	Local (1) resilient modulus, $M_{R^{L1}}$ (MPa)	Local (2) resilient modulus, $M_{R^{L2}}$ (MPa)	Avg. cyclic recoverable vert. strain, ϵ_R (local), (%)	Avg. local vertical strain initial, ϵ_{z_i}, (%)	Avg. local vertical strain final, ϵ_{z_f}, (%)	Avg. local volumetric strain initial, ϵ_{V_i}, (%)	Avg. local volumetric strain final, ϵ_{V_f}, (%)
1*	13.3	2.9	10.5	31.6	1413.4	436.6	0.001	-0.02	-0.02	-0.10	-0.11
2	27.9	5.9	20.9	48.8	648.2	423.4	0.003	-0.04	-0.05	-0.11	-0.11
3	37.7	7.7	28.1	57.7	602.3	435.7	0.004	-0.05	-0.05	-0.11	-0.10
4	52.5	10.8	38.7	67.2	569.1	454.7	0.006	-0.06	-0.06	-0.09	-0.08
5	82.1	16.7	59.9	83.7	583.2	503.7	0.008	-0.07	-0.07	-0.05	-0.04
6	15.0	2.9	18.2	41.1	469.1	358.6	0.004	-0.05	-0.05	0.02	0.03
7	28.2	5.8	36.3	59.1	464.4	369.8	0.007	-0.06	-0.06	0.00	0.00
8	38.0	7.8	48.5	69.4	469.2	378.7	0.010	-0.06	-0.07	-0.01	-0.01
9	52.9	10.8	66.2	83.2	474.2	396.3	0.013	-0.07	-0.07	-0.02	-0.02
10	82.7	16.7	102.7	102.4	495.2	427.3	0.019	-0.06	-0.06	-0.02	0.00
11	14.8	2.9	33.3	52.9	405.7	310.4	0.009	-0.05	-0.05	0.06	0.06
12	28.6	5.5	66.3	76.7	397.7	315.7	0.017	-0.05	-0.05	0.04	0.03
13	38.5	7.5	88.6	87.3	393.9	323.2	0.023	-0.05	-0.05	0.03	0.03
14	53.3	10.6	121.8	104.3	396.9	340.5	0.030	-0.05	-0.05	0.02	0.02
15	83.4	16.3	188.6	125.2	428.4	381.0	0.043	-0.03	-0.03	0.02	0.05
16	14.5	2.9	48.4	64.3	352.0	278.7	0.015	-0.02	-0.03	0.11	0.10
17	28.8	5.4	96.9	88.6	347.5	284.2	0.029	-0.03	-0.03	0.09	0.08
18	38.7	7.8	128.8	99.6	349.9	294.9	0.038	-0.02	-0.03	0.08	0.08
19	53.5	10.4	177.5	112.5	370.8	322.2	0.048	-0.02	-0.02	0.08	0.08
20	83.6	16.4	274.7	128.7	413.6	365.1	0.067	0.00	0.03	0.08	0.11

* Outlier

Table C.8: CTX-2v1$_r$ test results (Continued)

CTX-2v1$_r$ Stress sequence	Confining stress, p_o (kPa)	Min. deviator stress, q_{min} (kPa)	Max. deviator stress, q_{max} (kPa)	Global resilient modulus, M_{R^G} (MPa)	Local (1) resilient modulus, $M_{R^{L1}}$ (MPa)	Local (2) resilient modulus, $M_{R^{L2}}$ (MPa)	Avg. cyclic recoverable vert. strain, ϵ_R (local), (%)	Avg. local vertical strain initial, ϵ_{z_i}, (%)	Avg. local vertical strain final, ϵ_{z_f}, (%)	Avg. local volumetric strain initial, ϵ_{V_i}, (%)	Avg. local volumetric strain final, ϵ_{V_f}, (%)
1	15.1	2.9	10.5	23.6	472.2	362.9	0.002	0.00	0.00	0.14	0.14
6	14.8	2.9	18.2	34.3	433.2	347.6	0.004	0.00	0.00	0.14	0.14
11	14.7	2.8	33.2	49.5	379.4	307.1	0.009	0.01	0.01	0.14	0.14
16	14.5	2.6	48.2	58.6	345.0	278.1	0.015	0.01	0.01	0.15	0.14
2	28.0	5.9	21.2	42.6	501.9	375.1	0.004	0.00	0.00	0.12	0.12
7	28.2	5.6	36.2	57.7	451.7	350.9	0.008	0.00	0.00	0.12	0.12
12	28.7	5.8	66.7	75.9	374.1	301.4	0.018	0.00	0.00	0.12	0.12
17	28.9	6.4	96.8	85.8	331.3	273.4	0.030	0.01	0.01	0.13	0.12
3	38.0	7.8	28.3	51.8	495.5	383.8	0.005	0.00	0.00	0.11	0.11
8	38.2	8.0	48.2	71.3	430.1	348.0	0.010	0.00	0.00	0.11	0.11
13	38.7	8.2	88.8	88.0	365.5	302.3	0.024	0.01	0.00	0.12	0.11
18	38.8	7.7	129.2	95.1	335.6	282.5	0.040	0.01	0.01	0.12	0.12
4	52.7	11.1	38.8	67.9	509.3	401.7	0.006	0.00	0.00	0.10	0.10
9	53.1	10.9	66.4	87.2	436.1	362.2	0.014	0.00	0.00	0.10	0.10
14	53.5	10.4	121.9	99.0	375.2	316.4	0.032	0.01	0.01	0.11	0.11
19	53.2	10.3	177.2	105.6	353.4	302.2	0.051	0.02	0.01	0.12	0.11

Table C.9: CTX-3v0 test results

CTX-3v0 Stress sequence	Confining stress, p_o (kPa)	Min. deviator stress, q_{min} (kPa)	Max. deviator stress, q_{max} (kPa)	Global resilient modulus, M_{R^G} (MPa)	Local (1) resilient modulus, $M_{R^{L1}}$ (MPa)	Local (2) resilient modulus, $M_{R^{L2}}$ (MPa)	Avg. cyclic recoverable vert. strain, ϵ_R (local), (%)	Avg. local vertical strain initial, ϵ_{z_i}, (%)	Avg. local vertical strain final, ϵ_{z_f}, (%)	Avg. local volumetric strain initial, ϵ_{V_i}, (%)	Avg. local volumetric strain final, ϵ_{V_f}, (%)
1*	21.5	2.9	10.6	22.8	384.6	1205.2	0.001	0.14	0.14	0.03	0.03
2	36.2	5.8	21.1	55.5	436.3	847.8	0.003	0.14	0.14	0.10	0.10
3	46.1	7.9	28.1	65.2	473.2	808.7	0.003	0.14	0.14	0.13	0.13
4	60.8	11.0	38.6	79.4	487.3	785.4	0.005	0.14	0.13	0.17	0.17
5	90.6	16.8	59.6	100.7	546.5	761.1	0.007	0.06	0.05	0.14	0.13
6	23.5	2.9	17.9	39.9	387.1	814.1	0.003	0.05	0.05	0.18	0.19
7	36.6	5.9	36.0	71.7	422.6	669.8	0.006	0.05	0.05	0.17	0.17
8	46.4	7.9	48.3	81.9	433.1	669.4	0.008	0.06	0.05	0.17	0.17
9	61.3	10.8	66.3	96.7	439.0	669.6	0.010	0.06	0.06	0.16	0.16
10	91.2	16.7	102.6	111.9	468.0	672.6	0.016	0.04	0.03	0.14	0.14
11	23.3	3.2	33.2	57.1	377.0	674.7	0.006	0.04	0.04	0.19	0.19
12	36.9	5.6	66.3	86.5	372.6	625.2	0.013	0.04	0.04	0.18	0.18
13	47.0	7.9	88.4	95.2	371.5	602.5	0.018	0.05	0.04	0.17	0.17
14	61.9	10.7	121.7	106.6	383.1	588.2	0.024	0.05	0.05	0.17	0.17
15	92.0	15.9	188.4	126.3	408.0	593.8	0.036	0.05	0.04	0.16	0.16
16	23.2	2.8	48.3	62.8	335.4	592.1	0.011	0.04	0.04	0.20	0.20
17	37.4	5.5	96.4	90.3	330.9	543.6	0.022	0.04	0.04	0.19	0.19
18	47.3	7.5	128.7	101.6	335.8	534.4	0.029	0.05	0.04	0.19	0.18
19	62.1	10.5	177.1	115.7	349.6	532.6	0.039	0.05	0.05	0.19	0.18
20	92.2	16.3	274.4	141.4	388.0	552.1	0.057	0.06	0.06	0.18	0.20

* Outlier

Table C.10: CTX-3v1 test results

CTX-3v1 Stress sequence	Confining stress, p_o (kPa)	Min. deviator stress, q_{min} (kPa)	Max. deviator stress, q_{max} (kPa)	Global resilient modulus, M_{R^G} (MPa)	Local (1) resilient modulus, $M_{R^{L1}}$ (MPa)	Local (2) resilient modulus, $M_{R^{L2}}$ (MPa)	Avg. cyclic recoverable vert. strain, ϵ_R (local), (%)	Avg. local vertical strain initial, ϵ_{z_i}, (%)	Avg. local vertical strain final, ϵ_{z_f}, (%)	Avg. local volumetric strain initial, ϵ_{V_i}, (%)	Avg. local volumetric strain final, ϵ_{V_f}, (%)
1*	11.8	3.4	10.5	26.1	419.6	1225.4	0.001	0.00	0.00	-0.40	-0.40
2*	25.8	6.1	21.0	49.3	414.9	1882.6	0.002	-0.12	-0.13	-0.42	-0.43
3	35.7	7.8	28.0	59.6	467.0	762.7	0.003	-0.17	-0.18	-0.44	-0.44
4	50.5	10.8	38.6	72.6	508.5	691.1	0.005	-0.21	-0.21	-0.44	-0.44
5	80.0	16.7	59.6	95.9	534.6	715.8	0.007	-0.24	-0.25	-0.43	-0.43
6	13.1	3.0	18.0	41.7	294.1	413.6	0.004	-0.13	-0.12	-0.31	-0.30
7	26.2	5.8	36.1	68.6	357.5	510.4	0.007	-0.17	-0.17	-0.36	-0.36
8	35.9	7.8	48.1	80.5	425.4	521.3	0.009	-0.19	-0.19	-0.39	-0.40
9	50.9	10.9	66.3	91.0	442.9	536.4	0.011	-0.21	-0.21	-0.41	-0.41
10	80.4	16.8	102.5	115.1	477.7	616.5	0.016	-0.23	-0.23	-0.41	-0.41
11	13.0	3.0	33.1	59.2	288.1	366.3	0.009	-0.14	-0.13	-0.31	-0.30
12	26.2	5.8	66.3	82.6	342.9	446.4	0.016	-0.17	-0.17	-0.35	-0.36
13	36.2	7.7	88.2	97.1	370.4	461.0	0.020	-0.18	-0.19	-0.38	-0.39
14	51.2	10.8	121.5	112.4	393.5	473.4	0.026	-0.20	-0.21	-0.40	-0.40
15	80.8	16.4	187.8	131.2	427.5	529.7	0.036	-0.22	-0.22	-0.40	-0.39
16	12.8	2.6	48.2	64.8	270.6	333.1	0.015	-0.14	-0.14	-0.31	-0.31
17	26.4	5.6	96.1	93.0	322.4	404.4	0.025	-0.16	-0.17	-0.35	-0.36
18	36.3	7.9	128.5	104.8	338.8	417.7	0.032	-0.18	-0.19	-0.37	-0.38
19	51.3	10.3	177.0	121.3	370.1	437.8	0.042	-0.19	-0.20	-0.39	-0.39
20	81.7	16.3	273.1	143.1	423.0	485.1	0.057	-0.20	-0.20	-0.39	-0.38

* Outlier

Table C.11: CTX-3v1$_r$ test results

CTX-3v1$_r$ Stress sequence	Confining stress, p_o (kPa)	Min. deviator stress, q_{min} (kPa)	Max. deviator stress, q_{max} (kPa)	Global resilient modulus, M_{R^G} (MPa)	Local (1) resilient modulus, $M_{R^{L1}}$ (MPa)	Local (2) resilient modulus, $M_{R^{L2}}$ (MPa)	Avg. cyclic recoverable vert. strain, ϵ_R (local), (%)	Avg. local vertical strain initial, ϵ_{z_i}, (%)	Avg. local vertical strain final, ϵ_{z_f}, (%)	Avg. local volumetric strain initial, ϵ_{V_i}, (%)	Avg. local volumetric strain final, ϵ_{V_f}, (%)
1*	15.7	3.1	10.6	25.9	287.2	478.3	0.002	-0.02	-0.02	0.04	0.04
2	30.4	6.0	21.0	48.3	653.6	485.5	0.003	-0.03	-0.03	0.13	0.13
3	40.3	7.8	28.1	56.2	588.7	520.2	0.004	-0.03	-0.03	0.16	0.16
4	55.1	10.7	38.6	70.5	637.8	543.0	0.005	-0.03	-0.03	0.20	0.20
5	84.8	16.7	59.8	90.9	635.5	598.5	0.007	-0.03	-0.03	0.27	0.28
6	17.7	2.9	18.1	42.9	384.5	470.1	0.004	-0.03	-0.03	0.32	0.32
7	30.7	5.9	36.4	67.2	432.0	491.5	0.007	-0.03	-0.03	0.30	0.30
8	40.6	7.7	48.5	76.8	455.4	499.1	0.009	-0.03	-0.03	0.30	0.29
9	55.4	10.9	66.5	89.7	484.9	512.0	0.011	-0.03	-0.03	0.29	0.29
10	85.2	16.5	102.8	110.6	530.9	539.4	0.016	-0.02	-0.02	0.30	0.30
11	17.5	3.0	33.4	59.2	383.4	445.0	0.007	-0.02	-0.03	0.34	0.33
12	31.1	5.7	66.6	84.9	401.7	445.8	0.014	-0.02	-0.03	0.32	0.32
13	41.0	8.0	88.6	96.9	411.5	445.5	0.019	-0.02	-0.02	0.32	0.31
14	55.9	10.9	122.3	109.6	432.1	454.1	0.025	-0.02	-0.02	0.31	0.31
15	86.0	16.8	188.7	130.7	468.9	476.9	0.036	0.00	0.00	0.32	0.34
16	17.3	2.7	48.6	69.4	352.8	415.2	0.012	-0.01	-0.02	0.36	0.35
17	31.4	5.3	96.9	94.9	366.8	408.0	0.024	-0.01	-0.01	0.35	0.34
18	41.2	7.5	129.3	108.6	379.3	406.3	0.031	0.00	-0.01	0.34	0.34
19	55.8	10.7	177.7	122.5	401.6	417.0	0.041	0.01	0.00	0.34	0.34
20	85.5	16.7	275.0	144.4	449.8	453.5	0.057	0.02	0.03	0.35	0.37

* Outlier

Table C.12: CTX-3v1$_r$ test results (Continued)

CTX-3v1$_r$ Stress sequence	Confining stress, p_o (kPa)	Min. deviator stress, q_{min} (kPa)	Max. deviator stress, q_{max} (kPa)	Global resilient modulus, M_{R^G} (MPa)	Local (1) resilient modulus, $M_{R^{L1}}$ (MPa)	Local (2) resilient modulus, $M_{R^{L2}}$ (MPa)	Avg. cyclic recoverable vert. strain, ϵ_R (local), (%)	Avg. local vertical strain initial, ϵ_{z_i}, (%)	Avg. local vertical strain final, ϵ_{z_f}, (%)	Avg. local volumetric strain initial, ϵ_{V_i}, (%)	Avg. local volumetric strain final, ϵ_{V_f}, (%)
1	17.6	2.8	10.4	26.0	441.2	450.4	0.002	-0.01	-0.01	0.38	0.37
6	17.6	2.8	18.2	38.6	413.9	480.1	0.003	-0.01	-0.01	0.37	0.37
11	17.3	2.7	33.4	55.1	394.8	445.5	0.007	-0.01	-0.01	0.37	0.37
16	17.1	3.0	48.5	67.5	359.5	418.3	0.012	0.00	-0.01	0.38	0.37
2	30.5	5.8	21.2	47.9	471.6	508.8	0.003	-0.01	-0.01	0.36	0.36
7	30.7	5.7	36.4	62.9	446.5	484.9	0.007	-0.01	-0.01	0.36	0.36
12	31.1	5.8	66.5	82.7	386.7	429.6	0.015	0.00	0.00	0.36	0.36
17	31.4	5.6	96.8	94.9	357.1	395.0	0.024	0.00	0.00	0.37	0.36
3	40.4	7.9	28.2	57.2	483.1	489.9	0.004	0.00	-0.01	0.35	0.35
8	40.6	7.9	48.4	76.3	446.7	469.3	0.009	0.00	0.00	0.35	0.35
13	41.1	7.4	88.9	96.2	394.7	422.4	0.020	0.00	0.00	0.36	0.35
18	41.3	7.7	129.2	106.7	368.0	391.7	0.032	0.01	0.00	0.36	0.36
4	55.2	10.8	38.9	68.4	508.9	521.3	0.005	0.00	0.00	0.35	0.34
9	55.5	10.7	66.6	91.7	464.9	480.9	0.012	0.00	0.00	0.35	0.35
14	56.0	10.6	122.1	110.8	409.7	427.5	0.027	0.01	0.01	0.35	0.35
19	55.7	10.0	177.7	120.5	386.0	399.1	0.043	0.02	0.01	0.36	0.36

Table C.13: CTX+1v1, CTX+1v2$_i$, CTX+1v2$_{ii}$, CTX+1v2$_{iii}$ and CTX+1v2$_{iii^m}$ test results

CTX+1v1 Stress sequence	Confining stress, p_o (kPa)	Min. deviator stress, q_{min} (kPa)	Max. deviator stress, q_{max} (kPa)	Global resilient modulus, M_{R^G} (MPa)	Local (1) resilient modulus, $M_{R^{L1}}$ (MPa)	Local (2) resilient modulus, $M_{R^{L2}}$ (MPa)	Avg. cyclic recoverable vert. strain, ϵ_R (local), (%)	Avg. local vertical strain initial, ϵ_{z_i}, (%)	Avg. local vertical strain final, ϵ_{z_f}, (%)	Avg. local volumetric strain initial, ϵ_{V_i}, (%)	Avg. local volumetric strain final, ϵ_{V_f}, (%)
1	12.5	3.0	10.7	14.6	20.8	19.4	0.038	0.33	0.90	0.56	1.04
2	26.4	5.9	21.3	22.3	27.4	30.5	0.053	1.45	2.90	1.37	1.82
3	36.3	8.0	28.5	28.1	34.5	40.0	0.056	2.96	3.78	1.87	1.93
4	50.9	11.0	39.2	32.9	44.5	51.3	0.059	3.84	4.88	1.98	2.19
5**	82.0	17.0	60.6	47.6	65.2	76.6	0.062	4.98	6.56	2.28	2.33
CTX+1v2$_i$											
1	14.1	3.0	10.4	13.4	28.2	25.7	0.028	0.19	0.31	0.10	0.22
6	14.3	3.2	18.1	16.9	22.6	20.5	0.070	0.35	1.42	0.26	0.61
11	14.5	3.4	33.6	21.5	29.4	26.9	0.107	1.50	3.86	0.69	2.09
2	28.5	6.0	21.2	26.7	48.9	42.3	0.034	3.95	3.92	2.18	2.14
7	28.6	5.8	36.7	29.5	41.2	36.7	0.080	3.91	4.15	2.13	2.38
CTX+1v2$_{ii}$											
2	28.0	6.1	21.1	20.8	34.9	30.8	0.046	0.80	1.50	0.67	0.81
7	28.0	6.2	36.7	25.5	38.7	36.4	0.081	1.54	3.47	0.85	2.14
12**	28.1	6.5	69.0	36.1	53.2	54.0	0.116	3.53	6.69	2.21	5.38
CTX+1v2$_{iii}$											
3	38.4	8.0	28.4	25.0	34.8	33.0	0.060	1.02	2.50	0.97	1.22
8**	38.5	7.7	49.1	31.8	41.9	40.1	0.101	2.55	5.17	1.27	2.59
CTX+1v2$_{iii^m}$											
3	39.1	5.8	26.2	24.6	34.7	27.1	0.067	1.80	2.96	0.96	1.06
8**	39.1	5.8	47.0	31.0	44.0	35.3	0.105	3.02	5.48	1.13	2.56

** $\epsilon_z > 5\%$